Magnetically driven jets and winds launched from turbulent accretion disks

Jonatan Jacquemin Ide

To cite this version:

Jonatan Jacquemin Ide. Magnetically driven jets and winds launched from turbulent accretion disks. Astrophysics [astro-ph]. Université Grenoble Alpes [2020-..], 2021. English. NNT : 2021GRALY055 . tel-03576454

HAL Id: tel-03576454
https://theses.hal.science/tel-03576454
Submitted on 16 Feb 2022

THÈSE

Pour obtenir le grade de

DOCTEUR DE L'UNIVERSITE GRENOBLE ALPES

Spécialité : Astrophysique et Milieux Dilués

Arrêté ministériel : 25 mai 2016

Présentée par

Jonatan JACQUEMIN IDE

Thèse dirigée par **Jonathan FERREIRA**, Professeur des Universités, Université Grenoble Alpes, et
codirigée par **Geoffroy LESUR,** chargé de recherche**,** Université Grenoble Alpes

préparée au sein de **L'Institut de Planétologie et d'Astrophysique de Grenoble**
dans **l'École Doctorale de Physique de Grenoble**

Magnetically driven jets and winds launched from turbulent accretion disks

---

Jets et vents émis et accélérés magnétiquement par les disques d'accrétion turbulents

Thèse soutenue publiquement le **30 septembre 2021**,
devant le jury composé de :

Monsieur Fabien CASSE
Professeur des universités, Université de Paris,
Rapporteur
Monsieur Gordon OGILVIE
Professeur, University of Cambridge,
Rapporteur
Monsieur Zhaohuan ZHU
Professeur associé, University of Nevada,
Examinateur
Monsieur Claudio ZANNI
Ingénieur docteur, INAF (Istituto Nazionale di Astrofisica),
Examinateur
Monsieur François MÉNARD
Directeur de recherche, CNRS Delegation Alpes,
Examinateur
Monsieur Gilles HENRI
Professeur des universités, Université Grenoble Alpes,
Président du jury

Acknowledgements

The work presented within this manuscript is the results of 3 years of work at the Institut of Planetology and Astrophysics of Grenoble (IPAG). While the Pandemic occupied two-thirds of them, they were, still, some of the best years of my below-average length life. The times were hard, but the struggle made in some way the experience worthwhile.

I want to thank François-Xavier Désert, the previous director of the IPAG, for receiving me into the laboratory during the beginning of my Ph.D. I'm also grateful to Guillaume Dubus, current director of the IPAG, for not kicking me out of the Institut after he took charge.

I wanted to thank all the members of my jury: Fabien Casse, Gordon Ogilvie, Claudio Zanni, Gilles Henri, Zhaohuan Zhu and, François Ménard. Special regards to Fabien Casse and Gordon Ogilvie for reviewing this manuscript. I also want to give a special acknowledgment to Gilles Henri for being the president of my Jury.

I want to express my deepest gratitude to both of my advisors Jonathan Ferreira and Geoffroy Lesur for taking me under their wing and teaching me everything I know about accretion disks. I feel extremely lucky to have had them as my advisors and, I believe that their skills and teachings complemented each other perfectly. Both the theoretical aspects and the numerical details were covered. I believe that their differences, often expressed in hour-long discussions, also allowed me to learn a lot and led me to be a more complete person and researcher. Last but not least, they are both dear friends to me and advised on more than science and for that, I'm very thankful.

I want to thank the SHERPAS team for welcoming me. I think there is no other team with such fun and exciting energy. I learned a lot of things during the team meetings. Especially things that could not be learned directly from my advisors. The sherpiades were an enriching experience and an amazing part of my stay in Grenoble.

I want to acknowledge the computing resources without which this manuscript would not have been possible. Indeed, this work was granted access to the HPC resources of TGCC under the allocation A0080402231 attributed by GENCI (Grand Equipement National de Calcul Intensif). All the data reduction presented in this paper was performed using the GRICAD infrastructure, which is supported by Grenoble research communities.

I also want to thank my fellow graduate students that accompanied me during the 3-year long Ph.D. Be it discussions about science, politics, or even anime there was no lack of fun to be had. Some of them require a special mention, my deepest apologies for the ones that are not featured on the page as I'm not the best at being exhaustive. I want to thank Aloïs and Guillaume G. for their company, especially on the breaks and trips to the cafeteria of which they were many. I want to mention Benjamin, Aloïs (again) and, Nico for our scientific discussions. I learned a lot during them. Finally, I want to thank Flo, Guillaume B., and Benjamin (again) for their support during the postdoc job hunting. That was a very stressful time for me and, being in the same boat during that time helped me a lot.

Finally, I also want to acknowledge my family and my non-physicist friends. I want to thank my father and sister as they were there when I needed them. I want to thank my roommate Mariel

as she had to endure my mental state during my Ph.D. I also want to thank Kim (even though he is a physicist) and Aline for their help with the adult aspects of french life. I want to also acknowledge Mel and Lou were there when I needed an escapade from my work.

To the memory of my mother. Who was always supportive and proud of my career as an astrophysicist. Those memories came to me in the hardest times and helped me push through.

Summary

We observe Accretion disks around several astrophysical objects across different length scales and at very different wavelengths. Accretion disks are detected around several objects: newborn stars, compact objects in binary systems, white dwarfs in binary systems, supermassive black holes, etc. In all cases, the accretion disk has a considerable impact on the emission properties of the object. Signatures of outflows, be it jets or winds, are often observed around accretion disks. Outflow ejection from accretion disks seems to be a ubiquitous process. Moreover, it is possible to measure a correlation between the outflow emission and the accretion signatures, showing that both processes are interrelated.

Disks around compact objects, like X-ray binaries and dwarf novae, are subject outbursts, powerful events where the luminosity of the system increases by several orders of magnitude. Outbursts are incredibly useful as they allow us to constrain the secular evolution of the accretion disk system. Hence, we can measure the long-term effects of accretion on the system.

Accretion is the consequence of angular momentum transport in the accretion disk system. When angular momentum is removed from the system, the matter, prived from its rotational support, falls into the central object. Angular momentum can be transported radially through turbulent torques or evacuated from the system by an outflow. Historically both processes have been studied separately: (1) effective 2D models have been used to study the vertical laminar torque imposed by an outflow, (2) while 3D shearing box simulations have been used to model turbulent torques. Nonetheless, both processes appear naturally in the presence of a large-scale vertical magnetic field.

Shearing box models excel at modeling the turbulence but can not accurately compute the dynamics of the outflow. In contrast, effective 2D models accurately compute the dynamics of the outflow, but they cannot resolve the 3D turbulence. Thanks to numerical improvements, it is now possible to accurately compute both torques. Indeed, 3D global simulations can accurately compute the dynamics of the outflow while resolving the turbulence. These 3D global simulations show a very different structure to the 2D effective models and point towards not understood physics. Moreover, these recent simulations show that it is possible to compute outflows with a weak magnetic field. In contrast, with self-similar solutions where no weakly magnetized solutions have been computed.

However, 3D global simulations prove difficult to compare with observations due to how numerically expensive they are. Hence, 2D effective models are still useful for comparison with observations and thus need to be educated by 3D global simulations.

In this manuscript, we attempt to bridge the gap between 2D effective models and global simulations. We focus on self-similar models, which are a kind of 2D effective model. First, we compute new weakly magnetized self-similar models. We analyze their properties and compare them with state-of-the-art numerical simulations of weakly magnetized accretion disks. Second, we compute global simulations of accretion disk emitting magnetized outflows. We analyze the global simulations and understand why their vertical structure is different from the one computed

in 2D effective models. We then constraint the secular evolution in the system and examine how it evolves as a function of the magnetic field strength. Finally, using the insight from our 3D global simulations, we construct a new turbulence model that will lead to more accurate 2D effective models.

Résumé

Les disques d'accrétion sont observés à différentes échelles spatiales et à différentes longueurs d'onde au voisinage d'une grande variété d'objets astrophysiques : étoiles en formation, binaires comprenant un objet compact ou une naine blanche, trous noirs supermassifs,... Ces disques ont un impact considérable sur les propriétés radiatives de l'objet. Par ailleurs, plusieurs observations suggèrent la présence d'écoulements, jets ou vents, émanant du disque. Ces écoulements sont extrêmement répandus et semblent être intrinsèquement liés aux disques d'accrétion. De plus, il est maintenant possible de mesurer une corrélation entre les propriétés de l'écoulement et de l'accrétion, illustrant l'interdépendance de ces deux phénomènes. Les disques autour d'objets compacts (binaires X ou novae naines), en particulier, sont extrêmement variables : la luminosité du système peut augmenter de plusieurs ordres de grandeur lors de "sursauts". Ces sursauts sont extrêmement utiles pour contraindre l'évolution séculaire du disque d'accrétion, et peuvent permettre de mesurer sur le long terme l'impact de l'accrétion sur le système.

L'accrétion résulte d'un transport de moment cinétique dans le disque. Lorsque la matière accrétante perd du moment cinétique, elle perd son inertie centrifuge et tombe vers l'objet central. Le transport radial de moment cinétique peut avoir lieu par l'intermédiaire d'un couple turbulent, ou peut être dû à un écoulement emportant au loin le moment cinétique du système. Historiquement, ces deux processus ont été étudiés séparément. Des modèles 2D effectifs ont été utilisés afin d'étudier le couple laminaire dû à la présence de l'écoulement , tandis que des simulations 3D locales, avec cisaillement, ont permis de modéliser le couple turbulent. Cependant, ces deux processus résultent de la présence d'un champ magnétique vertical ordonné, à grande échelle. Les simulations locales 3D capturent parfaitement la turbulence, mais sont incapables de modéliser précisément la dynamique de l'écoulement. A l'inverse, les modèles 2D effectifs capturent cette dynamique, mais ne peuvent résoudre la turbulence (qui est intrinsèquement tridimensionnelle).

Dans cette thèse, nous étudions des modèles auto-similaires, qui sont un cas particulier de modèle effectif 2D. De plus, l'amélioration des performances des supercalculateurs permet maintenant d'étudier à la fois les couples laminaire et turbulent dans une même simulation globale 3D. De telles simulations montrent des différences importantes par rapport aux modèles 2D effectifs, indiquant que la physique de ces disques reste mal comprise. De plus, ces simulations ont montré qu'il était possible de produire des écoulements à faible champ magnétique, ce qui entre en contradiction avec les prédictions des modèles auto-similaires. Malgré tout, les simulations 3D globales sont numériquement coûteuses, rendant leur comparaison avec les modèles 2D difficile. Ceux-ci restent un outil utile pour l'interprétation des observations, à condition qu'ils soient éduqués par des simulations 3D.

Dans cette thèse, nous cherchons à combler le fossé entre modèles 2D effectifs et simulations globales 3D. Tout d'abord, nous découvrons de nouvelles solutions auto-similaires faiblement magnétisées. Nous analysons leurs propriétés, et les comparons avec les simulations de disques faiblement magnétisés les plus récentes. Ensuite, nous réalisons des simulations globales de

disques d'accrétion avec écoulements. Nous analysons en particulier leur structure verticale, et expliquons les raisons derrière la différence avec les modèles effectifs 2D. Nous étudions également l'évolution séculaire du système, et détaillons la dépendance de cette évolution avec l'intensité du champ magnétique. Enfin, à partir de la compréhension acquise de ces simulations 3D, nous construisons un nouveau modèle de turbulence, qui conduira à la mise en place de modèles effectifs 2D plus précis.

Contents

CHAPTER 1

Introduction

Accretion disk emitting outflows are observed across many different scales and in many different astrophysical objects. It seems clear that accretion-ejection is a universal mechanism tightly linked to the transport of angular momentum. In this introduction, we first describe the observational properties of 3 distinct accretion disks: (1) Protoplanetary disks, (2) X-ray binaries, and (3) Dwarf novae. Our objective is not to give a complete picture of each observational field and the different modeling methods for each astrophysical object but to detail, the different constraints those objects impose on accretion and ejection. We then describe the evolution of accretion theory and the different modeling methods to study angular momentum transport. We follow that by describing the models that try to account for the secular evolution of accretion disks. Finally, we describe the aims of this manuscript and how we approach addressing those questions.

1.1 Observational properties of accretion and ejection in protoplanetary disks

In this section, we describe the accretion and ejection properties of protoplanetary disks. We mainly discuss the accretion and ejection properties of class 2 protostars also called T Tauri stars.

The first observations of jet-like outflows were performed in the 50's by Herbig 1951 and Haro 1952. We show in Fig. (1.1,top) the nebulous patches they discovered, in Orion. These objects were later named after them. The detection of velocities within Herbig-Haro objects had to wait the invention of the CCD. Snell et al. 1980 were able to detect, using the emission from the CO molecule, diametrically opposite red-shifted and blue-shifted lobes seen moving at velocities of a few tens of km s^{-1}. It was latter confirmed that the emission from the optical lines, seen in Herbig-Haro objects, was along the same axis as the molecular emission, the optical emission was being enclosed within the molecular emission (Snell and Schloerb 1985). The atomic and molecular outflows were both found to be emitted by young stellar objects (Snell et al. 1980; Snell and Schloerb 1985). We may call the atomic outflows jet-like outflows and the molecular outflows wind-like outflows.

T Tauri stars were classified as a separate class because of their peculiar spectral properties (Herbig 1962). To explain the presence of $H\alpha$ and Ca II H emission in the spectrum of a cool star several models were proposed: spherical accretion, spherical winds, strong chromosphere and hot envelopes. There was rapid convergence around the accretion disk paradigm proposed

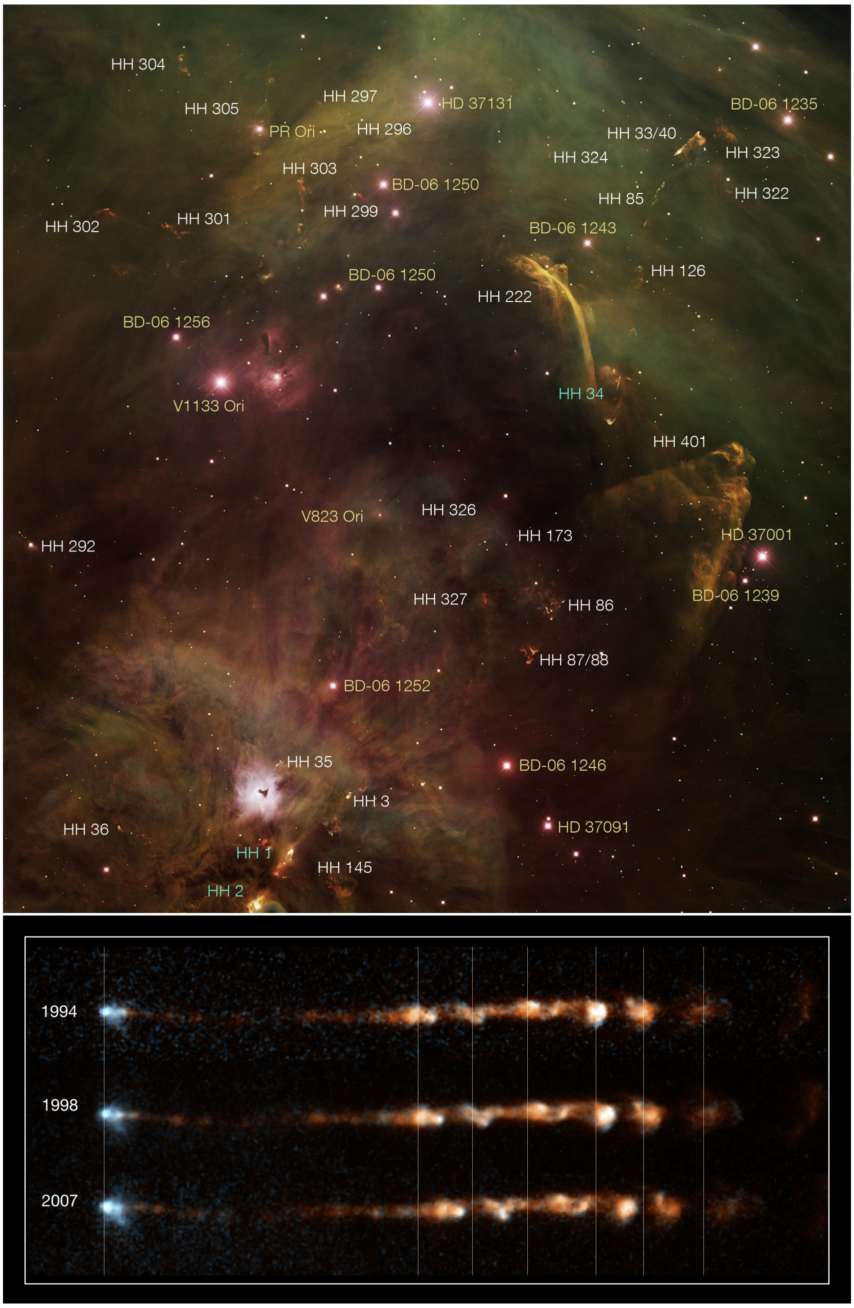

Figure 1.1: (top) This image from the Kitt Peak National Observatory shows the constellation of Orion. We can recognize multiple Herbig-Haro objects labelled here in white. Copyright: Z. Levay (STScI), T.A. Rector (University of Alaska Anchorage), and H. Schweiker (NOAO/AURA/NSF). (bottom) These images taken by the NASA/ESA Hubble Space Telescope show Herbig-Haro 34 (or HH 34). We can see the knot structures propagating with time. Copyright: NASA, ESA, and P. Hartigan (Rice University).

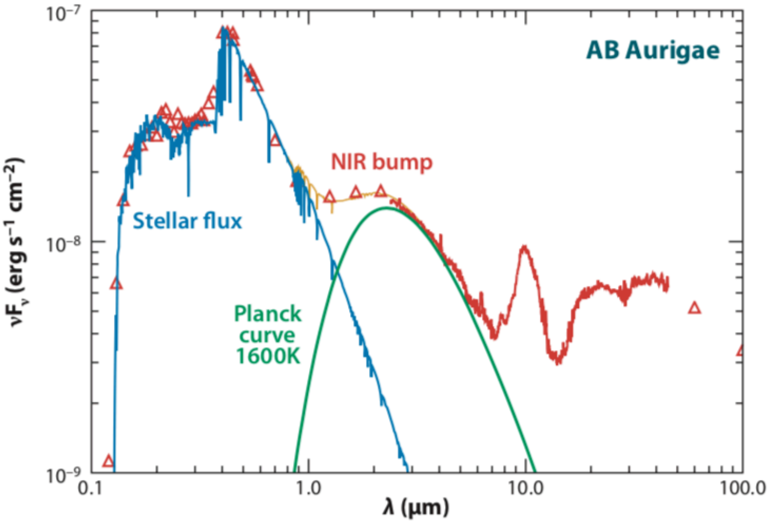

Figure 1.2: The spectral energy distribution of the Herbig Ae star AB Aurigae. Red is the measured emission. Blue is the steller spectrum predicted with a Kurucz stellar atmosphere model. The excess of flux above the atmosphere (the “IR excess”) is the thermal emission from dust in the disk. The emission in the near-IR (NIR) clearly has a bump-like structure and is often called the NIR bump. In green, a Planck curve at a temperature of 1,600 K is overplotted. The golden curve is the sum of the Planck curve and the stellar atmosphere. Adapted from Dullemond and Monnier 2010.

by Lynden-Bell and Pringle 1974, inspired by the success of Shakura and Sunyaev 1973 in X-ray binaries (see next section). In this paradigm, the star is surrounded by a disk that is constantly feeding it with matter. The transport of angular momentum becomes important, as it is transported outwards by turbulent viscous stresses and controls the accretion.

This picture was latter confirmed by observations of the near infrared excess. Cohen and Kuhi 1979 showed that the measured infrared excess was inconsistent with a spherical dust geometry. Moreover, the shape of the near infrared excess in T Tauri stars was shown to be consistent with models of irradiated dusty disks with a flat (Adams and Shu 1986) or flared (Kenyon and Hartmann 1987) geometry. In Fig.(1.2) we show the spectrum of AB Aurigae, we can recognize how the NIR excess is a consequence of the disk emission, modeled in this case as a Planck spectrum. Finally, Terebey et al. 1984 confirmed, using hydrodynamical simulations of gravitational collapse, that excess angular momentum from the parent cloud accumulates on an accretion disk that forms around the central star.

Let me comeback to the electromagnetic emissions from jet-like outflows. The electromagnetic emission (in optical and near infrared wavelengths) is due to a combination of permitted and forbidden lines. The presence of forbidden lines implies that electron densities are low ($\sim 10^4 \mathrm{cm}^{-3}$) within the emitting regions of the jet (Hartigan et al. 1995). The line emission in Herbig-Haro objects is a consequence of the cooling shock zones within the jet, rather than photoionization, as first recognized by Schwartz 1977. Indeed, the velocity variation within the ejecta implies that faster material catches up slower material ahead of it (Raga and Kofman 1992). This leads to the formation of ”working surfaces” or internal shocks that can be observed as knots within the jet emission (Fig. 1.1,bottom). The existence of knot structures is thus evidence for secular variability in the ejection or the presence of a instability that disrupts the jet structure.

YSO jets are highly supersonic with Mach numbers, $M_j \sim 30$, (Ray and Ferreira 2020)

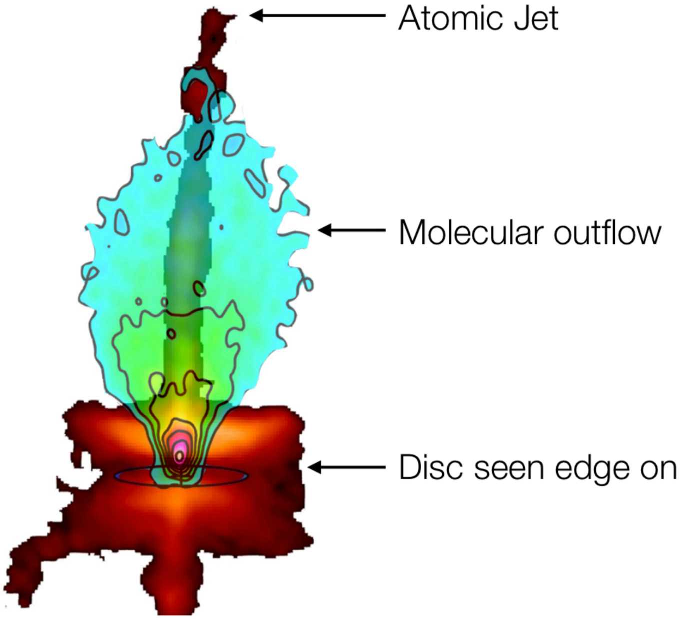

Figure 1.3: Observation of a disc and an atomic jet seen by the Hubble Space Telescope (Burrows et al. 1996) and a molecular wind observed in CO(2-1) by ALMA (Louvet et al. 2018) in HH30, a protoplanetary disc seen edge-on. Courtesy of F. Louvet. Adapted from Lesur 2020.

where M_j is the jet velocity divided by the sound speed. The opening angle of jet-like outflows, θ_j, is consistent with an unconfined supersonic flow, for which $\theta_j \sim \frac{1}{M_j}$. We can conclude that jets, for the most part, are not necessarily confined laterally. However, this is only relevant at a distance of several hundreds of AU from the source. Closer to the source, the jet-like outflows still need to be launched and collimated. Snell et al. 1980 proposed that an external pressure gradient (created by the envelope) could collimate a stellar wind forming thus a jet. However, such a configuration would be unstable and could not explain jets from old protostars, that lack an envelope. The only possible mechanism that can focus the jet close to the star is a magnetic field (Cabrit 2007).

Thanks to the development of adaptive optics and to the launch of the HST, a multitude of compact optic jets have been detected being launched from T Tauri stars (Burrows et al. 1996; Bacciotti et al. 2000; Dougados et al. 2000; Agra-Amboage et al. 2011, 2014). These observation measure velocities of $100 - 400\mathrm{km\ s^{-1}}$ and are able to resolve the transverse structure of the jet at small scales. They also reveal an onion-like structure in which the outer regions have lower velocities, $< 100\mathrm{km\,s^{-1}}$. In Fig. (1.3) we show the atomic jet, the molecular outflow and the disk of HH 30. The high velocity jets from T Tauri stars appear extremely poor in molecules. Molecules are only visible at the base of the outflow (Louvet et al. 2018).

Outflow are now observed being emitted from many young stellar object of different masses and evolutionary phases. However, the presence of an outflow is always accompanied by the presence of an accretion disk around the young stellar object (Ray and Ferreira 2020). It may seem that an accretion disk is needed for a jet to be launched. Moreover, a correlation between the forbidden line luminosity of [OI] and the infrared excess (Cabrit et al. 1990) links the mass loss rate of the jet with the mass accretion rate of the disk. These correlations were calculated explicitly by Hartigan et al. 1995. They use the veiling flux to compute the mass accretion rate. In T Tauri stars the absorption lines are partially filled in, this is known as veiling and is believed to represent the continuum flux emitted by the accretion shock on the surface of the star. It is

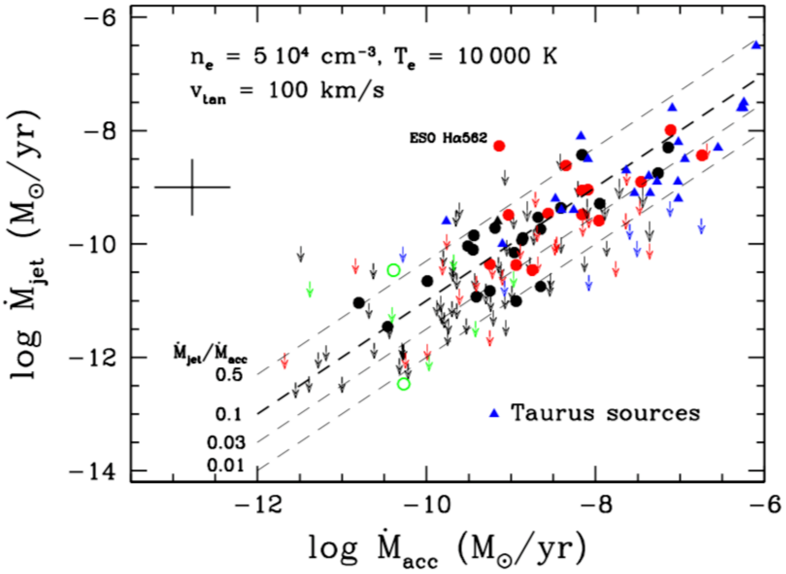

Figure 1.4: Mass ejection rate, $\dot{M}_j$ as a function of the mass accretion rate, $\dot{M}_a$, for 131 T Tauri stars. The different colors indicate sources from different clouds. Adapted from Nisini et al. 2018.

therefore a robust method to measure the accretion rate, $\dot{M}_a$, on the T Tauri star (Venuti et al. 2014). They then compare the value obtained with this method to the value obtained using the infrared excess. Hartigan et al. 1995 then measured the velocity of the jet and estimated the density of the jet using the forbidden line emission, from this they computed the mass loss rate $\dot{M}_j$. The mass loss rate was shown to be highly correlated with the mass accretion rate.

We show this correlation in Fig. (1.4) adapted from Nisini et al. 2018, they measure $\dot{M}_j \sim 0.1\dot{M}_a$. This correlation shows that the processes of accretion and ejection must be dynamically linked. This could be easily explained if the jet-like outflows are magnetically driven winds (Blandford and Payne 1982). The dynamical engine of jets in T Tauri is still highly disputed (Ray and Ferreira 2020). However, the three main contenders are of magnetic origin (Ferreira et al. 2006a):

- A disk wind, driven by magnetic field lines threading the disk. It can come in two forms: (1) an extended magneto-centrifugal disk wind being ejected from the whole disk (Ferreira 1997), (2) or a localized X-wind that is ejected from one annulus close to the central object (Shu et al. 1994).
- The magnetic field lines of the stellar dipole can open at the pole and lead to the ejection of stellar winds that remove angular momentum from the star (Sauty et al. 2002; Matt and Pudritz 2005).
- The star-disk interaction can drive magnetospheric ejections. These ejections depend on the configuration of the magnetic field (parallel or anti-parallel) but always lead to non-steady ejection (Ferreira et al. 2006a). In the parallel configuration a non-steady wind, called Re-X-Wind, appears (Ferreira et al. 2000). In the anti-parallel configuration, the ejection takes the form of CME-like ejecta that are episodic (Hayashi et al. 1996; Zanni and Ferreira 2013).

Bacciotti et al. 2002 were able to measure the rotation velocity of a jet-like outflow. Hence, jets have an azimuthal component and thus a 3D velocity structure. As we discuss below the

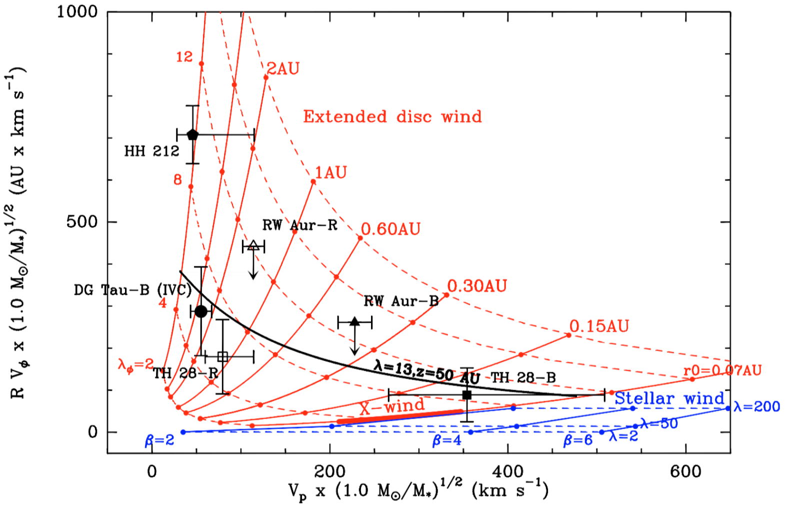

Figure 1.5: Comparison of predicted specific angular momentum vs. poloidal velocities with observations of T Tauri microjets. Full and dashed curves show expected theoretical relations for MHD disc and stellar winds. Adapted from Ferreira et al. 2006a.

rotational signatures are crucial for constraining the ejection processes. However, it must be noted that the measurements of jet rotation are very imprecise due to the low spectral resolution of HST. Anderson et al. 2003 and Ferreira et al. 2006a showed that the asymptotic properties of an outflow could be used to constrain the theoretical models of the launching engine behind the outflow. Indeed, by measuring the terminal velocity and angular momentum of the outflow it is possible to constrain the launching radii, R_0, and the magnetic lever arm, λ of the outflow. The magnetic lever arm is an MHD invariant (see more details section 2.5.1), it is a measure of the angular momentum of the outflow and can be linked to its terminal velocity. Therefore, λ is deeply linked to the acceleration efficiency of the outflow by the disk, λ can thus be used to differentiate outflow solutions from one another. In Fig. (1.5) we show the asymptotic angular momentum as a function of the terminal velocity for different jet-like outflows. Ferreira et al. 2006a use those values to constrain the ejection radii as well as the magnetic lever arm. We can conclude that the values of λ are constrained between 4 and 12 which is consistent with an MHD driven disk-wind (Casse and Ferreira 2000b). Figure (1.5) shows that the X-winds and stellar models do not agree with observations as they lack angular momentum.

The engine behind the launching of molecular outflows is still not clear. Snell et al. 1980 were the first to observe a molecular outflow and they attributed the structure to a wind driven shell (Shu et al. 1991). In this paradigm the molecular outflow is a consequence of an interaction between a stellar or X wind and the infalling envelope remaining from the star formation process. The second paradigm was first proposed by Pudritz and Norman 1983, where they interpreted the molecular outflows as MHD winds being emitted from the outer regions of the accretion disk.

Thanks to the dramatic improvements in resolution achieved by ALMA we are starting to constrain the engine behind the launch of molecular outflows. In Fig.(1.6) we show the outflow of DG tau b observed by ALMA in exquisite detail, we recognize the onion like structure and the red/blue shifted emission from the disk. It may seem objects that are consistent with one or the other object are readily available:

- Wind driven shells models have successfully reproduced the molecular outflows of HH 46/47 (Zhang et al. 2016, 2019).

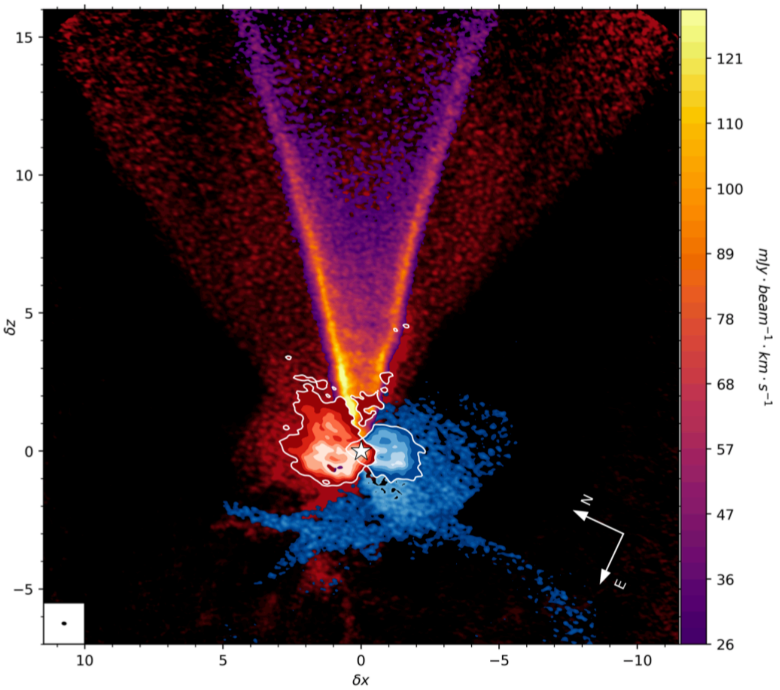

Figure 1.6: Summary of the various kinematical components in DG Tau B: The inner conical the ^{12}CO flow is shown in purple to yellow shades. The individual low-velocity ^{12}CO channel maps at are shown in red and blue shades. Inside the white contours, the ^{13}CO channel maps are shown in blue and red highlighting the upper and lower disk surfaces Adapted from de-Valon et al. 2020.

- MHD driven winds have been found to reproduce the structure of a considerable amount of molecular outflows (Launhardt et al. 2009; Bjerkeli et al. 2016; Hirota et al. 2017; Louvet et al. 2018; de-Valon et al. 2020).

We can apply the methods developed by Ferreira et al. 2006a to constrain the kinematics on various outflows: (1) In HH30, Louvet et al. 2018 estimate $\lambda \simeq 1.6$ and a launching radius $R_0 \simeq 1.5$ au. (2) While de-Valon et al. 2020 measure $\lambda \simeq 1.6$ and $R_0 \simeq 2$ au for DG Tau B. (3) Hirota et al. 2017 measure a launching radii $R_0 \simeq 10$ au, using their observations we can compute $\lambda \simeq 1.6$ in Orion Source 1. (4) From the data reduction of Bjerkeli et al. 2016 we can compute $R_0 \simeq 4$ au and $\lambda \simeq 4$. We conclude that if molecular outflows are MHD-driven winds then they must have very small values of λ. Indeed, the magnetic lever arm is in the range $1.5-4$ for all outflows.

Thanks to ALMA we are now able to probe the radial structures of protoplanetary disk with exquisite detail (cf Andrews et al. 2018). Even though these observation probe the dust distribution within the disk, they are very useful for constraining the formation of exotic structures, like rings and vortices, within the disk. For example Teague et al. 2019 have been able to constrain the kinematics of the gas and were able to compare them to the kinematics of the dust using simultaneous observations in continuum and line emissions. They were able to measure meridional motions within the disk. Najita et al. 2021 used high-resolution infrared spectroscopy to probe the surface of the disk. They discovered a supersonic accretion flow at the surface of the disk. This measurement may provide an observational test for accretion theories.

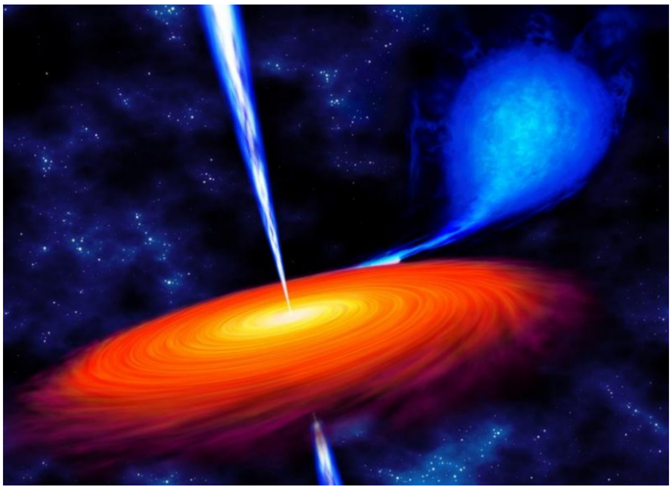

Figure 1.7: An artist's impression of the Scorpius X-1 LMXB system. (Courtesy of Ralf Schoofs)

1.2 Observational properties of accretion and ejection in X-ray binaries

Giacconi et al. 1962 where the first to observe an extrasolar source of X-ray radiation, it was discovered in the constellation of scorpio and is named ScoX1. Morton 1964 suggested that the X-ray emission of the object could be related to a compact object, a neutron star. Bowyer et al. 1965 discovered a second Xray source in the sky, Cygnus X1.

In 1972, Cygnus X1 is found to be composed of a spectrum that varies with a period of 5/6 days (Webster and Murdin 1972). The spectral variation is strong evidence of Cygnus X1 being a binary system with an orbit period of 5/6 days. That same year, Tananbaum et al. 1972 observed for the first time an X-ray transition for Cygnus X1. They report a remarkable change on the average X-ray intensity, with a decrease of about a factor of 2 on the $2-6\,\mathrm{keV}$ energy range and an increase of a factor of 2 in the $10-20\,\mathrm{keV}$ range. They also describe that a weak radio source suddenly appeared after the transition, this radio signal was also described by Hjellming and Wade 1971.

Pringle and Rees 1972 and Shakura and Sunyaev 1973 propose that such systems could be a binary system composed of a star and a compact object: A black hole or a neutron star. In such a system, the mass would flow from the star to the compact object through Roche overflow. The accumulation of matter around the compact object forms an accretion disk around it (Fig. 1.7).

Angular momentum transport becomes now essential as the gas needs to lose angular momentum for it to fall towards the compact object. Even though Shakura and Sunyaev 1973 did not propose a physical process, they already understood that the magnetic field and turbulence would have an important role in driving the turbulent torque. The accretion process feeds on the gravitational energy: the closer we are to the compact object the more energy will be available. Compact objects like black holes or neutron stars have very small inner radii which lead to enormous amounts of gravitational energy (Pringle and Rees 1972). The gravitational energy ends up feeding the turbulence which dissipates into heat, the heat is then irradiated as X-rays.

It is now clear that X-ray binaries transition between very different spectral (hard and soft) and luminosity (outburst or quiescence) states (Done et al. 2007). We do not discuss the precise properties of each state or the transition between them as it is outside the scope of this introduction. Nonetheless, we show in Fig. (1.8) a typical outburst of an LMXRB. Figure (1.8) shows

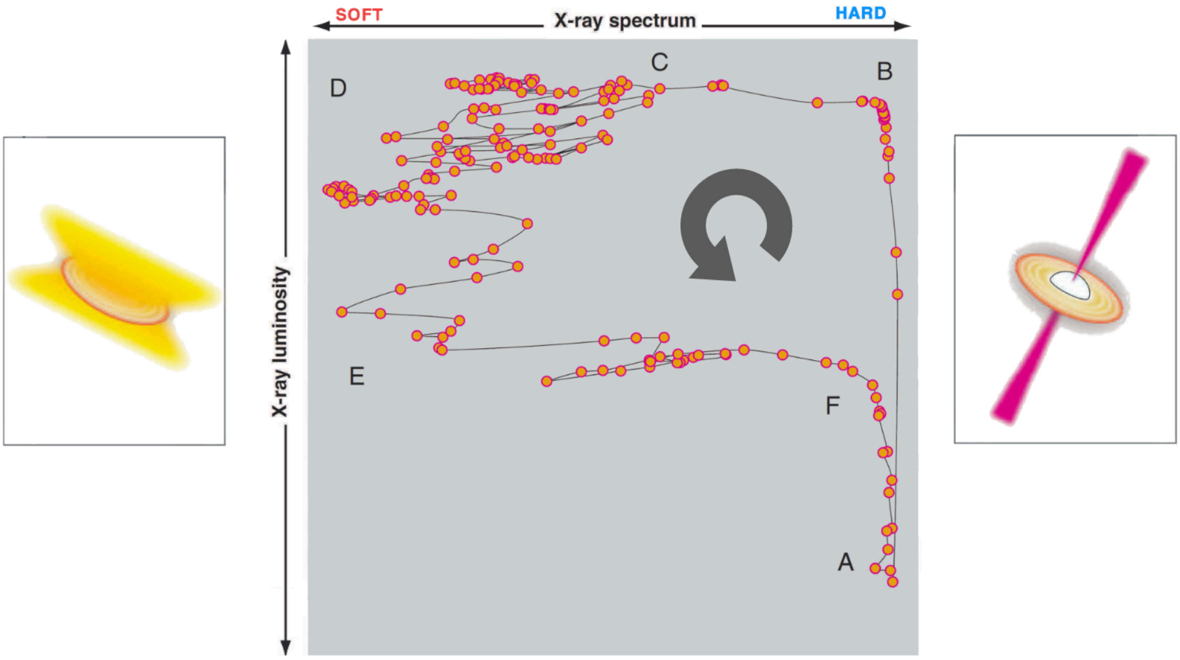

Figure 1.8: Typical outburst of an X-ray binary showing its X-ray luminosity as a function of the Hardness of the spectrum. The sketch on the left shows that wind-like outflows are present when the system is in the soft state, while the sketch on the right shows that jet-like outflows are present when the system is in the hard state. The system will evolve by following the arrow. Figure from G. Marcel's thesis, adapted from Zhang 2013

the X-ray luminosity as a function of the spectrum hardness ratio. The hardness ratio is a measure of whether the flux of the hard photons, with energies of $10-20\,\mathrm{keV}$, dominates the flux of the soft photons, with energies of $2-10\,\mathrm{keV}$. In Fig.(1.9) we show two different spectra of an LMXRB that underwent an outburst. We see that the flux from the high-energy photons is more important during the hard state.

The radio component of the spectrum, likely the signature of a jet-like outflow (see below), is only visible on the hard state (Corbel et al. 2003; Fender et al. 2009). In addition, the absorption lines, a signature of a wind-like outflow (see below), are only visible in the soft state (Ponti et al. 2012, 2016). See also Fig. (1.8).

The radio component detected on X-ray binaries has some properties that can be associated with a jet-like outflow: the flat spectrum, the relative steadiness, and the lack of polarization suggests that the emission originates from a continuously replenished partially self-absorbed outflow (Corbel et al. 2000). This emission is reminiscent of what was observed in AGN jets (Blandford and Königl 1979). Furthermore, some sources were confirmed to be situ of superluminal motions (Mirabel and Rodríguez 1994). The presence of superluminal motion is strong evidence of the radio emission being a consequence of a jet-like outflow.

It's hard to derive stringent theoretical constraints from X-ray binaries as we only have access to the SED and the variability. Indeed, the only way to determine the accretion rate is by using a model where $\dot{M}_a$ is used as a fitting parameter. All estimations of the accretion rate are thus model dependent (Ghosh et al. 2010; Nagarkoti and Chakrabarti 2016; Marcel et al. 2018a, 2019). This is even more true for estimates of the jet properties, like velocity or power. However, the change of luminosity during the higher luminosity can be easily linked with a higher accretion rate. Indeed, the outburst state has a higher accretion rate than the quiescent state.

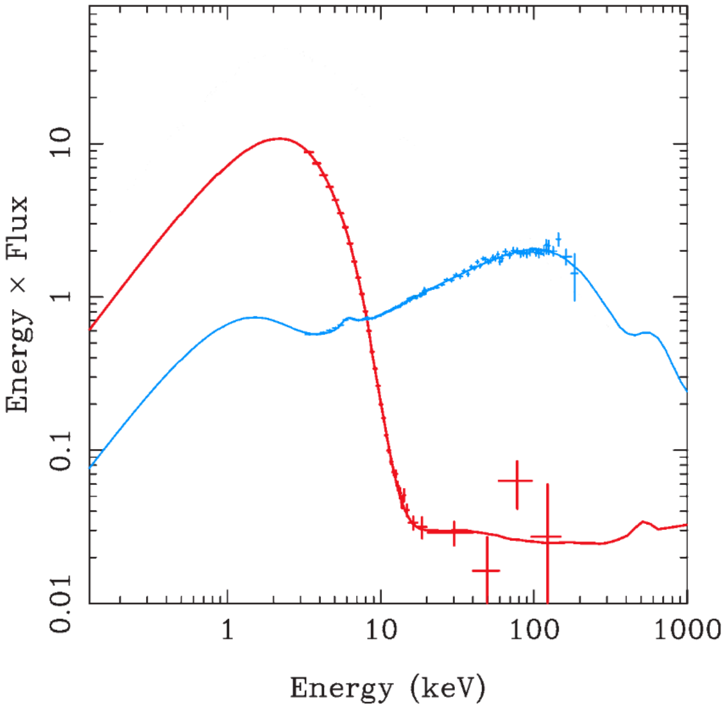

Figure 1.9: Spectra of GRO J1655-40 during its outburs in 2005. We show the hard state (blue) and the soft state (red). Figure from G. Marcel's thesis, adapted from Zhang 2013.

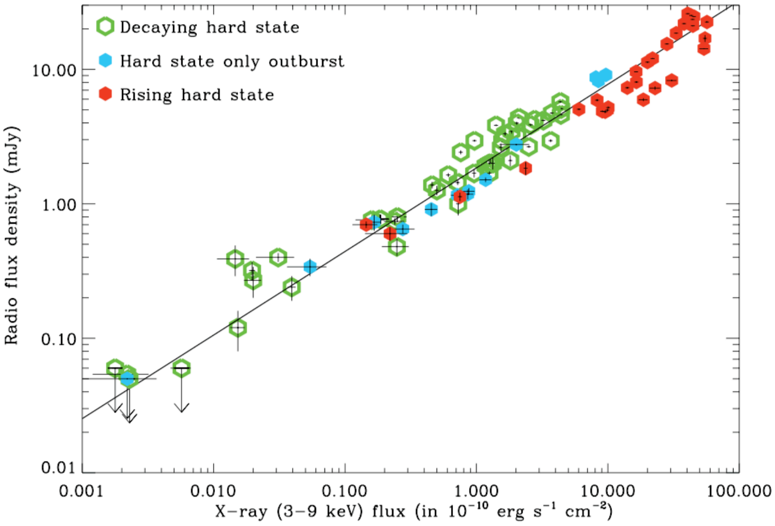

Figure 1.10: Correlation between X-ray (3-9keV) and radio (8.6GHz) for 14 years of observation of GX 339-4. The solid line show the correlation $F_R \propto F_X^{0.62}$. Adapted from Corbel et al. 2013.

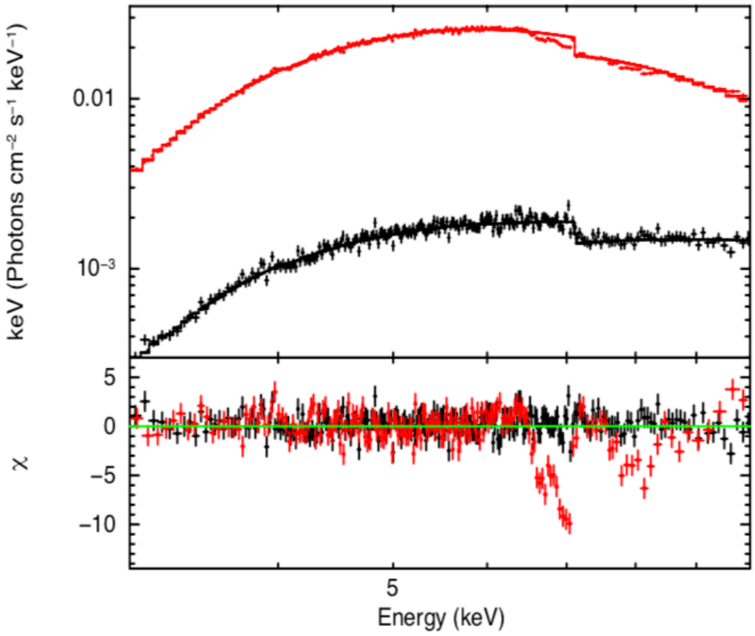

Figure 1.11: XMM-Newton X-ray spectra of AX J1745.6-2901 during the soft (red) and hard (black) states. We observe absorption features in the soft state that are not visible in the hard state. Adapted from Ponti et al. 2016

It is possible to measure a correlation of the X-Ray luminosity, which is expected to be coming from the disk, and the radio luminosity that should be emitted from the jet. Hjellming and Wade 1971 had already observed that the radio luminosity seem to increase when the X-ray luminosity increased. However, it was not until the work of Corbel et al. 2003 that the correlation was properly constrained. We show in Fig.(1.10) the results of Corbel et al. 2013. They show the correlation extracted from the hard states of multiple Outburst of GX 339 - 4 measured between 1997 and 2011. They show, in the same manner as Corbel et al. 2003, the radio (8.6GHz) luminosity as a function of the X-ray (3-9keV) luminosity. We see an impressive correlation, $F_R \propto F_X^{0.62}$, on 5 orders of magnitude in Fig.(1.10). The exact reasons for this correlation are still unclear. However, such a correlation indicates that the dynamic processes of accretion and ejection must be linked.

The latest generation X-ray telescopes lead to the discovery of narrow absorptions lines (Brandt and Schulz 2000; Lee et al. 2002; Parmar et al. 2002; Tetarenko et al. 2018), a new component in the spectrum of X-ray binaries. The absorption lines are observed to be variable and produced by a highly ionized plasma. These characteristics indicate that they originate locally in the X-ray binary. We show an example of the absorption lines in Fig. (1.11) at ~ 7keV, we appreciate that they are absent in the hard state. In several cases, these lines are found to show a significant blue shift or a P-Cygni profile, indicating an outflow. The typical outflow velocities measured are $v_{\text{out}} \sim 100 - 2000 \text{km s}^{-1}$ (Ponti et al. 2016). The absorption lines are only present in high inclination systems (Ponti et al. 2012). This is strong evidence towards a wind with equatorial geometry and a limited covering factor (Higginbottom and Proga 2015). Recent optical observations have also measured the absorption profiles of wind-like outflows (Charles et al. 2019; Jiménez-Ibarra et al. 2019). It is unclear whether the optical absorption lines are a signature of the same outflows that are observed in the X-ray or an entirely new component.

As mentioned before the winds are only observed in soft states (Ponti et al. 2012), this is still not understood. One possibility could be that jet-like outflows become wind-like outflows when the X-ray binary changes spectral state. Another possibility could be that the wind is over ionized in the hard state due to a thermal instability, if the gas is over ionized the iron lines could be undetectable (Chakravorty et al. 2016; Petrucci et al. 2021).

Begelman et al. 2015 showed that illumination from the inner regions of the accretion disk could lead to the launching of Compton-winds from the outer regions in X-ray binaries. Whether these winds are magnetically driven or thermally driven is a topical subject (Díaz Trigo and Boirin 2016; Ponti et al. 2016). The radiative signatures of Compton winds have been extensively compared to the absorption lines observed in X-ray binaries (Higginbottom and Proga 2015; Tomaru et al. 2019), they can reproduce the absorption lines. The radiative signatures of self-similar solutions of MHD-driven outflows have been compared to observations with mostly positive results (Chakravorty et al. 2016; Fukumura et al. 2021). They found that the MHD-driven outflows can also reproduce the absorption lines.

1.3 Observational properties of accretion and ejection in dwarf novae

Dwarf novae (DN) are very similar to X-ray Binaries, they are both binary systems composed of a solar mass star and a compact object, in DNs the compact object is a white dwarf. The white dwarf accretes through Roche lobe overflow and ends up surrounded by an accretion disk. Like LMXRBs, DNs also undergo outburst where their luminosity increases dramatically and their spectral properties are modified. The average increase in magnitude for DNs during the outburst phase is 2 to 6 orders of magnitude. In Fig.(1.12) we show the light curves of V1504 observed by Kepler (Cannizzo et al. 2012). We observe that the eruptions can be incredibly regular with an average duration of 2 days and an interval between eruptions of approximately 10 days. However, some eruptions, called super-outbursts, can last 5 times more and lead to a more irregular duration for the interval between outbursts. The scenarios invoked to explain the outburst in the white draft will be described in section 1.5. We note that the higher luminosity of the accretion disk is often related, in the models, to an enhanced accretion rate.

Using a technique known as eclipse mapping Horne and Cook 1985 was able to reconstruct the radial structure of the disk of Z Cha. They measure the brightness temperature in the optical (around 441nm) as a function of radius. They were able to show that the emission from the disk during an outburst is consistent with a viscous disk (Shakura and Sunyaev 1973), where the angular momentum is transported through turbulent torques. In Fig. (1.13,left) we show that the brightness temperature is consistent with an accretion rate of $\dot{M}_a \simeq 10^{-9} M_\odot \text{ yr}^{-1}$.

Wood et al. 1986 performed the same analysis of Z Cha but during the quiescent state (Fig. 1.13,right). They confirm that it is also roughly consistent with a viscous disk model. However, they measure a smaller accretion rate, $\dot{M}_a \simeq 10^{-10} M_\odot \text{ yr}^{-1}$, required by the lower luminosity. They also find that the brightness temperature scales differently as a function of radii in the inner regions during quiescence.

When the accretion flow falls into the central white dwarf it connects with the surface of the star creating a boundary layer, within this boundary layer the plasma is torqued down until it reaches the angular velocity of the star (Pringle and Savonije 1979; Patterson and Raymond 1985). The violent torques involved lead to energy deposition within this region, which leads to an efficient emission of X-rays. Using the cooling model of the boundary layer, Pandel et al. 2005 where able to measure the accretion rate in 9 DN during quiescent state, they measure $\dot{M}_a = 10^{-12} - 10^{-13} M_\odot \text{ yr}^{-1}$.

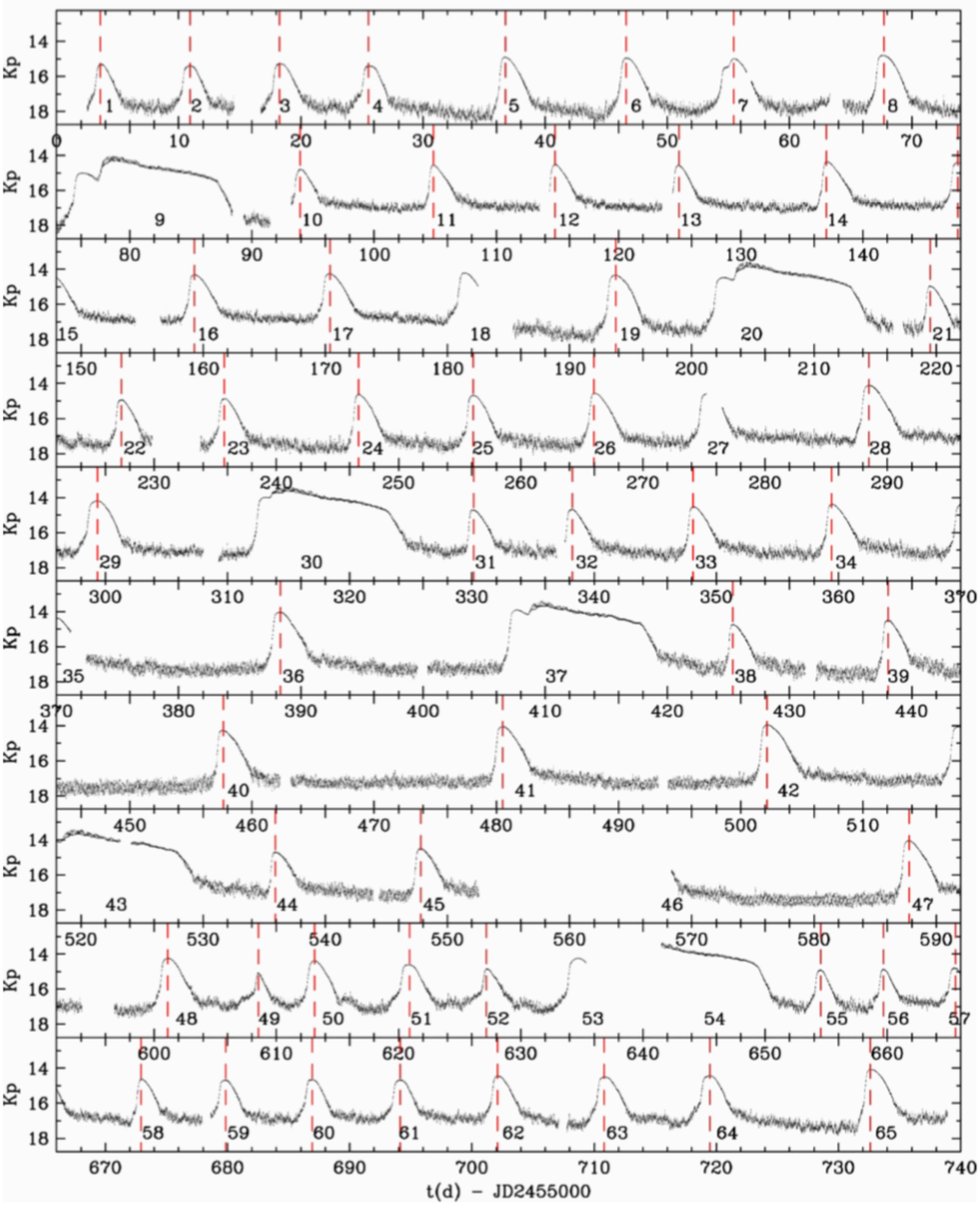

Figure 1.12: Kepler light curve for V1504 Cyg at one-minute cadence, spanning $\sim$ 736 days. The light curve covers 6 super-outbursts and 59 normal outbursts. The vertical red lines indicate the local maxima for the normal outbursts in which coverage permits a reliable determination, and with well-sampled decays down to 2 mag below maximum. Adapted from Cannizzo et al. 2012

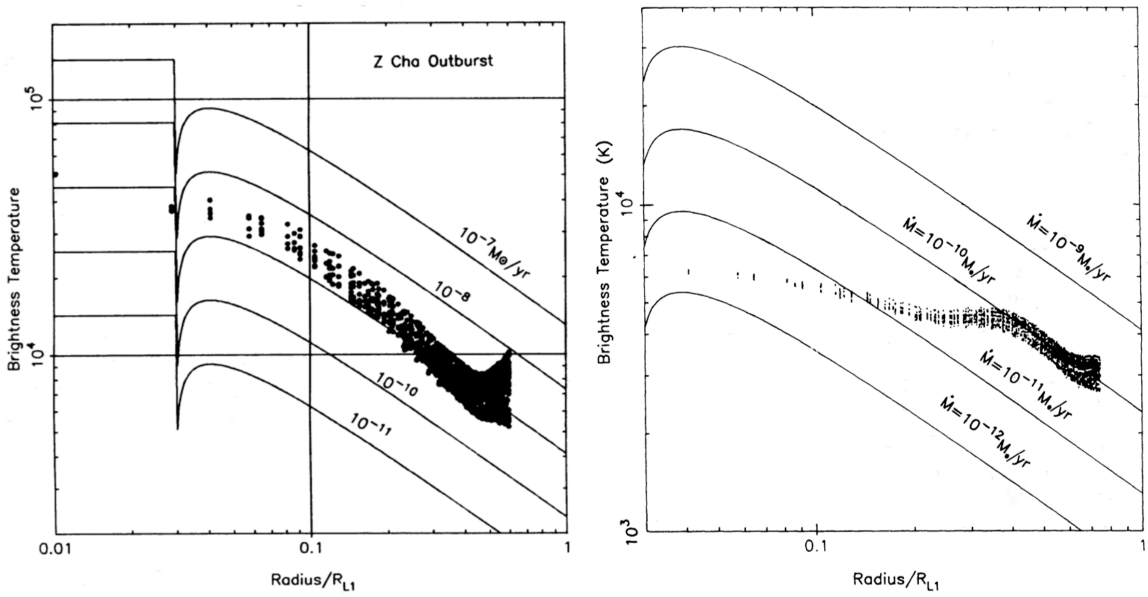

Figure 1.13: Brightness temperature in the disk for a disk an outburst state (left) and a disk in quiescence (right). Models of steady state optically thick discs for several mass transfer rates are also shown. Adapted from Horne and Cook 1985 and Wood et al. 1986.

An interesting property of the X-ray emission attributed to the boundary layer is that it is not detectable during the outburst (Wheatley et al. 1996; Wheatley et al. 2003). A possible explanation is that the enhanced accretion rate during the outburst leads to an optical thick boundary layer that emits in the extreme ultraviolet (Pringle and Savonije 1979; Patterson and Raymond 1985).

Wind-like outflows are also observed in DNs as in LMXRB and protoplanetary disks. The winds are emitted from the accretion disks (Cordova and Mason 1982; Mauche and Raymond 1987) and are recognized by their P Cygni profiles in the UV. The velocities of the wind-like outflows are measured to be around 3000 – 5000km s^{-1} (Drew 1990). Furthermore, as in X-ray binaries, the emission lines are consistent with a bi-conical geometry, they are not consistent with spherical geometry (Drew 1990; Knigge and Drew 1997). Wind-like outflows have only been observed during the outburst state, they appear to be absent in the quiescent state, opposite to what is observed in LMXRB. It is possible that this a consequence of the disk being less luminous during the quiescent state, complicating the observation of the P Cygni profiles. However, it has been proposed recently by Hernández Santisteban et al. 2019 that an observed choc front with the interstellar medium could be the signature of a wind-like outflow emitted during quiescence.

Coppejans et al. 2016 showed that radio emissions are ubiquitous in dwarf novae DNs. However, the origin of radio emissions in DNs remains unclear. The possibility that the origin of the radio emissions are jet-like outflows has not yet been discarded.

1.4 Accretion theory

Two main different mechanisms have been proposed to explain the angular momentum transfer within an accretion disk. Historically, theoretical work in accretion followed two distinct but related paths: One focussing on the outflow torque due to an MHD outflow and the other on the turbulent torque due to (magneto)-hydrodynamic instabilities.

1.4.1 Jets as carriers of angular momentum

In their seminal work Blandford and Payne 1982 were the first to compute magnetically driven stationary self-similar[1] outflows. They find that, if a large scale vertical magnetic is present outflows are ejected from a surface above the disk. They also found, like other before them (Lovelace 1976), that when a magnetized outflow is launched a magnetic torque emerges. Indeed, the outflow feeds on the angular momentum of the disk leading to accretion within the disk. Blandford and Payne 1982 then computed the accretion rate, $\dot{M}_{\rm acc}$, resulting from the laminar torque of the outflow. However, in their work the outflow launching surface was not connected to an accretion disk of any kind.

In a strictly stationary solution[2] the accretion flow can not cross the large scale vertical magnetic field lines, a consequence of Alfvén 's theorem. Hence, connecting the outflow to an accreting disk requires a supplementary ingredient: a magnetic diffusivity. A magnetic diffusivity can be the consequence of molecular non-ideal MHD effects within the disk. For instance Konigl 1989 and Wardle and Koenigl 1993 studied such a case in the self-similar framework. Ferreira and Pelletier 1993 postulated that such a diffusivity could be of turbulent origin and thus be another consequence of the magnetized turbulence, like the Shakura and Sunyaev 1973 viscosity described above. Moreover, Ferreira and Pelletier 1993 realized that a magnetic diffusivity is an essential ingredient of the launching mechanism and is needed to deviate the accretion flow into and outflow.

Ferreira and Pelletier 1995 and Li 1995 then computed consistent self-similar solutions of magnetized outflow that connected to a turbulent accretion disk. The former assumed a fully self-similar magnetized accretion disk where the magnetic equilibrium of the disk was fully computed. However, they calculated only super slow magneto-sonic outflows. The latter simplified the vertical equilibrium of the accretion disk, considering only a vertically thin disk, and used a patching method to couple the disk to the super Alfvénic solutions. In both cases the turbulent resistivity is only present within the accretion disk and vanishes within the laminar outflow. This lead to outflows solutions that have similar properties to the ones computed by Blandford and Payne 1982 but are also geometrically constrained by the presence of the accretion disk. Ferreira and Pelletier 1995 found that the presence of a disk constrained the parameter space, due to the compression effect of the magnetic field on the disk vertical structure. A similar computation was performed by Ogilvie and Livio 1998 and Ogilvie and Livio 2001. Ogilvie and Livio 1998 solved the local vertical structure and connected such a structure with a centrifugally driven outflow. They showed that heating could be an important ingredient in the launching of outflows from accretion disks. But, they did not consider the toroidal magnetic field in their computation, which has an important effect on the acceleration of the outflow. Ogilvie and Livio 2001 computed the effect of the toroidal magnetic field on the disk vertical structure. However, in their modeling, the value of the toroidal magnetic field at the disk surface is a free parameter and is not fixed by the magnetic structure of the outflow.

The work of Ferreira and Pelletier 1995 was later extended to super-Alfvénic outflows by Ferreira 1997 where they showed that the Alfvén point introduces strong constraints on the properties of the outflow. In the end, the parameter space of super Alfvénic self-similar solutions is quite small. The parameter space is restrained to highly magnetized solutions and jet-like diluted outflows. Casse and Ferreira 2000a later include the effects of the turbulent torque. Finally, Casse and Ferreira 2000b included the effects of heating due to the irradiation from the

---

[1] Self-similarity is a procedure that removes the radial dimension of the system, simplifying the equations (more details chapter 3).

[2] and in ideal MHD

central object. These solutions where compared with observations of class 2 YSO jets and were found to be in good agreement (Dougados et al. 2004).

The inclusion of heating lead to more massive outflows that have been compared with observations of proto-protoplanetary molecular outflows (Tabone et al. 2017) and X-ray binaries winds (Chakravorty et al. 2016). However, in both cases the authors have found that the existing self-similar solutions still produce diluted winds that struggle to fit the data. There is a need to compute denser self-similar solutions that better reproduce the data. Furthermore, the small values of $\lambda \sim 2-4$ found in molecular outflows (Launhardt et al. 2009; Bjerkeli et al. 2016; Hirota et al. 2017; Louvet et al. 2018; de-Valon et al. 2020) are hard to reproduce with the self-similar solutions of Casse and Ferreira 2000b. The inclusion of heating and a turbulent torque dit not extend the parameter space with respect to the magnetization [3], it is still constrained to highly magnetized solutions. As we will see later this is an important problem that requires further investigation. We note that the main drawback of effective self-similar models is that they do not compute the turbulent structure. Therefore, the turbulent structure needs to be imposed.

The self-similar models were followed by 2.5D simulations of accretions disk launching jet-like outflows (Casse and Keppens 2002, 2004; Zanni et al. 2007; Tzeferacos et al. 2009; Murphy et al. 2010). They computed similar outflows to the ones observed in self-similar solutions. However, they could probe the variability of said outflows and the temporal evolution on longer time scales. They suffer from the same drawback as self-similar solutions, they also depend on the model of turbulence.

We conclude that a large scale vertical magnetic field crossing a Keplerian disk spontaneously leads to the launching of an outflow (Ferreira and Pelletier 1995; Konigl and Pudritz 2000; Pudritz et al. 2007), which carries away angular momentum. However, it is not the only way to transport angular momentum.

1.4.2 Turbulence as the main agent for anomalous viscosity

As said before, the seminal work of Shakura and Sunyaev 1973 paved the way for effective viscosity models of accretion disks. In such models, the accretion is a consequence of turbulence within the disk that drives angular momentum transport radially towards the outer regions. An instability capable of producing such a turbulent transport was discovered by Balbus and Hawley 1991 and is now a corner stone of the field. The Magneto-Rotational instability (MRI) can drive a powerful magnetized turbulence from a vertical or toroidal magnetic field. This powerful turbulence will then drive the angular momentum transport through turbulent torques. To quantify the strength of this turbulent torque a parameter known as the Shakura-Sunyaev α parameter was defined (see more details section 2.4.2). This parameter controls the strength of the turbulent resistivity, $\nu_v \propto \alpha$, and hence the strength of the turbulent torque.

Properly assessing the non-linear saturation of this instability required some improvements in the numerical end. A new numerical model called the shearing box model was developed to study the non-linear saturation of the MRI. It allowed to isolate the essential ingredients of the MRI, mainly the shear and the magnetic field. Using this newly developed method Hawley et al. 1995 were able to explore the growth and saturation of the MRI in non-stratified simulations. They measured a growth rate for the MRI that agreed quite well with the theoretical work on the instability (Balbus and Hawley 1991) and also confirmed the work of Goodman and Xu 1994. Balbus and Hawley 1991 had already shown that the MRI develops channel mode solutions[4].

---

[3] The magnetization is defined as $\frac{B_{z0}^2}{4\pi P_0}$, where B_{z0} is the vertical magnetic field at the disk midplane and P_0 is the thermal pressure at the disk midplane (see chapter 2).

[4] that are exact solutions of the MHD equations

The channel mode solutions are vertical oscillatory structures that grow in amplitude with time.

Goodman and Xu 1994, following the work of Balbus and Hawley 1991, worked on the parasitic instabilities of MRI. They showed that the channel mode structures are eaten away by secondary instability which are essentially Kelvin-Helmhotz types modes. This breakup of the channel mode solutions eventually ends up in fully-developed turbulence. Hawley et al. 1995 also showed that the MRI-driven turbulent torque scales with mean magnetic field strength. To be more precise, the turbulent torque scales with the magnetization, as the magnetization increases, the strength of the turbulent torque also increases. Finally, they found that the MRI is the strongest with a vertical magnetic field instead of a toroidal magnetic field. For this reason, in the rest of this manuscript, we will focus on the configuration with a mean vertical magnetic field. Moreover, if we want to launch a magnetized outflow a vertical magnetic field is required.

For this same reason, we will not discuss the zero-net flux configuration.

Gammie 1996 put forward the dead-zone model of protoplanetary disks, he proposed that the outer ($R > 1$ AU) cold regions of protoplanetary disks could be weakly ionized. This would lead to the presence of Ohmic resistivity which could quench the MRI within the disk. He proposed that the accretion would happen at the surface of the disk, where the illumination from the star is strong enough to ionize the gas. Instability analysis of the MRI in presence of non-ideal effects showed that the MRI is stabilized (Jin 1996; Wardle 1999; Kunz and Balbus 2004; Kunz 2008). Numerical experiments using the shearing box model confirmed that the MRI is stabilized in the presence of non-ideal MHD effects (Fleming et al. 2000; Bai and Stone 2011). It is now clear that non-ideal effect stabilize the MRI in the outer regions of protoplanetary disks. MRI-driven turbulence is restricted to the inner regions of protoplanetary disks ($R < 1$A.U.). Therefore, the analysis performed in this manuscript is only accurate within those regions.

A very similar effect occurs in DNs. During the quiescent state, the disk is too cold and becomes weakly ionized. This weakly ionized state leads to Ohmic resistivity becoming dynamically important (Gammie and Menou 1998). The appearance of non-ideal effects leads to the disappearance of MRI-driven turbulence and its associated turbulent torque (Scepi et al. 2018a).

The absence of MRI turbulence leads to the absence of a mechanism that can transport angular momentum. A new mechanism was needed to explain accretion in the outer regions of protoplanetary disk. The theoretical community looked back to Blandford and Payne 1982 and tried to implement the disk wind component into shearing box simulations. Most shearing box simulations with a vertical magnetic field where done in the non-stratified regime. The unstratified nature of those simulations forbids the existence of a wind. Indeed, a stratified configuration with a vertical magnetic field leads to ”high magnetic pressures that disrupt the vertical structure of the disk before the flow makes the transition to MHD turbulence” (Stone et al. 1996).

It was until 2009 that the first stable ideal-MHD shearing box simulations of a vertically stratified disc with a mean vertical magnetic field was performed by Suzuki and Inutsuka 2009 and Suzuki et al. 2010. This achievement was possible thanks to more robust numerical techniques as well as carefully designed vertical boundary conditions.

The computation of outflows ejected from MRI active accretion disks was now possible using the shearing box model. The work of Suzuki and Inutsuka 2009 was followed by computations of highly (Ogilvie 2012; Lesur et al. 2013) and weakly (Moll 2012; Bai and Stone 2013a; Fromang et al. 2013) magnetized accretion disks launching magnetized outflows. They show a similar structure to the solutions of Ferreira 1997 where a laminar magneto-centrifugal wind is launched from a turbulent accretion disk (Fromang et al. 2013; Lesur et al. 2013), see Fig. (1.14). In contrast to self-similar solutions, weakly magnetized outflows are possible in shearing-box simulations. This inconsistency is one of the main motivations behind the work

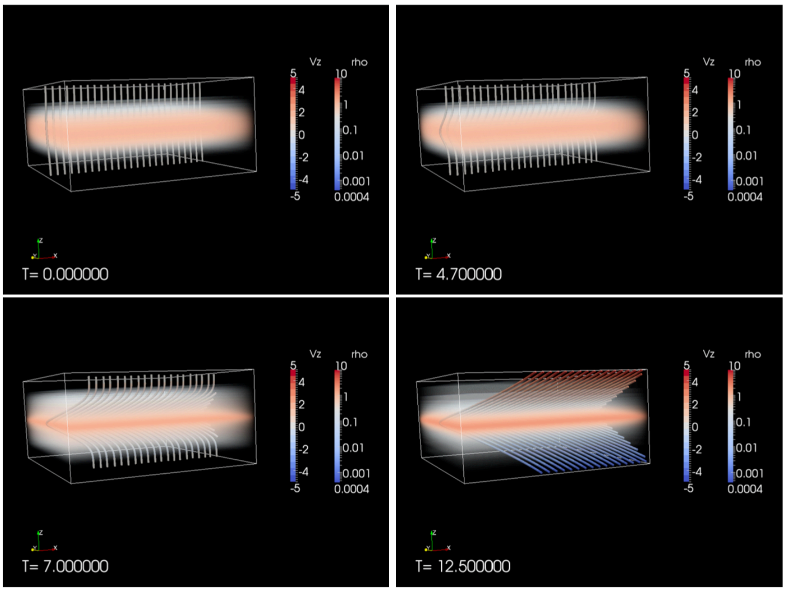

Figure 1.14: Growth and saturation of the MRI in presence of strong mean vertical magnetic field. Tubes are magnetic field lines while gas density is represented with volume rendering. The structure is similar to the one obtained by Ferreira and Pelletier 1995 with a turbulent disk and a laminar outflow. Adapted from Lesur et al. 2013

presented in this manuscript.

Despite their other successes shearing-box simulations struggle simulating realistic outflows:

- Fromang et al. 2013 found that the mass ejection rate depends on the box size, taller boxes leading to smaller mass loss rates, a consequence of the shape of the gravitational potential in shearing box simulations.
- Lesur et al. 2013 found that unless symmetry was artificially forced the magnetic configuration reached an unphysical top/down symmetry. In this unphysical configuration the wind is ejected towards the central object. This is probably a consequence of the shearing box having too many symmetries (Lesur 2020). This implies that global curvature effects, absent from the shearing box model, are mandatory to obtain physically valid outflow solutions.

Magnetized outflow were then obtained for shearing box simulations with non-ideal effects (Ambipolar and Ohm) by Bai and Stone 2013b. They found that in such a configuration the disk was laminar, MRI was suppressed by the non-ideal effects, and a magneto-centrifugal laminar outflow was launched from the surface of the disk. This laminar outflow exerted a laminar torque on the disk leading to accretion without the need of any turbulence. However, these non-ideal models suffer from the same drawbacks as the ideal ones.

It was necessary to go beyond two dimensional effective models, like the self-similar solutions, and the shearing box models. To this end, global numerical simulations combining MRI-driven turbulence and magnetically-driven outflows were computed (Suzuki and Inutsuka 2014). However, the work of Suzuki and Inutsuka 2014 had to deal with a limited radial and latitudinal extent, making the simulations difficult to interpret.

It was until 2018 that more robust algorithms and more numerical resources lead to the first consistent computation of 3D global numerical simulations combining MRI-driven turbulence

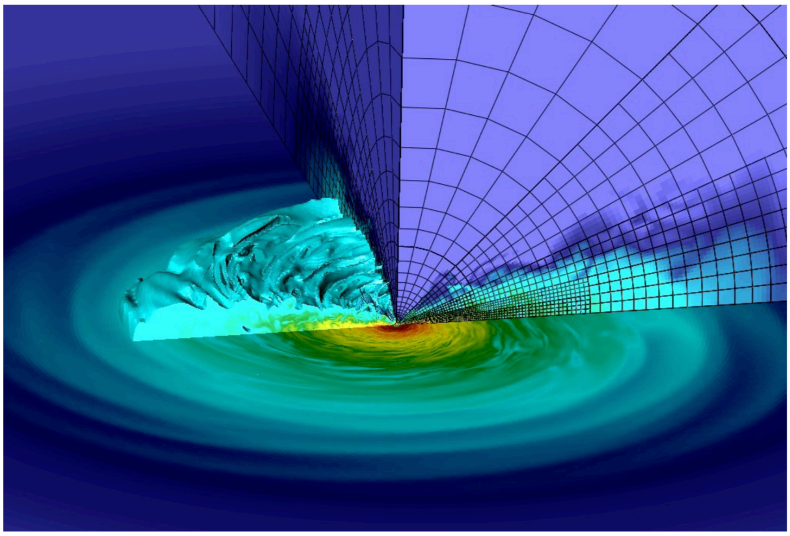

Figure 1.15: Snap shot of a the simulation computed by Zhu and Stone 2018, we recognize the outflow and the turbulent disk. Static mesh refinement is necessary to capture the MRI turbulence at the disk midplane and to extend the calculations to the pole. Adapted from Zhu and Stone 2018.

and magnetically-driven outflows (Zhu and Stone 2018). We show in Fig. (1.15) a snapshot of the numerical simulation performed by Zhu and Stone 2018, in it we appreciate the enormous numerical scale of a 3D global simulation that can compute the outflow and resolve MRI turbulence. These weakly magnetized simulations show that it is possible to launch an outflow with a weak magnetic field and are thus in tension with self-similar models (Ferreira 1997). Furthermore, these weakly magnetized simulations are known to exhibit an exotic global configuration. For instance, the stationary state found by Zhu and Stone 2018 and Mishra et al. 2020 possess 3 distinct features: a turbulent disk, a supersonically accreting atmosphere, mostly driven by a laminar Maxwell torque, and a tenuous wind that does not transport a considerable amount of angular momentum and mass.

These numerical results are in flagrant contradiction with usual two dimensional 'effective' models of outflow-emitting disks. In these models, accretion typically occurs in the disk bulk and angular momentum escapes through a magnetized outflow launched from the disk surface (Murphy et al. 2010; Stepanovs and Fendt 2016). Even though some effective models predict accretion preferentially located within the disk surface ($\simeq 3h$:Guilet and Ogilvie 2013; Jacquemin-Ide et al. 2019), where h is the disk pressure scale-height, none of these models produce accretion in the disk atmosphere at $z \sim 10h$, as is observed in the numerical simulations of Zhu and Stone 2018 and Mishra et al. 2020. Furthermore, Zhu and Stone 2018 (see their Fig. 10) and Mishra et al. 2020 (see their Fig. 7) show that this accreting atmosphere features turbulent torques at high magnetization, high above the disk. The dynamical role and the origin of this 'second' turbulence it not known as of today. For the sake of clarity, we show in Fig. (1.16) the vertical structure of the simulations of Zhu and Stone 2018 (left) and of a typical 2.5D effective model (right).

Global numerical simulations combining non-ideal MHD effects (Ambipolar and Ohm) and magnetically-driven outflows do not have this problem (Béthune et al. 2017). Indeed, it may seem that when non-ideal effects are included the 2 dimensional approximation is accurate. Hence, the inconsistency in ideal MHD simulations must be related to the MRI-driven turbulence.

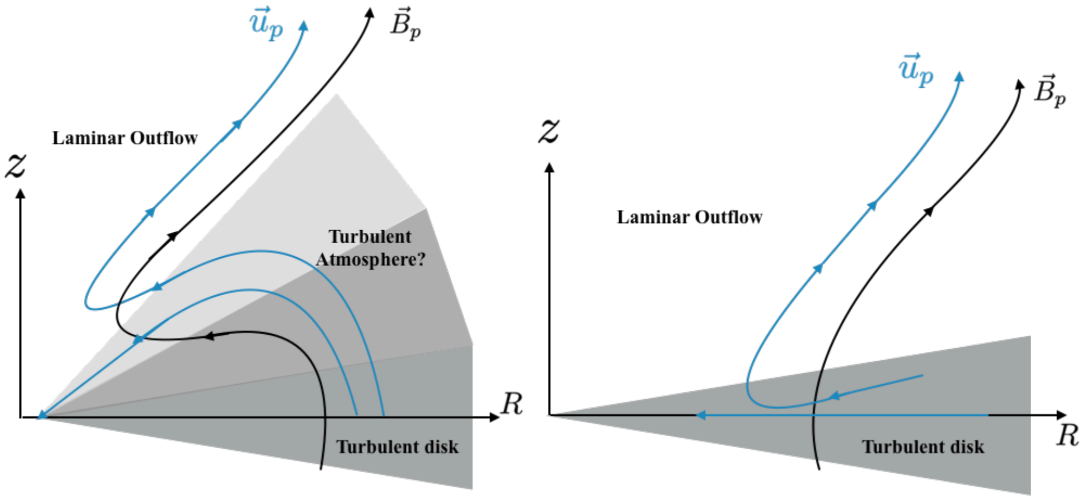

Figure 1.16: Schema showing the the magnetic topology (B_p) and velocity field lines (u_p) of self-similar solution (right) and the simulation of Zhu and Stone 2018 (left)

1.5 Secular evolution in accretion disk

As was discussed above, the outbursts in DNs and LMXRBs are expected to have a higher accretion rate during the outburst state when compared to the quiescent state. The disk instability model (DIM) can model the temporal behavior of those objects during an outburst (see Lasota 2001 for a review). The DIM only includes the MRI-driven turbulent torque. The DIM uses two different values of the Shakura-Sunyaev α parameter to model the different magnitudes of the luminosity, during outburst and quiescence, of DNs and LMXRBs (Lasota 2001).

To be more precise, in DNs it was shown that during the eruption $\alpha \simeq 0.1$ (Kotko and Lasota 2012) while in quiescence $\alpha \simeq 0.03$ (Cannizzo et al. 2012). However, shearing box simulations clearly showed that MRI-driven turbulence fails to reproduce the dramatic changes of the α parameter, and thus the lights curves of DNs (Latter and Papaloizou 2012). Furthermore, as was mentioned before the low ionization during the quiescent state in DNs leads to the disappearance of MRI-driven turbulence during the quiescent state (Scepi et al. 2018b).

The DIM could also explain the spectral transitions and the outburst in X-ray binaries (Mineshige and Wheeler 1989). If that were the case, the DIM could unify the behavior observed in DNs with the one observed in X-ray binaries (Dubus et al. 2001; Coriat et al. 2012). The DIM can be a useful model to understand the luminosity evolution in X-ray binaries. However, the DIM struggles to model the spectral variations of X-ray binaries during the outburst (Coriat et al. 2012; Hameury et al. 2017). The thermal instability of the DIM happens at low temperature and are therefore confined to the outer radii of Xray binaries. Therefore, the DIM could be part of the mechanism behind the outburst of LMXRBs but it can not be the main driver behind the spectral transition.

An alternative mechanism to explain the outburst of LMXRBs was proposed by Ferreira et al. 2006b. We show in Fig (1.17) a simplified picture of this hybrid disk model. In this model the system is composed of two distinct disks:

- An inner highly magnetized accretion disk where the laminar torque dominates. This inner disk is called the Jet Emitting Disk (JED) (Ferreira 1997).

- An outer weakly magnetized accretion disk where the turbulent torque dominates. This outer disk is called the standard accretion disk (SAD) (Shakura and Sunyaev 1973).

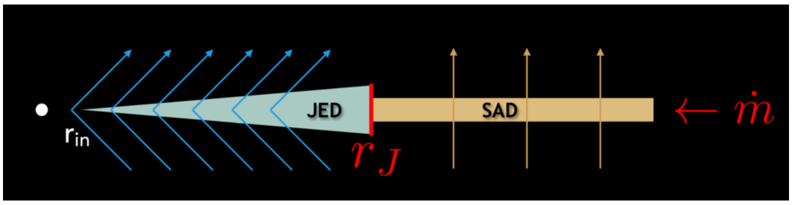

Figure 1.17: Schema of the JED-SAD model, showing the important parameters r_j and $\dot{m}$. Figure courtesy of G. Marcel.

The accretion velocity is supersonic in the inner regions and subsonic in the outer regions. The JED-SAD model has two main parameters the forcing accretion rate arriving from the donor star, $\dot{m}$ and the transition radii between the disks, r_j.

However, as was discussed above once an outflow is included a large-scale vertical magnetic field is required. In the absence of a large-scale vertical magnetic field, no outflow could be launched. Moreover, if a large-scale vertical magnetic field is present, its transport becomes a critical issue. Indeed, the vertical magnetic field is going to react to turbulence and accretion. The vertical magnetic field will be advected by the accretion flow or diffused by the turbulence.

While most of the literature has focused on mass and angular momentum transport, the question of magnetic field transport is also a key element if one is to predict the secular evolution of a disk subject to a magnetized outflow. It is this secular evolution that then leads to interesting observational evidence, like for example eruptions in X-ray binaries (Ferreira et al. 2006b; Marcel et al. 2018a, 2019) or dwarf novae (Scepi et al. 2019; Scepi et al. 2020). The question of magnetic field transport was tackled in the seminal work of Lubow et al. 1994 who showed how the magnetic field could be advected towards the inner regions of the disk by the accretion flow. They also show that when the accretion is driven by turbulent torques the field advection is inefficient. The turbulent diffusion of the magnetic field dominates the transport of magnetic flux. Rothstein and Lovelace 2008 later showed that taking into account the laminar torque due to an MHD wind could lead to magnetic field transport towards the inner regions. Guilet and Ogilvie 2014 and Li and Cao 2021 showed that even without the presence of a laminar torque, inward transport of the magnetic field could be possible if the computation took into account the vertical structure of the disk. General relativistic MHD (GRMHD) simulations have shown that it is possible to transport the magnetic flux towards the central object (McKinney et al. 2012; Liska et al. 2020). However, those results seem to be in contradiction with the analysis of MHD numerical simulations (Mishra et al. 2020) that do not measure the advection of the magnetic field.

The picture of Ferreira et al. 2006b was tested observationally by Marcel et al. 2019. They were able to observationally reproduce an outburst by only varying the main parameters ($\dot{m}$ and r_j). However, the question remains if such a hybrid configuration could naturally occur from a simpler initial condition. Such a configuration is supposed to be reached naturally, thanks to the magnetic field advection (Ferreira et al. 2006b).

In the context of DNs Scepi et al. 2019 included the effect of the laminar torque acting on the accretion into the DIM model. When they introduced the laminar torque a hybrid disk configuration, like the JED-SAD model, naturally appeared. They then computed outbursts that resemble the data without the need for an unphysical double α model. However, they realized that in the presence of a vertical magnetic field, the transport of magnetic flux needed to be taken into account. Scepi et al. 2020 included a prescribed model for the magnetic field transport into their DIM model and were able to also reproduce the behavior of DN outbursts. Moreover, they also recovered a hybrid disk configuration similar to the JED-SAD model and consistent with

Scepi et al. 2019.

1.6 Aims and contents

As was discussed during the introduction there is no perfect way to simulate the dynamical properties of outflow launching accretion disks. Indeed, all modeling methods have their advantages and drawbacks:

- 2D effective models, like self-similar models or 2.5D simulations, are numerically cheap, they can capture the properties of the outflow and its constraint on the disk structure. However, their accuracy depends on the ad-hoc turbulent closure that is imposed.
- 3D shearing box simulations are numerically mildly expensive and can accurately model the MRI-driven turbulence and its structure. However, they are unable to model the asymptotic properties of the outflow. Furthermore, the outflows launched by shearing-box simulations are subjected to several numerical biases.
- 3D global simulations are highly expensive. However, they are the only numerical model that can capture the MRI-driven turbulence and the asymptotic properties of the outflow.

Due to the unconstrained nature of the magnetic field, thoroughly exploring a parameter space with 3D global simulations is impossible. Hence, 3D global MHD simulations are hard to compare with observations of outflows while radiative transfer simulations are not (Tomaru et al. 2019). This is not true for self-similar solutions as the parameter space is considerably easier to explore.

However, self-similar models face several challenges that need to be addressed:

1. Self-similar models can not produce weakly magnetized solutions (Casse and Ferreira 2000b) in contrast with 3D global simulations and shearing box simulations.
2. Self-similar models struggle to produce dense solutions that fit the observations of molecular outflows or X-ray binary winds.
3. Self-similar models produce a very different vertical structure than 3D global simulations (Zhu and Stone 2018). We illustrate this in Fig.(1.16).

As said before, the secular evolution of the magnetic flux in accretion disks could be essential to reproduce the outburst of DNs (Scepi et al. 2020) or LMXRBs (Marcel et al. 2019). Self-similar solutions by themselves cannot compute the secular evolution of accretion disks. Only 3D global numerical simulations can constrain the global evolution of the magnetic flux. Hence, our final objective is to address the transport of magnetic flux in 3D global numerical simulations. (4) We need to address if magnetic flux transport exists and if it can modify the radial structure of the accretion disk.

The manuscript is organized as follows:

- In chapter 2 we present the magnetohydrodynamical foundations of accretion and ejection. We derive a set of Reynolds average equations, the dispersion relation of compressible MRI, the main properties of outflow acceleration.
- In chapter 3 we compute new self-similar solutions that address questions (1) and (2). We then describe their properties, detail the constraints imposed by the different critical points, and explore the consequences of our turbulent closure.

- In chapter 4 we compute a set of 3D global MHD simulations to address the question (3). We then compute the secular evolution of the angular momentum and the magnetic field to address the question (4). We use the set of Reynolds averaged equations to understand the role of turbulence on the dynamics of the system. We then elucidate the properties of the outflow. Finally, we explore the effect of different magnetizations and geometrical thickness on the properties of the system.
- In chapter 5 we derive a set of turbulent closures using our set of 3D global simulations to educate future self-similar models to fully address question (3). The turbulent model educated from the global simulations will allow us to produce more accurate effective models that will be compared to observations in future work.

CHAPTER 2

Magnetohydrodynamical theory of accretion and ejection

In this chapter, we describe the theoretical background needed to model the dynamics of magnetized accretion disks. We start by introducing how we hydrodynamically model an accretion disk, next we compute the hydrostatic equilibrium of such an object. Then we introduce the magnetohydrodynamical model of an accretion disk and we discuss their regimes of validity.

Afterward, we perform a linear analysis on the ideal MHD equations to discuss the ideal MHD waves as well as the instability that arises in a disk with a Keplerian shear. Next, we Reynolds average the ideal MHD equations to distinguish the turbulent from the average components. We show how the turbulent components have an important impact on the dynamics of the accretion disk. Finally, we describe the phenomenology of outflow launching and propagation with the help of the MHD invariants.

2.1 Magnetohydrodynamic preliminaries

2.1.1 Disk hydrodynamics

We define an astrophysical disk as an ensemble of gas particles orbiting at an angular velocity Ω around a central object of mass M. This gas or plasma has fluid properties and thus has a density ρ and a pressure P. The gravitational potential from the central object has the form

$$\Phi_G = -\frac{GM}{r}, \tag{2.1}$$

where r is the spherical radius and G is the universal gravitational constant. In this manuscript we will use both spherical coordinates (r,θ,φ) as well as cylindrical coordinates (R,φ,z), where we define the cylindrical radius $R = r\sin\theta$ and the cylindrical height $z = r\cos\theta$.

We model the dynamics of astrophysical disks using the (magneto)hydrodynamic approximation. This fluid approximation is accurate if collisions between ions and elections are frequent enough, this is equivalent to

$$\Omega_{\text{scale}} \ll \nu_{ei}, \tag{2.2}$$

$$\lambda_{\text{scale}} \gg \lambda_{ei} = \frac{v_{Te}}{\nu_{ei}}, \tag{2.3}$$

where Ω_{scale} and λ_{scale} are the frequency and spatial scales of the astrophysical disk system. We also define ν_{ei} the frequency of ion-electron collision and v_{Te} the thermal velocity of the electrons. More precisely

$$\nu_{ei} = \frac{2\pi e^4}{m_e^{1/2} k_B^{3/2}} \frac{n_e \ln\Lambda}{T^{3/2}}, \tag{2.4}$$

$$v_{Te} = \sqrt{\frac{k_B T_e}{m_e}}, \tag{2.5}$$

where e is the electron charge, n_e is the electron density, T_e is the electron temperature and $\ln\Lambda \sim 20$ is the coulomb potential. This fluid approximation is accurate for most regions of the accretion disks considered in this manuscript (X-ray binaries, YSO, Novae-like variables). However, it is important to note that in regions close to the central object (in the coronal or magnetosphere) where n_e is much smaller and T is much larger the fluid approximation breaks and kinetic effects need to be taken into account. In those conditions, a particle in cell (PIC) methods or even a brute force resolution of the Vlasov equation could be the only method to accurately model the plasma.

We consider an astrophysical disk in hydrostatic equilibrium around the central object. In this configuration the radial and vertical components of the Euler equations can be written as

$$0 = -\frac{1}{\rho}\frac{\partial P}{\partial R} - \frac{\partial \Phi_G}{\partial R} + \Omega^2 R, \tag{2.6}$$

$$0 = -\frac{1}{\rho}\frac{\partial P}{\partial z} - \frac{\partial \Phi_G}{\partial z}, \tag{2.7}$$

where $\Omega = v_\varphi / R$ is the angular velocity of the flow. Close to the disk mid-plane it is a good approximation to assume that

$$\Omega(z \ll R, R) \simeq \Omega_K \equiv \sqrt{\frac{GM}{R^3}}, \tag{2.8}$$

where we have defined the Keplerian frequency Ω_K which corresponds to the orbital frequency of a point particle around the central object. We further assume that the disk is locally isothermal, $T(R)$, which imposes a isothermal sound speed that is only a function of R, $c_s(R) = \sqrt{P/\rho}$. Since we assume that the disk is thin ($z \ll R$), we can simplify the vertical acceleration due to the gravitational potential,

$$-\frac{\partial \Phi_G}{\partial z} = -z\frac{GM}{[R^2 + z^2]^{\frac{3}{2}}} \simeq -z\Omega_K + O(z^3). \tag{2.9}$$

Putting this all together into Eq. (2.6) we find

$$\rho = \rho_{\mathrm{mid}}(R) \exp\left[-\frac{z^2}{2h^2}\right], \tag{2.10}$$

where we define the disk scale height as

$$h = \frac{c_s}{\Omega_K}. \tag{2.11}$$

For the thin disk approximation to remain valid we require $c_s \ll V_K$, where $V_K = R\Omega_K$ is the Keplerian velocity. We define the disk geometrical thickness as

$$\varepsilon = \frac{h}{R} = \frac{c_s}{V_K}. \tag{2.12}$$

We notice that $\varepsilon \ll 1$ in all cases considered since the Keplerian rotation is highly supersonic.

In the radial direction (Eq. 2.7) we obtain

$$\frac{\partial \Phi_G}{\partial R} \simeq \Omega_K^2 R = \Omega^2 R, \tag{2.13}$$

where we have neglected the pressure gradient since it is $(h/R)^2$ times smaller. This result implies that the disk is in Keplerian rotation, $\Omega \simeq \Omega_K$. The Keplerian rotation profile is an essential piece of the accretion puzzle as we will see in section 2.2.2.

2.1.2 MHD equations and their validity

Within this manuscript, we model astrophysical plasmas within the (ideal) MHD approximation. Hence, we start by discussing the validity of the ideal MHD approximation in the context of X-ray binaries and the inner regions of protoplanetary disks. For the sake of simplicity, we assume quasi neutrality as it is a good approximation for most astrophysical plasmas. To be more precise we assume

$$n_i = Zn_e, \tag{2.14}$$

where n_i and n_e are the particle densities of ions and electrons and Z is the average of charges of the ions. We note that for electro-neutrality to be respected, the Debye sphere of the plasma needs to be much smaller than the length scales of the accretion disk. Furthermore, the plasma frequency needs to be larger than the characteristic frequencies of the accretion disk. Both conditions are easily satisfied in most astrophysical plasmas.

Once electro-neutrality is assumed, three conditions need to be satisfied for a plasma to be properly modeled by the ideal MHD approximation:

- The plasma should be ionized enough for the ideal MHD approximation to be adequate.
- As described above, there must be frequent collisions between electron and ions to establish fluid behavior.
- The macroscopic length and frequency scales, defined as λ_{scale} and Ω_{scale} respectively, should be much larger than the Larmor radius and cyclotron frequency so that the latter can be averaged out.

Approximating the ionization fraction is straightforward for X-ray binaries, assuming thermal equilibrium, their ionization fraction can be computed with the Saha equation

$$\frac{n_i}{n_n} = \left[\frac{2\pi m_e k_B}{h_p^2}\right]^{\frac{3}{2}} \frac{T^{3/2}}{n_i} e^{-U_i/(kT)}, \tag{2.15}$$

where n_n is the particle density of neutrals, m_e is the electron mass, k_B is the Boltzmann constant, h_p is the Plank constant, T is the temperature, U_i is the ionization energy. Since X-ray binaries are very hot $T \sim 10^7 - 10^9$K (Done et al. 2007) we get $\frac{n_i}{n_n} \gg 1$.

Computing the ionization fraction is not as straightforward for protoplanetary disks. The ionized state of the inner regions of protoplanetary disks is a consequence of the thermal ionization of alkali metals (Armitage 2011). Therefore, we would need to consider the metallicity of the gas. Moreover, as was discussed in chapter 1 in the outer regions of protoplanetary disks the degree of ionization is a consequence of non-thermal processes like X-ray illumination from the star, cosmic-ray ionization, and turbulent heating (Armitage 2011; Lesur 2020). Because of the low degree of ionization within those regions non-ideal effects like ambipolar diffusion or Ohmic resistivity become important (Gammie 1996; Perez-Becker and Chiang 2011). Within this manuscript, we will ignore those non-ideal effects.

For the microscopic behavior to be averaged out in our macroscopic description, the cyclotron length and frequency scales must be constrained as

$$\Omega_{\text{scale}} \ll \omega_{ci} \tag{2.16}$$

$$\lambda_{\text{scale}} \gg R_{ci} = \frac{v_\perp}{\omega_{ci}} \tag{2.17}$$

where Ω_{scale} and λ_{scale} are the frequency and spatial scales of the astrophysical disk system and ω_{ci} is the cyclotron frequency of the ions defined as

$$\omega_{ci} = \frac{eB}{m_e} \tag{2.18}$$

where B is the magnetic field and R_{ci} is the Larmor radius of the for the ions, the ions length and times scales as they provide the most stringent constraints. In all cases considered in this manuscript the astrophysical scales involved are larger than the inherent cyclotron scales we can conclude that the microscopic behavior is averaged out and that the accretion disk is well modeled by MHD. If we modeled the accretion disk with a PIC method resolving the cyclotron scales as well as the Debye length scale would be critical. The PIC approach is better suited for highly magnetized small scale phenomena.

Since the magnitude of the magnetic field in accretion disks is badly constrained, it is useful to define the plasma beta

$$\beta = \frac{B^2}{8\pi P}, \tag{2.19}$$

the strength of the magnetic field pressure compared to the plasma pressure. This quantity is one the main parameters of the system.

We can now write the equations of ideal MHD for an accretion disk around an object of mass M

$$\frac{\partial \rho}{\partial t} + \nabla \cdot [\rho \mathbf{u}] = 0, \tag{2.20}$$

$$\rho\left(\frac{\partial \mathbf{u}}{\partial t} + (\mathbf{u}\cdot\nabla)\mathbf{u}\right) = -\nabla P + \rho\nabla\Phi_G + \frac{1}{c}\mathbf{J}\times\mathbf{B}, \tag{2.21}$$

$$\frac{\partial P}{\partial t} + \mathbf{u}\cdot\nabla P + \gamma P \nabla\cdot\mathbf{u} = (\gamma-1)\Lambda_{\text{cool}} \tag{2.22}$$

$$\frac{\partial \mathbf{B}}{\partial t} = \nabla\times[\mathbf{u}\times\mathbf{B}], \tag{2.23}$$

where ρ, $\mathbf{u}$, P, and $\mathbf{B}$ are respectively the plasma density, velocity, thermal pressure, and magnetic field, $\Phi_G = -GM/r$ is the gravitational potential, γ is the heat capacity ratio and $\mathbf{J} = c\nabla\times\mathbf{B}/4\pi$ is the current. We note that Eq.(2.22) assumes and ideal equation of state

$$P = \frac{\rho}{\mu_{\text{mol}} m_p} k_B T, \tag{2.24}$$

where μ_{mol} is the mean molecular weight, we note that $\mu_{\text{mol}} \sim 1$. The precise value of μ_{mol} depends on the astrophysical object considered. In a realistic treatment, the cooling function Λ_{cool} would represent the effect of cooling radiation emitted by the accretion disk. However, in this manuscript the effect of radiative transfer is ignored, the cooling function will be prescribed depending on the modeling method. It is important to note, that to rederive Eq. (2.23) from the Maxwell equations we have assumed that the displacements of the fluid are non-relativistic. This is accurate for the inner regions of protoplanetary disks, however not so much for X-ray binaries where even general relativistic effects could become important.

Finally, we define the poloidal velocity and magnetic field as

$$\mathbf{u_p} = u_r\mathbf{e_r} + u_\theta\mathbf{e_\theta} = u_R\mathbf{e}_R + u_z\mathbf{e}_z$$
$$\mathbf{B_p} = B_r\mathbf{e_r} + B_\theta\mathbf{e_\theta} = B_R\mathbf{e}_R + B_z\mathbf{e}_z.$$

2.2 Linear analysis of the MHD equations

In this section, we perform a linear perturbation analysis on the MHD equations: (1) We start by describing the role of the magnetic field on wave propagation in a uniform medium. We use this example to define the different waves propagating in a homogeneous ideal MHD plasma. This example also allows us to build some insight into the dynamical role of the magnetic field. (2) We then address the dynamical impact of the magnetic field on a disk with a Keplerian profile but with a compressible plasma. We see that in this case, an MHD instability appears. We then quickly describe the impact of magnetic field strength on this instability. (3) Finally, we consider a compressible plasma with a Keplerian velocity profile and recognize how the role of the magnetic field strength changes in this configuration.

2.2.1 MHD waves

We need to start from the ideal MHD equations (2.20-2.23), as well as the adiabatic gas law

$$\frac{\mathrm{d}P\rho^{-\gamma}}{\mathrm{d}t} = 0, \tag{2.25}$$

which can be derived from Eq. (2.22) by taking $\Lambda_{\text{cool}} = 0$.

We decompose our quantities using linear perturbation theory: $\mathbf{B} = \mathbf{B}_0 + \mathbf{b}$, $\mathbf{u} = \mathbf{u}'$, $P = P_0 + P'$ and $\rho = \rho_0 + \rho'$, where the $|\mathbf{B}_0| \gg |\mathbf{b}|$, $P_0 \gg P'$ and $\rho_0 \gg \rho'$. We look for wave like solutions of Eq. (2.20,2.23) where the perturbed quantities vary $\propto e^{i\mathbf{k}\cdot\mathbf{r}-i\omega t}$, where ω is the wave frequency and $\mathbf{k}$ the wave vector. It follows that

$$\begin{aligned}
\omega\rho' + \rho_0\mathbf{k}\cdot\mathbf{u}' &=0, && (2.26)\\
-\omega\rho_0\mathbf{u}' + \mathbf{k}\rho' - \frac{1}{4\pi}\left[\mathbf{k}\times\mathbf{b}\right]\times\mathbf{B}_0 &=0, && (2.27)\\
\omega\mathbf{b} + \mathbf{k}\times\left[\mathbf{u}'\times\mathbf{B}_0\right] &=0, && (2.28)\\
-\omega\left[\frac{P'}{\rho_0} - \gamma\frac{\rho'}{\rho_0}\right] &=0. && (2.29)
\end{aligned}$$

We combine the equations into the linearized equation of motion to find

$$\left[\omega^2 - \frac{(\mathbf{k}\cdot\mathbf{B}_0)^2}{4\pi\rho_0}\right]\mathbf{u} = \left(\left[\frac{\gamma P_0}{\rho_0} + \frac{B_0^2}{4\pi\rho_0}\right]\mathbf{k} - \frac{(\mathbf{k}\cdot\mathbf{B}_0)}{4\pi\rho_0}\mathbf{B}_0\right)(\mathbf{k}\cdot\mathbf{u}') - \frac{(\mathbf{k}\cdot\mathbf{B}_0)\,(\mathbf{u}\cdot\mathbf{B}_0)}{4\pi\rho_0}\mathbf{k}. \tag{2.30}$$

Without loss of generality, we can assume that $\mathbf{B}_0 = B_0\mathbf{e_z}$ and $\mathbf{k} = k_x\mathbf{e_x} + k_z\mathbf{e_z}$. We define θ the angle between $\mathbf{B}_0$ and $\mathbf{k}$. Thanks to this consideration we write Eq. (2.30) as $\overleftrightarrow{\mathcal{M}}\mathbf{u} = 0$ with $\overleftrightarrow{\mathcal{M}}$ a matrix function of ω. Non trivial solutions for $\mathbf{u}$ satisfy $\det(\overleftrightarrow{\mathcal{M}}) = 0$, this computation leads to the dispersion relation

$$\left(\omega^2 - k^2V_A^2cos^2(\theta)\right)\left[\omega^4 - \omega^2k^2\left(V_A^2 + c_s^2\right) + k^4V_A^2c_s^2cos^2(\theta)\right] = 0, \tag{2.31}$$

with $V_A = \sqrt{\frac{B_0^2}{4\pi\rho_0}}$ and $c_s = \sqrt{\frac{\gamma P_0}{\rho_0}}$ the Alfvén speed and sound speed respectively. The 3 solutions to this polynomial define the dispersion relations for the different ideal MHD waves.

Shear Alfvén waves: Their dispersion relation is:

$$\omega = \pm kV_Acos\theta, \tag{2.32}$$

with $V_A = \sqrt{\frac{B_0^2}{4\pi\rho_0}}$ being the phase speed of the wave.

Magneto-sonic waves: Their dispersion relation is:

$$\omega = kV_{\pm}, \tag{2.33}$$

$$V_{\pm} = \left(\frac{1}{2}\left[V_A^2 + c_s^2 \pm \sqrt{\left(V_A^2 + c_s^2\right)^2 - 4V_A^2 c_s^2 cos^2\theta}\right]\right)^{\frac{1}{2}}. \tag{2.34}$$

We define $V_{fm} \equiv V_+$ the wave velocity associated with the fast wave and $V_{sm} \equiv V_-$ the wave velocity associated with the slow wave.

The magnetic field modifies wave propagation through both components of the Lorentz force: (1) The magnetic tension leads to Alfvén wave that propagates only through the magnetic field lines and disappears in the absence of a magnetic field. (2) The magnetic pressure modifies the dynamics of acoustic waves by adding a compression effect.

We note that the fast waves are a magneto-acoustic perturbation that propagates in a quasi-isotropic manner. The slow waves also transport magneto-acoustic information, however, they propagate in a highly anisotropic manner, they follow the magnetic field. The Alfvén wave is a purely magnetic perturbation, they bend the magnetic field lines without compressing them and, they do not perturb the plasma density.

2.2.2 Lagrangian analysis of the MRI

The Magneto-Rotational instability (MRI) was discovered by Hawley and Balbus 1991, who showed that it could create strong turbulence in Keplerian disks. Once a mean magnetic field is coupled with a disk in Keplerian rotation the MRI appears. In this manuscript, we only address the MRI in the presence of a mean vertical magnetic field $\mathbf{B}_0 = B_0\mathbf{e}_z$. We start our study of the MRI by constraining its growth rate with Lagrangian analysis. The equation of motion of a fluid particle in a gravitational well with an ambient vertical magnetic field are

$$\frac{\mathrm{d}^2R}{\mathrm{d}t^2} - R\left(\frac{\mathrm{d}\varphi}{\mathrm{d}t}\right)^2 = -\frac{\partial\Phi_G}{\partial R} + F_R, \tag{2.35}$$

$$R\frac{\mathrm{d}^2\varphi}{\mathrm{d}t^2} + 2\frac{\mathrm{d}R}{\mathrm{d}t}\frac{\mathrm{d}\varphi}{\mathrm{d}t} = F_\varphi, \tag{2.36}$$

where $\mathbf{F}$ is the magnetic Lorentz force. We use local coordinates as they simplify the analysis. We consider an infinitesimal displacement around a radius R_0 that is rotating at an angular velocity Ω_0. We define the cartesian local coordinates (x, y) as

$$R = R_0 + x, \tag{2.37}$$

$$\varphi = \Omega_0 t + \frac{y}{R_0}, \tag{2.38}$$

where $\Omega_0 = \Omega_K(R_0)$. If we consider horizontal perturbations of the form $\xi = (x, y) \propto e^{i(\omega t - kz)}$, we can linearize the induction equation (Eq. 2.23)

$$\frac{\partial\boldsymbol{\delta}\mathbf{B}}{\partial t} = B_0\frac{\partial\boldsymbol{\delta}\mathbf{u}}{\partial z} \Longrightarrow \boldsymbol{\delta}\mathbf{B} = -ikB_0\xi, \tag{2.39}$$

where $\boldsymbol{\delta}\mathbf{u}$ is the velocity of the fluid particle. We now write the linearize Lorentz force as

$$
\begin{aligned}
\frac{\mathbf{F}}{\rho} &= \frac{1}{4\pi\rho}\left[\mathbf{B}\cdot\nabla\mathbf{B} - \frac{1}{2}\underbrace{\nabla B^2}_{=0}\right] = \frac{\mathbf{B}_0\cdot\nabla\delta\mathbf{B}}{4\pi\rho} \\
&= -\frac{k^2 B_0^2 \xi}{4\pi\rho} = -V_A^2 k^2 \xi,
\end{aligned}
$$

the only term that does not vanish is the horizontal component of the magnetic tension.

We can rewrite the equation of motion as

$$
\frac{\mathrm{d}^2 x}{\mathrm{d}t^2} = 3\Omega_0^2 x + 2\Omega_0 \frac{\mathrm{d}^2 y}{\mathrm{d}t^2} - V_A^2 k^2 x, \tag{2.40}
$$

$$
\frac{\mathrm{d}^2 y}{\mathrm{d}t^2} = -2\Omega_0 \frac{\mathrm{d}^2 x}{\mathrm{d}t^2} - V_A^2 k^2 y, \tag{2.41}
$$

which can be rewritten as

$$
\left[-\omega^2 + k^2 V_a^2 - 3\Omega_0^2\right] x - 2i\omega\Omega_0 y = 0 \tag{2.42}
$$

$$
2i\omega\Omega_0 x + \left[-\omega^2 + k^2 V_A^2\right] y = 0. \tag{2.43}
$$

In the same way as before this can be recast as $\overleftrightarrow{\mathcal{M}}\xi = 0$, with $\overleftrightarrow{\mathcal{M}}$ a matrix function of ω. The dispersion relation can be derived by computing $\det \overleftrightarrow{\mathcal{M}} = 0$, it can be written as

$$
\omega^4 - \omega^2\left[2k^2 V_A^2 - 3\Omega_0^2 + 4\Omega_0^2\right] + k^2 V_A^2\left[k^2 V_A^2 - 3\Omega_0^2\right] = 0. \tag{2.44}
$$

For this dispersion relation to describes a linear instability ω^2 needs to be negative, this is equivalent to

$$
k^2 V_A^2 - 3\Omega_0^2 < 0, \tag{2.45}
$$

for kV_A values above this limit the MRI is suppressed. The maximum growth rate of the linear instability are obtained for $V_A k = \sqrt{3}\Omega_0/2$ with $\omega_{\max} = \frac{3}{4}\Omega_0$. One can interpret the MRI as the consequence of 2 parcels of fluid attached by a vertical field line. When we slightly move the fluid parcels radially they will start to drift azimuthally as they arrive at a region with a different local angular momentum. As they drift apart, the magnetic tension will act as restoring force to bring the fluid parcels back together, slowing down the inner parcel and accelerating the outer fluid parcel. Indeed, the inner parcel of fluid will lose angular momentum while the outer one will gain angular momentum. This causes the inner parcel to fall towards the central object and reversely for the outer fluid parcel. For the mechanism to be effective the magnetic restoring force needs to be sufficiently weak or else it will completely stabilize the system and restore the fluid parcels to their original position.

The mechanism detailed above leads to the development of oscillatory channel mode structures that grow exponentially (Balbus and Hawley 1991). Eventually the channel mode structures break down due to the development of parasitic instabilities of Kelvin-Helmhotz type (Goodman and Xu 1994). The break down of the channel mode structures leads to the development of MRI-driven turbulence.

We define the magnetization parameter μ as

$$
\mu = \frac{V_{a0}^2}{c_{s0}^2}, \tag{2.46}
$$

where both velocities are evaluated at the disk mid-plane. This quantify is only defined at the disk mid-plane and is related to the plasma beta, $\mu = 2/\beta$. In contrast, in this manuscript the plasma beta will be defined on the entire domain.

Equation (2.45) shows that when the disk is highly magnetized, the only way for MRI to remain active is if the MRI wavelength ($\frac{2\pi}{k}$) is large. Indeed, the MRI can exist at an arbitrarily strong magnetic field, provided large enough wavelengths are possible. Moreover, for a constant MRI wavelength, the MRI cannot exists at an arbitrarily high magnetic field. We can consider that the MRI wavelength is dictated by the accretion disk scale height ($k \sim 1/H$). Indeed, we expect the MRI wavelength to be constrained by the stratification of the system. Then by using $V_A^2 = c_s^2\mu$ we rewrite Eq. (2.45) as

$$\mu < 3 \tag{2.47}$$

we derive a critical value for μ for which the accretion disk is stable to MRI. Latter et al. 2010 performed a linear analysis of the stratified MRI and found a critical value of the magnetization of 0.7. This is, within a factor of two, consistent with our value. However, in their analysis, they consider a Gaussian density profile for the stratification of the disk. If the disk density profile is modified by the presence of a mean magnetic field this analysis could be no longer valid (see chapter 4).

2.2.3 MRI at strong magnetic field

We now rederive the dispersion relation for the compressible magneto rotational instability in the limit of a strong magnetic field (or cold plasma), then we rederive in a simplified manner some of the results shown by Kim and Ostriker 2000. We consider an ideal, isothermal plasma in rotation around a central object, we perform this analysis in the local rotating coordinates defined by Eq. (2.37). Indeed, we take a fiducial radius R_0 and attach a cartesian frame (x, y, z) centered on R_0 and rotating at $\Omega = \Omega(R_0)$ so that x corresponds to the local radial direction $R - R_0$ and y the local azimuthal direction φ. We assume that the plasma is initially at equilibrium, with angular velocity $\Omega_K(R)$, constant density ρ_0, pressure $c_s^2\rho_0$ and magnetic field $\mathbf{B}_0$. As in section 2.2.1, we add a small perturbation to this plasma so that $\rho = \rho_0 + \delta\rho$, $\mathbf{u} = R\Omega_K\mathbf{e}_\varphi + \boldsymbol{\delta}\mathbf{u}$ and $\mathbf{B} = \mathbf{B}_0 + \boldsymbol{\delta}\mathbf{b}$, where $\rho_0 \gg \delta\rho$, $\mathbf{B} \gg \boldsymbol{\delta}\mathbf{b}$ and $R\Omega_K\mathbf{e}_z \gg \boldsymbol{\delta}\mathbf{u}$. In order to characterize the evolution of this perturbation, we use the displacement vector field $\boldsymbol{\xi}$, defined by its relation to the velocity perturbation

$$\boldsymbol{\delta}\mathbf{u} = \frac{D\boldsymbol{\xi}}{Dt} - (\boldsymbol{\xi}\cdot\nabla)R\Omega_K\mathbf{e}_\varphi. \tag{2.48}$$

The equation of perturbed motion for the displacement vector in the rotating frame (x, y, z) reads

$$\begin{aligned}\rho_0\frac{D^2\boldsymbol{\xi}}{Dt^2} = -c_s^2\nabla\delta\rho - \frac{1}{4\pi}\nabla(\mathbf{B}_0\cdot\delta\mathbf{b}) + \frac{1}{4\pi}\mathbf{B}_0\cdot\nabla\delta\mathbf{b}\\ - 2\rho_0\Omega_K\mathbf{e}_z\times\frac{D\boldsymbol{\xi}}{Dt} - 2\rho_0\Omega_K\frac{d\Omega_K}{d\log R}\xi_x\mathbf{e}_x.\end{aligned} \tag{2.49}$$

One recognizes in the last two terms the Coriolis force and the radial effective potential. We chose to neglect the vertical effect of gravity since it is not relevant for the behavior of instability. We can then rewrite Eq. (2.20) and Eq. (2.23) by using the displacement vector (Ogilvie 2016), the density and magnetic perturbations are easily deduced by integration

$$\begin{aligned}\delta\rho &= -\rho_0\nabla\cdot\boldsymbol{\xi},\\ \delta\mathbf{b} &= \mathbf{B}_0\cdot\nabla\boldsymbol{\xi} - \mathbf{B}_0(\nabla\cdot\boldsymbol{\xi}),\end{aligned}$$

which can be combined to the equation of motion on ξ to get

$$\begin{aligned}\frac{D^2\boldsymbol{\xi}}{Dt^2} &= (c_s^2 + V_{\rm A}^2)\nabla(\nabla\cdot\boldsymbol{\xi}) - \nabla\left[\mathbf{V}_{\rm A}\cdot\nabla(\mathbf{V}_{\rm A}\cdot\boldsymbol{\xi})\right]\\ &+ \mathbf{V}_{\rm A}\cdot\nabla\left[(\mathbf{V}_{\rm A}\cdot\nabla)\boldsymbol{\xi}\right] - \mathbf{V}_{\rm A}\left[\mathbf{V}_{\rm A}\cdot\nabla(\nabla\cdot\boldsymbol{\xi})\right]\\ &- 2\mathbf{\Omega_K}\times\frac{D\boldsymbol{\xi}}{Dt} + 2q\Omega_K^2\xi_x\mathbf{e}_x,\end{aligned}$$

where we define the Alfvén velocity vector $\mathbf{V}_{\rm A} \equiv \mathbf{B}_0/\sqrt{4\pi\rho_0}$ and $q \equiv -\mathrm{d}\log\Omega/\mathrm{d}\log R$. This equation is reminiscent of the traditional stability analysis of ideal plasmas (e.g. Frieman and Rotenberg 1960), with the addition of inertial and gravitational forces.

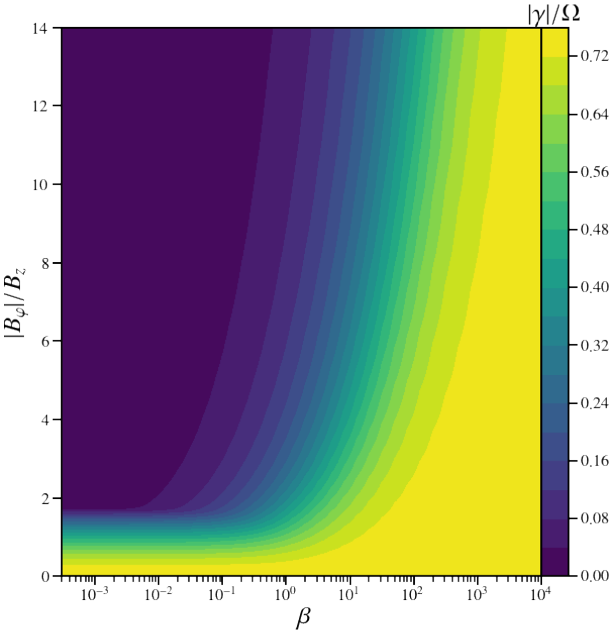

Figure 2.1: Maximum growth rate as a function of the field shear B_φ/B_z and the local plasma β for the Keplerian shear case $q = 3/2$

We assume a background field with only toroidal and vertical components $\mathbf{B}_0 = B_{0,\phi}\mathbf{e}_y + B_{0,z}\mathbf{e}_z$, and perturbations with only a vertical spatial dependency. We then seek for growing (unstable) solutions of the form $\boldsymbol{\xi}(z,t) = \hat{\boldsymbol{\xi}}\exp(\gamma t + ikz)$. Injecting this solution functional into the equation for the displacement vector one gets

$$\left[\gamma^2 + V_{\rm Az}^2k_z^2\right]\boldsymbol{\xi} = -(c_s^2 + V_A^2)k_z^2\xi_x\mathbf{e}_z + k_z^2V_{\rm Az}\left(\mathbf{V}_{\rm A}\cdot\boldsymbol{\xi}\right)\mathbf{e}_x + V_{\rm Az}k_z^2\xi_z\mathbf{V}_{\rm A} - 2\gamma\Omega_K\mathbf{e}_z\times\boldsymbol{\xi} + 2q\Omega_K^2\xi_x\mathbf{e}_x, \tag{2.50}$$

which can be rewritten in matrix form, $\overleftrightarrow{\mathcal{M}}\boldsymbol{\xi} = 0$, where

$$\overleftrightarrow{\mathcal{M}} = \begin{pmatrix} 2q\Omega_K^2 - \left[\gamma^2 + V_{\rm Az}^2k_z^2\right] & 2\gamma\Omega_K & 0 \\ -2\gamma\Omega_K & -\left[\gamma^2 + V_{\rm Az}^2k_z^2\right] & V_{\rm A\varphi}V_{\rm Az}k_z^2 \\ 0 & V_{\rm A\varphi}V_{\rm Az}k_z^2 & -\left[\gamma^2 + V_{\rm Az}^2k_z^2\right] \end{pmatrix}. \tag{2.51}$$

non trivial solutions are defined by det $\overleftrightarrow{\mathcal{M}} = 0$, one eventually gets the dispersion relation

$$\begin{aligned} c_s^2 k^2 \left[\gamma^4 + (2V_{\mathrm{A}z}^2 k^2 + \kappa^2)\gamma^2 + V_{\mathrm{A}z}^2 k^2 (V_{\mathrm{A}z}^2 k^2 - 2q\Omega_K^2)\right] & \\ + \gamma^6 + \gamma^4 \left[(V_\mathrm{A}^2 + V_{\mathrm{A}z}^2)k^2 + \kappa^2\right] & \\ + \gamma^2 V_\mathrm{A}^2 k^2 \left(V_{\mathrm{A}z}^2 k^2 + 4\Omega_K^2 \frac{V_{\mathrm{A}\varphi}^2}{V_\mathrm{A}^2} - 2q\Omega_K^2 \right) &= 0. \end{aligned} \tag{2.52}$$

where we introduce the epicyclic frequency $\kappa^2 \equiv 2\Omega^2(2-q)$. Although general solutions can be derived for this dispersion relation, they are not enlightening. It is more instructive to look at the weakly magnetized and strongly magnetized limits.

In the weakly magnetized case ($V_\mathrm{A}/c_s \to 0$) the first line of Eq. (2.52) dominates, and we recover[1] the usual dispersion relation for the MRI in the incompressible limit (Balbus and Hawley 1991). The stability condition is then the same as in our previous calculation and is given by Eq. (2.45) when $q = 3/2$. As discussed before, the stability of the MRI in this regime depends completely on the size of the perturbation k.

If we now take the strong field limit $V_\mathrm{A}/c_s \to \infty$, things become more interesting. The first line of the dispersion relation is now negligible. We can write the stability condition now as $V_{\mathrm{A}z}^2 k^2 + 4\Omega^2 V_{\mathrm{A}\varphi}^2 / V_\mathrm{A}^2 - 2q\Omega^2 < 0 \to$ instability. A weak enough $V_{\mathrm{A}\varphi}$ is necessary for the MRI to exist *independently of* k, in contrast to the weak field case. More precisely, a necessary condition for the instability to exist is

$$V_{\mathrm{A}\varphi}^2 / V_\mathrm{A}^2 < q/2. \tag{2.53}$$

In this limit Eq. (2.52) reduces to equation (46) in Kim and Ostriker 2000.

In the strongly magnetized regime, $V_\mathrm{A} \gg c_s$, the existence of the MRI is constrained by the strength of the toroidal magnetic field, a strong enough B_φ can stabilize the plasma. We can confirm this by computing the growth rate, γ, in the general case from Eq. (2.52). We show this in Fig. 2.1, which shows the growth rate (maximized on k) as a function of the field strength $V_{\mathrm{A}\varphi}/V_{\mathrm{A}z} = B_\varphi/B_z$ and the plasma beta β for the Keplerian case $q = 3/2$.

2.3 Magnetized and turbulent disks

2.3.1 Reynolds averaged MHD equations

The MRI discussed in the previous section will lead to the development of MHD turbulence within the accretion disk system. Once the MRI-driven turbulence appears the characteristics of the system become harder to quantify. It is hard to diagnostic the properties of the flow ($\mathbf{u}$, ρ, $\mathbf{B}$) due to its unsteadiness and variability. It is useful to separate the non-steady length and time scales from the average ones. To do this we introduce a coarse-graining procedure known as Reynolds decomposition

$$X = \langle X \rangle + \delta X, \tag{2.54}$$

where $\langle\rangle$ is an ensemble average. The Reynolds decomposition allows us to distinguish the low frequency or quasi-stationary component ($\langle X \rangle$), that we refer to as mean, average or laminar, from the variable or intermittent component (δX). The intermittent component (δX) has the important property

$$\langle \delta X \rangle = 0. \tag{2.55}$$

---

[1] We note that we also get sound waves propagating vertically from the γ^6 and $\gamma^4 c_s^2 k^2$ terms. These however have no importance on the stability criterion.

Correlations between different turbulent fluctuations do not vanish under averaging, indeed, terms of the form $\langle \delta X \delta Y \rangle \neq 0$. These emergent terms represent the average feedback of turbulence on the mean outflow. In this manuscript they will be computed using 3D numerical simulations (chapter 4) or approximated with a turbulent closure (chapter 3 and 5).

An ensemble average is computed by repeating the same numerical experiments multiple times and averaging over the multiple realizations. It is therefore a quantity that is very numerically expensive to compute. We can assume ergodicity so that the ensemble average is computed as a simple integral on t and φ, see Eq. (4.14) in chapter 4. This simplifies the dependencies of the average components to $\langle X \rangle (R, z)$, while $\delta X(R, \varphi, z, t)$. However, one must be careful when reducing averaging out the temporal dependence of the equations. One must consider the temporal time scale separation of the problem during the averaging procedure.

In this section we compute a set of ensemble averaged MHD equations without assuming ergodicity, our average quantities still depend on time. However, to simplify the resulting Reynolds average set of equations we also average with respect to the toroidal coordinate[2], φ. Hence, our average has the following useful property due to the toroidal symmetry of the system

$$\left\langle \frac{\partial X}{\partial \varphi} \right\rangle = 0. \tag{2.56}$$

For the sake of simplicity, we also define the following useful average

$$\langle X \rangle_\rho = \frac{1}{\langle \rho \rangle} \langle X \rho \rangle, \tag{2.57}$$

noting that $\langle X \rangle \neq \langle X \rangle_\rho$, since we define our turbulent fluctuation with respect to the $\langle . \rangle$ average. Indeed, Eq.(2.54) also implies that $\langle \delta X \rangle_\rho \neq 0$, which leads to additional complications when dealing with high order correlations.

Before averaging the MHD equations we project the momentum equation with respect to the spherical coordinates

$$\frac{\partial u_r \rho}{\partial t} + \nabla \cdot \left[\rho u_r \mathbf{u} - \frac{1}{4\pi} B_r \mathbf{B} \right] = \frac{1}{r} \left[\rho \left(u_\varphi^2 + u_\theta^2 \right) - \frac{1}{4\pi} \left(B_\varphi^2 + B_\theta^2 \right) \right] - \frac{\partial}{\partial r} \left(\frac{B^2}{8\pi} + P \right) - \rho g, \tag{2.58}$$

$$\frac{\partial r u_\theta \rho}{\partial t} + \nabla \cdot r \left[\rho u_\theta \mathbf{u} - \frac{1}{4\pi} B_\theta \mathbf{B} \right] = \cot\theta \left[\rho u_\varphi^2 - \frac{1}{4\pi} B_\varphi^2 \right] - \frac{\partial}{\partial \theta} \left(\frac{B^2}{8\pi} + P \right), \tag{2.59}$$

$$\frac{\partial R u_\varphi \rho}{\partial t} + \nabla \cdot R \left[\rho u_\varphi \mathbf{u} - \frac{B_\varphi \mathbf{B}}{4\pi} \right] = -\frac{\partial}{\partial \varphi} \left(\frac{B^2}{8\pi} + P \right). \tag{2.60}$$

Equation 2.60 is the angular momentum conservation equation and is obtained from the toroidal component of Eq. (2.21),

We now proceed to Reynolds average Eq. (2.20-2.23), we decompose the toroidal velocity into fluctuating and average components

$$R\rho \frac{\partial \langle u_\varphi \rangle}{\partial t} + \frac{\partial R \delta u_\varphi \rho}{\partial t} + R \langle u_\varphi \rangle \underbrace{\left(\frac{\partial \rho}{\partial t} + \nabla \cdot \rho \mathbf{u} \right)}_{=0} + \rho \mathbf{u} \cdot \nabla \left[R \langle u_\varphi \rangle \right] + \nabla \cdot R \left[\rho \delta u_\varphi \mathbf{u} - \frac{B_\varphi \mathbf{B}}{4\pi} \right] = -\frac{\partial}{\partial \varphi} \left(\frac{B^2}{8\pi} + P \right).$$

---

[2] This is consistent with our computations of chapter 4

we then decompose the rest of the quantities and average this expression to find

$$R\rho\frac{\partial\left\langle u_\varphi\right\rangle}{\partial t}+\frac{\partial R\left\langle\rho\delta u_\varphi\right\rangle}{\partial t}+\langle\rho\rangle\left\langle\mathbf{u_p}\right\rangle_\rho\cdot\nabla R\left\langle u_\varphi\right\rangle+\nabla\cdot R\left[\langle\rho\rangle\left\langle\delta u_\varphi\mathbf{u_p}\right\rangle_\rho-\frac{1}{4\pi}\left\langle\delta B_\varphi\boldsymbol{\delta}\mathbf{B_p}\right\rangle-\frac{1}{4\pi}\left\langle B_\varphi\right\rangle\left\langle\mathbf{B_p}\right\rangle\right]=0, \tag{2.61}$$

where $\left\langle\mathbf{u_p}\right\rangle_\rho=\left\langle\mathbf{u_p}\right\rangle+\left\langle\delta\mathbf{u_p}\right\rangle_\rho$ and

$$\left\langle\delta u_i\mathbf{u_p}\right\rangle_\rho=\left\langle\delta u_i\delta\mathbf{u_p}\right\rangle_\rho+\left\langle\mathbf{u_p}\right\rangle\langle\delta u_i\rangle_\rho.$$

We note that the toroidal component of the divergence vanishes thanks to Eq. (2.56), the averaged quantities are only functions of r and θ. We repeat the same procedure for the latitudinal projection of Eq. (2.21) equation to rewrite it as

$$r\rho\frac{\partial\langle u_\theta\rangle}{\partial t}+\frac{\partial r\delta u_\theta\rho}{\partial t}+\rho\mathbf{u_p}\cdot\nabla r\langle u_\theta\rangle+\nabla\cdot r\left[\rho\delta u_\theta\mathbf{u}-\frac{1}{4\pi}B_\theta\mathbf{B}\right]=\cot\theta\left[\rho u_\varphi^2-\frac{1}{4\pi}B_\varphi^2\right]-\frac{\partial}{\partial\theta}\left(\frac{B^2}{8\pi}+P\right), \tag{2.62}$$

we then average it with respect to time and the azimuthal coordinate to find

$$\begin{gathered}r\rho\frac{\partial\langle u_\theta\rangle}{\partial t}+\frac{\partial r\langle\rho\delta u_\theta\rangle}{\partial t}+\langle\rho\rangle\left\langle\mathbf{u_p}\right\rangle_\rho\cdot\nabla r\langle u_\theta\rangle+\nabla\cdot r\left[\langle\rho\rangle\left\langle\delta u_\theta\mathbf{u_p}\right\rangle_\rho-\frac{1}{4\pi}\left\langle\delta B_\theta\boldsymbol{\delta}\mathbf{B_p}\right\rangle\right]=\\ \frac{1}{4\pi}\left\langle\mathbf{B_p}\right\rangle\cdot\nabla r\langle B_\theta\rangle-\frac{\partial}{\partial\theta}\left[\langle P\rangle+\frac{1}{8\pi}\left(\langle B\rangle^2+\left\langle\delta B^2\right\rangle\right)\right]+\cot\theta\left[\langle\rho\rangle\left(\left\langle u_\varphi\right\rangle^2+\left\langle\delta u_\varphi^2\right\rangle\right)-\frac{1}{4\pi}\left(\left\langle B_\varphi\right\rangle^2+\left\langle\delta B_\varphi^2\right\rangle\right)\right],\end{gathered} \tag{2.63}$$

where we have used

$$\langle\nabla\cdot\mathbf{B}B_i\rangle=\left\langle\mathbf{B_p}\right\rangle\cdot\nabla\langle B_i\rangle+\nabla\cdot\left\langle\delta\mathbf{B_p}\delta B_i\right\rangle.$$

We repeat the same procedure for the radial projection of Eq. (2.21) equation to rewrite it as

$$\rho\frac{\partial\langle u_r\rangle}{\partial t}+\frac{\partial\delta u_r\rho}{\partial t}+\rho\mathbf{u_p}\cdot\nabla\langle u_r\rangle+\nabla\cdot\left[\rho\delta u_r\mathbf{u}-\frac{1}{4\pi}B_r\mathbf{B}\right]=\frac{1}{r}\left[\rho\left(u_\varphi^2+u_\theta^2\right)-\frac{1}{4\pi}\left(B_\varphi^2+B_\theta^2\right)\right]-\frac{\partial}{\partial r}\left(\frac{B^2}{8\pi}+P\right)-\rho g, \tag{2.64}$$

we then average it in the same way as before to find

$$\begin{aligned}&\rho\frac{\partial\langle u_r\rangle}{\partial t}+\frac{\partial\langle\rho\delta u_r\rangle}{\partial t}+\langle\rho\rangle\left\langle\mathbf{u_p}\right\rangle_\rho\cdot\nabla\langle u_r\rangle+\nabla\cdot\left[\langle\rho\rangle\left\langle\delta u_r\mathbf{u_p}\right\rangle_\rho-\frac{1}{4\pi}\left\langle\delta B_r\boldsymbol{\delta}\mathbf{B_p}\right\rangle\right]=\\ &-\frac{\partial}{\partial r}\left[\langle P\rangle+\frac{1}{8\pi}\left(\langle B\rangle^2+\left\langle\delta B^2\right\rangle\right)\right]+\frac{1}{4\pi}\left\langle\mathbf{B_p}\right\rangle\cdot\nabla\langle B_r\rangle\\ &+\frac{\langle\rho\rangle}{r}\left[\left\langle u_\varphi\right\rangle^2+\left\langle\delta u_\varphi^2\right\rangle+\langle u_\theta\rangle^2+\left\langle\delta u_\theta^2\right\rangle\right]-\langle\rho\rangle g-\frac{1}{4\pi r}\left[\left\langle B_\varphi\right\rangle^2+\left\langle\delta B_\varphi^2\right\rangle+\langle B_\theta\rangle^2+\left\langle\delta B_\theta^2\right\rangle\right]\end{aligned} \tag{2.65}$$

We now average Eq. (2.20), thanks to its simple form this is straight forward

$$\left\langle\frac{\partial\rho}{\partial t}\right\rangle+\nabla\cdot\langle\rho\rangle\left[\langle\mathbf{u}\rangle+\langle\delta\mathbf{u}\rangle_\rho\right]=0. \tag{2.66}$$

The induction equation is also straight forward to average

$$\left\langle\frac{\partial\mathbf{B}}{\partial t}\right\rangle=\nabla\times\left[\langle\mathbf{u}\rangle\times\langle\mathbf{B}\rangle+\mathcal{E}\right], \tag{2.67}$$

where the turbulent emf is defined as

$$\mathcal{E}=\langle\boldsymbol{\delta}\mathbf{u}\times\boldsymbol{\delta}\mathbf{B}\rangle. \tag{2.68}$$

We can then project with respect to the toroidal direction to find

$$\left\langle \frac{\partial B_\varphi}{\partial t} \right\rangle = \nabla \times \left[\langle \mathbf{u} \rangle \times \langle \mathbf{B} \rangle + \mathcal{E} \right]\Big|_\varphi . \tag{2.69}$$

While we could treat the latitudinal and radial components of the induction equation separately it is less cumbersome to average the toroidal component of the equation for the vector potential. Indeed, the average poloidal magnetic field can be written as

$$\left\langle \mathbf{B_p} \right\rangle = \frac{1}{R} \nabla \left[R \left\langle A_\varphi \right\rangle \right] \times \mathbf{e_\varphi}, \tag{2.70}$$

hence the average poloidal magnetic field is fully described by the toroidal component of the vector potential equation, which is written as

$$\frac{\partial \mathbf{A}}{\partial t} = \mathbf{u} \times \mathbf{B} + \nabla G, \tag{2.71}$$

where **A** is the vector potential for the magnetic field and G emerges to satisfy the gauge condition. To simplify the equations we assume that G is φ symmetric and thus $\left\langle \frac{\partial G}{\partial \varphi} \right\rangle = 0$. Averaging the toroidal projection of Eq. (2.71) leads to

$$\left\langle \frac{\partial A_\varphi}{\partial t} \right\rangle = \left\langle \mathbf{u_p} \right\rangle \times \left\langle \mathbf{B_p} \right\rangle \Big|_\varphi + \mathcal{E}_\varphi, \tag{2.72}$$

the term $\nabla G|_\varphi$ is averaged out. Finally, we also define the flux function $a = R \left\langle A_\varphi \right\rangle$, $a(R, z) = C^{te}$ defines surfaces where the magnetic flux, Φ_B is constant,

$$\Phi_B = \int_S \mathbf{B} \cdot \mathrm{d}\mathbf{S} = 2\pi a(R, z). \tag{2.73}$$

We can appreciate that a considerable amount of new terms, in the form of turbulent correlations appear thanks to the averaging procedure, luckily the majority of these turbulent correlations do not have a considerable impact on the dynamics. However, some of them have been the subject of countless studies: like the turbulent emf, $\mathcal{E}$, that influences the behavior of the large scale magnetic or the turbulent Reynolds and Maxwell stresses that have an essential impact on the accretion, we will concentrate our analysis on those terms as well as on the newly revealed turbulent magnetic pressure.

Using this notation we rewrite the magnetization parameter as

$$\mu = \frac{\langle B_z \rangle^2 (R, z = 0)}{4\pi \langle P \rangle (R, z = 0)}, \tag{2.74}$$

the magnetization is a function of the mean field variables and does not include turbulent correlations.

2.3.2 Two torques

As discussed in chapter 1, accretion is the consequence of angular momentum transport, for accretion to exist angular momentum needs to be removed from the system. We also discussed, that two processes can drive angular momentum transport laminar and turbulent processes. The

Reynolds decomposition allows us to differentiate both terms. We return to Eq.(2.61), the conservation of angular momentum

$$\langle\rho\rangle\left\langle\mathbf{u_p}\right\rangle_\rho\cdot\nabla R\left\langle u_\varphi\right\rangle+\nabla\cdot R\left[\langle\rho\rangle\left\langle\delta u_\varphi\mathbf{u_p}\right\rangle_\rho-\frac{1}{4\pi}\left\langle\delta B_\varphi\boldsymbol{\delta}\mathbf{B_p}\right\rangle-\frac{1}{4\pi}\left\langle B_\varphi\right\rangle\left\langle\mathbf{B_p}\right\rangle\right]=0, \tag{2.75}$$

where we assume stationarity and we neglect the terms that have no dynamical importance. The terms $\left\langle\mathbf{u_p}\right\rangle\left\langle\delta u_\varphi\right\rangle_\rho$ do not play an important role in the dynamics computed in numerical simulations.

We can then define two fundamental stresses acting on the system

$$\mathcal{T}=\mathcal{T}_{tu}+\mathcal{T}_{la}, \tag{2.76}$$

where we define

$$\mathcal{T}_{la}=-\frac{1}{4\pi}\left\langle B_\phi\right\rangle\left\langle\mathbf{B_p}\right\rangle, \tag{2.77}$$

the laminar stress tensor, and

$$\mathcal{T}_{tu}=\langle\rho\rangle\left\langle\delta u_\phi\boldsymbol{\delta}\mathbf{u_p}\right\rangle_\rho-\frac{1}{4\pi}\left\langle\delta B_\phi\boldsymbol{\delta}\mathbf{B_p}\right\rangle, \tag{2.78}$$

the turbulent stress tensor. These two stresses are the main agents driving the accretion of the system. The laminar torque depends on the magnetic topology and is often, but not exclusively, the consequence of a magnetized wind. The turbulent torque is often associated with hydrodynamic or magnetohydrodynamic turbulence but can also be driven by spiral waves. By assuming $\left\langle u_\varphi\right\rangle\simeq R\Omega_K$, where Ω_K is the Keplerian angular frequency we find

$$\langle\rho\rangle\left\langle u_R\right\rangle_\rho\frac{\partial R^2\Omega_K}{\partial R}=-\nabla\cdot R\left[\mathcal{T}_{tu}+\mathcal{T}_{la}\right]. \tag{2.79}$$

The bulk velocity $\langle\rho\rangle\left\langle u_R\right\rangle$ is entirely determined by the laminar and turbulent torques. We compute the accretion rate defined as

$$\dot{M}_a=-\int_{-z_h}^{z_h}2\pi R\langle\rho\rangle\left\langle u_R\right\rangle_\rho\mathrm{d}z=\frac{4\pi}{\Omega_K}\left[M_{R\varphi}+M_{z\varphi}\right], \tag{2.80}$$

where z_h is an arbitrary height where the accretion stops, its exact definition will depend on the system considered. We also define the accretion torques as

$$M_{z\varphi}=-\frac{R}{4\pi}\left[\left\langle B_z\right\rangle\left\langle B_\phi\right\rangle\right]_{-z_h}^{z_h}+R\left[\mathcal{T}_{tu,z}\right]_{-z_h}^{z_h}, \tag{2.81}$$

$$M_{R\varphi}=-\frac{1}{4\pi R}\int_{-z_h}^{z_h}\frac{\partial}{\partial R}\left[R^2\left\langle B_R\right\rangle\left\langle B_\phi\right\rangle\right]\mathrm{d}z+\frac{1}{R}\int_{-z_h}^{z_h}\frac{\partial R^2\mathcal{T}_{tu,R}}{\partial R}\mathrm{d}z. \tag{2.82}$$

We can conclude that accretion is entirely driven by the turbulent and mean magnetic torques, the radial torque transports angular momentum outward radially while the vertical torque evacuates the angular momentum by a torque applied at the disk surface. We note that both the latitudinal and radial torques are composed of mean and turbulent components. Finally, we define their ratio as

$$\Lambda=\frac{M_{z\varphi}}{M_{R\varphi}}. \tag{2.83}$$

This quantity is useful for characterizing the transport properties as it indicates the dominant torque. Furthermore, it can be related to the properties of the outflow as we show in section 2.5.5. We compute this quantity in chapter 3 and measure its correlation to other parameters like the magnetization.

2.3.3 Alfvén theorem and its average

The induction equation has an insightful geometrical interpretation called the flux freezing or Alfvén theorem. We define the magnetic flux circulating though a surface S of differential surface element $\mathrm{d}\mathbf{S}$ enclosed by the curve C with the differential line element $\mathrm{d}\mathbf{l}$ as

$$\Phi_B = \int_S \mathbf{B} \cdot \mathrm{d}\mathbf{S}. \tag{2.84}$$

We can use Leibniz integral rule to compute its Lagrangian derivative with respect to time

$$\frac{\mathrm{d}\Phi_B}{\mathrm{d}t} = \int_S \left[\frac{\partial \mathbf{B}}{\partial t} + \mathbf{u}\,\underbrace{(\nabla \cdot \mathbf{B})}_{=0} \right] \cdot \mathrm{d}\mathbf{S} - \int_C \mathbf{u} \times \mathbf{B} \cdot \mathrm{d}\mathbf{l}, \tag{2.85}$$

where $\mathbf{u}$ is the velocity of the surface, using Stokes theorem we rewrite this as

$$\frac{\mathrm{d}\Phi_B}{\mathrm{d}t} = \int_S \left[\frac{\partial \mathbf{B}}{\partial t} - \nabla \times (\mathbf{u} \times \mathbf{B}) \right] \cdot \mathrm{d}\mathbf{S}, \tag{2.86}$$

by recognizing Eq. (2.23) we deduce

$$\Phi_B = \int_S \mathbf{B} \cdot \mathrm{d}\mathbf{S} = C^{st}. \tag{2.87}$$

The magnetic flux traversing a surface advected by the fluid is constant. Indeed, the fluid is free to travel along the magnetic field but perpendicular motions will cause the magnetic field to push the flow or to be advected with the fluid.

The simplicity of this picture can be modified for the mean magnetic field in the presence of turbulence. We define the average magnetic and turbulent flux circulating through the same surface

$$\langle \Phi_B \rangle = \int_S \langle \mathbf{B} \rangle \cdot \mathrm{d}\mathbf{S}$$

we also define the average Lagrangian derivative with respect to time

$$\frac{\bar{\mathrm{d}}}{\mathrm{d}t} = \frac{\partial}{\partial t} + \langle u \rangle \cdot \nabla,$$

we again use Leibniz integral rule to compute it

$$\frac{\bar{\mathrm{d}}\,\langle \Phi_B \rangle}{\mathrm{d}t} = \int_S \left[\frac{\partial \langle \mathbf{B} \rangle}{\partial t} - \nabla \times (\langle \mathbf{u} \rangle \times \langle \mathbf{B} \rangle) \right] \cdot \mathrm{d}\mathbf{S}, \tag{2.88}$$

by using Eq. (2.67) we deduce

$$\frac{\bar{\mathrm{d}}\,\langle \Phi_B \rangle}{\mathrm{d}t} = \int_S [\nabla \times \mathcal{E}] \cdot \mathrm{d}\mathbf{S}, \tag{2.89}$$

we see that the Alfvén theorem does not hold for the *average* magnetic flux. The mean magnetic field is *not* frozen in with the mean movements of the fluid, the mean flow is free to cross the magnetic field lines. The flow needs to cross the mean vertical magnetic field lines for accretion to take place. Indeed, turbulence allows accretion to take place. However, even in fully developed turbulence, the Alfvén theorem *always* holds for the *instantaneous* magnetic field, as long as we are in ideal MHD. In reality, the *average* magnetic field is not a physical quantity but a mathematical tool that quantifies the large scale behavior of the *instantaneous* magnetic field in the presence of strong turbulence.

2.4 Turbulent transport

2.4.1 Turbulent viscosity

Mixing length theories have achieved great success in numerous areas to model the effect of turbulence on the mean flow. Shakura and Sunyaev 1973 developed a mean field closure to model the radial turbulent torque, $\mathcal{T}_{tu,R}$, akin to a mixing length theory. Using dimensional analysis, Shakura and Sunyaev 1973 postulated that the turbulence within the disk should have two specific properties: First, the fluid perturbation should have a size of the order of the disk geometrical thickness, $h = c_s/\Omega_K$, and then, since the source of energy is gravity, the forcing frequency of the turbulence should be of the order of the Keplerian frequency, Ω_K. If we put this together we have

$$\delta u \sim lH\Omega_K,$$

where l is a dimensionless constant of order unity. We can then use the definition of the turbulent torque to find

$$\mathcal{T}_{tu,R} \sim l^2 H^2 \Omega_K^2 \rho \sim l^2 c_s^2 \rho = \alpha_v P \tag{2.90}$$

where $\alpha_v = l^2$ is the alpha Shakura and Sunyaev 1973 constant. The turbulent torque can be rewritten as a purely viscous torque[3],

$$\mathcal{T}_{tu,R} = -\frac{2}{3}\nu_t \rho R \frac{\partial \Omega}{\partial R}, \tag{2.91}$$

where we define the turbulent viscosity as $\nu_t = \alpha_v c_s h$. This coefficient has been measured successfully in local non-stratified (Hawley et al. 1995) and stratified (Salvesen et al. 2016) shearing box simulations. In the case of stratified shearing box simulations with mean vertical magnetic field it has been computed to depend on the strength of the magnetic field, or more precisely

$$\alpha_v \simeq 7\mu^{1/2}, \tag{2.92}$$

for $\mu \in [10^{-5}, 10]$. We use a similar prescription for the turbulent torque in chapter 3 in the context of self-similar solutions. In chapter 5 we measure the dependence of α_v as a function of the magnetization (or plasma beta) to see if our 3D simulations are consistent with the results of Salvesen et al. 2016.

Finally, we estimate the accretion time scale as

$$t_{\text{acc}} = \frac{R^2}{\nu_t} = \frac{1}{\alpha_v \Omega_k}\left(\frac{R}{h}\right)^2 \gg \frac{2\pi}{\Omega_K}, \tag{2.93}$$

where we used $\nu_t = \alpha_v c_s h$. Accretion in the Shakura and Sunyaev 1973 prescription occurs on very long time scale when compared to the orbital period.

2.4.2 Turbulent resistivity

The turbulent term responsible for matter diffusing through the field lines is the turbulent emf, $\mathcal{E}$. This term has garnered less attention than the turbulent viscosity, due to it not being a direct contributor to accretion. Moreover, the dynamics of ejection are highly influenced by the profile and magnitude of the turbulent emf and this turbulent term allows accretion through the field lines (as explained in section 2.3.3). In dynamo theories (Moffatt 1978; Rincon 2019) it is

---

[3] This an accurate closure if α_v becomes a function of z (Fromang et al. 2011)

common to close $\mathcal{E}$, to a first approximation, as a turbulent resistivity acting on the magnetic field,

$$\mathcal{E} = -\frac{4\pi}{c}\eta_t \langle \mathbf{J} \rangle = -\eta_t \nabla \times \langle \mathbf{B} \rangle \,. \tag{2.94}$$

The diffusivity could be taken as being proportional to the turbulent viscosity as they are both a consequences of the same processes, $\eta_t \sim \alpha_\eta c_s h$. While this is correct, it leads in the same way as for the viscosity, to a α_η that is a function of the magnetic field strength. In this work, we prefer to first define the effective magnetic Prandtl number that measures the ratio between the two transport coefficients

$$\mathcal{P}_m = \frac{\nu_t}{\eta_t}, \tag{2.95}$$

this dimensionless number has been measured in local shearing box simulations (Fromang and Stone 2009; Guan and Gammie 2009; Lesur and Longaretti 2009), they measure

$$\mathcal{P}_m \sim 2, \tag{2.96}$$

for $\mu \in [10^{-4}, 10^{-2}]$.

In contrast to Shakura and Sunyaev 1973, Ferreira and Pelletier 1993 assume that the resistivity is proportional to the Alfvén velocity defined at the disk mid-plane.

$$\eta_t = \alpha_m V_{a0} h, \tag{2.97}$$

this leads, when combined with the measurements of the magnetic Prandtl number to

$$\alpha_\nu = \mathcal{P}_m \alpha_m \mu^{\frac{1}{2}}, \tag{2.98}$$

which is pretty close to the scaling measured in shearing box numerical simulations (Salvesen et al. 2016) as long as $\alpha_m \sim 3$. It should be noted that α_m does not depend on μ. In Eq. (2.94) we have assumed that the resistivity is isotropic, however, shearing box simulations show that this is not the case for MRI turbulence (Lesur and Longaretti 2009). In such a case, the closure is no longer valid and the resistivity needs to be defined as a tensor

$$\mathcal{E} = -\frac{4\pi}{c}\overleftrightarrow{\eta} \langle \mathbf{J} \rangle \,, \tag{2.99}$$

and most approaches consider a diagonal tensor

$$\overleftrightarrow{\eta} = \begin{pmatrix} \eta_{RR} & 0 & 0 \\ 0 & \eta_{\varphi\varphi} & 0 \\ 0 & 0 & \eta_{zz} \end{pmatrix}. \tag{2.100}$$

Even a diagonal tensor can vastly complicate the modeling as well as the measurement of the transport coefficients in simulations. Ferreira and Pelletier 1995 consider a diagonal tensor for the resistivity with the coefficients of the form

$$\eta_{RR} = \eta_{zz} = \eta'_m \tag{2.101}$$

$$\eta_{\varphi\varphi} = \eta_m. \tag{2.102}$$

They argue that the toroidal resistivity linked to the toroidal magnetic field and the poloidal current, could be different from the poloidal resistivity linked to the poloidal magnetic field and the toroidal current. A possible source of anisotropy could be the reconnection processes occurring at the disk mid-plane linked to the poloidal current. The parameter measuring the degree of anisotropy is defined as

$$\chi_m = \frac{\eta_m}{\eta'_m}, \tag{2.103}$$

and a typical value was found to be $\chi_m \sim \frac{1}{3}$ (Eq.(19) in Ferreira and Pelletier 1995). This quantify has been measured in shearing box simulations to be $\chi_m \sim 0.3$ (Lesur and Longaretti 2009).

In chapter 3 we explore the effect of the turbulent parameters defined here (α_m, $\mathcal{P}_m$, χ_m) in the properties of the outflow and the disk using self-similar solutions. In chapter 5 we measure those parameters directly in our 3D numerical simulations and compare them with the results from shearing box simulations.

2.4.3 Magnetic flux transport

As discussed in chapter 1, it has been proposed that the secular evolution of accretion disk in Xray binaries and CV is related to the transport of the vertical magnetic flux (Marcel et al. 2019; Scepi et al. 2020). Therefore, it is important to understand the mechanisms involved in the advection of large scale the magnetic field. The transport of magnetic flux is the consequence of the competition between the turbulent diffusion driven by $\mathcal{E}$ and the advection due to the inward transport of matter. It is possible to differentiate both mechanisms involved by recasting the vector potential equation

$$\left\langle \frac{\partial \mathbf{A}}{\partial t} \right\rangle = \langle \mathbf{u} \rangle \times \langle \mathbf{B} \rangle + \mathcal{E}(t), \tag{2.104}$$

as

$$\frac{\partial \langle \Psi \rangle}{\partial t} = R \langle B_z \rangle \left[\langle u_z \rangle \frac{\langle B_R \rangle}{\langle B_z \rangle} - \langle u_R \rangle + \frac{\mathcal{E}_\varphi(t)}{\langle B_z \rangle} \right], \tag{2.105}$$

where $\langle \partial_t \Psi \rangle = R \left\langle \partial_t A_\varphi \right\rangle$, we then use the fact that $R \langle B_z \rangle = \partial_R \langle \Psi \rangle$ to rewrite this equation as

$$\frac{\partial \Psi}{\partial t} + v_\Psi \frac{\partial \Psi}{\partial R} = 0, \tag{2.106}$$

where v_Ψ is the transport velocity that commands the evolution of the magnetic field and is defined as

$$v_\Psi = \langle u_R \rangle - \langle u_z \rangle \frac{\langle B_R \rangle}{\langle B_z \rangle} - \frac{\mathcal{E}_\varphi(t)}{\langle B_z \rangle}. \tag{2.107}$$

We can see that v_Ψ is a consequence of the competition between the accretion and the turbulent emf, the difficulty of the problem will arise from the way we model this term. Equation 2.107 may look like a simple advection problem. However, the diffusion term is hidden within the turbulent emf and depends strongly on the prescribed closure. Furthermore, another important difficulty, hidden by our notation, is that the average velocity, $\langle u_r \rangle$, intervenes in the advection of the magnetic field and not the density averaged velocity, $\langle u_r \rangle_\rho$. Indeed, both quantities are not necessarily equal to each other, $\langle u_r \rangle \neq \langle u_r \rangle_\rho$. Hence, the existence of accretion does not imply the existence of field advection towards the inner regions.

In chapter 4 we use Eq. (2.106) to characterize the secular evolution of the magnetic field. We then measure v_Ψ and study how it changes as a function of the magnetization and the disk geometrical thickness.

2.5 Outflow dynamics

In this section, we will discuss the dynamics of the outflow, including the outflow launching and the phenomenology of its propagation.

Once the outflow is launched it will be accelerated through three critical surfaces, the slow point , where $\left\langle u_p \right\rangle = V_{sm}$, the Alfvén point, where $\left\langle u_p \right\rangle = V_{Ap}$, and, finally the fast point, where $\left\langle u_p \right\rangle = V_{fm}$. We will define the field line anchoring radius (the radii where the wind is launched) as $R_{\rm SM}$, this corresponds to the slow magneto-sonic critical surface.

2.5.1 MHD invariants

In the regions where the outflow is propagating the flow is approximately laminar. In this region, MRI-driven turbulence is quenched by the strong magnetic field and the perturbations are quickly advected by the fluid motions. If the outflow is also quasi-stationary it is possible to define a set of MHD invariants that characterize the properties of the outflow. Under these conditions, Eq. (2.72) reduces to

$$\left\langle \mathbf{u_p} \right\rangle \times \left\langle \mathbf{B_p} \right\rangle = 0, \tag{2.108}$$

we deduce that the poloidal magnetic field and velocity are parallel, e.g.

$$\left\langle \mathbf{u_p} \right\rangle = l \left\langle \mathbf{B_p} \right\rangle, \tag{2.109}$$

this condition is just the Alfvén theorem in explicit form. If the flow is laminar and stationary the conservation of mass, Eq. (2.66), can be simply written as

$$\nabla \cdot \left[\left\langle \mathbf{u_p} \right\rangle \langle \rho \rangle \right] = 0, \tag{2.110}$$

which we recast by using Eq. (2.109)

$$\left\langle \mathbf{B_p} \right\rangle \cdot \nabla \langle \rho \rangle \, l = 0, \tag{2.111}$$

this result implies that $\tilde{\eta} \equiv 4\pi \langle \rho \rangle l$ is constant along the magnetic field lines. We rewrite Eq. (2.109) as

$$\left\langle \mathbf{u_p} \right\rangle = \frac{\tilde{\eta}}{4\pi \langle \rho \rangle} \left\langle \mathbf{B_p} \right\rangle, \tag{2.112}$$

where we have introduced the constant 4π to keep our definitions consistent with Blandford and Payne 1982. The invariant $\tilde{\eta}$ is called the mass loading invariant because it can be linked to the density at the Alfvén point, ρ_A, by remembering $\left\langle u_{pA} \right\rangle = V_{Ap} = B_p / \sqrt{4\pi \rho_A}$. We show

$$\tilde{\eta} = \sqrt{\rho_A 4\pi}. \tag{2.113}$$

The toroidal component of the induction equation simplifies to

$$\frac{\partial}{\partial z} \left[\left\langle u_\varphi \right\rangle \langle B_z \rangle - \langle u_z \rangle \left\langle B_\varphi \right\rangle \right] + \frac{\partial}{\partial R} \left[\left\langle u_\varphi \right\rangle \langle B_R \rangle - \langle u_R \rangle \left\langle B_\varphi \right\rangle \right] = \nabla \cdot \frac{1}{R} \left[\left\langle u_\varphi \right\rangle \left\langle \mathbf{B_p} \right\rangle - \left\langle B_\varphi \right\rangle \left\langle \mathbf{u_p} \right\rangle \right] = 0, \tag{2.114}$$

it can be rewritten using Eq. (2.112) as

$$\left\langle \mathbf{B_p} \right\rangle \cdot \nabla \left[\frac{\left\langle u_\varphi \right\rangle}{R} - \frac{\tilde{\eta} \left\langle B_\varphi \right\rangle}{4\pi \langle \rho \rangle R} \right], \tag{2.115}$$

we define the invariant as

$$\Omega_\star = \frac{\left\langle u_\varphi \right\rangle}{R} - \frac{\tilde{\eta}\left\langle B_\varphi \right\rangle}{4\pi \langle\rho\rangle R} = \frac{\left\langle u_{\varphi,A} \right\rangle}{R_A} - \frac{V_{A,\varphi}(R_A)}{R_A}, \tag{2.116}$$

where $\Omega_\star$ is a measure of the angular velocity of the magnetic field lines.

The conservation of angular momentum can be recast using the conservation of mass as

$$\nabla \cdot R\left[\langle\rho\rangle \left\langle \mathbf{u_p} \right\rangle \left\langle u_\varphi \right\rangle - \frac{\left\langle B_\varphi \right\rangle \left\langle \mathbf{B_p} \right\rangle}{4\pi}\right] = 0, \tag{2.117}$$

it can then be rewritten by using Eq. (2.112) as

$$\left\langle \mathbf{B_p} \right\rangle \cdot \nabla\left[\left\langle u_\varphi \right\rangle R - \frac{R\left\langle B_\varphi \right\rangle}{\tilde{\eta}}\right], \tag{2.118}$$

which allows us to define the angular momentum invariant

$$L = \left\langle u_\varphi \right\rangle R - \frac{R\left\langle B_\varphi \right\rangle}{\tilde{\eta}} = R_A\left\langle u_{\varphi,A} \right\rangle - R_A V_{A,\varphi}(R_A) \tag{2.119}$$

$$L = \Omega_\star R_A^2, \tag{2.120}$$

the angular momentum transported by the outflow can be stored in two forms: a classical kinetic part or a magnetic contribution in the form of the toroidal magnetic field. To derive the energy invariant we need to project the equation of conservation of momentum in its stationary and laminar form

$$\langle \mathbf{u} \rangle \cdot \nabla \langle \mathbf{u} \rangle = -\frac{1}{\langle\rho\rangle}\nabla \langle P \rangle + \nabla\Phi_G + \frac{1}{c\langle\rho\rangle}\langle \mathbf{J} \rangle \times \langle \mathbf{B} \rangle, \tag{2.121}$$

with respect to the average velocity $\langle \mathbf{u} \rangle$. Remembering that

$$\langle \mathbf{u} \rangle \cdot \nabla \langle \mathbf{u} \rangle = [\nabla \times \langle \mathbf{u} \rangle] \times \langle \mathbf{u} \rangle + \frac{1}{2}\nabla\langle u \rangle^2 \tag{2.122}$$

we derive

$$\langle \mathbf{u} \rangle \cdot \nabla\left[w - \Phi_G + \frac{\langle u \rangle^2}{2}\right] = \langle \mathbf{u} \rangle \cdot \frac{1}{c\langle\rho\rangle}\langle \mathbf{J} \rangle \times \langle \mathbf{B} \rangle, \tag{2.123}$$

where w is the thermal energy term which can be written as

$$w = \int \frac{\nabla\langle P \rangle}{\langle\rho\rangle} \cdot \mathrm{d}\mathbf{s}, \tag{2.124}$$

here s is the coordinate along the field line. It is straightforward to show that

$$\langle \mathbf{u} \rangle \cdot \frac{1}{c\langle\rho\rangle}\langle \mathbf{J} \rangle \times \langle \mathbf{B} \rangle = \left\langle \mathbf{u_p} \right\rangle \cdot \nabla\left[\frac{1}{\tilde{\eta}}R\Omega_\star\left\langle B_\varphi \right\rangle\right], \tag{2.125}$$

combining this with Eq. (2.123) we finally obtain the Bernoulli invariant for an MHD outflow

$$\left\langle \mathbf{B_p} \right\rangle \cdot \nabla\mathcal{B} = 0, \tag{2.126}$$

where

$$\mathcal{B} = \frac{\left\langle u_p \right\rangle^2 + \left\langle u_\varphi \right\rangle^2}{2} + \Phi_G - \Omega_\star \frac{R \left\langle B_\phi \right\rangle}{\tilde{\eta}} + w. \tag{2.127}$$

The Bernoulli invariant can also be recast by using Eq.(2.119) into

$$\mathcal{B} = \frac{\left\langle u_p \right\rangle^2}{2} + \Phi_G + \Omega_\star^2 R_A^2 + w - \frac{\langle \Omega \rangle R^2}{2} \left[2\Omega_\star - \langle \Omega \rangle\right]. \tag{2.128}$$

It is important to note that, when heating is applied, w is a function of the full stream line because of its integral form, here it cannot be computed from a single point within the field line as the other terms. Depending on the form of the applied heating w can be rewritten as

$$w = \mathcal{H} + \int Q \cdot \mathrm{d}\mathbf{s}, \tag{2.129}$$

where $\mathcal{H}$ is the enthalpy and Q is the radiative heating/cooling and s is again a coordinate along the magnetic field line.

We combine Eq. (2.119,2.116) to derive the angular velocity as a function of the Mach number and the MHD invariants

$$\langle \Omega \rangle = \Omega_\star \left(1 - g\right), \tag{2.130}$$

where

$$g = \frac{m^2}{m^2 - 1} \left[1 - \frac{R_A^2}{R^2}\right], \tag{2.131}$$

where we define the Alfvénic Mach number as a function of the mass loading invariant (Eq.2.112)

$$m = \frac{\left\langle u_p \right\rangle}{V_{Ap}} = \tilde{\eta} \sqrt{\frac{1}{4\pi\rho}} = \sqrt{\frac{\rho_A}{\langle \rho \rangle}}. \tag{2.132}$$

The function g measures the discrepancy between the two angular velocities and is related to the poloidal current flowing in the jet, or the toroidal magnetic field. It may seem that this function is singular when $m = 1$, however, at this particular point $R = R_A$ smooths out the function. The Bernoulli invariant can be rewritten using the Eq. (2.130)

$$\mathcal{B} = \frac{\left\langle u_p \right\rangle^2}{2} + \Phi_G + \Omega_\star^2 R_A^2 + w - \frac{\Omega_\star R^2}{2} \left[1 - g^2\right]. \tag{2.133}$$

To compare the values of the MHD invariants with respect to quantities defined within the disk it is useful to normalize them to their values at the SM radii

$$\kappa \equiv \frac{\tilde{\eta} R_{SM} \Omega_K(R_{SM})}{B_{z,SM}}, \tag{2.134}$$

$$\omega \equiv \frac{\Omega_\star}{\Omega_K(R_{SM})}, \tag{2.135}$$

$$\lambda \equiv \frac{L}{\left[R^2 \Omega_K\right]\big|_{SM}}, \tag{2.136}$$

$$e \equiv \frac{2\mathcal{B}}{\Omega_K^2(R_{SM}) R_{SM}^2}, \tag{2.137}$$

our normalizations are the equivalent to the ones used by Blandford and Payne 1982. With this normalization λ becomes the magnetic lever arm

$$\lambda = \omega \frac{R_A^2}{R_{SM}^2}, \tag{2.138}$$

it is precisely the lever arm of the torque exerted on the disk by the outflow and by counter-reaction, it is a good measure of the acceleration the disk exerts on the outflow. In section 2.5.2 we will derive a relation linking the magnetic lever and the terminal velocity of the outflow.

2.5.2 Energetic requirements

For the outflow to be launched some energetic requirements need to be fulfilled:

First of all, the outflow needs to remove energy from the system. Hence, the poloidal component of the laminar MHD pointing flux

$$\mathbf{S}_p = \frac{c}{4\pi} \langle \mathbf{E} \rangle \times \left\langle B_\varphi \right\rangle \mathbf{e}_\varphi = \frac{-\left\langle B_\varphi \right\rangle}{4\pi} \left[\left\langle \mathbf{B_p} \right\rangle \left\langle u_\varphi \right\rangle - \left\langle \mathbf{u_p} \right\rangle \left\langle B_\varphi \right\rangle \right], \tag{2.139}$$

$$\mathbf{S}_p = -R\Omega_\star \frac{\left\langle B_\varphi \right\rangle \left\langle \mathbf{B_p} \right\rangle}{4\pi}, \tag{2.140}$$

needs to be pointing away from the disk and the central object. Indeed, S_z needs to be positive above the disk and negative below. The radial component, S_R needs to be always positive. We derive Eq. (2.140) by using the definition of $\Omega_\star$. The sign of the pointing flux imposes a certain topology to the magnetic field on the outflow region.

If we assume $\langle B_z \rangle > 0$ then the toroidal magnetic field needs to be negative in the upper hemisphere and positive in the lower hemisphere, on the contrary, $\langle B_R \rangle > 0$ in the upper hemisphere and $\langle B_R \rangle < 0$ in the lower hemisphere.

For the outflow to escape the gravitational potential the Bernoulli invariant must be positive, $e > 0$. We can estimate the value of e at the base of the outflow, where $\left\langle \mathbf{u_p} \right\rangle \ll V_K(R_{SM})$, $R = R_{SM}$ and $\Omega \simeq \Omega_K(R_SM)$ as

$$e \simeq 2\omega\left(\lambda - 1\right) + \Theta - 1, \tag{2.141}$$

where $\Theta = 2w/(\Omega_K^2(R_{SM})R_{SM}^2)$. From Eq. (2.141) we see that λ, the magnetic lever arm, has a strong impact on the energetics of an MHD outflow. Indeed, as will be more clear in section 2.5.4 the magnetic angular momentum plays a quintessential role in the acceleration mechanism. For an MHD outflow to exists $e > 0$, this leads to a constraint on the value of the magnetic lever arm

$$\lambda > \frac{1}{2\omega}\left(1 - \Theta\right) + 1. \tag{2.142}$$

In most MHD driven outflows $\omega \simeq 1$ is a very good approximation. Furthermore, if we assume that the thermal driving is negligible we can derive the simple constraint

$$\lambda > \frac{3}{2}. \tag{2.143}$$

We can also use Eq. (2.141) to approximate the terminal velocity of the outflow, if we assume that when $R \rightarrow \infty$ all magnetic energy is consumed, and that $\langle \Omega \rangle \rightarrow 0$ (which is appropriate as we will see in section 2.5.4) we show

$$\left\langle u_{p,\infty} \right\rangle = V_K(R_{SM}) \sqrt{2\lambda - 3}. \tag{2.144}$$

2.5.3 Escaping the accretion disk

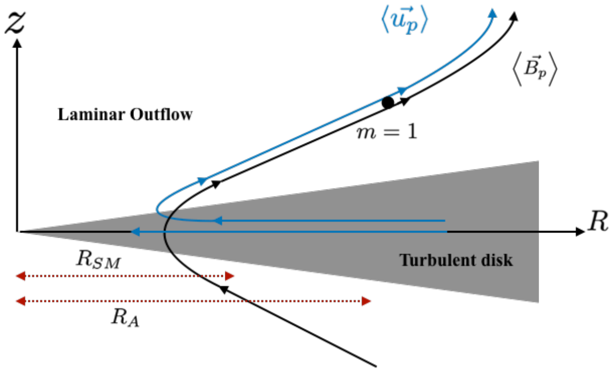

Figure 2.2: Sketch of an accretion disk ejection, we mark the Alfvénic point ($m = 1$).

For the outflow to take flight above the disk it needs first to escape the accretion disk. For that to happen there are a couple of conditions that need to be fulfilled. Analyzing those conditions can lead to useful constraints on the structure of the flow and the accretion disk. First of all, the accretion flow needs to change direction, $\langle u_R \rangle (z_R, R_R) = 0$, for it to become an ejection flow. We evaluate Eq. (2.72) at this point to find

$$\langle u_z \rangle|_{z_R} = -\frac{\mathcal{E}_\varphi}{\langle B_R \rangle} = \frac{4\pi}{c} \frac{\eta \left\langle J_\varphi \right\rangle}{\langle B_R \rangle} \simeq \eta \frac{\frac{\partial \langle B_R \rangle}{\partial z}}{\langle B_R \rangle} \sim \frac{\eta}{h}, \tag{2.145}$$

where we use a resistive closure for the turbulent emf. We find, that the vertical velocity at the inflection point is related to the turbulent resistivity. The matter is diffusing through the field lines to be loaded into the outflow. From Eq.(2.145) it is not clear which force is deflecting the matter vertically to be loaded onto the field lines.

To understand this we need to write the poloidal components of the momentum conservation equation.

$$\left\langle \mathbf{u_p} \right\rangle \cdot \nabla \langle u_R \rangle = \left(\langle \Omega \rangle^2 - \Omega_K^2 \right) R + \frac{F_R}{\langle \rho \rangle} - \frac{1}{\langle \rho \rangle} \frac{\partial \langle P \rangle}{\partial R}, \tag{2.146}$$

$$\left\langle \mathbf{u_p} \right\rangle \cdot \nabla \langle u_z \rangle \simeq -\Omega_K^2 z + \frac{1}{\langle \rho \rangle} \frac{\partial}{\partial z} \frac{\langle B_R \rangle^2 + \left\langle B_\varphi \right\rangle^2}{8\pi} - \frac{1}{\langle \rho \rangle} \frac{\partial \langle P \rangle}{\partial z}, \tag{2.147}$$

where for the sake of brevity we ignore the turbulent terms. We remark that as we exit the disk the radial and toroidal magnetic field increases, the disk is being compressed by the magnetic field. This magnetic compression can be understood for $\langle B_R \rangle$ by looking at Fig. (2.2), the curvature of the poloidal field lines induces a positive gradient in $\langle B_R \rangle$. The only force that can always counteract both gravity and magnetic compression is the pressure gradient (Ferreira and Pelletier 1995). The hydrostatic or magneto-static equilibrium within the disk plays an important role in the acceleration mechanism.

Once the matter has been deflected upwards the magnetic acceleration needs to activate so that it can continue on its journey. The toroidal magnetic field in the same ways as $\langle B_R \rangle$ also exerts compression on the disk, it is also one of the main contributors to the acceleration of the outflow. We can write the toroidal component of the Lorentz force as

$$F_\varphi = \langle J_z \rangle \langle B_R \rangle - \langle J_R \rangle \langle B_Z \rangle \simeq - \langle J_R \rangle \langle B_z \rangle = \frac{\partial \left\langle B_\varphi \right\rangle}{\partial z} \langle B_z \rangle, \tag{2.148}$$

as argued by Ferreira and Pelletier 1995 for the outflow to accelerate toroidally $\langle J_R \rangle$ must change sign around the disk surface. To understand the constraints imposed by this sign change we analyze Eq. (2.69)

$$-\nabla \times \mathcal{E}|_{\varphi} = \nabla \cdot \frac{1}{R}\left[\left\langle u_{\varphi}\right\rangle\left\langle \mathbf{B_p}\right\rangle - \left\langle B_{\varphi}\right\rangle\left\langle \mathbf{u_p}\right\rangle\right], \tag{2.149}$$

$$\frac{4\pi}{c}\,\nabla \times \left[\eta_t \langle \mathbf{J}\rangle\right]\Big|_{\varphi} = \nabla \cdot \left[\frac{\eta_t}{R^2}\nabla R\left\langle B_{\varphi}\right\rangle\right], \tag{2.150}$$

where we have assumed a resistive closure for the turbulent emf. We can neglect $\langle J_z \rangle$ and $\left\langle B_{\varphi}\right\rangle$ advection, and then integrate this equation with respect to z to find

$$\eta_t(z)\,\langle J_R\rangle\,(z) \simeq \eta_t(z=0)\,\langle J_R\rangle\,(z=0) + R\int_0^z \mathrm{d}z\left\langle \mathbf{B_p}\right\rangle \cdot \nabla\langle\Omega\rangle, \tag{2.151}$$

$$\langle J_R\rangle\,(z) \simeq \langle J_R\rangle\,(z=0)\frac{\eta_t(z=0)}{\eta_t(z)}\left[1 - \frac{3}{2}\frac{\Omega_K}{\eta_t(z=0)\,\langle J_R\rangle\,(z=0)}\int_0^z \mathrm{d}z\,\langle B_R\rangle\right]. \tag{2.152}$$

From Eq. (2.152), we can understand that the altitude where the radial current changes sign emerges as a competition between the differential rotation effect and the induced current, $\langle J_R\rangle\,(z=0)$. We can also understand that the vertical profile of resistive, $\eta_t(z)$, could have an important impact on the acceleration mechanism.

The radial electric current, $\langle J_R\rangle$, is the vertical derivative of $\left\langle B_{\varphi}\right\rangle$ the altitude where $\langle J_R\rangle\,(z_J) = 0$ defines the maximal amplitude of $\left|\left\langle B_{\varphi}\right\rangle\right|$. Hence, z_J defines the start of the toroidal acceleration and the start of the vertical acceleration. The vertical acceleration is driven by the gradient of the toroidal field (Eq. 2.147). Once the toroidal acceleration is activated the outflow will also start to accelerate radially thanks to the magneto-centrifugal force (Eq. 2.146). We show in Fig. (2.3) a sketch resuming this mechanism. We show the extremum of the toroidal magnetic field as well as the poloidal current lines $\left\langle \mathbf{J_p}\right\rangle$.

2.5.4 Ejection phenomenology

We use the definition of g, the discrepancy between the two angular velocities, $\langle\Omega\rangle = \Omega_\star\,[1-g]$, to understand the acceleration mechanism of magnetized outflows. To that end, we compute the toroidal magnetic field as a function of g and the MHD invariants

$$-\frac{R\left\langle B_{\varphi}\right\rangle}{\tilde{\eta}} = \Omega_\star R^2\left[\frac{R_A^2}{R^2} + g - 1\right]. \tag{2.153}$$

We can expand the g function in two different limits before and after the Alfvén point

$$g \simeq m^2\left(\frac{R_A^2}{R^2} - 1\right) \ll 1 \quad \text{for } m^2 \ll 1, \tag{2.154}$$

$$g \simeq 1 - \frac{R_A^2}{R^2} \quad \text{for } m^2 \gg 1. \tag{2.155}$$

$$\tag{2.156}$$

By injecting these expression into Eq. (2.130) we see that before the Alfvén point the angular velocity is constant

$$\langle\Omega\rangle \simeq \Omega_\star \quad \text{for } m^2 \ll 1, \tag{2.157}$$

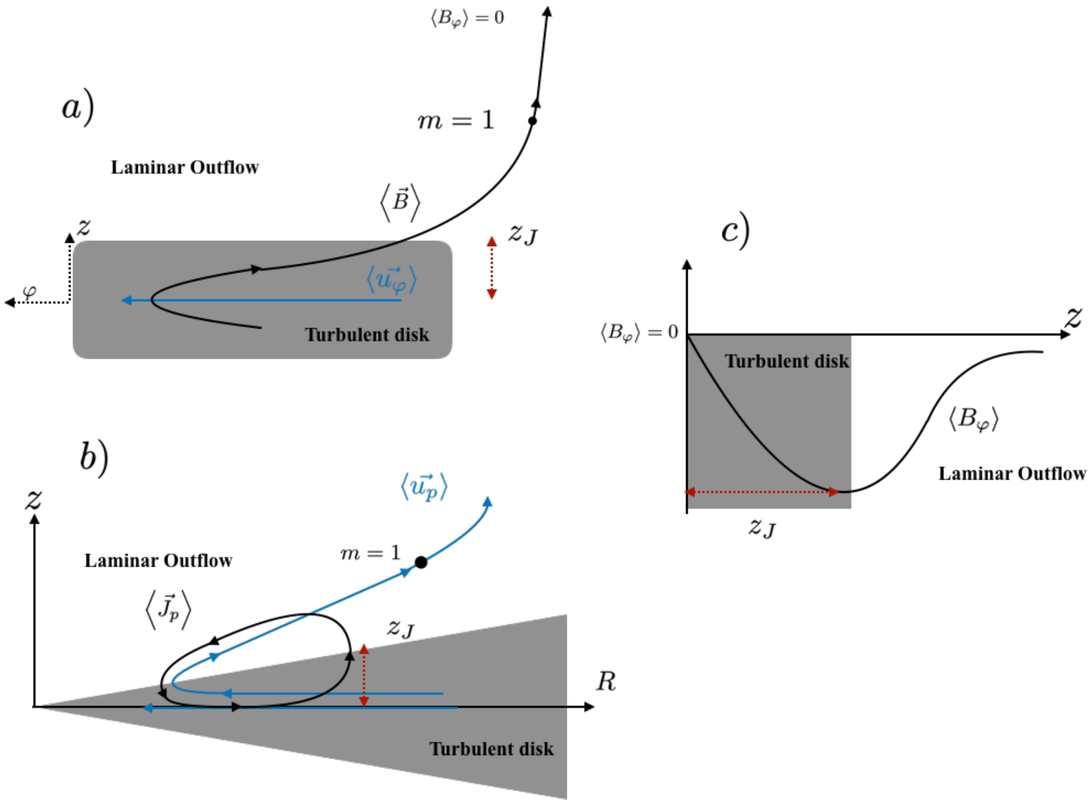

Figure 2.3: a) Sketch of an accretion disk ejection viewed from a different angle, we mark the point where the toroidal and vertical acceleration start as z_J. We also mark the Alfvénic point ($m = 1$). b) Same as Fig. (2.2) but instead of showing the poloidal magnetic field lines we show the poloidal electric current lines. c) Typical vertical profile of the toroidal magnetic field in highly magnetized self-similar models (Ferreira 1997).

the flow spins at the velocity of the field lines. In this configuration most of the angular momentum is stored in the toroidal magnetic field, the magnetic field is progressively accelerating the flow via F_φ, leading to a constant velocity profile.

After the Alfvén point the toroidal magnetic field tends to 0, indeed, injecting Eq. (2.155) into Eq. (2.153) leads to $R\left\langle B_\varphi\right\rangle = 0$. The magnetic angular momentum has been consumed, by injecting Eq. (2.155) into Eq. (2.130) we get

$$\langle\Omega\rangle \simeq \Omega_\star \frac{R_A^2}{R^2}, \tag{2.158}$$

a constant angular momentum profile.

The acceleration of the outflow will be due to a combination of the radial magneto-centrifugal (Eq. 2.146) acceleration and the vertical gradient of the magnetic pressure due to the toroidal and radial magnetic fields (Eq. 2.147). We note, that the magneto-centrifugal acceleration is the consequence of the azimuthal acceleration generated by the magnetic field,, F_φ. Following this observation, the magnetic force can be divided into a component perpendicular to the magnetic field line and a component parallel to the magnetic field line (Ferreira 1997)

$$F_\varphi = \frac{\left\langle B_p\right\rangle}{4\pi}\nabla_{\|}R\left\langle B_\varphi\right\rangle, \tag{2.159}$$

$$F_{\|} = -\frac{\left\langle B_\varphi\right\rangle}{4\pi}\nabla_{\|}R\left\langle B_\varphi\right\rangle, \tag{2.160}$$

where

$$\nabla_{\|} = \frac{\left\langle \mathbf{B_p}\right\rangle}{\left\langle B_p\right\rangle}\cdot\nabla. \tag{2.161}$$

This splitting of the magnetic force allows us to define two distinct types of outflows depending on the dominant acceleration mechanism. If $F_\varphi > F_{\|}$ we can say that the outflow is magneto-centrifugally driven, in the opposite case, we say that the outflow is a magnetic tower. In the second case, the main driver of the acceleration is the laminar magnetic pressure associated to $\left\langle B_\varphi\right\rangle^2$. In both cases, both forces accelerate the outflow, they are both needed as they push in different directions.

2.5.5 Linking accretion and ejection

Accretion and ejection physics are intrinsically linked in MHD winds, in what follows we will develop a simple relation linking the ejection efficiency with the angular momentum transport and the magnetic lever arm.

We define the outflow ejection rate from the two sides as

$$\dot{M}_\mathrm{o} = 2\times 2\pi\int_{R_\mathrm{in}}^{R}\left[\langle\rho\rangle\,\langle u_z\rangle_\rho\right]_{SM} R\,\mathrm{d}R, \tag{2.162}$$

it can be linked to the accretion rate by integrating Eq. (2.66)

$$\frac{1}{R}\frac{\partial}{\partial R}\left[\dot{M}_\mathrm{o} - \dot{M}_\mathrm{a}\right] = 0 \tag{2.163}$$

We can define the ejection efficiency as

$$\xi = \frac{\mathrm{d}\log \dot{M}_\mathrm{a}}{\mathrm{d}\log R}, \tag{2.164}$$

assuming a steady state we can show from the continuity equation that

$$\xi = \frac{1}{\dot{M}_\mathrm{a}} \frac{\mathrm{d}\dot{M}_\mathrm{o}}{\mathrm{d}\log R}. \tag{2.165}$$

The ejection efficiency defines what fraction of mass is being lost to the outflow, it is linked to the power law exponent of the accretion rate, the steeper the power law, the more mass will be lost to the outflow. However, this is only the case if the system reaches a steady state where the accretion can be described by a power law.

We start by rewriting Eq. (2.80) by using the definition of $\Lambda = M_{z\varphi}/M_{r\varphi}$

$$\dot{M}_\mathrm{a} = \frac{4\pi}{\Omega_K} M_{z\varphi} \frac{1+\Lambda}{\Lambda}, \tag{2.166}$$

if we ignore the vertical turbulent component of the magnetic stress[4], $\mathcal{T}_{tu,z}$, we recast $M_{z\varphi}$ by using the definition of the angular momentum invariant

$$M_{z\varphi} = -2\, B_z|_{SM} \left.\frac{RB_\varphi}{4\pi}\right|_{SM} = 2\tilde{\eta} \left.\frac{B_z}{4\pi}\right|_{SM} \left[\Omega_\star R_A^2 - \Omega R^2\right]_{SM}, \tag{2.167}$$

where we have also assumed that the outflow is top/dow symmetric. We then use the definition of the mass loading invariant to show

$$M_{z\varphi} = 2\left[\Omega_\star R_A^2 - \Omega R^2\right]_{SM} \left[\langle\rho\rangle \langle u_z\rangle_\rho\right]_{SM}, \tag{2.168}$$

we reformulate[5] the definition of the outflow ejection rate to find

$$\frac{1}{R^2} \frac{\mathrm{d}\dot{M}_\mathrm{o}}{\mathrm{d}\log R} = 4\pi \left[\langle\rho\rangle \langle u_z\rangle_\rho\right]_{SM} \simeq 4\pi \left[\langle\rho\rangle \langle u_z\rangle\right]_{SM}, \tag{2.169}$$

and then combine this expression with Eq. (2.166) to derive

$$\dot{M}_\mathrm{a} = \frac{2}{R^2\Omega_K} \frac{1+\Lambda}{\Lambda} \frac{\mathrm{d}\dot{M}_\mathrm{o}}{\mathrm{d}\log R} \left[\Omega_\star R_A^2 - \Omega R^2\right]_{SM} \simeq 2\left[\lambda - 1\right] \frac{1+\Lambda}{\Lambda} \frac{\mathrm{d}\dot{M}_\mathrm{o}}{\mathrm{d}\log R} \tag{2.170}$$

we finally have

$$\lambda \simeq 1 + \frac{\Lambda}{\Lambda+1} \frac{1}{2\xi}. \tag{2.171}$$

This expression was first derived by Casse and Ferreira 2000b without considering the vertical evolution of the turbulent and laminar torques. This expression reveals several properties of MHD outflows. It reveals that the magnetic lever and a quantity directly related to the outflow acceleration, depends on two main quantities the ejection efficiency, ξ, of the outflow and the angular momentum transport within the disk. We can intuitively understand those dependencies: First, the more massive the outflow is (the bigger the ξ) the harder it will be to accelerate it (the smaller the λ). Second, if the angular momentum transport is dominated by the vertical component, $\Lambda \gg 1$, the value of the magnetic lever arm will only depend on ξ, $\lambda \sim 1 + 1/(2\xi)$. However, if the angular momentum transport is dominated by the radial component, $\Lambda \ll 1$, the value of the magnetic lever will also depend on Λ, $\lambda \sim 1 + \Lambda/(2\xi)$. Indeed, if the angular momentum is lost radially before reaching the outflow, the maximal acceleration achievable by the outflow will be affected, decreasing the effective value of the magnetic lever arm.

---

[4] in practice this is an good approximation for MRI turbulence, as MRI turbulence mostly transports angular momentum radially

[5] Were we neglect $\langle\delta u_z\rangle_\rho$

CHAPTER 3

Weakly magnetized self-similar jets and winds

3.1 Self-similar framework

3.1.1 General framework

We assume that the system is stationary, axisymmetric and, that the turbulent correlations present can be modeled as a turbulent resistivity and a turbulent viscosity. For the sake of brevity within this section we drop the $\langle . \rangle$ around average quantities, as we will never mention the turbulent fluctuating terms, δX. Under these conditions we can simplify the Reynolds averaged MHD equations. The equation of conservation of poloidal momentum is more complicated to rewrite from Eq. (2.65,2.63) instead we recast it from the poloidal projection of Eq. (2.21). We rewrite the poloidal projection of the Lorentz force term to find

$$\mathbf{F}_p = \frac{1}{c} J_\varphi \begin{pmatrix} B_z \\ 0 \\ -B_R \end{pmatrix} + \frac{1}{c} B_\varphi \begin{pmatrix} -J_z \\ 0 \\ J_R \end{pmatrix} = \frac{1}{c} J_\varphi \nabla a - \frac{1}{8\pi R^2} \nabla \left[R^2 B_\varphi^2 \right], \tag{3.1}$$

where the magnetic flux function $a = RA_\varphi$ is consistent with section 2.3.1. The magnetic topology is assumed bipolar, with an even symmetry with respect to the disk equatorial plane (a is even, while B_φ is odd). We can rewrite the complete set of MHD equations as

$$\nabla \cdot (\rho \mathbf{u}) = 0, \tag{3.2}$$

$$\rho(\mathbf{u_p} \cdot \nabla)\mathbf{u_p} = \Omega^2 R \mathbf{e}_R - \nabla P + \rho \nabla \Phi_G + \frac{1}{c} J_\varphi \nabla a - \frac{1}{8\pi R^2} \nabla \left[R^2 B_\varphi^2 \right], \tag{3.3}$$

$$\nabla \cdot \left[\rho \Omega R^2 \mathbf{u_p} - \frac{R B_\varphi}{4\pi} \mathbf{B_p} + R \mathcal{T}_{tu} \right] = 0, \tag{3.4}$$

$$\frac{4\pi}{c} \eta_m J_\varphi \mathbf{e_\varphi} = \mathbf{u_p} \times \mathbf{B_p}, \tag{3.5}$$

$$\nabla \cdot \left(\frac{\eta'_m}{R^2} \nabla R B_\varphi \right) = \nabla \cdot \frac{1}{R} \left(B_\varphi \mathbf{u_p} - \mathbf{B_p} \Omega R \right), \tag{3.6}$$

where $\mathcal{T}_{tu}$ is the turbulent stress and is related to the turbulent viscosity defined in section 2.4.1. We follow Ferreira and Pelletier 1995, by defining two different turbulent resistivities to account for anisotropies due to the reconnection events in the disk mid-plane. We close Eq. (3.2-3.6) by using an ideal equation of state. Finally, for simplicity we assume that the temperature structure is isothermal along the magnetic field lines. The complete form of the energy equation is given in Appendix A.

The turbulent resistivities and viscosity, defined in section 2.4.2 and section 2.4.1 respectively, are assumed to vanish outside of the disk, the outflow region is described by ideal MHD. Our description allows for a smooth transition from a resistive and viscous MHD regime (the disk) to an ideal MHD regime (the outflow) on a few pressure scale heights. For the sake of simplicity and lack of precise knowledge, the vertical behavior of the transport coefficients is modeled by a simple gaussian profile of the self-similar variables, see Appendix A. The amplitude of the turbulent transport coefficients are modeled as in Ferreira and Pelletier 1995, as explained in section 2.4.1 and section 2.4.2, we have

- The poloidal turbulent diffusivity is modeled using the Alfvén velocity, $\eta_m = \alpha_m V_{A0} h$, where α_m is a constant independent of μ that represents the strength of the magnetized turbulence and V_{A0} is the Alfvén velocity at the disk mid-plane.

- The viscosity is modeled following Shakura and Sunyaev 1973, it is chosen as $\nu_v = \alpha_v c_s h$, where α_v is the usual Shakura-Sunyaev alpha coefficient. As seen in section 2.4.1, the α_v coefficient can be related to the level of turbulence α_m by defining the magnetic Prandtl number, $\mathcal{P}_m = \nu_v / \eta_m$ so that $\alpha_v = \alpha_m \mathcal{P}_m \mu^{1/2}$ (assuming $\mathcal{P}_m$ independent of μ). Hence, α_v is not a constant and depends on the magnetization at the disk mid-plane.

- The toroidal turbulent resistivity is modeled in the same way as the poloidal resistivity, $\eta'_m = \alpha'_m V_A h$. However, its magnitude is imposed by defining the resistive anisotropy $\chi_m = \eta_m / \eta'_m$.

To write Eq. (3.5) we have assumed that the transport velocity of the magnetic flux, discussed in section 2.4.3, is negligible. Indeed, if $v_\psi \simeq 0$ Eq. (2.106) yields Eq. (3.5). The validity of this approximation will be tested in section 4.3 using 3D global simulations. If this approximation is not correct the effect of field advection needs to be included in the resolution of the equations. Contopoulos et al. 2017 included this effect in the self-similar framework. However, they only compute the outflow and paid no attention to the accretion disk physics. Ogilvie and Livio 2001 computed the disk equilibrium and wind launching separately. They included the effect of magnetic field transport by simultaneously solving the vertically averaged induction equation (Lubow et al. 1994) and the dynamical equilibrium of the disk. However, they neglect the dynamical effect of the toroidal magnetic field. As we discussed in chapter 2 the toroidal magnetic field has an important role in the acceleration mechanism of the outflow.

3.1.2 Self-similar approximation

The set of stationary axisymmetric equations is still cumbersome to solve through conventional methods. To make progress in this endeavor we assume that the 2.5D plasma follows a self similar symmetry. This reduces the set of partial differential equations into a set of ordinary differential equations. Since, gravity is the leading energy reservoir of the accretion disk system we expect that the other quantities follow a similar scaling. We assume the following self-similar *ansatz*:

$$X = X_0 \left(\frac{R}{R_0}\right)^{\zeta_X} f_X(x), \tag{3.7}$$

where $x = z/h = z/(\varepsilon R)$ is the self-similar variable and ε is the disk geometrical thickness. In this radial self-similarity all quantities are power laws of radius and a constant x corresponds to a cone in the (R,z) plane. Since, self-similarity forces a certain geometry to the system it will also affect the propagation of the MHD waves. Indeed, waves can only propagate in the direction defined by the vector

$$\mathbf{n} = -\mathbf{e}_\theta = \frac{\mathbf{e}_z - x\varepsilon\mathbf{e}_R}{1 + x^2\varepsilon^2}. \tag{3.8}$$

The only direction of variation is along the self-similar $x = z/h = 1/\tan\theta$, therefore only waves propagating along this direction can exists. After injecting the self-similar *ansatz* into Eq. (3.2-3.6) we can separate the set of PDEs into a set of ODEs for the quantities $f_X(x)$ and a set of algebraic equations for the exponents, ζ_X. Solving the algebraic set of equations leads $\zeta_X = \zeta_X(\xi)$, all exponents are determined by the ejection index defined by $\dot{M}_a \propto R^\xi$. All quantities $f_X(x)$ are then obtained by solving the system of ODEs (the complete set of equations will be found in appendix A) which we recast into the form,

$$\overleftrightarrow{\mathcal{M}} \begin{pmatrix} \frac{\mathrm{d}f_1}{\mathrm{d}x} \\ \vdots \\ \frac{\mathrm{d}f_n}{\mathrm{d}x} \end{pmatrix} = \overleftrightarrow{\mathcal{U}} \tag{3.9}$$

where $\overleftrightarrow{\mathcal{M}}(f_i, x)$ and $\overleftrightarrow{\mathcal{U}}(f_i, x)$ are respectively a matrix function and a vector function of the different quantities, $f_X(x)$, and the self-similar variable x. A solution is therefore possible whenever the matrix $\overleftrightarrow{\mathcal{M}}(f_X, x)$ is invertible,

$$\det(\overleftrightarrow{\mathcal{M}}(f_X, x)) = 0. \tag{3.10}$$

This condition defines the different critical points of the system, which can be written as

$$V^2\left(V^2 - V_{sm}^2\right)\left(V^2 - V_{fm}^2\right)\left(V^2 - V_{An}^2\right)^2 = 0, \tag{3.11}$$

where $V_{An} = \mathbf{V}_{Ap} \cdot \mathbf{n}$ is the projected Alfvén speed, $V = \mathbf{u} \cdot \mathbf{n} = \mathbf{u}_p \cdot \mathbf{n}$ is the critical velocity, and the modified slow and fast waves are now defined as

$$V_{fm,sm}^2 = \frac{1}{2}\left[c_s^2 + V_{At}^2 \pm \sqrt{\left[c_s^2 + V_{at}^2\right]^2 - 4c_s^2 V_{An}^2}\right], \tag{3.12}$$

where V_{At} is the total Alfvén speed. We recognize the fast and slow magneto-sonic wave velocities defined in section 2.2.1, although in a modified form, affected by the self-similar ansatz. Due to the projection effect imposed by the self-similarity, at the disk surface we have $V \simeq u_z$, whereas far from the disk it becomes $V \simeq u_R$. Contrary to the magneto sonic critical points, the Alfvén point is the usual Alfvénic critical point encountered in jet theory

$$V = V_{An} \;\Leftrightarrow\; \mathbf{V}_{Ap} \cdot \mathbf{n} = \mathbf{u} \cdot \mathbf{n} \;\Leftrightarrow\; \mathbf{V}_{Ap}^2 \mathbf{n}^2 = \mathbf{u}_p^2 \mathbf{n}^2 \;\Leftrightarrow\; V_{Ap} = u_p. \tag{3.13}$$

Using the self-similar framework we define a coordinate, s, along the magnetic field lines. The magnetic flux function $a = RA_\phi$ is used to define a surface along which the magnetic flux is constant (see section 2.3.1). The shape of a magnetic surface anchored at R_0 is defined by $a(r,z) = a_0 = C^{te}$ and is provided by

$$\frac{R}{R_0} = f_a(x)^{-\frac{1}{\zeta_a}}. \tag{3.14}$$

We can inject this expression into the self-similar ansatz to find

$$X = X_0 f_a^{-\frac{\zeta_X}{\zeta_a}} f_X(x) = X_0 F_X(s), \tag{3.15}$$

where s is the coordinate along the magnetic field line.

3.1.3 Parameter space

The self-similar solution of Eq. (3.2-3.6) will be entirely determined by a set of parameter that we describe below. The first relevant parameter is the disk geometrical thickness, $\frac{h}{R} = \varepsilon$. It is normally a consequence of the energy equation. But as shown before, we do not compute the complete energy equation in this work, we will instead fix it to the value $\varepsilon = 0.1$. The second relevant parameter is the disk magnetization μ, defined in section 2.2.1, this parameter controls the strength of the magnetic field at the disk mid-plane. The third relevant parameter is the disk ejection index, ξ, defined in section 2.5.5, it is the power law exponent of the accretion rate, it will also set the magnetic flux distribution, $a \propto R^{\frac{3}{4}+\frac{\xi}{2}}$. The fourth relevant parameter is p, it controls the toroidal electric current at the disk mid-plane, $p = \frac{4\pi}{c}\frac{hJ_{\varphi 0}}{B_{z0}}$. It also provides a rough estimate of the bending of the field lines at disk surface, $B_{R,SM}/B_{z0} \sim p$. We complement the above list of parameters with the turbulent parameters described in the previous section (α_m,$\mathcal{P}_m$,χ_m). We write the complete set of parameters as

$$\begin{array}{lll} \varepsilon = \frac{h}{r} & \alpha_m = \frac{\eta_m}{V_A h} & \mu = \frac{B_{z0}^2}{4\pi P_0} \\ \xi = \frac{d\ln \dot{M}_a}{d\ln R} & \mathcal{P}_m = \frac{\nu_v}{\nu_m} & p = \frac{4\pi}{c}\frac{hJ_{\varphi 0}}{B_{z0}} \\ & \chi_m = \frac{\eta_m}{\eta'_m} & \end{array} \tag{3.16}$$

Two parameters (p,μ) will be constrained by the crossing of the critical surfaces (see section 3.1.4), this leaves 5 free parameters, we fix $\varepsilon = 0.1$ and $\mathcal{P}_m = 1$ and we explore the other three (ξ, α_m, χ_m). We will explore the values $\alpha_m = [0.8, 1, 2, 8]$ and $\chi_m = [0.01, 0.1, 1, 2]$. Our reference

Table 3.1: List of all the dimensionless parameters used in this work.

Name	Symbol	Type
Disk geometrical thickness	ε	Fixed to 0.1
Magnetic Prandtl number	$\mathcal{P}_m$	Fixed to 1
Level of turbulence	α_m	Free
Anisotropy of turbulence	χ_m	Free
Disk ejection index	ξ	Free
Disk magnetization	μ	SM regularity condition
Toroidal current at the disk mid-plane	p	Alfvén regularity condition
Ratio between the vertical and the radial torque	Λ	Calculated
Rotation of the magnetic surfaces	ω	Calculated
Magnetic lever-arm	λ	Calculated
Jet mass load	κ	Calculated
Bernoulli invariant	e	Calculated
Initial jet magnetization	σ	Calculated

set of parameters will be $\alpha_m = 1$ and $\chi_m = 1$. Finally, the ejection index ξ will be varied from 5×10^{-3} to 1. Table 3.1 contains the list of the disk parameters evaluated at the disk mid-plane as well as their type. We also included other useful quantities. While previously published JED solutions were found for a magnetization $\mu \in [0.1; 0.8]$, we now wish to reproduce the results of global simulations and achieve super-A jets with magnetization values as low as 10^{-4}. In this regime, MRI is active and should be the source of the MHD turbulence. However, around $\mu \sim 10^{-4}$ and below, MRI dynamo becomes significant (Scepi et al. 2018a), the value of α_v reaches a minima. Since such an effect is not included in our calculations, we restrict ourselves to solutions with a magnetization no smaller than $\mu \sim 5 \times 10^{-4}$.

3.1.4 Numerical method

Once the set of ODEs has been written (see Appendix A for their expressions) they can be numerically solved from the disk mid plane ($x = 0$) to infinity using a Burlish-stoer method for stiff equations. We follow the method described by Ferreira 1997. At the disk mid-plane all magnetic field components except for the vertical field are null, $B_R(x = 0) = B_\varphi(x = 0)$, the rest of the initial conditions for all fields are explicitly defined in Appendix A. The integration starts slightly above $x = 0$ with a guess for the parameters (μ, p). The integration cannot start at $x = 0$ since this is a critical point of nodal type (Ferreira and Pelletier 1995), we have to perform a Taylor expansion to compute the equations above this point.

After setting the boundary conditions the integration is propagated upwards using the resistive viscous MHD equations. As we move upward, the magnitude of the turbulent emf $(\frac{4\pi}{c}\overleftrightarrow{\eta}\mathbf{J})$ decreases, the poloidal velocity and magnetic field become parallel to each other. When this is achieved to a high precision, we stop solving the resistive MHD equations and start solving the ideal MHD equations. The integration then continues up to the slow magneto-sonic critical point.

The regularity conditions is not necessarily achieved by our choice of p and μ. We fine tune the value of μ so that we get close enough to the critical point, to safely perform a leapfrog. This is done by extrapolating across the critical point (using a leap-frog jump) while conserving the various MHD invariants (section 2.5.1). As we can see in Fig. (3.1) if μ is too large the flow will be accelerated too efficiently, which results in a shock. If μ is too small the acceleration will not be efficient enough and the flow decelerates before terminating in shock higher at a larger x (see Fig. (3.1). This simple picture is roughly accurate for oscillatory solutions (see below), those solutions accelerate and decelerate an even number of times before terminating in a shock. Indeed, each of their maxima of $M_{SM} = V/V_{SM}$ behaves in the same way, leading to a shock before the critical point or after the critical point depending on the value of μ.

After the flow becomes super SM it needs to also become super Alfvénic , this condition will constraint the parameter p. If p is too small, the magnetic tension overcomes the centrifugal acceleration and $B_R \to 0$. If p is too large, the centrifugal acceleration is too efficient leading to $B_\varphi \to 0$. One can again fine tune the parameter p to approach the Alfvénic point and perform a leap frog (where once again we conserve the MHD invariants through the jump). After every change in p the solution is re-computed from the origin, hence a new μ is also found. This can be computationally expensive when a big enough parameter space is explored.

In the remaining of this chapter we describe newly discovered weakly magnetized solutions that feature spatial oscillations. There are several reasons why those solution where not found up till now. The solution finding procedure as it was implemented in Ferreira and Pelletier 1995 explicitly forbid spatial oscillations in the radial magnetic field **within the disk**. This choice was purposeful one, oscillating solutions even though stationary in the self-similar sense

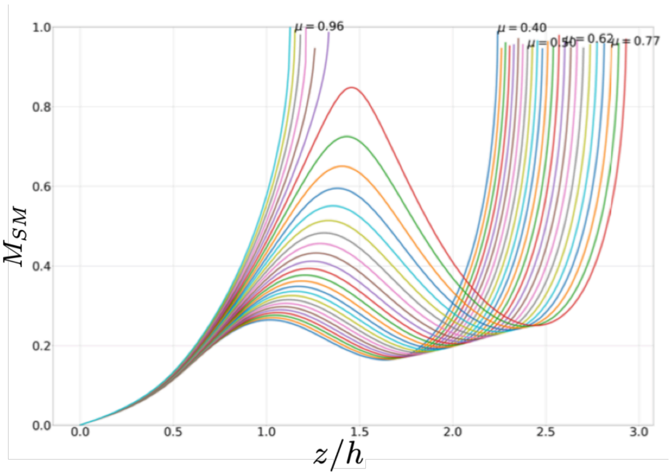

Figure 3.1: $M_{SM} = V/V_{SM}$ as a function of z/h, the slow magneto sonic critical point is defined by the condition $M_{SM} = 1$. We show the fine tuning procedure that takes places in order to cross the SM point. The critical value lies somewhere in between $\mu = 0.96$ and $\mu = 0.77$.

may not be stable to Kelvin Helmholtz instabilities that can not be calculated within the self-similar framework. Furthermore, when the solutions where first found the magneto rotational instability was still recently discovered, it was hard to imagine that such a oscillatory behavior could physically emerge from the accretion disk structure. Hence, previous self-similar works decided to ignore oscillatory solutions as they were though to be unphysical. More explicitly they implemented the condition $B_R > 0$ within the turbulent disk.

A careful look at global simulations (ie Fig.12 in Béthune et al. 2017 or Fig.6 in Zhu and Stone 2018) shows that this situation is actually realized, with B_R first becoming negative in the disk upper layers before becoming positive at higher altitude. To be consistent with these simulations, we thus relax this constraint and allow for negative radial fields **within the disk**. The fact that all previous JED solutions have been obtained only for $\mu > 0.1$ is a direct consequence of the explicit requirement (within our code) that the poloidal magnetic field has a monotonous vertical behavior within the resistive MHD disk zone[1]. As shown in the next section, relaxing this constraint (ie, removing any condition on B_R), allows for new solutions at much smaller magnetization levels. Although we still recover the previous ones at near equipartition fields, we will mainly focus our attention on the new ones.

3.2 Super-slow magneto-sonic outflows

3.2.1 The Super slow magneto sonic parameter space

Figure 3.3 shows the parameter space of the super SM outflows that have $\alpha_m = 1$ and $\chi_m = 1$. Each point represents an outflow that becomes super SM. We have been able to enlarge the parameter space of Ferreira and Pelletier 1995 (see Fig. 3.2) by 4 orders of magnitude in magnetization. We see several distinct features from the parameter space show in figure 3.3 :

- There are distinct and well separated islands, zones in the (μ,p) plane, where solutions are found. The parameter space studied by Ferreira and Pelletier 1995 (see Fig. 3.2) is consistent with the one, computed here at strong magnetization ($\mu > 0.4$).

---

[1] As will be discussed in section 3.5, the lack of weakly magnetized solution may also be the consequence of an inadequate profile for the turbulent resistivities and viscosity.

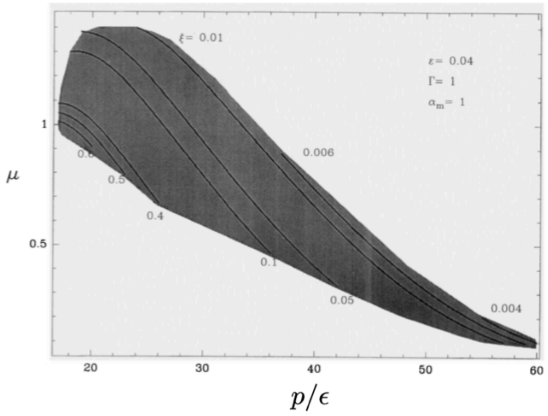

Figure 3.2: Super SM parameter space for highly magnetized solutions ($\mu > 0.4$) for $\varepsilon = 0.04$, $\alpha_m = 1$ and $\chi_m \sim 1$. Adapted from Ferreira and Pelletier 1995.

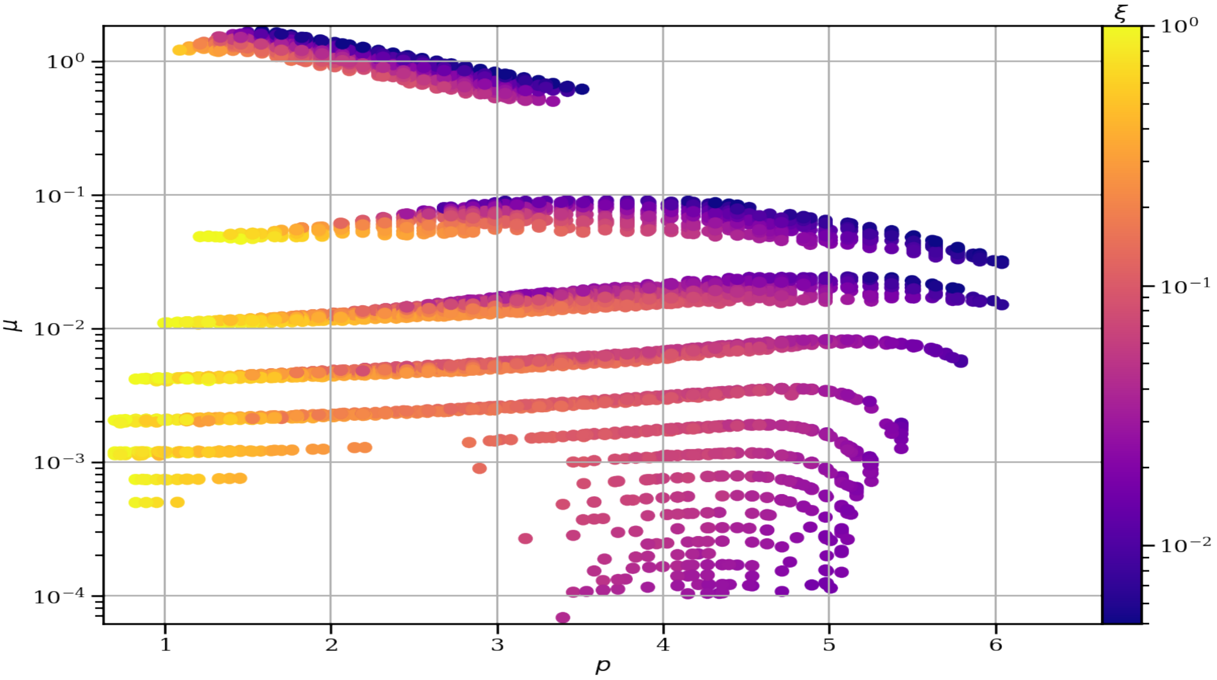

Figure 3.3: Parameter space $\mu(p)$ for super-SM isothermal solutions in our fiducial case $\alpha_m = 1$, $\chi_m = 1, \mathcal{P}_m = 1$ and $\varepsilon = 0.1$. Each point in this plane corresponds to a solution characterized by an ejection index ξ whose value is shown in color. The old near-equipartition solutions found by Ferreira and Pelletier 1995 correspond to the top island (see for instance their Fig.3, with $\mathcal{R}_m = p/\varepsilon$).

- The solution space has a monotonous behavior for $p(\xi)$, this is again consistent with Ferreira and Pelletier 1995. They show that this monotonous behavior is a consequence of the disk vertical equilibrium, which leads to smaller mass ejection index (ξ) when p is increased. We present this argument below.
- For a given ξ, the function $\mu(p)$ is bi-valued in some islands, for $\mu < 0.1$. This is a signature of two distinct vertical equilibria. As we will see in section 3.3 in one branch the toroidal magnetic field dominates whereas the other has a dominant radial magnetic field.
- Finally, the range $[\xi_{\min}, \xi_{\max}]$ of super slow magneto sonic solutions varies with μ. The maximal and minimal ejection indexes increase when the magnetization decreases. This will also be further detailed in section 3.3.

The effect of the parameter p on the ejection index can be understood by studying the vertical equilibrium of the system. We neglect the acceleration term in Eq. (2.147) to rewrite it as

$$\rho\Omega_k^2 z \simeq -\frac{\partial}{\partial z}\left[P + \frac{1}{8\pi}\left(B_R^2 + B_\varphi^2\right)\right], \tag{3.17}$$

which is verified close to the disk mid-plane. We integrate with respect to z up to z_j, the height where the acceleration of the ouflow starts (defined in section 2.5.4). We get

$$\int_0^{z_j} \rho\Omega_k^2 z \,\mathrm{d}z \simeq \rho_0\Omega_K^2 h_\rho^2 \simeq P_0 - P(z_j) - \frac{1}{8\pi}\left(B_R^2 + B_\varphi^2\right)\Big|_{z_j}, \tag{3.18}$$

where we aproximate the first integral, by defining the density scale height h_ρ. We neglect $P(z_j)$ and write $P_0 = \rho_0\Omega_K^2 h^2$, Eq. (3.18) can then be written as

$$h_\rho^2 \simeq h^2\left[1 - \frac{\mu}{2}\left(\frac{B_R^2}{B_{z0}^2} + \frac{B_\varphi^2}{B_{z0}^2}\right)\Big|_{z_j}\right]. \tag{3.19}$$

The equation above states that the disk density scale height is reduced by the effect of the magnetic compression. Furthermore, since the density scale is related to the mass loading of the outflow we can deduce that when the magnetic compression increases ξ must decrease, the density decreases in the upper layers. Since, $p \simeq B_{R,SM}/B_{z0}$ we can deduce that when p increases the mass ejection index must decrease. We can also use Eq. (3.19) to relate the magnetization to p, when the magnetization increases if we want to keep ξ constant we will need to decrease p so that the magnetic compression is unmodified. At constant ξ when p increases μ decreases. This is true even if the toroidal magnetic field dominates. It can be shown that the magnitude of J_{R0} is also determined by p (they are linked by the accretion mach number defined below). An increases in p also tends to increase the toroidal magnetic field (see section 3.3 for more details). This behavior combined with the super Alfvénic constraint leads to an increasing ejection index when the magnetization increases (Ferreira 1997). However, as mentioned above we will be dealing with two types of vertical equilibria depending on which of the two magnetic components (B_R or B_φ) dominate, the behavior of $\xi(\mu)$ will be modified. We can finally express a final general constrain from Eq. (3.19)

$$\mu\left(\frac{B_R^2}{B_{z0}^2} + \frac{B_\varphi^2}{B_{z0}^2}\right)\Big|_{z_j} < 2, \tag{3.20}$$

this very restrictive condition states that the strength of the magnetic compression must be bounded or else the disk will be destroyed under the effect of the magnetic field. We will also return to this constraint in section 3.3. The constraint of the vertical equilibrium was also recovered by Ogilvie 1997 and Ogilvie and Livio 1998. They show that when one increases the strength of the magnetic field, the gas pressure increases and thus the magnetization tends towards a constant value. The solution adapts as to not disrupt the disk magneto-static equilibrium.

We show the vertical profiles of several quantities as functions of the variable $s = z/h$ along a magnetic surface for two solutions (Fig 3.4). These two solutions have the same parameters ($\alpha_m = 1$, $\chi_m = 1$, $\xi \simeq 0.1$) except for the magnetization, one was obtained with $\mu = 6.7 \times 10^{-2}$ (left) and the other one with $\mu = 5.7 \times 10^{-3}$ (right). While the former has one sign inversion of the radial magnetic field, B_R, the second has 3 spatial oscillations. The differential islands seen in Fig. (3.3) correspond to different spatial oscillation modes in the radial magnetic field. For example, $n = 0$ (no oscillation) corresponds to $\mu > 0.1$, the island located at $3 \times 10^{-2} < \mu < 0.5$ correspond to $n = 1$ and the solutions within it exhibit 1 spatial oscillation, while the island located at $3 \times 10^{-3} < \mu < 8 \times 10^{-3}$ corresponds to $n = 3$ and the solutions within it feature 3 spatial oscillations. We also distinguish that as the magnetization decreases the extent of the islands, $\delta\mu$, and the distance between the islands, $\Delta\mu$ get smaller and smaller.

The oscillatory behavior can also be seen in the other physical quantities, mainly, the other components of the magnetic field, the density and the velocity components. The spatial oscillation start above the disk mid-plane and they disappear before the SM point. Putting the oscillations aside, the behavior of the solutions at high n is very similar to the behavior of the solutions described in Ferreira 1997, which correspond to $n = 0$. The mass ejection is controlled by the parameter ξ. The deflection of the matter is a consequence of the thermal pressure gradient (section 2.5.4). The cold criterion for ejection index applies, indeed, the field lines are bent by more than 30 degrees with respect to the vertical axis (Blandford and Payne 1982).

3.2.2 MRI driven outflows

The oscillatory solutions obtained are a manifestation of channel flows, MRI-like modes that have been described by Latter et al. 2010 in their stratified form and by Goodman and Xu 1994 in their non stratified form. They resemble the ”exotic solutions” computed by Ogilvie 1997. Note that the equations we solve are stationary, the solutions found in our work *are not* linear unstable MRI modes. They are exact non-linear solutions of the stationary MHD equations that exhibit behavior similar to that of the MRI. Indeed, Lesur et al. 2013 have shown that MRI modes can spontaneously saturate into wind-like solutions. Nevertheless, The linear behavior will prove useful in understanding the behavior of the oscillating solutions.

Since MRI is an ideal instability, these mode develop only when the Alfvén time scale l/V_{Az} is smaller than the resistive time scale l^2/η_m, where l is the dynamical length scale. The wavelength of the fastest growing MRI mode needs to fit inside the region where the instability develops. The wavelength of the fastest growing MRI mode is defined by $2\pi V_A/\lambda_{\rm MRI} \sim \Omega_K$. We need this wavelength to be of the order of the dynamical length scale or more precisely $\lambda_{\rm MRI} \sim l/n$, where n is the number of spatial oscilations. For the outflow to exists, the radial oscillation need to stop when the radial magnetic field is positive, this imposes an integer number of oscillations.

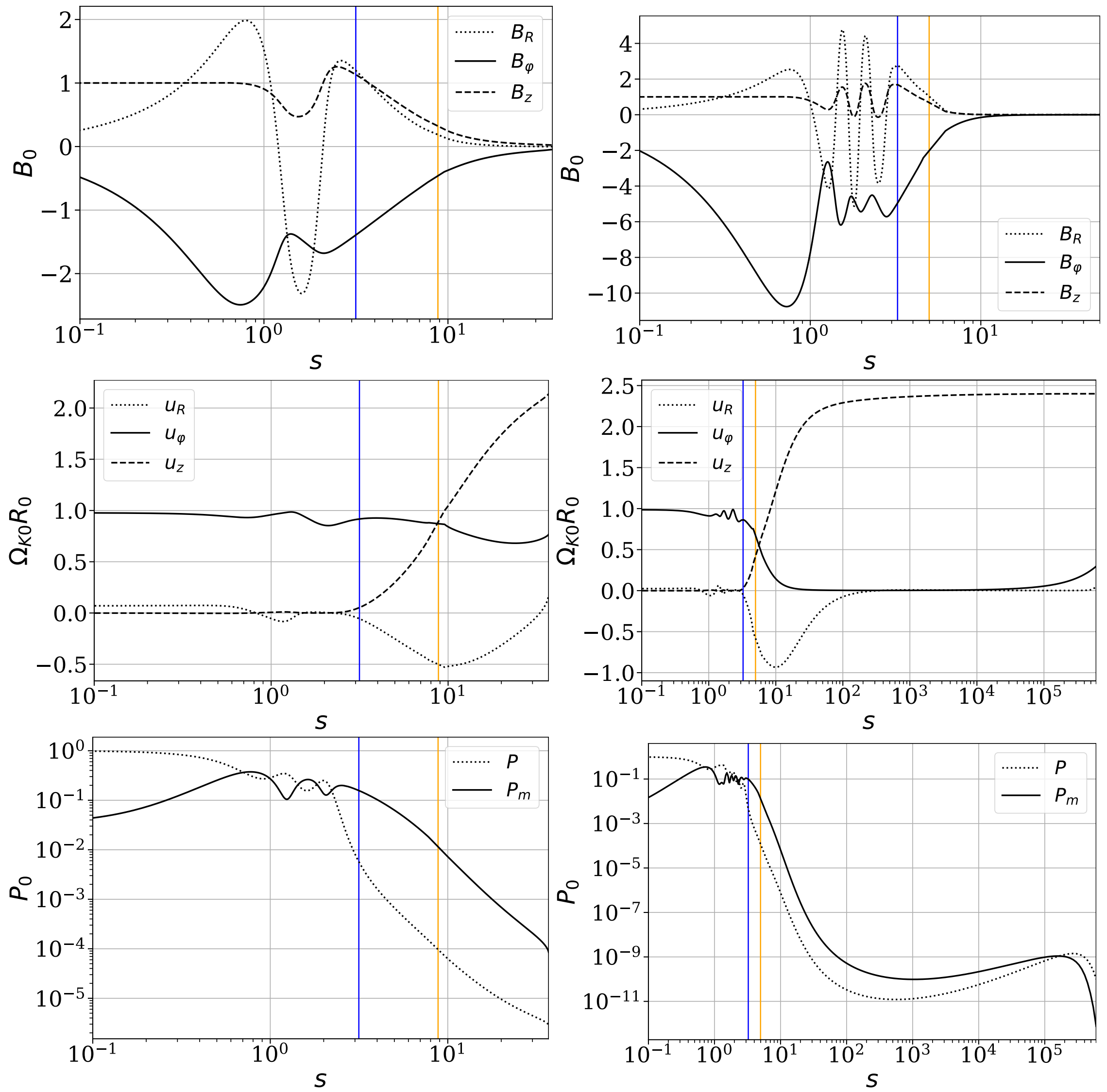

Figure 3.4: Vertical profiles for several quantities as function of the variable $s = z/h$ along a magnetic surface (Eq. 3.15) for two solutions obtained with $\alpha_m = 1, \chi_m = 1, \mathcal{P}_m = 1, \varepsilon = 0.1$, the same ejection index $\xi = 0.1$ and $\mu = 6.7 \times 10^{-2}$ (left), $\mu = 5.7 \times 10^{-3}$ (right). The magnetic field components (left) are normalized to the vertical field at the disk midplane B_o, the velocity components (middle) to the Keplerian velocity $\Omega_{Ko}R_o$ and the kinetic P and magnetic P_m pressures (right) to the kinetic pressure at the disk midplane. The blue and orange vertical lines represent respectively the SM and Alfvén critical points.

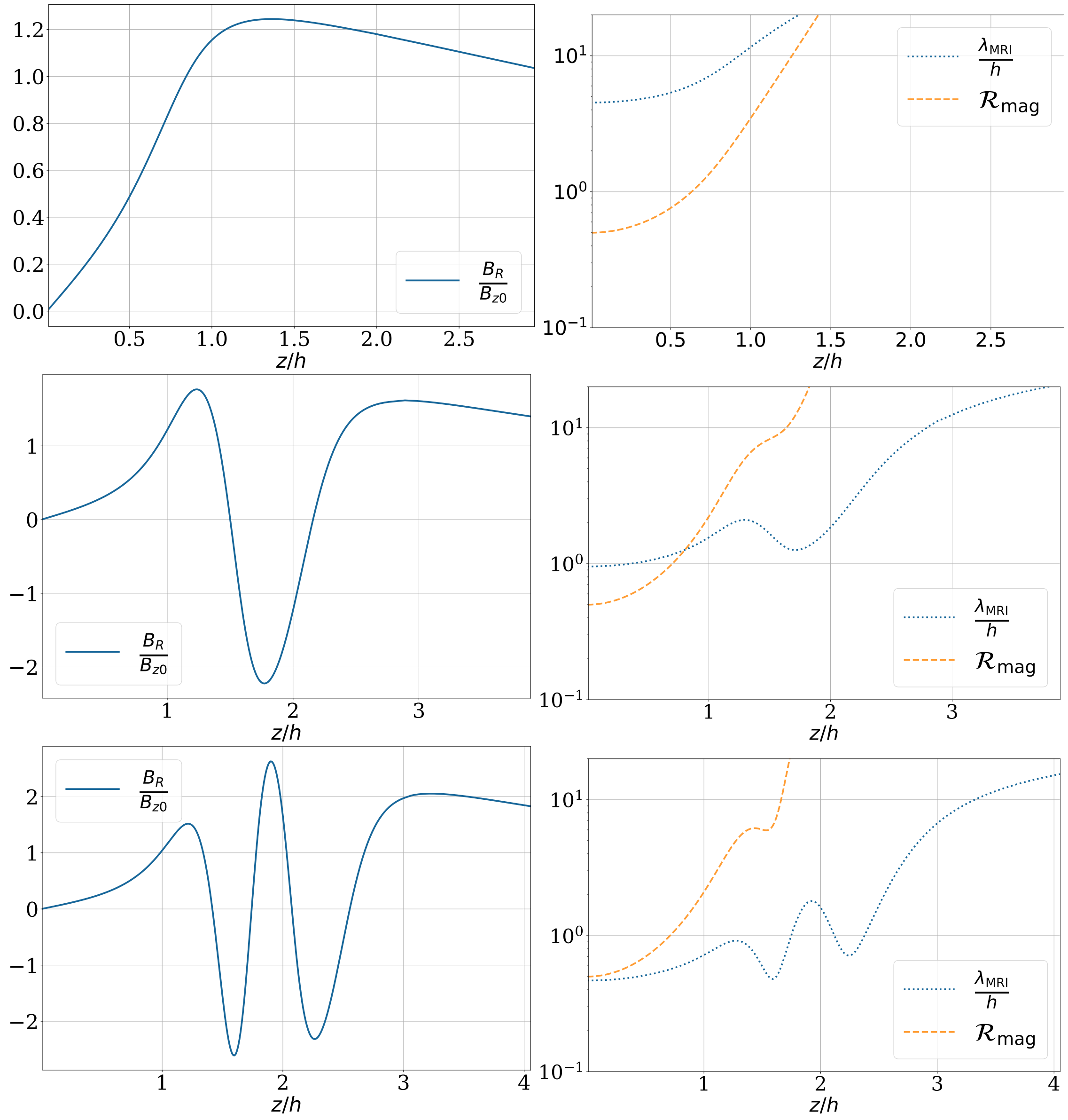

Figure 3.5: Vertical profile of the radial magnetic field as well as the Linquist number and the dimensionless MRI wavelength defined in Eq.(3.21) as function of the variable z/h for 3 different solutions. The three solutions are obtained with $\alpha_m = 2, \chi_m = 1, \mathcal{P}_m = 1, \varepsilon = 0.1$, roughly the same ejection index $\xi \sim 0.1$ and $\mu = 5.2 \times 10^{-1}$ (top), $\mu = 2.3 \times 10^{-2}$ (middle), $\mu = 5.4 \times 10^{-3}$ (bottom). The magnetic field components are normalized to the vertical field at the disk midplane B_{z0}.

Taking $l \sim h$ we have the following crude conditions

$$\mathcal{R}_{\text{mag}} = \frac{hV_{Az}}{\eta} > 1 \tag{3.21}$$

$$\frac{\lambda_{\text{MRI}}}{h} = 2\pi \frac{B_z}{B_{z0}} \sqrt{\mu \frac{\rho_0}{\rho}} \sim \frac{1}{n}, \tag{3.22}$$

The validity of these considerations is shown in Fig. (3.5). We see that the disk mid plane is always too diffusive and no spatial oscillations are present regardless of the magnetization μ. However, since both the density and diffusivity decrease vertically, $\mathcal{R}_{\text{mag}}$ becomes large enough for spatial oscillations to develop on a length scale of order h. Spatial oscillations develop at the disk surface ($z \simeq h$), where the flow reaches the ideal MHD regime. The expression of λ_{MRI} harbors several features:

- The number of spatial oscillations depends on μ: Smaller μ leads to larger n, as can be seen in Fig. (3.5). However, there is some leeway in the precise value of μ, that permits to define the thickness of the islands, $\delta\mu$, around an average value μ_n. This leeway will be given by the vertical profile of density and is therefore a consequence of p and ξ.
- As the density decreases, the wavelength increases and eventually becomes larger than the local dynamical scale. In Fig. (3.5) we show that the oscillations stop whenever the MRI wavelength becomes larger than a few h, there is no longer any space for the MRI modes. This leads to the MRI modes being localized below the SM point, x_{SM}.

The above properties help us understand the existence of islands seen in Fig.(3.3) as well as their separation with μ. The MRI wavelength and the SM point can be approximately related by $n\lambda_{\text{MRI}} \sim hx_{SM}$, which leads to $\mu_n \sim \frac{f(x_{SM})}{n^2\alpha_m^2}$, where $f(x_{SM})$ is a function that depends on the altitude x_{SM} and $\mu_n = (\mu_{\max} + \mu_{\min})/2$ is the average value of μ for a given n and p. Since x_{SM} is weakly dependent of the magnetization μ, we write

$$\frac{\mu_n}{\mu_{n+1}} \sim \left(\frac{n+1}{n}\right)^2. \tag{3.23}$$

To test this expression we used three different super SM parameters spaces obtained with $\mathcal{P}_m = 1$ and $\varepsilon = 0.1$ but with different values for α_m and χ_m. For a constant value of p we measured the average μ_n where the island is located for the different parameter spaces. We then computed the ratio μ_n/μ_{n+1} as a function of n, as shown in Fig.(3.6). This figure clearly demonstrates that the analytical estimate can accurately reproduce the behavior of the islands. This expression also explains why the distance between the island, $\Delta\mu = \mu_n - \mu_{n+1}$, decreases as the magnetization decreases.

The existence of the islands is a consequence of the MRI-driven channel modes as well as of our boundary conditions at the disk mid plane. The imposed boundary conditions at $z = 0$, namely $B_R = B_\varphi = 0$ and $u_R < 0$ (inward accretion motion), have a selection effect on the MRI channel modes. This clearly forbids modes leading to an outward motion ($u_R > 0$) at the disk mid plane and modes with a half-integer number of oscillations ($n + 1/2$). Allowing for such a boundary condition would lead to a supplementary half wavelength $(n + 1/2)\lambda_{\text{MRI}} \sim hx_{SM}$. Breaking the z-symmetry could also allow other modes with $B_\varphi = 0$ located above or below $z = 0$. Computing such solutions is beyond the scope of this work. We nevertheless argue that the parameter space of Fig. (3.3) is actually a subset of the real parameter space of super-SM accretion ejection structures. Such solutions should only fill in the actual ”forbidden” zones between the islands.

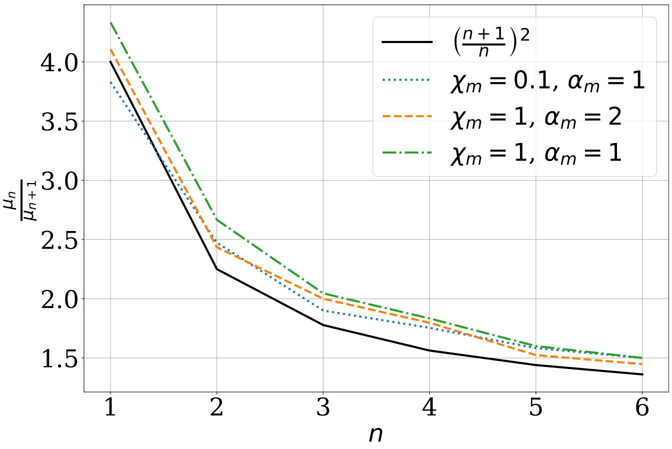

Figure 3.6: Ratio μ_n/μ_{n+1} as function of the number n of spatial oscillations for three different sets of super-SM solutions obtained with $\mathcal{P}_m = 1, \varepsilon = 0.1$ and a constant p. The value μ_n is obtained as the regularity condition for a super-SM flow exhibiting n spatial oscillations (see text). The black solid line is our simple analytical estimate Eq.(3.23) and the colored curves are for the following parameter sets: $\alpha_m = 1, \chi_m = 1$ (green), $\alpha_m = 2, \chi_m = 1$ (red) and $\alpha_m = 1, \chi_m = 0.1$ (blue).

The channel flow described in this section are essential for the acceleration mechanism. Blandford and Payne 1982 show that the outflow launching mechanism (in the case of negligible outflow enthalpy) requires a radial magnetic field component comparable or larger than the vertical magnetic field. Ferreira and Pelletier 1995 then showed that for near equipartition solutions the creation of a radial component of the magnetic field is a natural outcome of the transfer of the disk angular momentum to the outflow base. Lesur et al. 2013 then showed that this process can also be understood in the framework of the MRI instability. The channel modes are essential, by driving the spatial oscillations they provide the bending of the poloidal magnetic surface necessary for ejection. This will be further discussed in section 3.3.

We finally note that, the spatial oscillation exhibited by our solutions are in contradiction with the prescribed smooth resistivity and viscosity. Parasitic instabilities, such as Kelvin-Helmholtz, should be triggered and lead to the destruction of these channel modes (Goodman and Xu 1994; Latter et al. 2010). This would lead to an internal rearrangement and a modification of the turbulent transport coefficients. This will be discussed in section 3.5. In practice the oscillations are a consequence of an inadequate choice of the profiles of the turbulent resistivity and viscosity.

3.3 Super Alfvénic outflows

3.3.1 The magnetic shear as a function of the disk magnetization

We compute the MHD invariants defined in section 2.5.1 for all our super-SM solutions (see Fig. 3.3) and then show them as function of the magnetization and the ejection index ξ, see Fig. (3.7). We see that the mass loading invariant κ shows a linear dependence on the ejection index ξ, we also see that κ increases with decreasing magnetization. We can understand this dependence by computing an approximate expression of the mass loading invariant. We start from the conservation of mass in its integrated forms (Eq. (2.164))

$$\xi = \frac{\mathrm{d}\ln \dot{M}_a}{\mathrm{d}\ln R} = \frac{1}{\dot{M}_a}\frac{\mathrm{d}\dot{M}_o}{\mathrm{d}\ln R}, \tag{3.24}$$

we approximate the mass accretion rate as $\dot{M}_a \simeq 4\pi\rho_0 u_{R0} hR$ and the mass ejection rate as $\dot{M}_o \simeq 2 \times 2\pi R^2 \left.[\rho u_z]\right|_{SM}$, leads to

$$\left.[\rho u_z]\right|_{SM} \simeq \xi\rho_0 u_{R0}\varepsilon. \tag{3.25}$$

We then use the definition of the mass loading invariant to compute

$$\kappa = 4\pi \left.\frac{\rho u_z}{B_z}\right|_{SM} \left.\frac{R\Omega_K}{B_z}\right|_{SM} \simeq \frac{\xi}{\mu}\frac{u_{R0}}{c_s} = \xi\frac{m_s}{\mu}, \tag{3.26}$$

where we have assumed that $B_z|_{SM} \simeq B_{z0}$. Finally, μ can be related to the sonic Mach number of accretion, $m_s = u_{R0}/c_s$, through Eq.(3.5)

$$\frac{4\pi}{c}\eta_{m0}J_{\varphi 0} = \alpha_m V_{A0} hp\frac{B_{z0}}{h} = u_{R0}B_{z0} \quad \Leftrightarrow \quad m_s = p\alpha_m \mu^{1/2}, \tag{3.27}$$

where u_{R0} is evaluated at the disk mid-plane. The Mach number at the disk mid-plane is determined by the strength of the magnetic field as well as the current flowing thorough the disk.

We use the relation above to rewrite the mass loading invariant as

$$\kappa \simeq \xi p \frac{\alpha_m}{\mu^{1/2}}, \tag{3.28}$$

the outflow mass load is thus a function of ξ and μ. This expression was first derived in Casse and Ferreira 2000b. For a given ejection index ξ, increasing κ can be done by decreasing the magnetic field strength. Matter dominated super-SM flows with $\kappa > 1$ become thus achievable at low μ. To convince ourselves that the magnetization dependence observed in Fig. (3.7) is truly on $\mu^{-1/2}$ we show three dashed lines computed using Eq.(3.28) for different magnetizations, calculated with $p = 1$ and $\alpha_m = 1$. We confirm that Eq.(3.28) provides a good approximation for the dependence of κ on the disk parameters μ and ξ.

We remark from Fig. (3.7) (right) that the magnetic lever arm, λ, does not have a strong dependence on μ, λ is only a function of the ejection index. Indeed, $\lambda = 1 + K/(2\xi)$, where $K = \Lambda/(\Lambda + 1)$ where $\Lambda = M_{z\varphi}/M_{R\varphi}$ (see section 2.5.5) is a rather weak function of μ and ξ. This is impressive as ξ and μ span respectively 2.5 and 4 decades. The remarkable dependence of λ as only a function of ξ must be the outcome of some intrinsic physics. We compute the toroidal magnetic field as a function of λ and κ, by using Eq. (2.153), as

$$-\left|\frac{B_\varphi}{B_{z0}}\right|_{SM} \simeq \kappa(\lambda - 1). \tag{3.29}$$

Using this expression, the derived dependency for κ, and the fact that λ is only a function of the ejection index we derive

$$\left|\frac{B_\varphi}{B_{z0}}\right|_{SM} = \frac{p\alpha_m}{2\mu^{1/2}}K \propto \mu^{-1/2}, \tag{3.30}$$

since K is a weakly varying function and p has a small range. The magnetic shear is thus a function of the magnetization. We can construct a rather simple argument to understand this behavior of the magnetic shear. We start from the previously derived expression (Eq. 2.145) for the vertical velocity of the outflow at the inflection point ($u_R = 0$),

$$u_z|_{z_R} \simeq \frac{\eta_m}{h}. \tag{3.31}$$

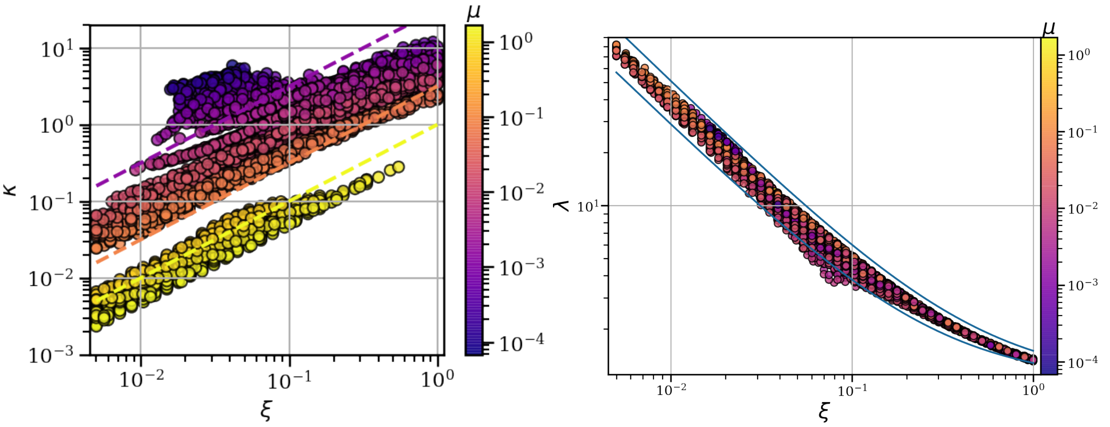

Figure 3.7: (Left) Mass loading parameter κ calculated using Eq.(2.112) as function of ξ for all super-SM solutions appearing in Fig. 3.3. The dashed lines correspond to curves $\kappa \simeq \xi p \frac{\alpha_m}{\mu^{1/2}}$, computed with $p = 1$ and $\alpha_m = 1$, for different values of the magnetization, μ. The yellow curve corresponds to $\mu = 1$, the orange one corresponds to $\mu = 0.1$ and the purple one corresponds to $\mu = 10^{-3}$. (Right)Magnetic lever arm parameter λ calculated using Eq.(2.119) as a function of ξ for all super-SM solutions appearing in Fig. 3.3. The solid lines correspond to curves $\lambda = 1 + \frac{K}{2\xi}$, computed using $K = 1$ (top) and $K = 0.6$ (bottom).

The outflow needs to become super SM, where we approximate $V_{SM} \sim C_S \frac{V_{Az}}{V_A}$, close to the disk surface. Hence, we compare this diffusive velocity with the super slow magneto sonic velocity, $u_z|_{z_R} \sim V_{SM}$ to find

$$\alpha_m^2 \mu = F_{SM}^2(x) \frac{1}{1 + \left(\frac{B_{R,SM}}{B_{Z0}}\right)^2 + \left(\frac{B_{\varphi,SM}}{B_{Z0}}\right)^2}, \tag{3.32}$$

where F_{SM} is a function depending on the vertical profiles of the temperature and the magnetic resistivity. For this expression to be valid for all μ, the magnetic shear must be

$$\left|\frac{B_\varphi}{B_{z0}}\right|_{SM} \propto \mu^{-1/2}. \tag{3.33}$$

It therefore appears that it is the SM constraint that imposes a scaling on the toroidal magnetic field. This scaling is a direct consequence of the dependence of η_m on μ. If the scaling of the magnetic diffusivity is different, as for example if one considers ambipolar diffusion (Lesur 2021), the scaling of the toroidal magnetic field would be different (see section 3.5).

As a consequence, a rather good approximation for the outflow torque exerted on the accretion disk, $M_{z\varphi}$, reads

$$\frac{M_{z\varphi}}{RP_0} \simeq 2\mu \left|\frac{B_\varphi}{B_{z0}}\right|_{SM} \propto \mu^{1/2}, \tag{3.34}$$

this scaling is shown in Fig. 3.8. The outflow torques can be modeled as a function of the magnetization, i.e. the strength of the mean vertical magnetic field and the plasma pressure at the disk mid-plane. This prescription can be used to include the effect of the magnetic field on hydrodynamic models. This is the scaling that was used in Scepi et al. 2020.

3.3.2 The super Alfvénic constraint

In this section we compute the constraint imposed by the crossing of the Alfvén point on the outflow properties. This constraint will follow from the Grad-Shafranov equation or the transverse

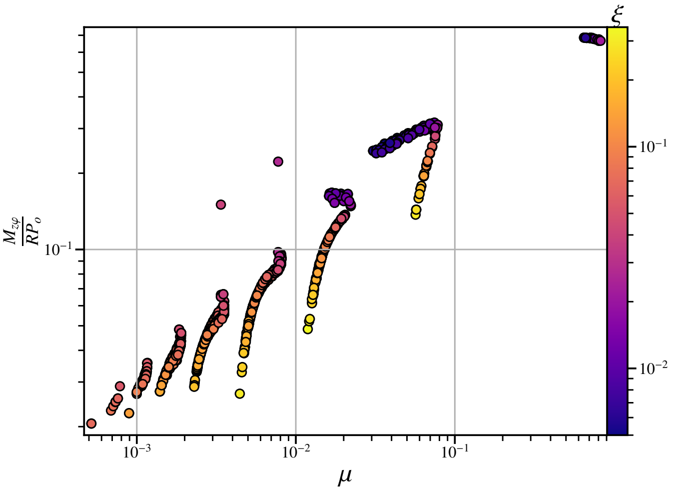

Figure 3.8: Vertical torque defined by Eq.(2.80) as a function of the magnetization μ and the mass ejection index ξ. Every point corresponds to a super-Alfvénic solution, section 3.3

outflow equilibrium

$$\nabla\cdot\left[\left(m^2-1\right)\frac{\nabla a}{4\pi R^2}\right]=\rho\left\{\frac{\mathrm{d}\mathcal{B}}{\mathrm{d}a}-\Omega\frac{\mathrm{d}\Omega_* R_A^2}{\mathrm{d}a}+\left(\Omega R^2-\Omega_* R_A^2\right)\frac{\mathrm{d}\Omega_*}{\mathrm{d}a}\right\}+\frac{B_\varphi^2+m^2B_p^2}{4\pi}\frac{\mathrm{d}\ln\tilde{\eta}}{\mathrm{d}a},\quad(3.35)$$

where $\mathcal{B}$ is the Bernoulli invariant and

$$\frac{\mathrm{d}}{\mathrm{d}a}=\frac{1}{\nabla a\cdot\nabla a}\nabla a\cdot\nabla.\quad(3.36)$$

The Grad-Shafranov equation (GSE) is a very complicated nonlinear partial differential equation, it is obtained by projecting the poloidal conservation of momentum across the magnetic surfaces (∇a), in practice, it is not used to compute the self-similar accretion ejection physics.

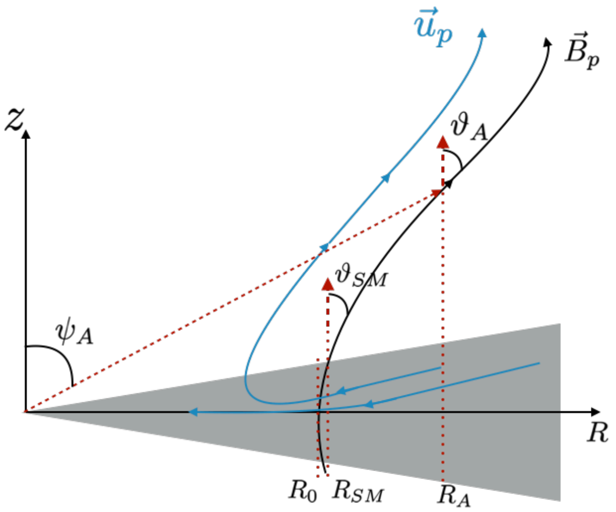

Figure 3.9: This schema defines the different angles ϑ_{SM}, ϑ_A and ψ_A as well as the different relevant radii R_0, R_{SM} and R_A.

We compute the regularity condition of Eq. (3.35) at the Alfvén point, where $m = u_p/V_{Ap} = 1$, in appendix B, we follow the partial derivation of Casse and Ferreira 2000b. This position

(z_A, R_A) is labelled by the angle ψ_A, defined as

$$\cot\psi_A = \frac{z_A}{R_A} = \varepsilon x_A, \tag{3.37}$$

we also define the local outflow opening angle as

$$\tan\vartheta = B_R/B_z. \tag{3.38}$$

At the SM point we have $\cos\vartheta_{SM} \simeq \frac{B_{R,SM}}{B_{z0}}$. For the sake of clarity, we show the different angles and the different radii in Fig. (3.9). The regularity condition will provide a value of $g_A = g(\psi_A, \kappa, \lambda, \omega, e)$, where g is defined by

$$\Omega = \Omega_\star(1-g), \tag{3.39}$$

as

$$g = \frac{m^2}{m^2-1}\left[1-\left(\frac{R_A}{R}\right)^2\right]. \tag{3.40}$$

This function is related to the acceleration efficiency of the outflow. The closer g_A is to 1 the more efficient the acceleration was before the Alfvén surface (section 2.5.4). The function g is also related to the poloidal current flowing through the disk (Ferreira 1997). The angle ψ_A is not known a priori, to solve the GSE the Alfvén surface needs to be imposed. In a time-dependent problem, the Alfvén surface would naturally emerge as a consequence of all causal connections. In a self-similar approach this translates into a conical Alfvén surface with a possible choice of the angle ψ_A (as done in Vlahakis et al. 2000). In our case the outflow is connected to an accretion disk, the value of ψ_A will be a consequence of that constraint. Since our integration starts from the disk mid-plane and is propagated upwards the trans Alfvénic solution can only be found if at some point x_A, $g(x_A) = g_A$ is verified, this will then fix ψ_A. The position of the Alfvén surface emerges then as a function of the disk parameters. In the following derivation we will ignore all thermal contributions to the GSE and the Bernoulli equation, we will also assume that $R_{SM} \simeq R_0$. We start by evaluating the Bernoulli invariant (Eq. 2.132) at the Alfvén point and normalizing it to $\frac{1}{2}\Omega_K(R_{SM})^2R_{SM}^2$, we find

$$\frac{2\mathcal{B}_A}{\Omega_K(R_{SM})^2R_{SM}^2} = v_A^2 - 2\sqrt{\frac{\omega}{\lambda}}\sin\psi_A + 2\omega\lambda - \omega\lambda(1-g_A^2) = e, \tag{3.41}$$

where v_A is the normalized poloidal velocity at the Alfvén point and e is the Bernoulli invariant evaluated at the SM point (Eq. 2.141). Using the expression above we compute the velocity at the Alfvén point as a function of the MHD invariants and ψ_A

$$v_A^2 = \omega\lambda\left(g_B^2 - g_A^2\right), \tag{3.42}$$

where

$$g_B^2 = 1 + \frac{1}{\omega\lambda}\left[-2-\omega^2+\sin\psi_A\sqrt{\frac{\omega}{\lambda}}\right]. \tag{3.43}$$

Here g_B represents the maximum value for the acceleration efficiency g_A as imposed by energy conservation. A similar constraint was derived by Casse and Ferreira 2000b. Since $g_B^2 > 0$, this gives a constraint on the minimum energy reaching the Alfvén point, namely a minimum magnetic lever arm given by

$$\lambda - 3 + \frac{2}{\lambda^{1/2}}\sin\psi_A > 0. \tag{3.44}$$

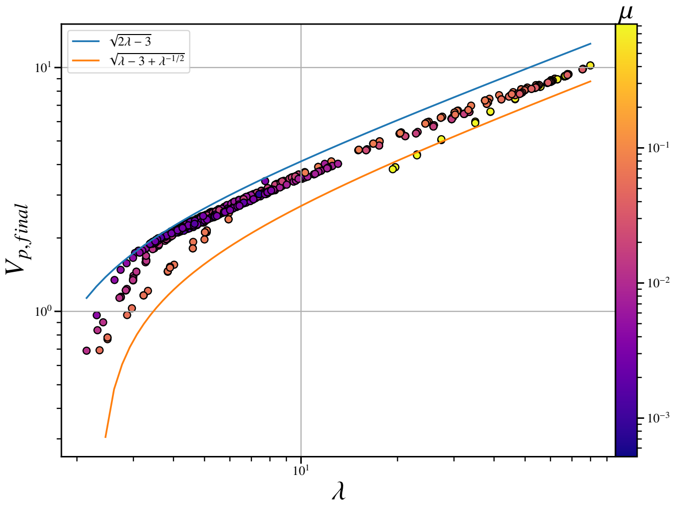

Figure 3.10: The terminal jet poloidal velocity (in units of the Keplerian speed at the foot-point) as function of the magnetic lever arm λ for our super-A solutions found in the fiducial case. The blue and orange solid curves correspond respectively to upper and lower analytical limits (see text). The fact that solutions do not reach the maximum speed indicates that the magnetic field still conserves a fraction of the available energy.

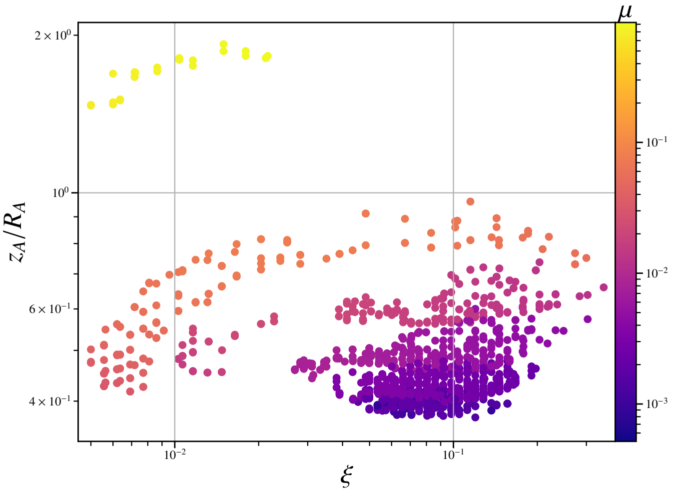

Figure 3.11: Position of the Alfvén point as function of the disk ejection efficiency ξ for our fiducial parameter set. The color scale is the disk magnetization μ. The behavior of the Alfvén position is different at high and low disk magnetizations, large ξ requiring both smaller μ and an Alfvén surface closer to the disk surface (see text).

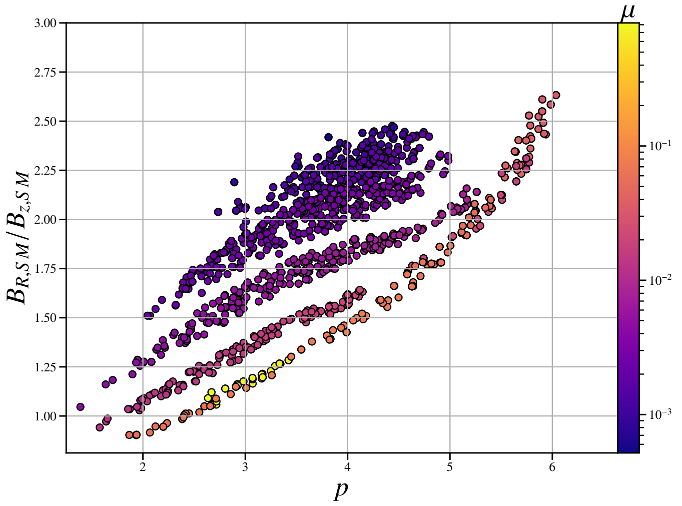

Figure 3.12: Bending B_R/B_z of the poloidal magnetic field evaluated at the SM point, as function of the parameter p (toroidal current density at the mid-plane) and the disk magnetization μ (colors) for our fiducial parameter set. The jet initial opening angle increases monotonously with increasing p and decreasing μ.

The closer the Alfvén surface is to the disk, the smaller the magnetic lever arm can be. For $\lambda > 3$, the position of the Alfvén surface plays no role. The velocity at the Alfvén point can be used to approximate the lower limit of the terminal outflow velocity, $u_{p\infty}$, while the upper limit is $V_K(R_0)\sqrt{2\lambda - 3}$. These two limits are shown in Fig.(3.10) for our super Alfvén solutions in the fiducial case. For the lower curve, we compute v_A with $\omega = 1$, $\sin\psi_A = 1$ and $g_A = 0$. All our super Alfvén solutions are indeed within those limits.

The GS equation can be analytically solved at the Alfvén point, this is computed in appendix B, we show that there are always two positive roots

$$\left.\frac{g_A}{g_B}\right|_{\pm} = \frac{c(k^2 - \sin^2\Psi_A) \pm \cos\Psi_A\sqrt{(k^2 - \sin^2\Psi_A)\left(c^2 - \frac{k^2-1}{k^2}\right)}}{k^2c^2 + \cos^2\Psi_A}. \tag{3.45}$$

From this computation we also extract the following useful constraint

$$\kappa_{\min}\lambda^3 g_B^2 = \omega. \tag{3.46}$$

this equation provides the absolute lower value for κ in order to find a super-A outflow. Indeed, for $g_A = 0$ the GS constraint can only be satisfied if $\kappa = \kappa_{\min}$. Equation (3.46) is a generalization of Eq.(3.1) in Blandford and Payne 1982 that reads

$$\kappa\lambda_{\min}(2\lambda_{\min} - 3)^{1/2} = 1. \tag{3.47}$$

Blandford and Payne 1982 deduce this constraint by studying the far-field solutions of the MHD equations. They find that the far field solutions depend on κ and λ through a parameter defined as $\beta_{\mathrm{BP}} = \kappa(2\lambda - 3)^{3/2}$. When β_{BP} is large the acceleration is driven by the centrifugal force to a large radius before the toroidal magnetic field is able to recollimate the flow. When β_{BP} is small recollimation happens closer to the disk. Hence, there must exist a limit where recollimation happens before the Alfvén surface and the super-A outflow does not exist anymore, they approximate this limit to be Eq.(3.47).

In Fig. (3.11) we see that the position of the Alfvén surface increases as the ejection index increases (λ decreases), for highly magnetized solutions this is always the case. However, for weakly magnetized solutions there exists a maxima, at a certain value of ξ, where the Alfvén surface retreats closer to the disk as ξ increases (λ decreases). It is also clear from looking at Fig. (3.12) that as p increases the outflow opening angle, θ_{SM}, also increases. Furthermore, when p increases the ejection index ξ decreases due to the enhanced compression of the accretion disk (see section 3.2.1). Therefore, when the ejection index increases (p decreases) the outflow opening angle decreases (see also Fig. 3.15).

In this picture, the monotonous behavior of Fig. (3.11) can be understood. If the outflow opening angle is small the magnetic field line will meet the Alfvén surface higher than if the opening angle were large, since R_A is fixed by the magnetic lever arm (see Fig. 3.9).

This picture is consistent with Fig. (3.11). However, once λ is smaller than 3, $\xi > 0.25$, the acceleration efficiency goes to 0 unless the Alfvén surfaces moves closer to the disk (ψ_A increases). This can be understood from the definition of g_B (Eq. 3.43), only if the Alfvén surface moves closer to the disk can g_B stay bigger than 0. Indeed, since g_B is a maximal value of g_A when g_B goes to 0 $g_A \to 0$.

In Fig. (3.11) we also see that when we decrease the magnetization the Alfvén surface moves closer to the disk. This can also be understood by looking at Fig. (3.12), as the magnetization decreases the outflow opening angle increases leading to a magnetic surface that meets the Alfvén radius closer to the disk.

3.3.3 The super Alfvénic parameter space

In Fig. (3.13) $\kappa - \lambda$ plane and where the color represents the magnetization. In the appendix B we computed a constraint that needs to be satisfied for a solution to cross the Alfvén point. For a given magnetic lever arm, there must be a minimum mass load $\kappa_{\min}$ for a cold flow such that

$$\kappa_{\min}^2 \lambda^3 g_b^2 = 1 \tag{3.48}$$

with

$$g_B^2 = 1 - \frac{3}{\lambda} + \frac{2}{\lambda^{3/2}} \sin\psi_A, \tag{3.49}$$

Eq. (3.46) with $\omega = 1$. This constraint expresses that for a magnetic lever arm λ (mostly determined by ξ), κ must be large enough. This expression is used to compute the two solid curves shown in Fig. (3.13), computed in two extreme cases for the location of the Alfvén surfaces:

- The first one is close to disk, near the SM surfaces with $x_{SM} = 2$, namely $\psi_A = \pi/2 - \arctan(2h/2)$ for the lower curve.

- The second on is much further out with $\psi_A = \pi/3$ for the upper curve, this value of ψ_A is typical for near-equipartition cold outflows.

This constraint rules out all super-SM solutions located at the left-hand side of these curves. We see that solutions with near equipartition fields ($n = 0$) will be constrained to large values of the magnetic lever arm, $\lambda > 7$, namely to mass loading values smaller than 0.1 and to ejection index values smaller than 0.08 (in agreement with Ferreira 1997). On the contrary, solutions with smaller magnetization can achieve smaller values of λ as well as bigger values of the ejection index and the mass loading, κ. These isothermal outflows could be interesting for reproducing dense outflow ($\xi > 0.1$) with low asymptotic speeds ($u_{p\infty} \simeq V_{K0}$). Weakly magnetized outflows seem better suited for massive outflows, the MRI-like mechanism providing the bending while a lower magnetization moves the Alfvén surface closer to the disk (see previous section).

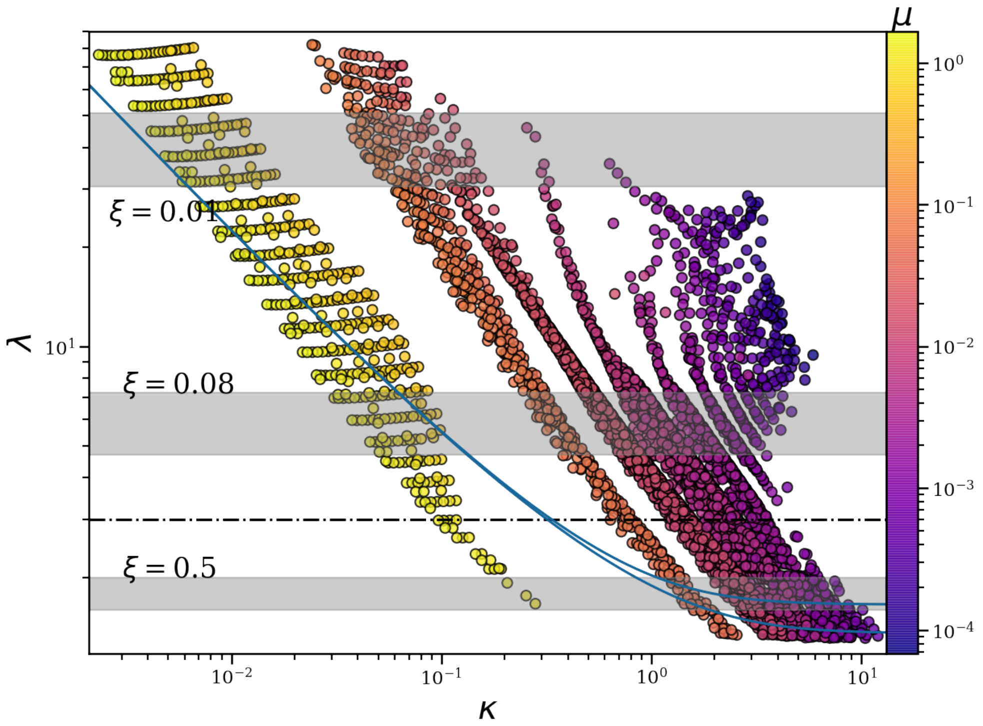

Figure 3.13: Projection on $\kappa - \lambda$ plane of all the super-SM solutions shown in Fig. 3.3. The color scale is the disk magnetization μ, while the grey areas correspond to zones with approximately a constant ejection index ξ whose value is indicated. Note that the stripes (best seen in the yellow high magnetization zone with $n = 0$) are an effect of our numerical procedure for seeking solutions.

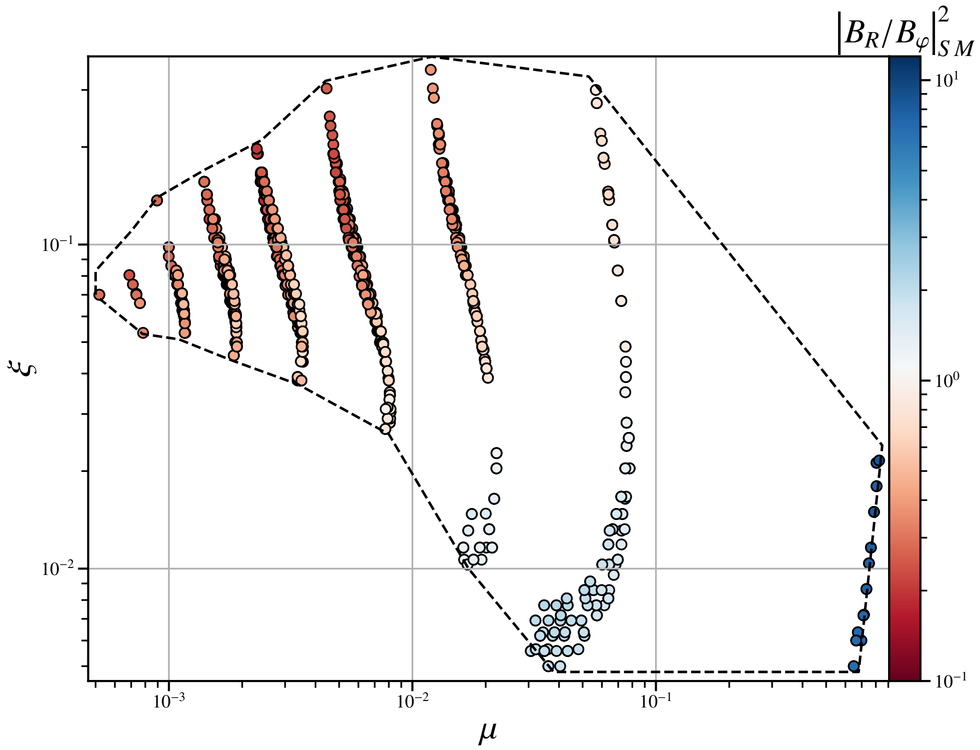

Figure 3.14: Parameter space $\xi(\mu)$ for isothermal super-A solutions with $\alpha_m = 1$, $\chi_m = 1$, $\mathcal{P}_m = 1$ and $\varepsilon = 0.1$. In colors are shown the ratio of the radial to the toroidal magnetic field at the SM point. A clear trend emerges, with small magnetizations leading to highly wound magnetic fields, whereas larger magnetizations correspond to more bent structures. This can be seen as an evolution from a vertical pressure lift at small μ to a magneto-centrifugal push at large μ. The black dashed line is a sketch of the border of the parameter space.

Not all Super-SM solutions located at the right hand side of the solid curves in Fig. (3.13) can become super Alfvénic . The constraint written in Eq. (3.46) only takes into account the energetics of the system and is not a direct consequence of the Grad-Shafranov equation. Indeed, not all couples (κ,λ) fulfill Eq. (3.45). If a solution is not possible it means that there is no altitude z_A of the Alfvén point that can be found starting from the condition provided at the base of the outflow (SM point). Modifying the value of p leads to a slight modification of κ, λ and the outflow opening angle $\cos\vartheta_{SM}$ allowing to possibly meet the Alfvén surface. As explained above the condition $g_B > 0$ highlights this aspect.

Figure (3.14) shows the super Alfvénic parameter space in the (ξ, μ) plane for our fiducial case. It is a subset of the SM parameter space shown in Fig. (3.3). The islands become almost vertical stripes in μ with a range in ejection index ξ. We recover the same behavior as in Ferreira 1997 for high magnetization solutions, near equipartition ($n = 0$). When the magnetization decreases the ejection index also increases. Furthermore, we enlarge the parameter space in the μ direction by almost 4 orders of magnitude (up to $n = 8$).

The color scale in Fig. (3.14) indicates the ratio of the radial to the toroidal magnetic field component at the SM point. Solutions with near equipartition magnetic fields are dominated by the radial component of the magnetic field, the toroidal field becoming gradually dominant as n increases (μ decreases). This is consistent with the scaling $B_\varphi/B_{z0} \propto \mu^{-1/2}$ imposed by the SM regularity condition. However, it highlights a possible complementarity between ”magnetic tower” outflows where ejection is due to a dominant B_φ field, and ”(magneto)centrifugally-driven” outflows (Blandford and Payne 1982), where the dominant B_R is of utmost importance.

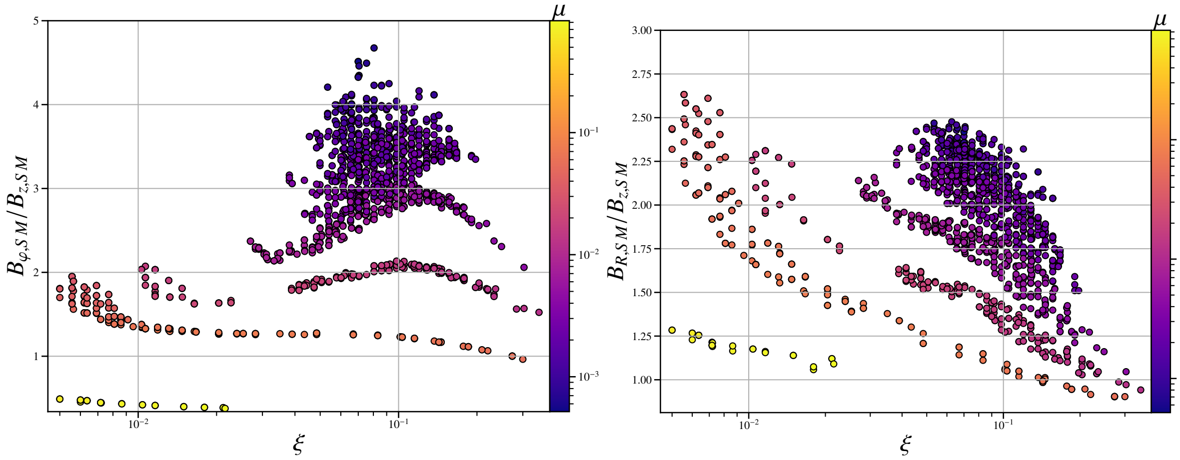

Figure 3.15: (left) Toroidal, B_φ/B_z, and (right) radial, B_R/B_z, magnetic field components evaluated at the SM point, as functions of the parameter ξ and the disk magnetization μ (colors) for our fiducial parameter set.

Indeed, we have a continuous transition between ”magnetic tower” outflows (at small μ and large ξ) and ”(magneto)centrifugally-driven” outflows (at large μ and small ξ).

The dependence of $\xi(\mu)$ changes for the two cases within each island. It can be seen that for $n = 0$ ξ increases when μ increases (although for a very limited range). On the other hand, for $n = 3$ ($\mu < 10^{-2}$), it is the other way around: ξ decreases for increasing μ. The functional dependence of $\xi(\mu)$ can be seen as a fingerprint of the dominant ejection mode, magneto-centrifugal or magnetic tower like.

To understand this new behavior at small μ we show in (Right) Fig. (3.15) the toroidal magnetic evaluated at the SM point normalized by the vertical magnetic field as a function of the ejection index and the magnetization μ. We see that, contrary to the radial magnetic field (left) (Fig. 3.15), the toroidal magnetic field features a more complicated behavior when seen as a function of the ejection index ξ. We saw before that the radial magnetic field increases as p increases, and that ξ decreases as p increases, therefore $B_{R,SM}$ decreases when ξ increases, which is clearly shown in (right) Fig. (3.15). We see in Fig. (3.15) that the behavior of the toroidal magnetic field at low μ and intermediate values of ξ ($3 \times 10^{-2} < \xi < 0.1$) is the opposite. Indeed, the strength of the toroidal magnetic field increases when the ejection index increases. This can be understood using the constraint of vertical equilibrium

$$\mu \left(\frac{B_R^2}{B_{z0}^2} + \frac{B_\varphi^2}{B_{z0}^2} \right) \Bigg|_{z_j} < 2. \tag{3.50}$$

When μ is very small it is easy to satisfy the vertical equilibrium for the radial magnetic field. However, the toroidal magnetic field scales as $\mu^{-1/2}$ and will dominate the magnetic compression of the disk as well as the acceleration of the outflow at low μ. It is the interplay between these two processes which cause the extremum in the dependence of $\xi(\mu)$ at small μ.

We see that at low ejection index ($\xi < 2 \times 10^{-2}$) the radial magnetic field is larger than or comparable to the toroidal magnetic field. Indeed, when $\xi < 2 \times 10^{-2}$ no matter the μ, the behavior of $\xi(\mu)$ follows the monotonous behavior of increasing μ leading to increasing ξ (Ferreira 1997). The radial magnetic field has the dominant role in the vertical equilibrium.

At intermediate values of the ejection index ($2 \times 10^{-2} < \xi < 0.1$) the toroidal compression is weak and a higher toroidal field is beneficial since it helps the magnetic vertical acceleration. Hence, increasing ξ or μ leads to an increase in $B_{\varphi,SM}/B_{z,SM}$. The behavior of $\xi(\mu)$ in this intermediate regime is now inverted, and increasing ξ leads to a decrease in μ.

On the contrary, at high ejection index and low-μ the toroidal magnetic field becomes too strong and needs to decreases for Eq. (3.50) to be respected. This leads to an extremum in the behavior of the toroidal magnetic field (Fig. 3.15), clearly seen for $n = 2$ and $n = 3$. The extremum can also be discerned in Fig. (3.14) for $n = 3$ and $\xi \simeq 0.1$, $\xi(\mu)$ is reaching another extremum and changing its behavior for the second time. We see that the toroidal magnetic field is modifying the dependency of the ejection index on the magnetization.

As discussed above, we expect to fill in the islands between the solutions by changing the boundary values at the disk mid-plane. Nevertheless, the general contour of the parameter space should not be modified by the discovery of these new solutions, namely the upper and lower contours $\xi_{\text{min}}(\mu)$ and $\xi_{\text{max}}(\mu)$ should not be modified.

It can be seen that, the minimum ejection index increases when the magnetization decreases. This is a fossil feature of the super SM parameter space (Fig. 3.3). As the magnetization decreases the toroidal magnetic field increases and dominates the acceleration, this leads to a stronger vertical acceleration and ”magnetic tower” like solutions, that live at small μ and have in general a higher ejection index. The terminal velocity of the outflow is going to be linked to the value of λ which is a function of ξ. The maximal velocity achievable in our fiducial parameter space is a function of only the disk magnetization μ.

The maximum ejection index, ξ_{max} is determined by the Alfvénic constraint. It is interesting that it has a non-monotonous behavior (Fig. 3.14), first increasing with μ until its maximum value 0.35 for $n = 2$ and then decreasing down to 0.08 for $n = 0$. As illustrated in Fig. 3.7, increasing ξ leads to a decrease in λ. Low values of λ are possible only for large values of κ, which are accessible only by decreasing μ. As a consequence, the Alfvén surface comes closer to the disk (z_A/R_A) decreases as ξ increases, see Fig. (3.11). However, if we keep decreasing μ, the magnetic energy available in the outflow becomes also smaller and the acceleration less efficient. The Alfvén surface moves away from the disk (z_A/R_A) increases as ξ increases), requiring thereby a larger magnetic lever arm λ to get super-A flows so that ξ_{max} decreases. The behavior of ξ_{max} follow from the Alfvénic constraint discussed in the previous section.

3.4 General properties

Our fiducial parameter achieved a maximal value of $\xi = 0.35$ obtained with $n = 2$ for $\mu \sim 10^{-2}$, while the minimum value is 5×10^{-3} and is obtained with $n = 0$ for $\mu = 0.5$. Our calculations have been done for cold outflows (isothermal magnetic surfaces) only. Thermal effects may drastically enhance ξ (Casse and Ferreira 2000a). For cold outflows and for all turbulent transport parameters explored (α_m,χ_m) we found a minimum $\xi_{\text{min}} \simeq 5 \times 10^{-3}$ and a maximum $\xi_{\text{max}} \simeq 0.47$, with a clear tendency of reaching larger ξ with low-μ solutions. Contrary to previous near-equipartition solutions, cold massive outflows with $\xi \sim 0.1$ are possible, in our framework, as long as spatial oscillations are allowed. But super-A solutions with $\xi > 0.5$ remain out of range for cold solutions.

In this section we first explore the effect of the turbulence parameter α_m as well as the turbulence anisotropy χ_m on the borders of the parameter space. We will then explore the accretion velocity of the system that determines its secular evolution. Finally, we will try to properly define what we mean by wind or jet and under which category are our solutions placed.

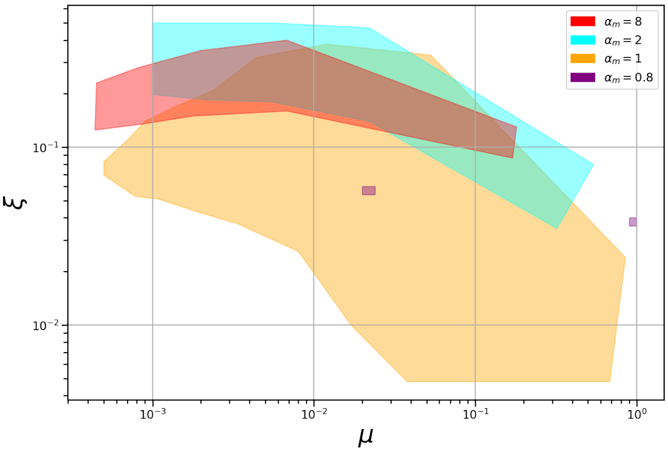

Figure 3.16: Effect of the MHD turbulence level α_m on the parameter space of super-A flows for $\varepsilon = 0.1, \chi_m = 1, \mathcal{P}_m = 1$. Only the contours of the parameter spaces are shown. Note that α_m affects all three coefficients (ν_v, ν_m, ν_m').

3.4.1 The influence of the level of turbulence α_m

Figure 3.16 shows that α_m has a dramatic impact on the structure of the parameter space. We notice two important trends

- Increasing the turbulence level above unity does not considerably modify the curve of ξ_{max}. On the contrary the curve ξ_{min} is raised drastically leading to a shrinking of the parameter space. Furthermore, as α_m increases, solutions of same ξ are displaced to smaller μ. We did not explore values of α_m larger than 8 because they were not consistent with the scaling measured in shearing box simulations (Salvesen et al. 2016).

- When the level of turbulence decreases below 1 the extent of the parameter space is greatly reduced. For $\alpha_m = 0.8$ we were only able to find two family of solutions, one with $n = 0$ and the other with $n = 3$. The fact that the parameter space reduces considerably when $\alpha_m < 1$ has already being reported in Ferreira and Pelletier 1995 and Ferreira 1997.

The fact that when α_m increases solutions are displaced to smaller magnetizations can be understood from the SM constraint (Eq. 3.32), that reads

$$\alpha_m^2 \mu = F_{SM}^2(x) \frac{1}{1 + \left(\frac{B_{R,SM}}{B_{Z0}}\right)^2 + \left(\frac{B_{\varphi,SM}}{B_{Z0}}\right)^2}. \tag{3.51}$$

For Eq. (3.32) to stay unmodified when we increase α_m the magnetization needs to decrease so that $\mu\alpha_m^2$ stays approximately constant. The drastic diminution of the parameter space when α_m is increased can be related to the change of sign of the electric current at the disk surface.

As we saw in section 2.5.3, for the outflow to escape the accretion disk, the radial current needs to change sign (the toroidal magnetic field needs to reach a maximum value) close to the disk surface. The change of sign of the radial current imposes certain constraints on the turbulent transport coefficients.

To derive those constraints, we start from Eq. (2.152) that we rewrite here in the notation of Ferreira and Pelletier 1995

$$J_R(z) \simeq J_R(z=0) \frac{\eta_m'(z=0)}{\eta_m'(z)} \left[1 - \frac{3}{2} \frac{\Omega_K}{\eta_m'(z=0) J_R(z=0)} \int_0^z \mathrm{d}z B_R \right], \tag{3.52}$$

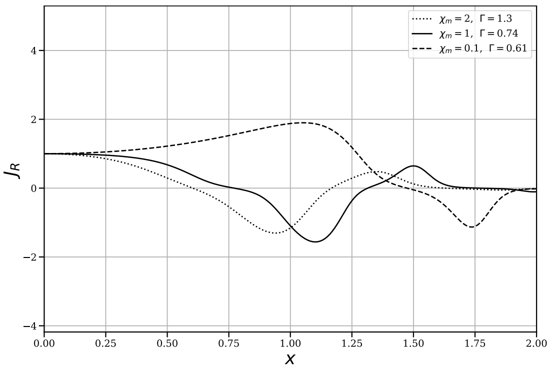

Figure 3.17: Vertical profiles of the radial electric current density J_R (normalized to J_{Ro}) for different values of χ_m and $\Gamma = 1.3, 0.74, 0.62$. These super-SM solutions were calculated with $\mu \sim 2 \times 10^{-2}$, $\xi = 0.4$ and $\alpha_m = \mathcal{P}_m = 1$.

if we assume that the radial magnetic field can be written as

$$B_R \simeq p B_{z0} \frac{z}{h} \tag{3.53}$$

close to the disk we simplify Eq. (3.52) into

$$\eta'_m(x) J_R = \eta'_{mo} J_{R0} \left(1 - \Gamma x^2\right) \quad \text{with} \quad \Gamma = \frac{3}{2} \frac{\chi_m}{\alpha_m^2} \frac{p}{p - \mathcal{P}_m \varepsilon}. \tag{3.54}$$

In the absence of any shear (rigid rotation), one would have $\eta'_m J_R = \eta'_{mo} J_{R0}$. The vertical profile of the radial current would only depend on the vertical profile of $\eta'_m(x)$. The differential rotation is therefore counteracting the radial current flowing at the disk mid-plane, J_{R0}. It is crucial to change the sign of the current towards the axis. The change of sign of the current is then related to the acceleration of the outflow as discussed in section 2.5.3. The change of sign of the current will be challenged by the vertical decrease of the turbulent diffusivity η'_m. If $\Gamma > 1$, J_R is going to quickly tend to zero, despite the decrease of η'_m. On the contrary, if $\Gamma < 1$, J_R is going to level off or reach a maximum before decreasing at a higher altitude.

We can clearly see this trend in Fig. (3.17), where different values of Γ have been obtained by varying χ_m. Furthermore, we see that for $\Gamma = 0.61$ the profile of the current increases before changing sign. This is due to the vertical profile of η'_m, we see in Eq. (3.54) that if $\eta'_m(x) \propto e^{-x^2} \simeq (1 - x^2)$ decreases faster than $(1 - \Gamma x^2)$ the radial current is forced to increase before changing sign. Hence, it is a consequence of $\Gamma < 1$. In our approach, Γ is not a free parameter and will be determined by the turbulent transport coefficients α_m, χ_m, and $\mathcal{P}_m$.

Figure 3.17 shows that the vertical profiles of the radial current are far more complex than the simple model in Eq. (3.54), in particular, the profiles of J_R show channel mode oscillations. Hence, the purpose of Eq. (3.54) is to provide us intuition on the dynamics of the system and not to give an accurate fit of J_R. Nonetheless, the fact that the profiles shown in Fig. (3.17) change sign as expected, solutions with larger Γ changing sign at a smaller x_j, gives credence to Eq. (3.54).

As argued above and in section 2.5.3 we need the acceleration to start around the disk surface. Hence, the position where the radial current changes sign x_J needs to be of the order of 1. This requires therefore Γ to also be of order unity. Assuming $\Gamma \sim 1$ leads to $\chi_m \sim \alpha_m^2$ which provides $\eta'_m \sim \alpha_m^{-1} V_A h$. This estimate is but an optimal case, solutions can be found for $\Gamma \neq 1$ even a bit larger than 1.

Ejection can only be achieved when

$$\Gamma = \frac{3}{2}\frac{\chi_m}{\alpha_m^2}\frac{p}{p-\mathcal{P}_m\varepsilon} \simeq 1, \tag{3.55}$$

where Γ controls the vertical scale of the turbulent emf $\eta'_m J_R$. We verify that this is true for all our super Alfvénic solutions, we measure $\Gamma \in [0.5, 3]$ which gives credence to our constraint. Hence, If p is of order unity, for the toroidal current density (controlled by p) to adapt to the constraint imposed by Eq. (3.32) implies that $p \sim \chi_m/\alpha_m^2$. Thus when α_m increases p needs to decrease. Since p controls the outflow opening angle (Fig. 3.12), a decrease in p leads to a decrease of magnetic vertical compression, thus to a larger mass loss rate from the disk. This feedback on the disk vertical equilibrium explains why $\xi_{\min}(\mu)$ increases when α_m increases.

In order to keep Γ near unity, as α_m increases one gets $p \rightarrow p_{\min} = \mathcal{P}_m\varepsilon$ which could be very small. This might be an indication that, for larger values of α_m, the MHD solution would eventually try to reverse the sign of the accretion speed, with an outward motion at the disk mid plane ($u_r > 0$ and $J_\varphi < 0$). Such a situation, seen in numerical simulations, is actually forbidden by our assumed boundary condition. This is a general bias that has been discussed previously.

When α_m decreases p increases, this will quickly lead to Γ becoming larger than unity since $\frac{p}{p-\mathcal{P}_m\varepsilon} \leq 1$, tthe ratio $p/(p-p_{\min})$ is bounded by 1. The magnetic diffusivity is now too strong, the generation of the toroidal field becomes inefficient and the torque F_φ remains negative, the magnetic acceleration is suppressed. As a consequence most solutions vanish and the parameter space is greatly reduced.

In contrast, when α_m increases, solutions with Γ of order unity require $p \rightarrow p_{\min}$, with $p_{\min} = \mathcal{P}_m\varepsilon$. Rather large values of α_m are thus allowed since the ratio $p/(p-p_{\min})$ can be very large. The parameter space is not constrained by the Eq.(3.54) in this case.

3.4.2 The influence of the anisotropy of turbulence χ_m

The effect of turbulent anisotropy, χ_m on the the super Alfvén parameter space is very similar to the one of α_m. In Figure 3.18 we show that when $\chi_m > 1$ the extent of the parameter space is reduced considerably. Indeed, For $\chi_m = 2$ and for $\alpha_m = 0.8$ we find the same kind of behavior, namely only two sets of separated solutions, one at $n = 0$ and the other at $n = 3$. Above this value of χ_m we find no super Alfvénic solutions.

Increasing χ_m leads to the same behavior as decreasing α_m, it leads to the increase of p, this quickly increases Γ that becomes larger than unity. When Γ is larger than unity the acceleration becomes inefficient and it is impossible to launch outflows.

Decreasing χ_m has a less pronounced effect than increasing α_m. This is due to the fact that the latter is controlling all magnetic field components while the former only affects the toroidal field. Furthermore, we do not see the strong shift to lower magnetizations as we increased α_m, this is to be expected as χ_m does not play a role in the SM constraint (Eq. 3.32). A value $\chi_m < 1$ corresponds to a stronger diffusion of the toroidal magnetic field wrt to the poloidal field. The parameter space for $\chi_m = 0.1$ is mostly unmodified when compared with the fiducial case. However, $\chi_m = 0.01$ leads to a reduced parameter space, the parameter space shifts to lower μ and has a smaller $\xi_{\max}$. A magnetic shear $|B_\varphi/B_z|$ too large produces a strong vertical pinch so that solutions need to exist at low μ and small ejection index. Near equipartition solution become now impossible.

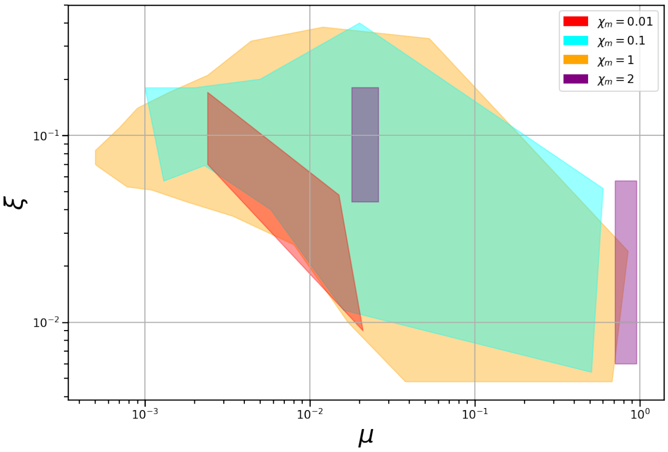

Figure 3.18: Effect of the anisotropy χ_m of the turbulent magnetic diffusivity on the parameter space of super-A flows for $\varepsilon = 0.1, \alpha_m = 1, \mathcal{P}_m = 1$.

3.4.3 Accretion velocity

The accretion Mach number is defined as $m_s = u_{R0}/c_s$, where u_{R0} is the radial accretion velocity due to turbulent and laminar torques. As we saw before the accretion Mach (Eq> 3.27) number can be related to the disk parameters like so

$$m_s = p\alpha_m \mu^{1/2}. \tag{3.56}$$

Since p covers a small range, we deduce that $m_s \propto \mu^{1/2}$ whatever the dominant torque. Hence, supersonic accretion ($m_s > 1$) can only be achieved for near equipartition solutions. Such a high accretion speed has profound consequences: it may lead to optically thin accretion disks with observable features in young stellar objects (Combet and Ferreira 2008; Combet et al. 2010) or X-ray Binaries (Marcel et al. 2018b). Since our solutions are prone to oscillations (Fig. 3.5) it is not obvious that all the accretion is concentrated at the disk mid-plane for $n \neq 0$. To verify that the only solutions capable of super-sonic accretion are the ones that have $n = 0$ we compute the mass weighted accretion velocity

$$\tilde{m}_s = \frac{\dot{M}_a}{2\pi R c_s \Sigma} = \frac{-1}{C_s} \frac{\int_0^{x_{SM}} u_R \rho \, \mathrm{d}x}{\int_0^{x_{SM}} \rho \, \mathrm{d}x}, \tag{3.57}$$

from the disk mid plane up to the SM point. We compute $\tilde{m}_s$ for all solutions found, and find $\tilde{m}_s$ is never larger than m_s by more than a factor of 3. This may seem surprising, but the spatial oscillations compensate each other leading to very little differences. We show the mass weighted accretion velocity normalized to the sonic speed for the fiducial parameter as well as for $\alpha_m = 8$ in Fig. (3.19). We can see that the only solutions capable of supersonic accretion are the near equipartition solutions for the fiducial parameter space. We also see in Fig. (3.19) that for the same value of n the mass weighted accretion, $\tilde{m}_s$, is smaller if $\alpha_m = 8$. Although Eq. (3.27) seems to imply the opposite, $m_s \propto \alpha_m$, this is a consequence of the radial current constraint. Indeed, $\Gamma \sim 1$ requires $p \sim 1/\alpha_m^2$ which leads to $m_s \propto 1/\alpha_m$. Hence, $\tilde{m}_s$ decreases when the level of turbulence, α_m, increases.

3.4.4 From winds to jets

Accretion is due to the vertical and radial torques acting on the accretion disk. To understand which torque (radial or vertical) is the dominant mode of angular momentum transport we com-

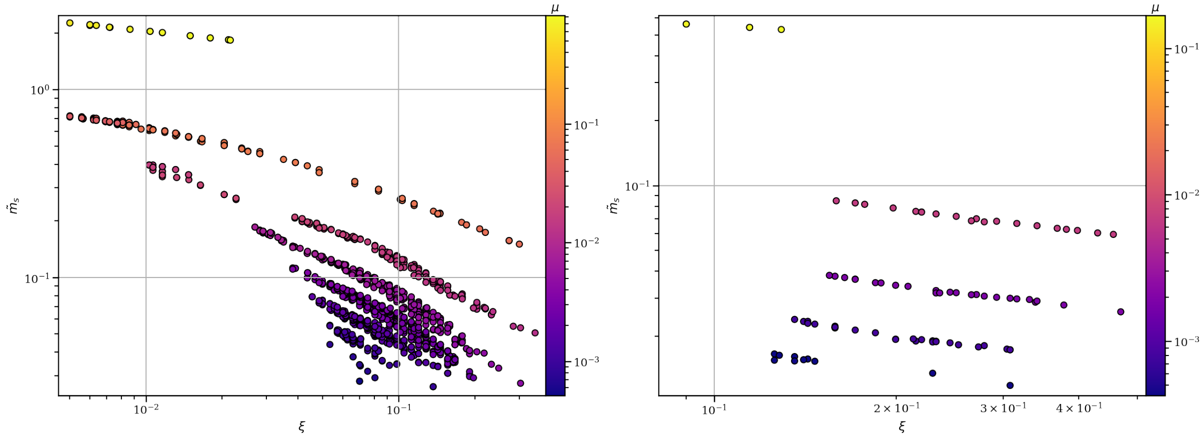

Figure 3.19: Mass weighted accretion mach number $\tilde{m}_s$ computed using Eq. (3.57) obtained with $\varepsilon = 0.1, \mathcal{P}_m = \chi_m = 1$ and $\alpha_m = 1$ (left), $\alpha_m = 8$ (right). Every point represents a super Alfvénic solution and the color is the disk magnetization μ.

pute $\Lambda = \frac{M_{z\varphi}}{M_{R\varphi}}$ (defined in section 2.3.2) the ratio of the vertical laminar torque to the radial (laminar and turbulent) torques acting on the disk. The different torques can be analytically estimated as

$$\left.\frac{4\pi}{RB_z^2}\right|_{SM} M_{z\varphi} \simeq b(\xi)\mu^{-1/2}, \tag{3.58}$$

$$\left.\frac{4\pi}{RB_z^2}\right|_{SM} M_{R\varphi,la} \simeq b(\xi)\mu^{-1/2} \left.\frac{B_R}{B_z}\right|_{SM} \varepsilon, \tag{3.59}$$

$$\left.\frac{4\pi}{RB_z^2}\right|_{SM} M_{R\varphi,tu} \simeq \alpha_v \frac{\varepsilon}{\mu} = \varepsilon \alpha_m \mathcal{P}_m \mu^{-1/2}, \tag{3.60}$$

where we define

$$b(\xi) = \mu^{1/2} \left|\frac{B_\varphi}{B_z}\right|_{SM} \simeq o(1), \tag{3.61}$$

to easily take into account the dependence of the toroidal field on the disk ejection index (Fig. 3.15). Putting everything together we get

$$\Lambda \simeq \frac{1}{\varepsilon} \frac{b}{b \left.\frac{B_R}{B_z}\right|_{SM} + \alpha_m \mathcal{P}_m}, \tag{3.62}$$

this equation is a generalization of Eq. (52) in Casse and Ferreira 2000b, we distinguish two limits:

- If the initial outflow opening angle is small (or the level of turbulence is large) $\left.\frac{B_R}{B_z}\right|_{SM} \ll \alpha_m \mathcal{P}_m \varepsilon$, which coincides with large ejection indexes ($\xi \sim 0.3$), we get

  $$\Lambda \sim \frac{b(\xi)}{\alpha_m \mathcal{P}_m \varepsilon}. \tag{3.63}$$

  In this limit $\Lambda(\xi)$ follows the dependency of the toroidal magnetic field on ξ, see Fig. (3.15), when ξ increases Λ decreases. In the cold $n = 0$ limit $\Lambda \sim 1/\varepsilon$.

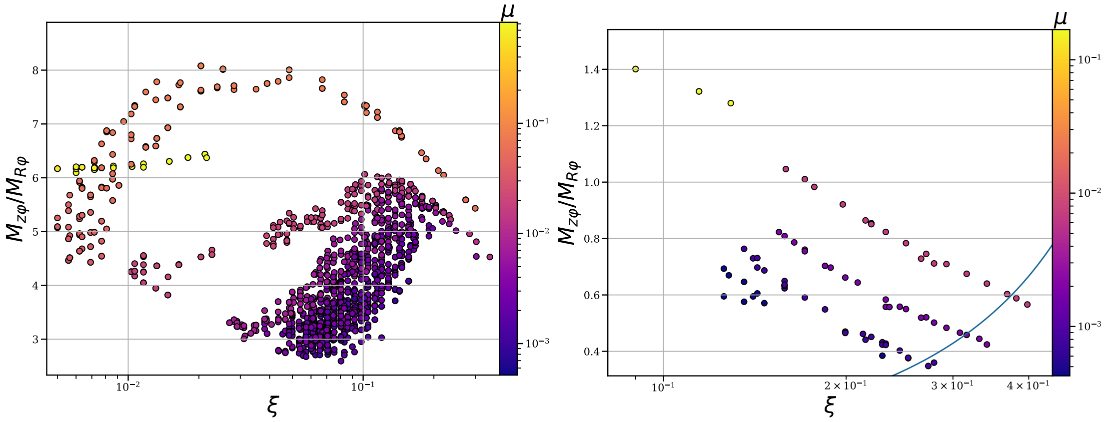

Figure 3.20: Ratio $\Lambda = M_{z\varphi}/M_{R\varphi}$ of the vertical stress $M_{z\varphi}$ to the radial stresses $M_{R\varphi}$ acting on the disk for solutions obtained with $\varepsilon = 0.1, \mathcal{P}_m = \chi_m = 1$ and $\alpha_m = 1$ (left), $\alpha_m = 8$ (right). Every point represents a super Alfvénic solution and the color is the disk magnetization μ. The non monotonous behavior with ξ and α_m is a consequence of the complex feedback of α_m on B_R and B_φ and the associated laminar torques (see text). The blue solid line on the right panel is the $\sigma = 1$ contour, defined in Eq. (3.65). All solutions located above it display $\sigma > 1$ (this is the case for all solutions on the left panel).

- If the initial outflow opening angle is large (or the level of turbulence is small) $\left.\frac{B_R}{B_z}\right|_{SM} \gg \alpha_m \mathcal{P}_m \varepsilon$, which coincides with small ejection indexes ($\xi \ll 1$), we get

$$\Lambda \sim \frac{1}{\varepsilon \left.\frac{B_R}{B_z}\right|_{SM}}. \tag{3.64}$$

  In this limit $\Lambda(\xi)$ follows the dependency of the radial magnetic field on ξ, see Fig. (3.12), when ξ increases Λ increases.

Fig. (3.20) shows that Λ is only weakly dependent on the magnetization, consistent with Eq. (3.62). We also see that Λ decreases strongly when the level of turbulence increases, also consistent with Eq. (3.62). For $\alpha_m = 1$, (left) Fig. (3.20), we distinguish an extremum in the dependence of Λ as a function of the ejection index, clearly visible for $n = 1$. This can be understood using our estimates above. Indeed, when $\xi \ll 1$ we are in the second limit (Eq. 3.64), the radial laminar torque dominates. This radial laminar torques is the result of strong spatial oscillation within the resistive disk, the channel modes. The radial laminar torque follows the same dependency as $(\left.\frac{B_R}{B_z}\right|_{SM})^{-1}$, this leads to an increasing Λ when ξ increases. However, at a certain critical ξ the radial laminar torque becomes smaller than the turbulent torque. Since the turbulent torque is independent of ξ, Λ now follows the dependency of the toroidal magnetic field, the first limit given by Eq. (3.63) and Λ decreases when ξ increases (Fig. 3.15).

In the case of $\alpha_m = 8$ the radial laminar torque is never stronger than the turbulent torque we only recover the first limit (Eq. 3.63). Furthermore, in the case of $\alpha_m = 8$ the turbulent torque is even stronger than the vertical laminar torque, this leads to a disk where most of the angular momentum is transported radially (contrary to Ferreira 1997).

As Λ decreases the function $K = \Lambda/(\Lambda + 1)$ starts deviating considerably from $K \sim C^{te}$, when this happens the relation $\lambda \simeq 1 + K/(2\xi)$ stops being a reliable way to estimate ξ from λ. Indeed, as K will depend on ξ we would need to take into account this dependence to find ξ as a function of λ. In Fig. (3.21) we show that, for $\alpha_m = 8$, $\lambda(\xi)$ deviates by about 50% from the

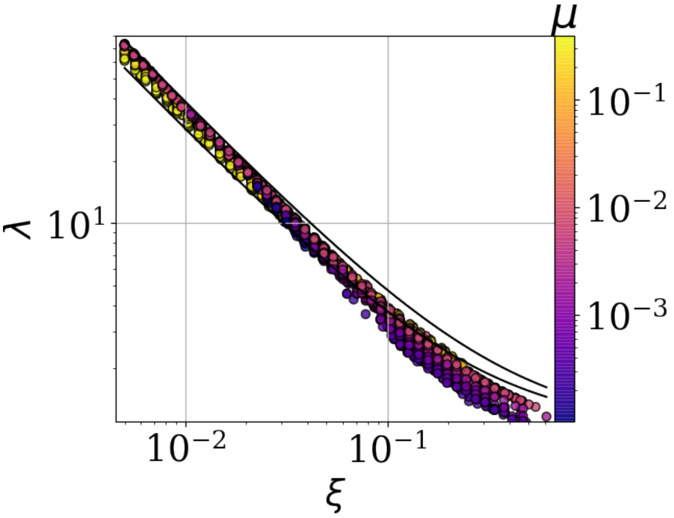

Figure 3.21: Magnetic lever arm parameter λ calculated using Eq.(2.119) as a function of ξ for all super-SM solutions appearing in Fig. 3.3. The solid lines correspond to curves $\lambda = 1 + \frac{K}{2\xi}$, computed using either $K = 1$ (top) or $K = 0.6$ (bottom).

curves calculated with $K = 0.6$ and $K = 1.0$. It is thus more problematic to derive ξ directly from the outflow asymptotic speed in the case of high-α_m outflows.

We have not yet tried to distinguish which of our outflows are winds and which of them are jets. A clear distinction between MHD winds and jets, which are both super-A MHD flows can be made. Defining the initial jet magnetization σ as the ratio of the MHD poloidal Poynting flux to the kinetic plus thermal (enthalpy) energy flux (measure at the base of the outflow) leads to the general useful relation for cold outflows

$$\sigma = \left. \frac{-\Omega_* r B_\varphi B_p}{\left(\frac{u^2}{2} + H\right) \rho u_p \mu_o} \right|_{SM} \simeq 2\omega(\lambda - 1) \simeq \frac{\omega}{\xi} \frac{\Lambda}{1 + \Lambda}. \tag{3.65}$$

Jets can be characterized by high speeds (high λ), they are also self-confined thanks to the dominant hoop stress, the hoop stress is stronger than the pressure gradient and the centrifugal force. Jets are therefore Poynting flux dominated flow with $\sigma > 1$. On the other hand, winds are low speed MHD flows with small λ, with almost no collimation besides the one introduced by the external pressure. Winds are therefore matter dominated outflows with $\sigma < 1$.

In Fig. (3.20) we have plotted the contour for $\sigma = 1$, computed using $\omega = 1$. All solutions obtained with $\alpha_m = 1$ (left) are jet like solutions as they are well above this contour ($\sigma > 1$). In Fig. (3.22) we show the magnetic surfaces for the two solutions displayed in Fig. (3.5). Even though these two solutions have low magnetizations they display very similar behaviors to the near-equipartition solutions (Ferreira 1997): the magnetic surfaces widen before recollimating towards the axis.

Figure 3.20 also reveals some solutions that cross the $\sigma = 1$ contour, wind-like outflows at $\alpha_m = 8$ and low magnetization. These solution have a magnetic lever arm very close to the minimal value of 3/2 and reach $\sigma = 1$ because ξ is large and Λ is small. Even though these solutions cross the Alfvén point, they then encounter pretty soon the modified fast magneto sonic (FM) surface, and stop. However, according to Ferreira and Casse 2004, for a solution to become super FM the outflow energy equations needs to be taken into account, this is not done in this work as we only compute isothermal outflows. Moreover, since the outflow have $\lambda \simeq 3/2$, they are exhausted once they cross the Alfvén surface, and heating could be quintessential in

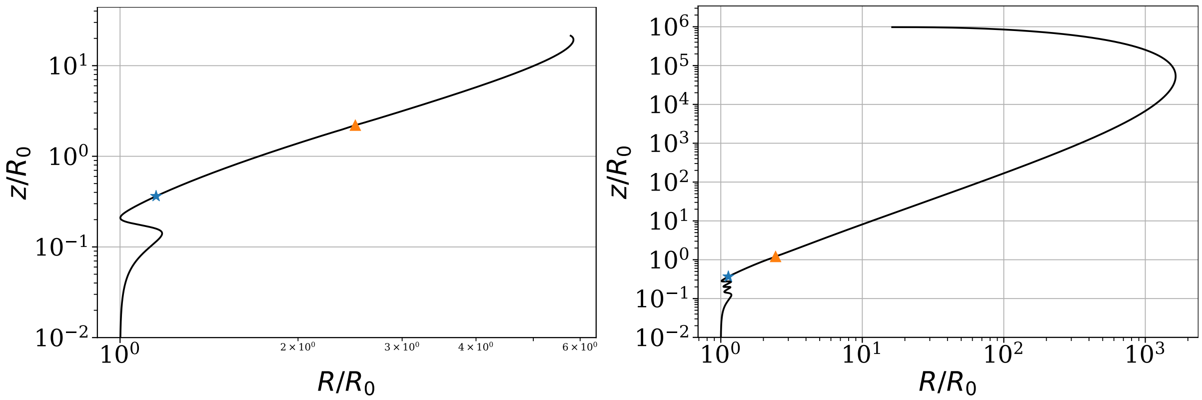

Figure 3.22: Shape of the poloidal magnetic surfaces for the two weakly magnetized solutions presented in Fig. 3.4, both having $\xi = 0.1$. Left: solution with $\mu = 6.7\,10^{-2}$ and $n = 1$ spatial oscillation. right: solution with $\mu = 5.7\,10^{-3}$ and $n = 3$. The SM point is marked by a blue star and the Alfvén point with a red triangle. Both jet solutions open up before recollimating towards the axis.

energizing these exhausted outflows (Casse and Ferreira 2000a). Our guess is therefore that warm low μ solutions obtained with $\alpha_m = 8$ will provide proper MHD wind solutions. This is postponed to future work.

The definition of σ already implies that only outflows with magnetic lever arm values close to the minimum value of $3/2$ could be categorized as wind like outflows. This would be consistent with observations of molecular outflows (Louvet et al. 2018; de-Valon et al. 2020). Nonetheless, recent self-similar solutions of non-ideal MHD outflows show that it is possible to obtain super FM solutions with $\lambda \simeq 3/2$ without any heating (Lesur 2021). They also show that those solutions are very dense and recollimate towards the axis. They exhibit a mix of jet-like and wind-like behavior. Recollimating outflow are also observed in 3D global simulation (Zhu and Stone 2018; Riols et al. 2020; Jacquemin-Ide et al. 2021). It remains unclear if recollimation is an intrinsic property of MHD-driven outflow or if it is the consequence of a bias:

- In the self-similar framework recollimation could be the consequence of a not understood bias in the self-similar ansatz. However, Contopoulos and Lovelace 1994 have computed self-similar solution that do not recollimate towards the axis by playing with the radial distribution of the magnetic field. They find that it is possible to produce conical outflows by reaching a certain value of the power law exponent. This value is equivalent to $\xi > 0.5$ in our framework. In our work we are unable to reach such high values.

- In 3D global simulations recollimation could be the consequence of a numerical bias. The boundary conditions at the vertical axis could be unphysical. Maybe the lack of an internal outflow launched by the central object is at fault. Furthermore, 3D numerical simulation need unphysical density floors close to the axis to deal with runaway magnetizations in those regions.

In short the recollimation of MHD driven outflow is still not understood and deserves further analysis.

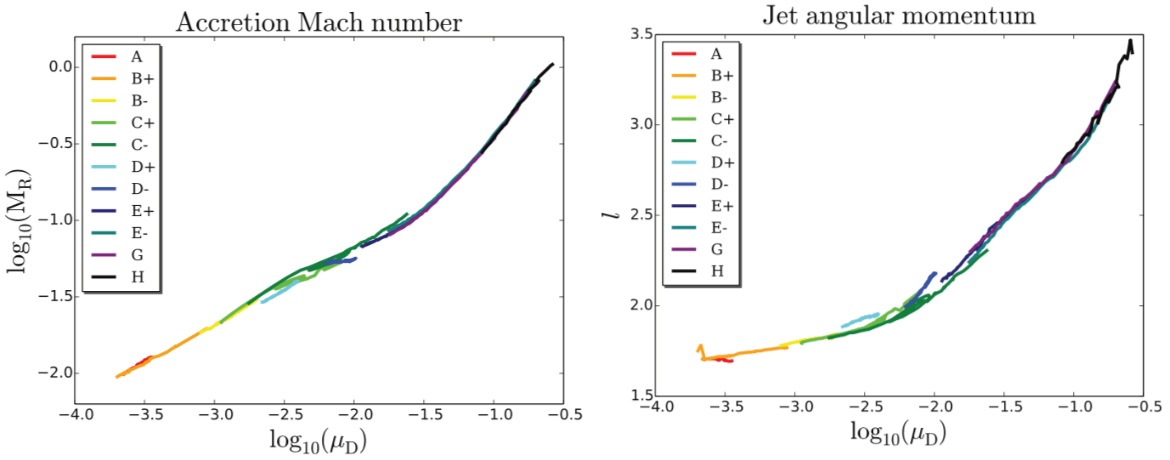

Figure 3.23: (Left) Logarithm of the averaged mach number at the disk mid plane as a function of the magnetization (their μ_D is equivalent to our μ), M_R is equivalent to our $\tilde{m}_s$. Adapted from Stepanovs and Fendt 2016. (Right) Normalized angular momentum invariant as a function of the magnetization (their l is equivalent to our λ).Adapted from Stepanovs and Fendt 2016.

3.5 Comparison with other work

The first paper showing the existence of super-A outflows flows from low magnetized accretion disks in 2.5D simulations was Murphy et al. 2010. Their work was then extended by a large numerical survey in μ done by Stepanovs and Fendt 2016, both authors used $\varepsilon = 0.1$. However, while Murphy et al. 2010 included viscosity with $\alpha_v = 0.9$ (all stress components), Stepanovs and Fendt 2016 neglected it. They effectively have $\mathcal{P}_m = 0$, the disk angular momentum removal is only done by the laminar torque. In terms of magnetic diffusivity, Murphy et al. 2010 used $\chi_m = 1$ and α_m starting from 20 and increasing with the radius as μ decreases. While Stepanovs and Fendt 2016 used $\chi_m = 2, \alpha_m \simeq 3$ and a constant μ across the accretion disk. Nevertheless, super-A jets were found by both authors with μ as low as 10^{-4}.

In Fig. (3.23) we show the dependences in μ of the MHD invariants λ as well as the accretion Mach number m_s computed in Stepanovs and Fendt 2016 (Left). We recognize that they recover the same scaling for the accretion Mach number, namely $m_s \propto \mu^{1/2}$ at low magnetizations. This scaling seems to be independent of viscosity at low magnetization as it is neglected in their work. Moreover, they also recover the same behavior as us for the magnetic lever arm, λ, namely as the magnetization decreases the magnetic lever arm tends to decrease (see Fig. (3.13)). The solutions with small μ tend to have a lower mass ejection index and therefore a higher λ. Moreover, they find a similar scaling for $|B_\varphi/B_R|$ which has lead them to deduce a dichotomy between the magnetic tower and magneto-centrifugal solutions, with a critical magnetization $\mu \simeq 0.01$ separating them. This is also consistent with our work, even though we find that a proper differentiation between solutions should also include the disk ejection efficiency ξ (our Fig. 3.14).

However, Stepanovs and Fendt 2016 have a Bernoulli invariant that diverges considerably from the analytical value of cold outflows ($\frac{e}{2} = \lambda - 3/2$), see Fig. (3.24). This figure shows that some heating is applied to the outflows leading to an enhanced value of e for the same value of λ, $\frac{e}{2} = \lambda - 3/2 + \Theta/2$. This makes it difficult to compare our values of the ejection index to the ones derived in their work as their values will be larger due to the presence of heating (Casse and Ferreira 2000a).

Lesur 2021 explore the parameter space of self-similar protoplanetary disk accretion ejection

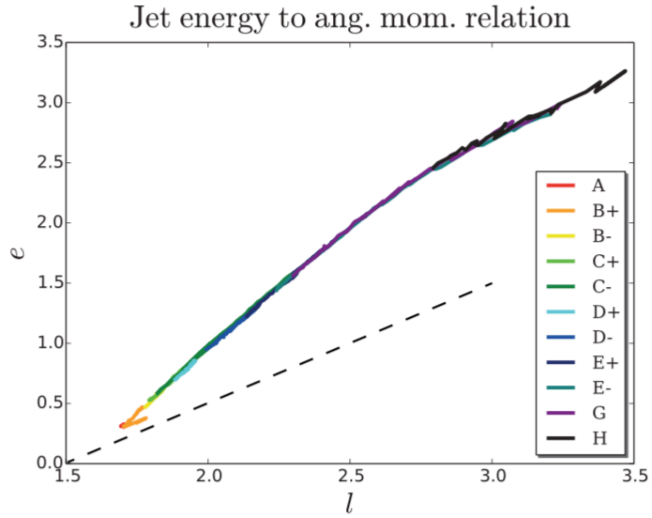

Figure 3.24: Normalized Bernoulli invariant, e, as a function of the angular momentum invariant l (which corresponds to our λ). Adapted from Stepanovs and Fendt 2016 they define their e as half our e.

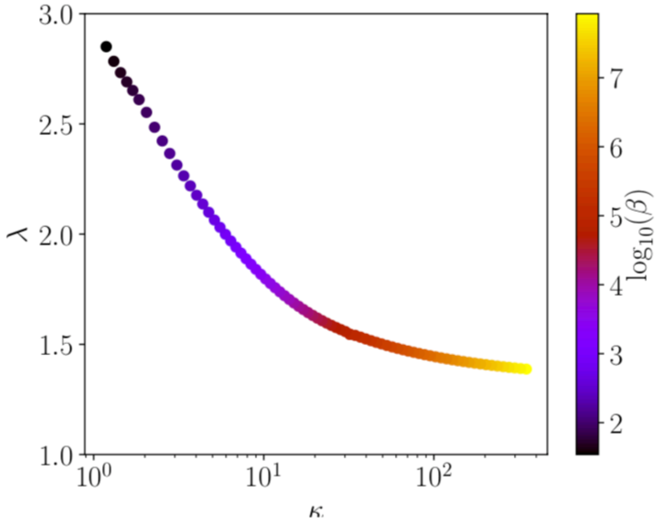

Figure 3.25: Projection on the $\kappa - \lambda$ plane of all the super fast magneto sonic solutions. Figure adapted from Lesur 2021.

solutions. Even though they also compute self-similar solutions, they do not compute purely stationary solutions, they solve the time dependent equations until the solution stabilizes into a steady state. Contrary to our work this allows them to calculate the transport velocity of the magnetic field, v_Ψ. They include the effects of ambipolar diffusion and ohmic resistive due to the low ionization in protoplanetary disks. This leads to different generalized Ohms laws, the form of Eq. (3.5) changes. Furthermore, they do not include a turbulent resistivity, since MRI would be quenched by ambipolar diffusion (Bai and Stone 2011).

We see in Fig. (3.25) that as the plasma beta increases (μ decreases) the magnetic lever arm decreases and κ increases, this trend is consistent with the one found in our models (Fig.3.13). They find similar lower values for λ for weakly magnetized solutions, they reach the theoretical limit of $3/2$, but larger values of κ of the order of 100. It is unclear if this a consequence of the different induction equation. It seems that non-ideal effects facilitate the launch of massive outflows. Note that the non-ideal region extends up to $5h$, which could facilitate the launching of massive outflows (Lesur 2021).

They report that all the solutions computed in their work recollimate towards the axis. We expect wind-like outflow to follow a conical trajectory that would be coherent with observations. The absence of a conical trajectory could be a bias of the self-similar framework. There seems to be no dichotomy in the asymptotic behavior of MHD-driven outflows, no clear distinction between jets and winds from a theoretical point of view. The reason why wind-like conical outflows are hard to obtain in an MHD framework remains hard to grasp.

The values of the mass ejection index they compute are also consistent with wind-like outflows, $\xi_{\text{computed}} > 0.4$, not to be confused with the radial scaling of self-similar solutions $\dot{M}_a \propto R^{\xi}$. One should be cautious with the definition of ξ in their solutions, as ξ is set to 0 in all their radial self-similar dependencies. In our solutions, ξ is not only related to the mass ejection but also dictates the radial scaling of the magnetic field,

$$B_z \propto R^{-\frac{5}{4}+\frac{\xi}{2}}. \tag{3.66}$$

In contrast, their radial scalings follow the same dependency as Blandford and Payne 1982 ($\xi = 0$). This is not in contradiction with the wind-like outflow they compute, as their solutions are not strictly stationary. However, varying the parameter ξ to achieve $\xi = \xi_{\text{computed}}$ should be addressed in those kinds of models.

The scaling for the toroidal magnetic field derived in Lesur 2021 differs from our own, namely they find

$$\left.\frac{B_\varphi}{B_z}\right|_{SM} \simeq 2\mu^{-0.22}. \tag{3.67}$$

This inconsistency is probably the consequence of the different scaling of their magnetic diffusivity as a function of the magnetic field. Indeed, the ambipolar diffusivity scales as

$$\eta_A = \Lambda_A^{-1}\frac{V_{At}^2}{\Omega_K}, \tag{3.68}$$

where V_{At} is the total Alfvén velocity and Λ_A is a gaussian function of the self-similar coordinate. We can compute the scaling of the toroidal magnetic, in the case of a dominant ambipolar diffusivity, by following the argument detailed in section 3.3.1. We have

$$\left.\frac{\eta_A}{h}\right|_{SM} \sim V_{SM}|_{SM}, \tag{3.69}$$

the diffusion velocity is of the order of the slow magneto-sonic velocity at the slow point. We can approximate the slow magneto-sonic velocity in the following ways:

$$V_{SM}(z_{SM}) \simeq c_s \frac{V_{Az}}{V_{At}}\bigg|_{SM} \quad \text{for } c_s(z_{SM}) \ll V_{Az}(z_{SM}), \tag{3.70}$$

$$V_{SM}(z_{SM}) \simeq V_{Az}|_{SM} \quad \text{for } c_s(z_{SM}) \gg V_{Az}(z_{SM}), \tag{3.71}$$

where the first approximation is for strongly magnetized outflows (and is the one used in section 3.3.1) and the second approximation is for weakly magnetized outflows. The outflows computed in Lesur 2021 are mostly weakly magnetized, the values of κ calculated can be quite large ($\kappa \sim 100$). Using both approximations we compute

$$\frac{V_{At}^4}{c_s^4}\bigg|_{SM} \sim \frac{V_{Az}^2}{c_s^2} V_{At}^2\bigg|_{SM} \quad \text{for } c_s(z_{SM}) \ll V_{Az}(z_{SM}), \tag{3.72}$$

$$\frac{V_{At}^4}{c_s^4}\bigg|_{SM} \sim \frac{V_{Az}^2}{c_s^2}\bigg|_{SM} \quad \text{for } c_s(z_{SM}) \gg V_{Az}(z_{SM}). \tag{3.73}$$

From the previous equations we deduce

$$\left(1 + \left(\frac{B_R}{B_{z0}}\right)^2 + \left(\frac{B_\varphi}{B_{z0}}\right)^2\right)^3\Bigg|_{SM} \sim \frac{1}{\mu^2} \quad \text{for } c_s(z_{SM}) \ll V_{Az}(z_{SM}), \tag{3.74}$$

$$\left(1 + \left(\frac{B_R}{B_{z0}}\right)^2 + \left(\frac{B_\varphi}{B_{z0}}\right)^2\right)^2\Bigg|_{SM} \sim \frac{1}{\mu} \quad \text{for } c_s(z_{SM}) \gg V_{Az}(z_{SM}), \tag{3.75}$$

in the case of a dominant toroidal field this reduces to

$$\left|\frac{B_\varphi}{B_{z0}}\right|_{SM} \propto \mu^{-1/3} \quad \text{for } c_s(z_{SM}) \ll V_{Az}(z_{SM}), \tag{3.76}$$

$$\left|\frac{B_\varphi}{B_{z0}}\right|_{SM} \propto \mu^{-1/4} \quad \text{for } c_s(z_{SM}) \gg V_{Az}(z_{SM}). \tag{3.77}$$

Both scaling are similar to the one measured by Lesur 2021. In particular, the scaling derived using the weakly magnetized outflows approximation is off by only a few percent. This shows that the scaling of the toroidal magnetic field is indeed controlled by the slow magneto sonic constraint and the generalized Ohms law.

The work of Zhu and Stone 2018 but also Mishra et al. 2020 show that global 3D simulations that include mean vertical magnetic field reach a steady state where most of the accretion happens above the disk mid-plane. Indeed, in Fig. (3.26) we show the steady state of the simulations computed in Zhu and Stone 2018 for $\mu = 2 \times 10^{-4}$ and $\varepsilon = 0.1$. We see that the vertical structure of the flow is very different from the one found in self-similar solutions computed here (Fig. 3.5). Moreover, for accretion to take place so high up in the disk's atmosphere, turbulent resistivities must also be maintained up there. In figure 18 of Zhu and Stone 2018 they show that the resistivity and the viscosity vertical profiles they have computed are very different from the one we have implemented in our self-similar solutions. Indeed, while our profiles follow a Gaussian, decreasing as we leave the disk, the profile computed by Zhu and Stone 2018 increases as the height increases. As a consequence, the resistive disk survives at larger altitudes and ideal MHD ejection occurs only further up, decreasing thereby the disk mass loss ξ.

This new feature can be easily incorporated within the self-similar framework through the use of different vertical profiles for ν_v, η_m and η'_m. Note that enhanced diffusion at higher altitudes (due to parasitic instabilities such as Kelvin-Helmholtz) could smooth out the spatial

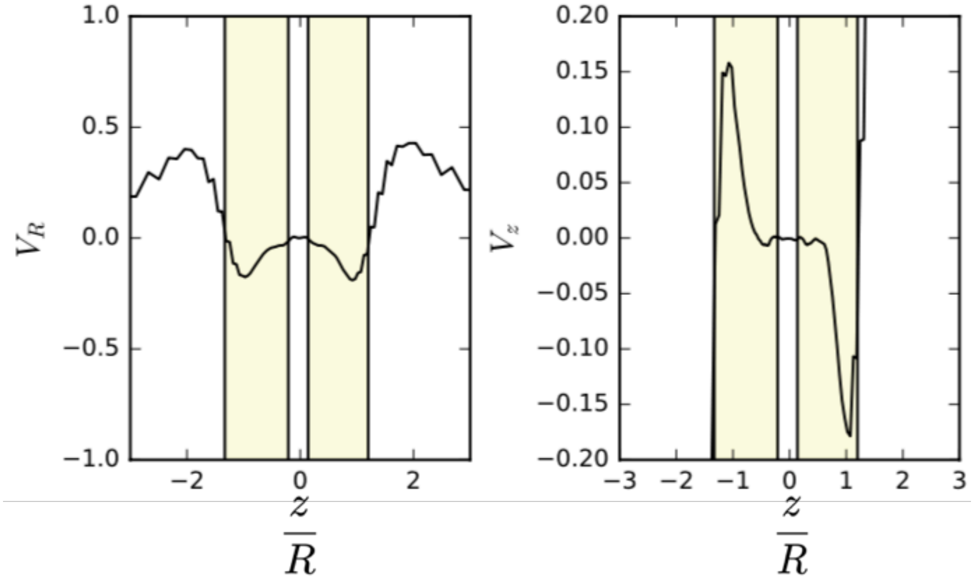

Figure 3.26: Radial and vertical velocities normalized to the Keplerian velocity at $R = 1$ as functions of the vertical variable for $R = 1$, adapted from Zhu and Stone 2018. Note the supersonic accretion flow at $z \sim R$ above the disk (since $\varepsilon = 0.1$).

oscillations, building up a magnetic configuration closer to the one obtained in 3D simulations.

As argued before, our choice of α_v, α_m and $\mathcal{P}_m$ were consistent with numerical studies of MRI turbulence and the way the stress (viscosity) scales with the initial magnetization μ (Salvesen et al. 2016 and references therein). We would like to stress however that knowledge on the turbulent diffusion of magnetic fields is scarce. Global simulations (Zhu and Stone 2018)) and shearing box studies (Fromang and Stone 2009; Guan and Gammie 2009; Lesur and Longaretti 2009) report an effective magnetic Prandtl number $\mathcal{P}_m$ of order unity, but this is far from being fully assessed. Besides, the anisotropy χ_m of MRI turbulence has been measured only in non stratified shearing box setups, i.e. a very idealized configuration. In section 5 we will measure the turbulent transport coefficients in 3D global numerical simulations to check if we are consistent with shearing box simulations.

Finally several terms from the Reynolds averaged equations have been ignored in this work (see section 2.3.1). In particular the pressure due to turbulent magnetic fluctuations $\left\langle \delta B^2 \right\rangle$. This term is known to strongly affect the disc vertical equilibrium (Salvesen et al. 2016) for $\mu \gtrsim 10^{-3}$, which could increase dramatically the disc thickness and therefore the quantitative predictions of our model. Indeed, in the next chapter we will show that the turbulent magnetic pressure has a considerable impact on the vertical structure of the accretion disk. We will further argue that it is the main agent behind the appearance of the elevated accretion structure. Then in chapter 5 we will compute a closure for the turbulent magnetic pressure that could be used in self-similar models.

CHAPTER 4

3D simulations of weakly and highly magnetized disks

4.1 Numerical method

4.1.1 Governing equations

In this chapter we compute and analyze 3D numerical simulations of magnetized accretion disks in the isothermal case. For the sake of completeness and simplicity we rewrite the ideal MHD equations that we solve

$$\frac{\partial \rho}{\partial t} + \nabla \cdot [\rho \mathbf{u}] = 0, \tag{4.1}$$

$$\rho \left(\frac{\partial \mathbf{u}}{\partial t} + (\mathbf{u} \cdot \nabla) \mathbf{u} \right) = -\nabla P + \rho \nabla \Phi_G + \frac{1}{c} \mathbf{J} \times \mathbf{B}, \tag{4.2}$$

$$\frac{\partial P}{\partial t} + \mathbf{u} \cdot \nabla P + \gamma P \nabla \cdot \mathbf{u} = -\Lambda_{\rm cool} \tag{4.3}$$

$$\frac{\partial \mathbf{B}}{\partial t} = \nabla \times [\mathbf{u} \times \mathbf{B}], \tag{4.4}$$

where γ, the heat capacity ratio, is fixed to 1.001 to facilitate an isothermal structure. To close Eq. (4.1-4.4), we assume an ideal equation of state.

The MRI feeds on the gravitational energy to create a turbulent state. The energy is then stored in the magnetic and kinetic turbulent fluctuations, where it can be exchanged between them. Ultimately, the energy is dissipated into heat. The disk scale height is determined by comparing the pressure gradient to gravity. It will therefore be affected by turbulent heating. In the absence of radiative losses, the disk scale height increases under the effect of heating. Since we focus here only on dynamical processes without specifying a particular astronomical object, we simplify the radiative (cooling) processes as much as possible.

The simplest choice would be to force a vertically isothermal structure at every time step. However, in the presence of a strict locally isothermal temperature profile the Vertical Shear Instability (VSI) will develop (Nelson et al. 2013). This is to be avoided since we do not want to study the influence of this instability on the accretion disk structure. Therefore, if cooling is applied instantly (at every time step) the VSI instability will also develop.

To avoid the development of the vertical shear instability we use a thermal relaxation method on a fixed time scale. We relax the temperature of our system on a time scale $\tau_{\rm cool}$, equal to 0.1 times the local Keplerian time scale. Hence, we prescribe a cooling function $\Lambda_{\rm cool}$, that allows us to relax our system to a locally isothermal temperature profile $T = T(R) \propto 1/R$. It has the following form

$$\Lambda_{\rm cool} = \frac{P - \rho c_s^2(R)}{\tau_{\rm cool}}, \tag{4.5}$$

where

$$\tau_{\rm cool} = 0.1 \frac{1}{\Omega_K(R)} \tag{4.6}$$

is the cooling time scale. Since the cooling time scale is short the cooling function dominates Eq. (4.3), this leads to an *effective* equation of state of the form

$$P = c_s^2(R) \rho, \tag{4.7}$$

where c_s is the local isothermal sound speed

$$c_s = h \Omega_K, \tag{4.8}$$

and h is the disk scale heigh.

4.1.2 Numerical method

To solve Eq. (4.1-4.7) on a spherical grid, we use the conservative Godunov-type code PLUTO (Mignone et al. 2007). A Godunov scheme is a conservative numerical scheme, where the fluxes

Name	$\mu_{\rm ini}$	ε	r domain	ϕ domain	Resolution	t_1	$t_2 = T_{\rm end}$
SB4	2×10^{-4}	0.1	$[1, 200]$	$[-\pi/4, \pi/4]$	[850,176L+64S,62]	$923T_{\rm in}$	$1114T_{\rm in}$
SB3	2×10^{-3}	0.1	$[1, 200]$	$[-\pi/4, \pi/4]$	[850,176L+64S,62]	$923T_{\rm in}$	$1114T_{\rm in}$
SB2	2×10^{-2}	0.1	$[1, 200]$	$[-\pi/4, \pi/4]$	[850,176L+64S,62]	$1719T_{\rm in}$	$1910T_{\rm in}$
SEp	2×10^{-4}	0.05	$[1, 100]$	$[-\pi/4, \pi/4]$	[1475, 96L+70S+2L, 62]	$923T_{\rm in}$	$1114T_{\rm in}$
S2pi	2×10^{-4}	0.1	$[1, 200]$	$[0, 2\pi]$	[850,176L+64S,256]	$923T_{\rm in}$	$1034T_{\rm in}$

Table 4.1: Parameters, grid spacing and radial extension of the simulations discussed in the paper. The latitudinal grid is not homogeneous, with grid spacing varying linearly (L) close to the disk and geometrically (S=stretched) close to the poles. We define $T_{\rm in} = T_K(R_{\rm in})$ where $T_K(R) = 2\pi/\Omega_K(R)$.

are computed by solving a Riemann problem at each inter-cell boundary. Constrained transport (Evans and Hawley 1988) ensures that the solenoidal condition for the magnetic field is satisfied at machine precision. The staggered magnetic field are defined on cell faces, different magnetic field components being defined at different locations.

We use a second order Runge-Kutta method for the time step combined with a HLLD solver with linear reconstruction to handle the Riemann problems. An HLLD type solver has the advantage of approximating the solution to the Riemann problem by using 5 waves (Miyoshi and Kusano 2005). This leads to a less diffusive solver, when compared to an HLL type solver that uses 2 waves.

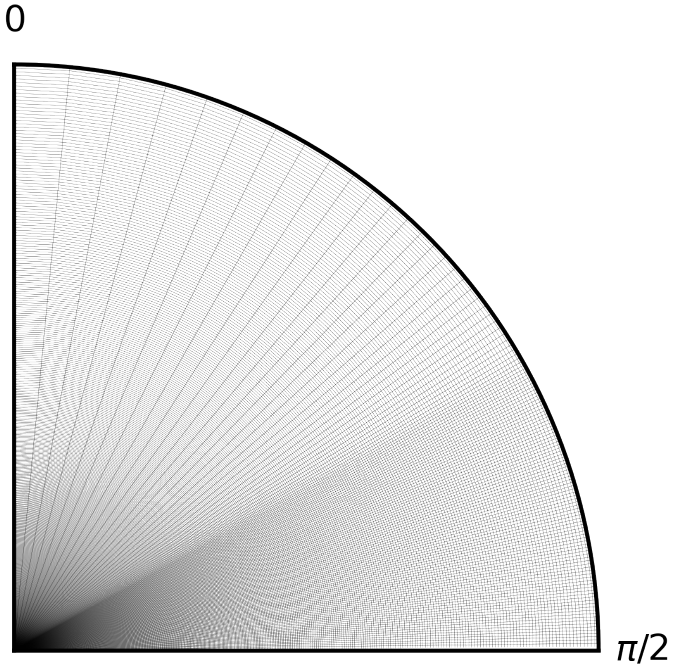

Figure 4.1: Computational Grid

It is important for the latitudinal domain to extend from 0 to π. If the numerical domain does not cover the full latitudinal domain the magnetic field lines are able to connect to the latitudinal boundary condition. If this happens the magnetic field lines could exchange angular momentum with the boundary condition. Furthermore, magnetic flux could also leak through the latitudinal boundary and escape through the boundary condition. Hence, our latitudinal extent is always $[0, \pi]$. We implement the same boundary condition regularisation as Zhu and Stone 2018 for the latitudinal direction.

The extent of our radial and toroidal domain varies from one simulation to the next. We summarize the domain properties, as well as the main control parameters for each simulations in Tab. (4.1). In the following, we use the innermost radius r_{in} as the unit length, so that $r_{\mathrm{in}} = R_{\mathrm{in}} = 1$ in all simulations, we also define R_{out} in Tab. (4.1). We use periodic boundary conditions in the toroidal direction and zero-gradient in the radial direction (mass flow into the numerical domain is forbidden).

We follow Nelson et al. 2013 for the hydrostatic initial condition. The initial density and temperature profiles are defined at the disk mid-plane as:

$$\rho_i(R, z=0) = \rho_i(R = R_{\mathrm{in}}, z=0)\left(\frac{\tilde{R}}{R_{\mathrm{in}}}\right)^p$$

$$T_i(R) = T_i(R = R_{\mathrm{in}})\left(\frac{\tilde{R}}{R_{\mathrm{in}}}\right)^q$$

where, for convenience, we use the cylindrical coordinates and we define $\tilde{R} = \max(R, R_{\mathrm{in}})$ to avoid singularities at the pole. In this initial condition, the temperature is constant on cylinders and remains so during the entire duration of the simulation, thanks to the *ad hoc* cooling function described above.

We can write the solution of Eq. (4.1-4.7) assuming a hydrostatic equilibrium (neglecting all velocities but the azimuthal one) and no magnetic fields using the initial density and temperature at the disk mid-plane defined above. We get

$$\rho_i(R, z) = \rho_i(R, z=0)\exp\left[\frac{\Omega_K^2(\tilde{R})\tilde{R}^3}{c_s^2(\tilde{R})}\left(\frac{1}{\sqrt{\tilde{R}^2+z^2}} - \frac{1}{\tilde{R}}\right)\right]$$

and

$$u_{\phi,i}(R, z) = V_K\left[(q+1) - q\frac{\tilde{R}}{\sqrt{\tilde{R}^2+z^2}} + \frac{c_s^2(\tilde{R})}{V_K^2(\tilde{R})}(p+q)\right]^{1/2}$$

where we have defined the Keplerian velocity $V_K = \Omega_K R$. We then use the Keplerian angular velocity and the sound speed to define the disk scale height

$$h = c_s/\Omega_K = \varepsilon R, \tag{4.9}$$

where ε is the constant disk geometrical thickness.

Following Zhu and Stone 2018, we assume a large scale vertical magnetic field that is constant with respect to z but follows a power law in R. In order to get a self-similar initial condition, we choose a radially constant initial magnetization,

$$\mu_{\mathrm{ini}} = \frac{B_{z,i}^2}{4\pi P_i}, \tag{4.10}$$

in the disk midplane, we note that $\mu = 2/\beta$. We will measure the magnetization only at the disk mid-plane, it will help us quantify the secular evolution of the magnetic structure. When analyzing the vertical structure we will compute the local plasma beta.

The magnetic field radial profile is then related to that of temperature and density:

$$B_{z,i}(R) = B_i\left(\frac{\tilde{R}}{R_{\mathrm{in}}}\right)^{\frac{p+q}{2}} \tag{4.11}$$

where

$$B_i = \sqrt{4\pi\mu_{\mathrm{ini}} P_i(R = R_{\mathrm{in}}, z=0)}. \tag{4.12}$$

To ensure that $\nabla \cdot \mathbf{B} = 0$ at $t = 0$, we initialize the magnetic field using the magnetic potential $\mathbf{A}$. We can solve the equation $\mathbf{B} = \nabla \times \mathbf{A}$ to find

$$A_\phi = \begin{cases} \frac{RB_i}{2} \text{ for } R \leq R_{\text{in}}, \\ B_i \left(\frac{\tilde{R}}{R_{\text{in}}}\right)^{\frac{p+q}{2}} \frac{2R}{(p+q)+4} + B_i \frac{R_{\text{in}}^2}{R}\left(\frac{1}{2} - \frac{2}{(p+q)+4}\right) \text{ for } R > R_{\text{in}}. \end{cases}$$

Finally, we choose $p = -3/2$ and $q = -1$ for all our simulations, in the same way as Mishra et al. 2020. To handle runaway magnetization close to the polar boundary we implement a density floor in our simulation

$$\rho_{\text{fl}} = \max\left(\rho_{\text{fl},0}\left(\frac{\tilde{R}}{R_{\text{in}}}\right)^p \frac{1}{z^2 + a_{\text{fl}}\varepsilon^2\tilde{R}^2}, 10^{-9}\right)$$

where $\rho_{\text{fl},0} = 10^{-7}$ and $a_{\text{fl}} \sim 1$. Finally, to minimize integration time, we enforce a maximal Alfvénic velocity $V_{A,\text{max}} = V_K(R_{\text{in}})$, where $V_A = B/\sqrt{4\pi\rho}$ is computed with the instantaneous magnetic components. This maximal Alfvénic velocity is imposed by changing the local density and not the magnetic field, hence it acts as an additional density floor. In our simulations, this numerical artifice is only noticeable close to the axis as well as near to the inner boundary, $r \sim r_{\text{in}}$, which are ignored in our analysis.

To resolve the MRI turbulence within the disk we use a nonuniform grid (Fig. 4.1):

- In the radial direction the grid points are logarithmically spaced.

- In the latitudinal direction the grid is linearly spaced up to $|z| = 5.5h$ and then geometrically stretched up to the axis. The latitudinal grid is identical for all the simulation except for the simulation at $\varepsilon = 0.05$ where the grid is spread differently. For this simulation the grid is linearly spaced up to $|z| = 3h$ and then stretched up until $|\pi/2 - \theta| > \pi/2 - 0.35$ where the spacing becomes linear again for two grid points close to the polar boundary. This particular grid maximizes the resolution within the disk and its surface as well as providing a buffer zone close to the polar boundary where the CFL condition is the smallest.

- In the toroidal direction the grid is linearly spaced.

The resolutions for the different simulations per region and direction are displayed in Tab. (4.1). This choice of resolution allow us to resolve the MRI in the disk with approximately 16 grid points per vertical scale height.

We integrate our simulations up to T_{end}, see Tab.(4.1). We define our reference time scale $T_{\text{in}} = T_K(R_{\text{in}})$, corresponding to orbits of the innermost radii, where $T_K(R) = 2\pi/\Omega_K(R)$.

4.1.3 Averaging procedure and turbulent decomposition

In section 2.3.1 we computed a set of Reynolds average MHD equations that we obtain by ensemble averaging the MHD equations. We now assume ergodicity and replace our ensemble averages with a set of average on ϕ, on (ϕ, t), and on (ϕ, t) density weighted:

$$\langle X\rangle_\varphi = \frac{1}{\Delta\phi}\int_{\phi_1}^{\phi_2} X\,\mathrm{d}\phi, \tag{4.13}$$

$$\langle X\rangle = \frac{1}{\Delta\phi}\int_{\phi_1}^{\phi_2} \frac{1}{t_2 - t_1}\int_{t_1}^{t_2} X\,\mathrm{d}\phi\,\mathrm{d}t, \tag{4.14}$$

$$\langle X\rangle_\rho = \frac{1}{\Delta\phi\,\langle\rho\rangle}\int_{\phi_1}^{\phi_2} \frac{1}{t_2 - t_1}\int_{t_1}^{t_2} \rho X\,\mathrm{d}\phi\,\mathrm{d}t = \frac{1}{\langle\rho\rangle}\langle X\rho\rangle\,. \tag{4.15}$$

In these definitions, ϕ_1 and ϕ_2 are taken as the boundaries of the whole computational domain (Tab. (4.1)). The average is computed on time scales comparable to the dynamical time scale, $T_K = 2\pi/\Omega_K$, the set of equations we derive are stationary, they describe the equilibrium state, and do not take into account the secular evolution of the system. Hence, The averages are taken from time t_1 to t_2, with a temporal resolution of $\Delta t = 1/\Omega_K(R_{\rm in}) \simeq 0.16T_{\rm in}$ and then azimuthally averaged over the whole domain (Tab. 4.1). We rewrite the complete set of Reynolds average equations:

$$\frac{1}{\Delta t}\Big[\langle\delta\rho\rangle_\varphi\Big]_{t_1}^{t_2} + \nabla\cdot\langle\rho\rangle\Big[\langle\mathbf{u}\rangle + \langle\delta\mathbf{u}\rangle_\rho\Big] = 0. \tag{4.16}$$

$$\begin{aligned}
&\frac{1}{\Delta t}\Big[\langle\rho\delta u_r\rangle_\varphi\Big]_{t_1}^{t_2} + \langle\rho\rangle\left\langle\mathbf{u_p}\right\rangle_\rho\cdot\nabla\langle u_r\rangle + \nabla\cdot\left[\langle\rho\rangle\left\langle\delta u_r\mathbf{u_p}\right\rangle_\rho - \frac{1}{4\pi}\left\langle\delta B_r\boldsymbol{\delta}\mathbf{B_p}\right\rangle\right] = \\
&-\frac{\partial}{\partial r}\left[\langle P\rangle + \frac{1}{8\pi}\left(\langle B\rangle^2 + \left\langle\delta B^2\right\rangle\right)\right] + \frac{1}{4\pi}\left\langle\mathbf{B_p}\right\rangle\cdot\nabla\langle B_r\rangle \\
&+\frac{\langle\rho\rangle}{r}\left[\left\langle u_\varphi\right\rangle^2 + \left\langle\delta u_\varphi^2\right\rangle + \langle u_\theta\rangle^2 + \left\langle\delta u_\theta^2\right\rangle\right] - \langle\rho\rangle g - \frac{1}{4\pi r}\left[\left\langle B_\varphi\right\rangle^2 + \left\langle\delta B_\varphi^2\right\rangle + \langle B_\theta\rangle^2 + \left\langle\delta B_\theta^2\right\rangle\right]
\end{aligned} \tag{4.17}$$

$$\begin{aligned}
&\frac{1}{\Delta t}\Big[r\langle\rho\delta u_\theta\rangle_\varphi\Big]_{t_1}^{t_2} + \langle\rho\rangle\left\langle\mathbf{u_p}\right\rangle_\rho\cdot\nabla r\langle u_\theta\rangle + \nabla\cdot r\left[\langle\rho\rangle\left\langle\delta u_\theta\mathbf{u_p}\right\rangle_\rho - \frac{1}{4\pi}\left\langle\delta B_\theta\boldsymbol{\delta}\mathbf{B_p}\right\rangle\right] = \\
&\frac{1}{4\pi}\left\langle\mathbf{B_p}\right\rangle\cdot\nabla r\langle B_\theta\rangle - \frac{\partial}{\partial\theta}\left[\langle P\rangle + \frac{1}{8\pi}\left(\langle B\rangle^2 + \left\langle\delta B^2\right\rangle\right)\right] + \cot\theta\left[\langle\rho\rangle\left(\left\langle u_\varphi\right\rangle^2 + \left\langle\delta u_\varphi^2\right\rangle\right) - \frac{1}{4\pi}\left(\left\langle B_\varphi\right\rangle^2 + \left\langle\delta B_\varphi^2\right\rangle\right)\right],
\end{aligned} \tag{4.18}$$

$$\langle\rho\rangle\left\langle\mathbf{u_p}\right\rangle_\rho\cdot\nabla R\left\langle u_\varphi\right\rangle + \nabla\cdot R\left[\langle\rho\rangle\left\langle\delta u_\varphi\mathbf{u_p}\right\rangle_\rho - \frac{1}{4\pi}\left\langle\delta B_\varphi\boldsymbol{\delta}\mathbf{B_p}\right\rangle - \frac{1}{4\pi}\left\langle B_\varphi\right\rangle\left\langle\mathbf{B_p}\right\rangle\right] = 0, \tag{4.19}$$

$$\frac{1}{\Delta t}\left[\left\langle\delta B_\varphi\right\rangle_\varphi\right]_{t_1}^{t_2} = \nabla\times[\langle\mathbf{u}\rangle\times\langle\mathbf{B}\rangle + \mathcal{E}]|_\varphi\,, \tag{4.20}$$

$$\left\langle\frac{\partial A_\varphi}{\partial t}\right\rangle = \frac{1}{\Delta t}\left[\left\langle\delta A_\varphi\right\rangle_\varphi\right]_{t_1}^{t_2} = \left\langle\mathbf{u_p}\right\rangle\times\left\langle\mathbf{B_p}\right\rangle\Big|_\varphi + \mathcal{E}_\varphi. \tag{4.21}$$

We define the two torques acting on the system

$$\mathcal{T}_{\rm la} = -\frac{1}{4\pi}\left\langle B_\phi\right\rangle\left\langle\mathbf{B_p}\right\rangle, \tag{4.22}$$

the laminar stress tensor, and

$$\mathcal{T}_{\rm tu} = \langle\rho\rangle\left\langle\delta u_\phi\boldsymbol{\delta}\mathbf{u_p}\right\rangle_\rho - \frac{1}{4\pi}\left\langle\delta B_\phi\boldsymbol{\delta}\mathbf{B_p}\right\rangle, \tag{4.23}$$

the turbulent stress tensor. The two α coefficients for the turbulent and laminar stress tensors can be written as

$$\alpha_{\rm ef} = \frac{\mathcal{T}_{r\phi}}{\langle P \rangle}, \tag{4.24}$$

$$\alpha_{\rm ef} = \alpha_{\rm la} + \alpha_{\rm tu} \tag{4.25}$$

where $\alpha_{\rm la}$ is related to the laminar torque and $\alpha_{\rm tu}$ to the turbulent one.

4.2 Fiducial case

4.2.1 Global picture

We show in Fig. (4.2) the mean poloidal stream lines and field lines, the Alfvén surface and the fast magneto-sonic surface for the fiducial run, with $\mu_{ini} = 2 \times 10^{-4}$. The Alfvén surface is defined with the poloidal velocity,

$$\left\langle u_p \right\rangle = V_{ap} = \frac{\left\langle B_p \right\rangle}{\sqrt{4\pi \left\langle \rho \right\rangle}}, \tag{4.26}$$

like in axisymmetric jet theory. We define the fast magneto-sonic surface as $\left\langle u_p \right\rangle = V_{fm}$, where

$$V_{fm}^2 = \frac{1}{2}\left(c_s^2 + V_{at}^2 + |V_{at}^2 - c_s^2|\right), \tag{4.27}$$

where the total Alfvénic velocity $V_{at} = \langle B \rangle / \sqrt{4\pi \langle \rho \rangle}$. We compute the fast magneto-sonic surface for waves propagating along the magnetic field lines. In the top panels of Fig.(4.2) we show the complete numerical domain of the fiducial simulation. The upper and lower hemispheres are approximately symmetric. The fast magneto-sonic surface is approximately conical. In contrast, the Alfvénic surface is conical up to a certain radii where its shape changes, this shows that the outer radii of the numerical domain has not yet reached a stationary state. This is further confirmed by the lack of toroidal magnetic field in the outer regions.

In Fig. (4.2) (top, right) we can clearly see some collimation happening for the inner field lines, close to where they meet the boundary condition. As discussed in, section 3.4.4, this is a general symptom from MHD outflows, most MHD outflows collimate. In our case it is unclear whether this is a physical or a numerical effect, like a bias in our boundary conditions or a consequence of the density floor. A study of outflow collimation is outside the scope of this manuscript.

The FM surface is the point where waves can no longer travel back to the disk through the magnetic field line. We can use this surface to estimate the last radius that has achieved stationary ejection. We compute this by calculating the anchoring radii of the last field line that crosses the FM surface, this corresponds to $R \sim 35$. Therefore, we will analyze the stationary inner regions of our numerical domain constrained beneath that radii (the grey rectangle in the top panel of Fig. (4.2)).

We can identify three distinct regions in the bottom panels of Fig. (4.2):

- A turbulent disk where the density is maximal and the flow is disorganized, indicating a turbulent flow. The toroidal component of the magnetic field exhibits a similar disorganized structure. The average poloidal field lines are remarkably straight.

- An accreting atmosphere where the poloidal flow is supersonic. The field lines in this region seem to be curved by the poloidal flow. In addition, a strong laminar toroidal field emerges.

- A super fast magneto-sonic outflow ejected from the atmosphere. The poloidal field lines are parallel to the poloidal stream lines in this region.

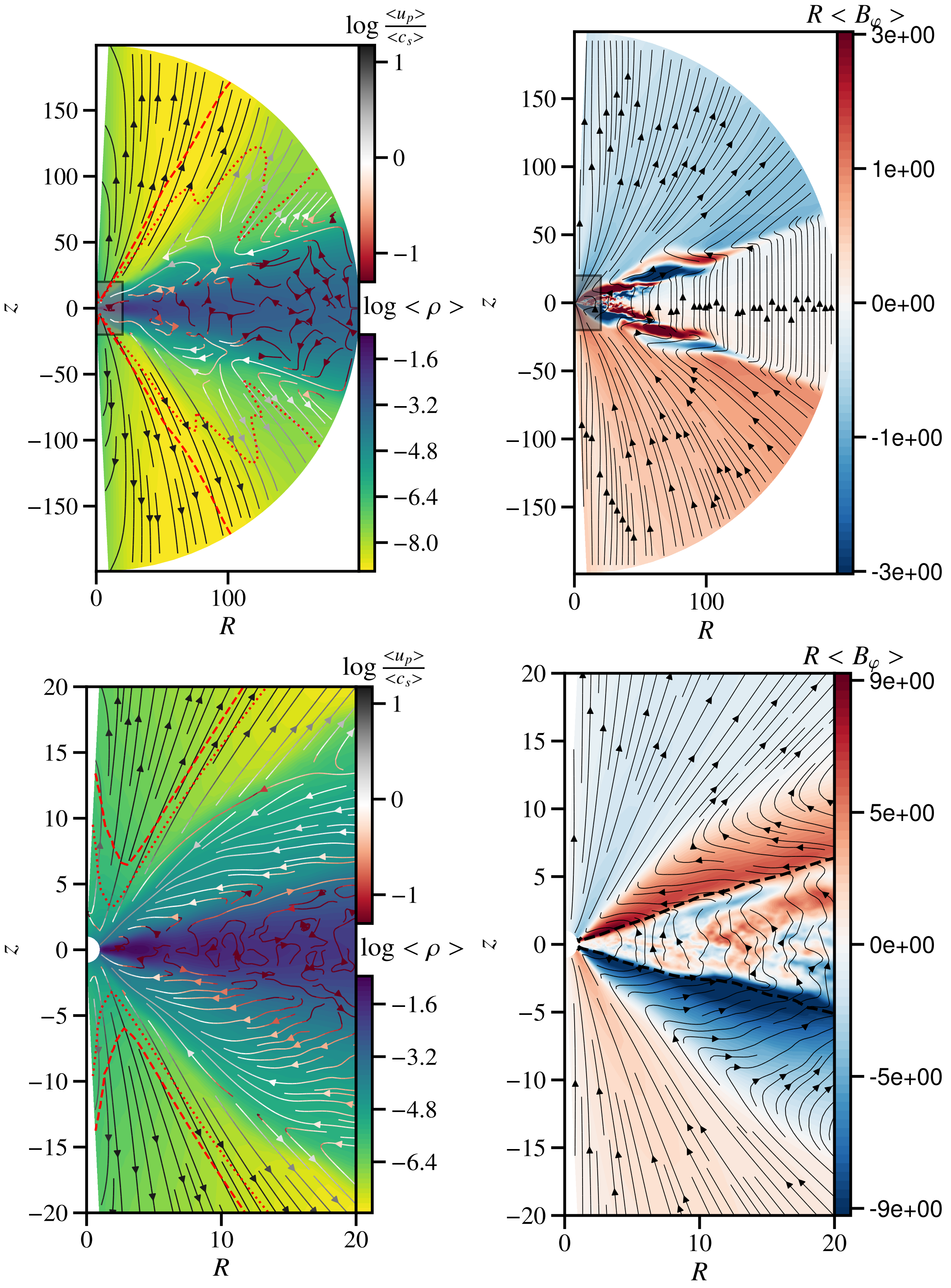

Figure 4.2: (top,left) Gas density and mean poloidal stream lines. The red dotted line corresponds to the Alfvénic surface, and the red dashed line corresponds to the fast magneto-sonic surface. The color of the poloidal stream lines correspond to the logarithm of their magnitude normalized to the sound speed. (top,right) RB_ϕ normalized to $B_i R_{in}$; and mean poloidal field lines. The grey square corresponds to the zoomed in region the bottom figure. (bottom) same as top but zoomed in the greyed region. The black dashed line indicates the surface where $\langle \beta \rangle = 8\pi \langle P \rangle / \langle B \rangle^2 = 1$.

We reiterate that the vertical structure of the accretion disk computed by Zhu and Stone 2018 is very different from the one of a standard accretion disk (Shakura and Sunyaev 1973). Indeed, in a standard accretion disk the accretion occurs at a heigh of the order of the disk geometrical thickness and not at a heigh of the order of R.

The region we have defined as the accreting atmosphere exhibits turbulence, which is not obvious from Fig. (4.2). To measure the dynamical importance of this turbulence, we measure the ratio α_{tu}/α_{la}, defined above. We show this ratio in Fig. (4.3,left), the disk is clearly dominated by the turbulent stress component. As we move towards the accreting atmosphere from the disk surface the stress becomes dominated by the laminar component before turning back to a turbulent stress dominated regions, as in the disk. Even higher still, in the outflow region, the torque is laminar as expected. We divide the accreting atmosphere into two distinct regions:

- A laminar atmosphere (LA) where the dominant stress is the laminar one, α_{la}, it is vertically adjacent to the turbulent disk.
- A turbulent atmosphere (TA) where the dominant stress is the turbulent one, α_{tu}, it is above the laminar atmosphere but below the laminar outflow.

As we saw in section 2.3.1, the Reynolds average equation for the vector potential reads

$$\left\langle \frac{\partial A_\varphi}{\partial t} \right\rangle = \left\langle \mathbf{u_p} \right\rangle \times \left\langle \mathbf{B_p} \right\rangle \Big|_\varphi + \mathcal{E}_\varphi, \tag{4.28}$$

in the case of a laminar and strictly stationary outflow (Mestel 1961), this equation simplifies into

$$\left\langle \mathbf{u_p} \right\rangle \times \left\langle \mathbf{B_p} \right\rangle \Big|_\varphi = 0. \tag{4.29}$$

Therefore, the angle between the average poloidal velocity stream lines and the average magnetic field lines

$$\cos\psi = \frac{\left\langle \mathbf{u_p} \right\rangle \cdot \left\langle \mathbf{B_p} \right\rangle}{\left\langle u_p \right\rangle \left\langle B_p \right\rangle}, \tag{4.30}$$

identifies the regions where turbulent terms are important. If $\cos\psi = \pm 1$ the average poloidal velocity is parallel to the average poloidal magnetic field and the system is laminar. On the contrary if $\cos\psi \neq \pm 1$ the average poloidal fields are not parallel to each other and turbulent correlations in Eq. (4.28) are important.

We show this angle in (right) Fig. (4.3), the disk can be easily identified as turbulent ($\cos\psi \sim 0$). Using this Fig. (4.3) we define the disk as $|z| < 3.5h$ (the central shaded area in Fig. 4.3 and Fig. 4.4), this definition is consistent with Fig. (4.3). The disk surface coincides with the location where the average radial velocity becomes negative (Fig. 4.4), marking the beginning of the accreting atmosphere. Above the disk, the average poloidal fields are aligned ($\cos\psi = \pm 1$). This defines the laminar atmosphere, also identified with the stress, located at an altitude of $3.5h < |z| \leq 6.5h$. As we move higher up still, $\cos\psi$ changes sign twice (Fig. 4.3). This suggest that ideal-MHD is broken in this region. We can identify this region with the turbulent atmosphere located previously using the turbulent stress, located at altitudes $6.5h < |z| \leq 12.5h$. This region ends at the surface delimiting the base of the outflow, where $\cos\psi$ changes sign for the last time. The base of the outflow coincides with the slow magneto-sonic surface, defined by

$$\left\langle u_p \right\rangle = V_{SM}, \tag{4.31}$$

where we compute the slow magneto-sonic surface for waves propagating along the magnetic field lines

$$V_{SM}^2 = \frac{1}{2}\left(c_s^2 + V_{at}^2 - |V_{at}^2 - c_s^2|\right). \tag{4.32}$$

Indeed, in Fig. (4.4) we see how the end of the turbulent atmosphere (the shaded area) roughly coincides with the slow magneto-sonic point, $\left\langle u_p \right\rangle \simeq \langle u_R \rangle = V_{SM}$. It is important to note that V_{SM} is indeed constant in units of c_s since the magnetic field is dominant inside the atmosphere (laminar and turbulent),

$$\langle \beta \rangle < 1, \tag{4.33}$$

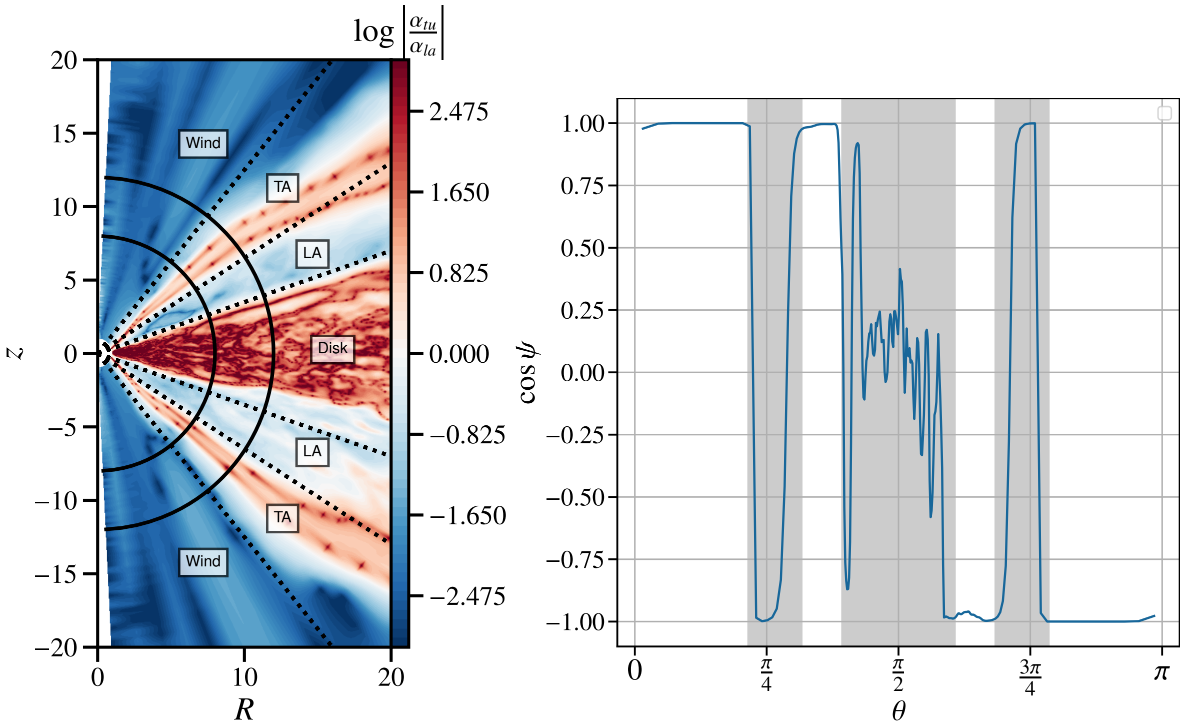

Figure 4.3: (left) Ratio $\alpha_{\mathrm{la}}/\alpha_{\mathrm{tu}}$ denoting turbulent (red) and laminar (blue) regions. The dotted lines delimit these regions and represent $|z| = 3.5h$, $|z| = 6.5h$ and $|z| = 12.5h$. The two different circles denote the radii used for the calculation of the fluxes ($r_1 = 8$, $r_2 = 14$), see text. TA and LA correspond for turbulent and laminar atmosphere, respectively. (right) Cosine of the angle ψ between the mean poloidal velocity and the mean poloidal magnetic field as a function of the latitudinal coordinate. The grey zones correspond to the turbulent regions in the top panel, delimited by the dotted lines.

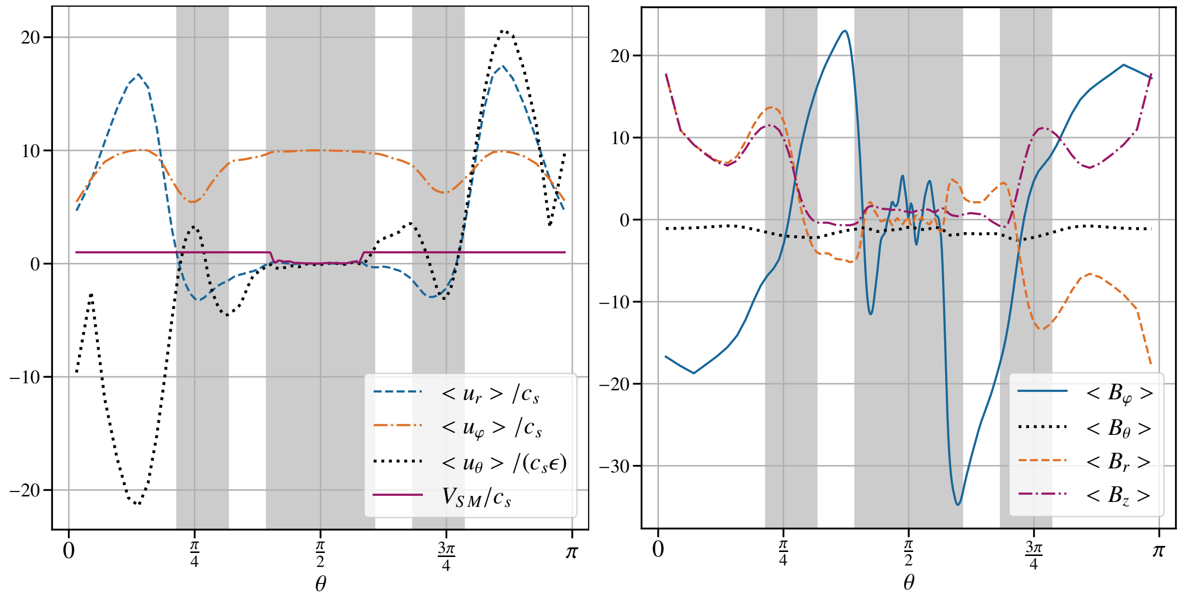

Figure 4.4: (left): Velocity profiles as functions of the latitudinal coordinate, θ, normalised to the local sound speed. (right): mean magnetic field profiles normalised to the vertical magnetic field in the disk mid-plane, $\langle B_z \rangle (r, \theta = \pi/2)$ as functions of the latitudinal coordinate. The grey zones correspond to the turbulent regions in figure 4.3. All profiles are radially averaged between $r_1 = 8$ and $r_2 = 14$ after being normalised.

where

$$\langle \beta \rangle = \frac{8\pi \langle P \rangle}{\langle B \rangle^2} \tag{4.34}$$

However, the mean poloidal magnetic field stays infra-thermal within the laminar atmosphere, $\left\langle \beta_p \right\rangle > 1$, where

$$\left\langle \beta_p \right\rangle = \frac{8\pi \langle P \rangle}{\left\langle B_p \right\rangle^2}, \tag{4.35}$$

but becomes supra-thermal within the turbulent atmosphere, $\left\langle \beta_p \right\rangle < 1$.

4.2.2 Computation of fluxes

To get a global understanding of mass accretion and ejection, let us define the fluxes through the different disk surfaces. Using the regions defined above (§4.2.1), we compute the fluxes through the boundaries of each regions, delimited radially by $r_1 = 8$ and $r_2 = 14$ (see figure 4.3, left). We compute the fluxes in the mass and angular momentum conservation equations

$$\frac{\partial R u_\varphi \rho}{\partial t} + \nabla \cdot R \left[\rho u_\varphi \mathbf{u} - \frac{B_\varphi \mathbf{B}}{4\pi} \right] = -\frac{\partial}{\partial \varphi} \left(\frac{B^2}{8\pi} + P \right), \tag{4.36}$$

by integrating them with respect to time and space.

First we define the average

$$\bar{X} = \int_{\theta_1}^{\theta_2} r \sin\theta X \mathrm{d}\theta. \tag{4.37}$$

We integrate Eq. (4.1) with respect φ and θ to find

$$\frac{\partial \Sigma}{\partial t} + \frac{1}{r} \frac{\partial r \overline{\langle \rho u_r \rangle_\varphi}}{\partial r} + \left[\sin\theta \left\langle \rho u_\theta \right\rangle_\varphi \right]_{\theta_1}^{\theta_2} = 0, \tag{4.38}$$

where $\Sigma = \overline{\langle\rho\rangle_\varphi}$ is the column density of the disk. Equation 4.38 can be integrate with respect to t and R which leads to

$$\Delta M = F_{m,r_1} - F_{m,r_2} + F_{m,\theta_1} - F_{m,\theta_2}, \tag{4.39}$$

where we introduce

$$F_{m,r_i} = -\int_{t_\alpha}^{t_\beta} r_i \left[\overline{\langle\rho u_r\rangle_\varphi}\right]\Big|_{r_i} \mathrm{d}t, \tag{4.40}$$

$$F_{m,\theta_i} = \int_{t_\alpha}^{t_\beta}\int_{r_1}^{r_2} r\sin\theta\,\langle\rho u_\theta\rangle_\varphi\big|_{\theta_i}\,\mathrm{d}r\,\mathrm{d}t \tag{4.41}$$

$$\Delta M = \int_{r_1}^{r_2}\left[r\overline{\langle\rho\rangle_\varphi}\right]_{t_\alpha}^{t_\beta}\mathrm{d}r. \tag{4.42}$$

The mass fluxes are time-averaged on a duration $t_\beta - t_\alpha$ that spans several local orbital periods. A strict steady state translates into $\Delta M = 0$. Computing the angular momentum fluxes is a little bit more engaged, we start by defining

$$v_\varphi = \left\langle u_\varphi\right\rangle_\varphi - R\Omega_s(r,\theta), \tag{4.43}$$

the deviation to the equilibrium velocity, we are free to choose the function $\Omega_s(r,\theta)$. Using the definition of v_φ and Eq. (4.1) we integrate the angular momentum equation with respect to t and φ to find

$$\langle\rho u_r\rangle\frac{\partial R^2\Omega_s}{\partial r}+\frac{\langle\rho u_\theta\rangle}{r}\frac{\partial}{\partial\theta}R^2\Omega_s+\frac{1}{r^2}\frac{\partial}{\partial r}r^2R\left[\left\langle\rho u_r v_\varphi\right\rangle-\frac{\left\langle B_rB_\varphi\right\rangle}{4\pi}\right]+\frac{1}{r\sin\theta}\frac{\partial}{\partial\theta}r\sin^2\theta\left[\left\langle\rho u_\theta v_\varphi\right\rangle-\frac{\left\langle B_\theta B_\varphi\right\rangle}{4\pi}\right]=0, \tag{4.44}$$

where we do not write the term originating from the derivative with respect to time as we find it to be dynamically negligible. We can simplify the second term by choosing $\Omega_s = \Omega_K/\sin^2\theta$. This leads to a mathematical form similar to the one obtained in the cylindrical coordinates (see section 2.3.2). It is important to note that the function $\Omega_s(r,\theta)$ is different from the mean angular velocity of the flow $\langle\Omega\rangle$. We integrate this equation with respect to θ using the operator defined in Eq. (4.37) to find

$$\overline{\langle\rho u_r\rangle}\frac{\partial}{\partial r}\left(R^2\Omega_s\right)+\frac{1}{r}\frac{\partial}{\partial r}r^2\left[\overline{\left\langle\rho v_\varphi u_\theta\right\rangle\sin\theta}-\overline{\frac{\left\langle B_\phi B_r\right\rangle\sin\theta}{4\pi}}\right]+\left[r\sin^2\theta\left(\left\langle\rho u_\theta v_\phi\right\rangle-\frac{1}{4\pi}\left\langle B_\phi B_\theta\right\rangle\right)\right]_{\theta_2}^{\theta_1}=0. \tag{4.45}$$

Like in section 2.3.2 we define a quantify Λ_s to indicate the dominant torque

$$\Lambda_s = \frac{\left[r\sin^2\theta\left(\left\langle\rho u_\theta v_\phi\right\rangle-\frac{1}{4\pi}\left\langle B_\phi B_\theta\right\rangle\right)\right]_{\theta_2}^{\theta_1}}{\frac{1}{r}\frac{\partial}{\partial r}r^2\left[\overline{\left\langle\rho v_\varphi u_\theta\right\rangle\sin\theta}-\overline{\frac{\left\langle B_\phi B_r\right\rangle\sin\theta}{4\pi}}\right]}, \tag{4.46}$$

this quantity is not exactly equivalent to the Λ defined in section 2.3.2 and computed in chapter 3. This is a consequence of the different coordinate system as well as the definition of v_φ (Eq. 4.43) that is different from the one in section 2.3.2. However, if the Maxwell torques (turbulent or laminar) dominate both quantities should be very similar.

Equation (4.45) above can be integrated with respect to r to find

$$F_{L,M_r} + \underbrace{F_{L,M_\theta}}_{=0} = F_{L,r_2} - F_{L,r_1} + F_{L,\theta_1} - F_{L,\theta_2}, \tag{4.47}$$

the left hand side denotes angular momentum transported inwards and outward by the flow, while the right-hand side measures the angular momentum flux due to the torques (turbulent and laminar), we define

$$F_{L,r_i} = \int_{t_\alpha}^{t_\beta} r_i^2 \left[\overline{\left\langle \rho v_\phi u_r \right\rangle_\varphi} \sin\theta - \frac{\overline{\left\langle B_\phi B_r \right\rangle_\varphi \sin\theta}}{4\pi} \right]\Bigg|_{r_i} \mathrm{d}t, \tag{4.48}$$

$$F_{L,\theta_i} = \int_{t_\alpha}^{t_\beta} \int_{r_1}^{r_2} r^2 \sin^2\theta \left[\left\langle \rho u_\theta v_\phi \right\rangle_\varphi - \frac{1}{4\pi} \left\langle B_\phi B_\theta \right\rangle_\varphi \right]\Bigg|_{\theta_i} \mathrm{d}r\,\mathrm{d}t, \tag{4.49}$$

$$F_{L,M_r} = \int_{t_\alpha}^{t_\beta} \int_{r_1}^{r_2} r \overline{\langle \rho u_r \rangle_\varphi} \frac{\partial \Omega_s r^2 \sin^2\theta}{\partial r} \mathrm{d}r\,\mathrm{d}t, \tag{4.50}$$

$$F_{L,M_\theta} = \int_{t_\alpha}^{t_\beta} \int_{r_1}^{r_2} \overline{\langle \rho u_\theta \rangle_\varphi} \frac{\partial \Omega_s r^2 \sin^2\theta}{\partial \theta} \mathrm{d}r\,\mathrm{d}t = 0. \tag{4.51}$$

We simplify the term F_{L,M_θ} by choosing $\Omega_s = \Omega_K / \sin^2\theta$.

4.2.3 Mass and angular momentum budgets

Mass fluxes

We first average the mass budget (Eq. 4.39) on a sliding window of duration $\Delta t = 200/\Omega_K(R_{\text{in}})$. We show in Fig. (4.5) the fluxes calculated within the disk region. We see a coherent latitudinal flux removing mass from the disk and transferring it to the atmosphere, and a quasi periodic radial mass flux with a period of the order of the local orbital period, $\sim T_K(r_1)$. This variability is probably due to the stochastic excitation of the spiral density waves driven by MRI turbulence (Heinemann and Papaloizou 2009a,b). The amplitude of the radial flux is scaled down by its distance to the central object.

The strong variability of the radial fluxes on orbital timescales makes their interpretation difficult. We now display the average of the mass flux over the whole time domain from $t_\alpha = 923 T_{\text{in}}$ to $t_\beta = 1114 T_{\text{in}}$ and show them as simple scalars in Fig. (4.6,left).

We recover the mass flux from the disk to the atmosphere. The radial mass flux indicates that mass is flowing on average outwards and that the disk is decreting. The flux budget indicates that $\Delta M = -6.19 < 0$, implying that the disk portion between r_1 and r_2 is not strictly stationary. On closer inspection we see that a form of secular self-organization is happening within the disk and leading to the appearance of ring-like structures. Our domain is located on two distinct gaps, the formation of ring-like structures will not be discussed in this manuscript, we refer to Jacquemin-Ide et al. 2021 for further details.

We now examine the regions above the disk, we see that the laminar atmosphere is accreting, but less efficiently than the turbulent atmosphere, despite the fact that both regions receive approximately the same amount of mass flux from the outer radial boundary. This is a consequence of the shape of the stream lines (Fig. 4.2). The mass is transported through the laminar atmosphere and ends up being accreted within the turbulent atmosphere at a smaller radii. We see in Fig. (4.6,left) that the turbulent atmosphere is fed in mass by the laminar atmosphere. Most of the mass received by the turbulent atmosphere is radially accreted, the mass ejected into the outflow being almost negligible. We measure $\Delta M \simeq 0$ within the laminar and turbulent atmospheres, corresponding to a steady state system. Overall, we find that mass is being channeled from a decreting turbulent disk, through the laminar atmosphere along the magnetic field lines, and is accreted once it reaches the turbulent atmosphere. To understand why the disk is decreting instead of accreting, we need to look at the angular momentum fluxes.

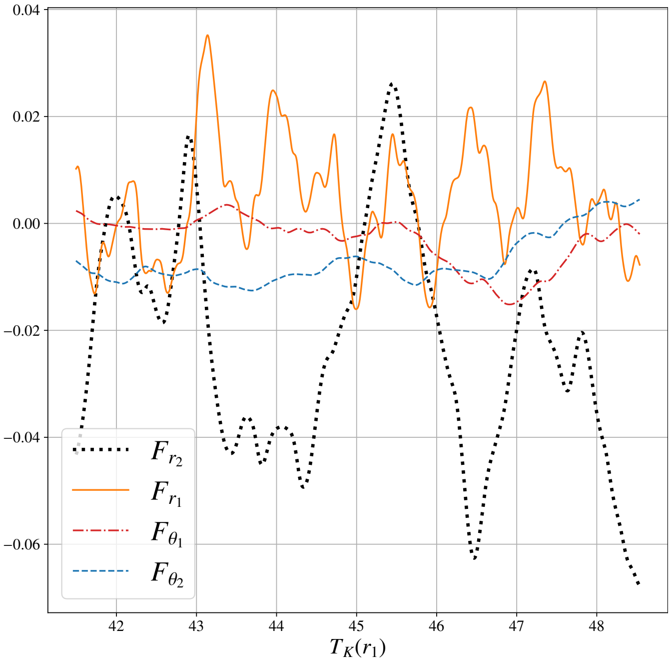

Figure 4.5: Mass fluxes inside the disk, defined for $|z| < 3h$ as function of the local orbital time at $r_1 = 8$. Negative fluxes corresponding to mass being removed from the disk.

Angular momentum fluxes

In the same manner as before we illustrate the time variability, by averaging the angular momentum budget (Eq. 4.47) on a sliding window of duration $\Delta t = 200/\Omega_K(R_{\rm in})$. We show in Fig. (4.7) the fluxes calculated within the disk region, a positive flux corresponding to angular momentum being removed from the disk. We see that angular momentum travels radially outwards within the disk, consistent with MRI turbulence. Surprisingly, the disk receives angular momentum from the laminar atmosphere (Zhu and Stone 2018): the disk is therefore azimuthally accelerated by its atmosphere. Contrary to the mass fluxes within the disk (Fig. 4.5) the angular momentum fluxes do not exhibit significant variability and appear quasi-stationary.

We now take a look at the angular momentum fluxes on the whole vertical structure by averaging over the whole time domain ($t_\alpha = 923T_{\rm in}$ to $t_\beta = 1114T_{\rm in}$) and show the fluxes as simple scalars in Fig. (4.6,right). We can see that angular momentum is always transported radially outwards for all the different regions. We recover again that the disk is receiving angular momentum from the atmosphere. Overall, the latitudinal flux from the laminar atmosphere overruns the radial loss of angular momentum in the disk and thus decretion must occur. In the absence of a latitudinal flux from the atmosphere the disk would be only losing angular momentum radially and thus accretion would occur.

The laminar atmosphere in turn gets its angular momentum radially, from the inner radius, as well as latitudinally from the turbulent atmosphere. The radial angular momentum flux within the laminar atmosphere is dominated by the laminar stress and not the turbulent stress (see section 4.2.1). Below the base of the outflow, in the turbulent atmosphere, angular momentum is lost from all sides. The outflow is not the main contributor of angular momentum loss, it carries less than 10% of the angular momentum extracted from this region. Most of the angular momentum is radially transported outward or transferred down to the laminar atmosphere. In contrast to the laminar atmosphere however, the radial angular momentum transport within the TA is due to the turbulent torques (see section 4.2.1).

We compute the ratio of angular momentum transported by the latitudinal torques to the radial torques.

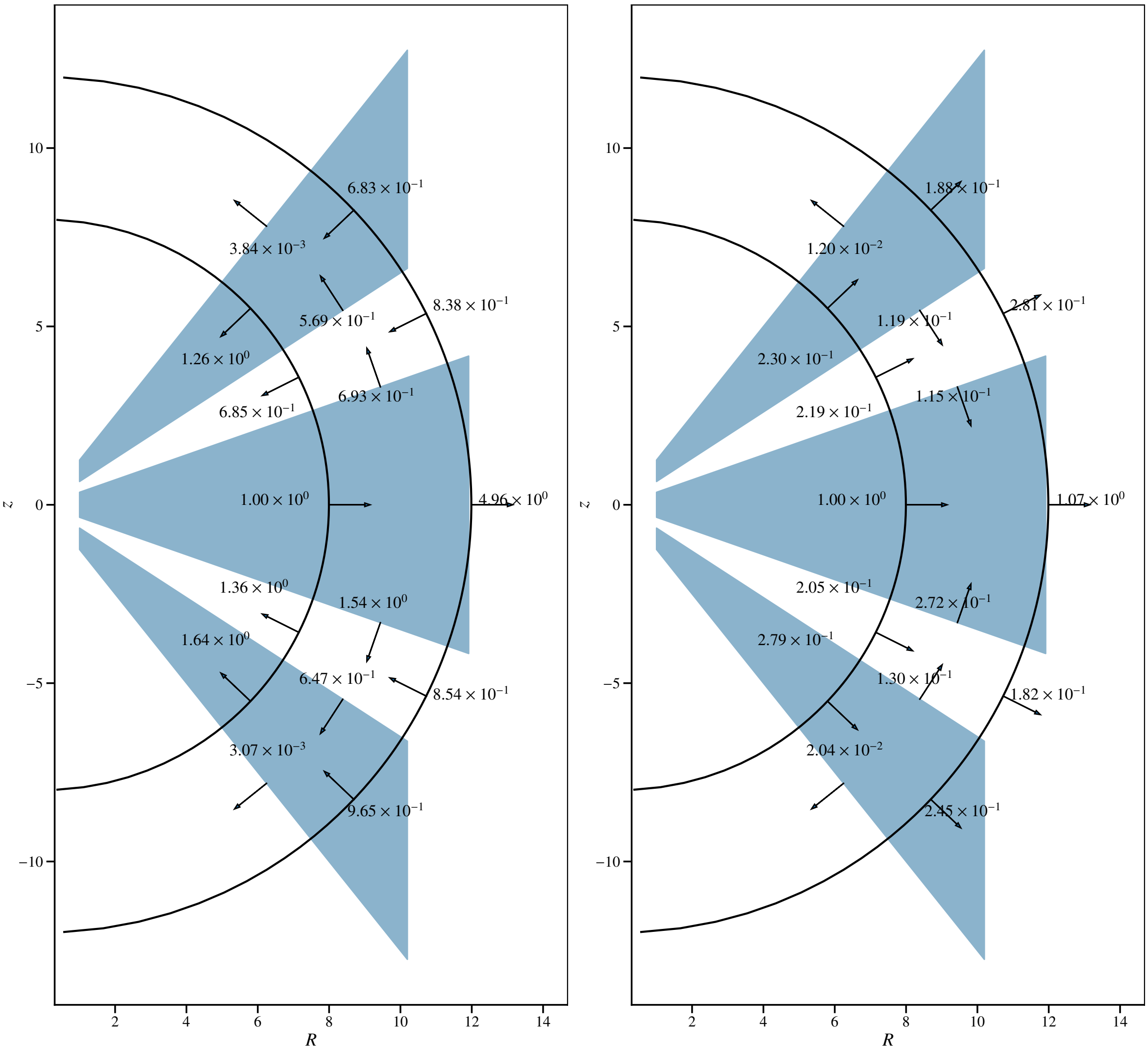

Figure 4.6: (left) Mass fluxes inside of the whole domain, the regions shaded blue are turbulent regions. The arrows represent the direction of the fluxes. Since we are representing the different mass fluxes of a region of the disk, their sum (taking into account their direction) should be equal to the mass difference between t_α and t_β. (right) Angular momentum fluxes across the whole domain, the regions shaded blue are turbulent regions. The different fluxes are integrated between t_α and t_β. The arrows represent the direction of the fluxes. In this figure we are only representing the fluxes that emerge from the Reynolds and magnetic stresses $F_{L,r_2}, F_{L,r_1}, F_{L,\theta_1}, F_{L,\theta_2}$ not the flux of angular momentum though accretion. However, the sum of these fluxes (taking in to account their direction) leads to the value of the angular momentum being transported by the accretion.

This ratio is equivalent to the parameter Λ_s defined above in Eq. (4.46) as

$$\Lambda_s = \frac{\left[r \sin^2\theta \left(\left\langle \rho u_\theta v_\phi \right\rangle - \frac{1}{4\pi}\left\langle B_\phi B_\theta \right\rangle\right)\right]_{\theta_2}^{\theta_1}}{\frac{1}{r}\frac{\partial}{\partial r} r^2 \left[\overline{\left\langle \rho v_\varphi u_\theta \right\rangle \sin\theta} - \overline{\frac{\left\langle B_\phi B_r \right\rangle \sin\theta}{4\pi}}\right]}. \tag{4.52}$$

If we assume that Λ_s is constant with radius we can rearrange the equation, multiply both sides by r and then integrate with respect to r to find

$$\Lambda_s = \frac{F_{L,\theta_1} - F_{L,\theta_2}}{F_{L,r_2} - F_{L,r_1}}, \tag{4.53}$$

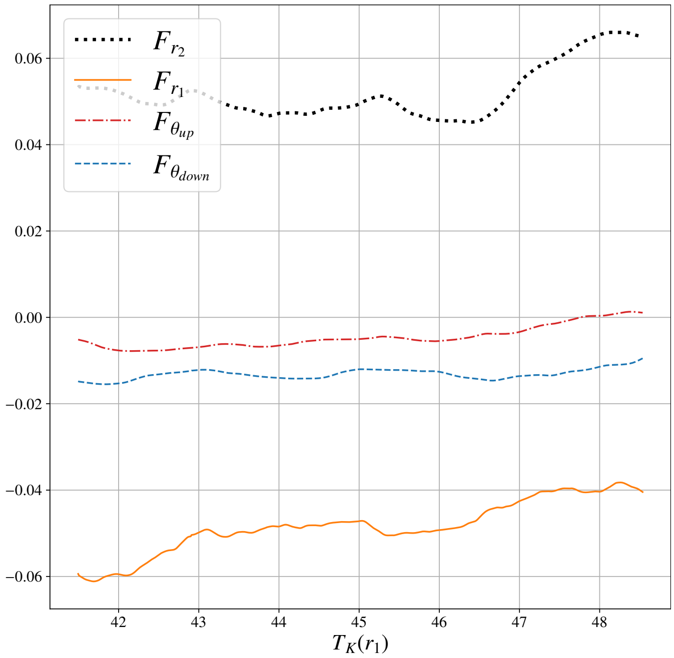

Figure 4.7: Angular momentum fluxes inside the disk, defined for $|z| < 3h$ as function of the local orbital time at $r_1 = 8$. Positive fluxes corresponding to angular momentum being removed from the disk.

where the fluxes are the ones defined in section 4.2.2. By taking the values of Fig. (4.7) we compute Λ_s only considering the fluxes entering or exiting the whole domain, ignoring the internal angular momentum fluxes. The latitudinal flux are taken as the outflow torques extracting angular momentum away from the system. The radial torques F_{L,r_2} and F_{L,r_1} are computed by summing all radial torques entering and exiting the system. Note that $F_{L,\theta_2} < 0$ and $F_{L,\theta_1} > 0$ while both radial fluxes are positive. We get

$$\Lambda_s \simeq 1. \tag{4.54}$$

Both torques transport approximately the same amount of angular momentum. It should be noted, that it is hard to simplify the complexity of the system into a single number (see Fig. 4.7). Hence, the measurement of Λ_s should be taken with care.

4.2.4 Secular transport

Accretion velocity

If we want to understand the global behavior of the accretion flow in our simulation, we need to compute the mass weighted accretion velocity,

$$v_{\rm acc} = \frac{\int_{\theta_{\rm SM,1}}^{\theta_{\rm SM,2}} r \sin\theta \ \langle u_r \rho \rangle \, \mathrm{d}\theta.}{\int_{\theta_{\rm SM,1}}^{\theta_{\rm SM,2}} r \sin\theta \ \langle \rho \rangle \, \mathrm{d}\theta.}, \tag{4.55}$$

where $\theta_{SM,1}$ and $\theta_{SM,2}$ are respectively the angles where the flow becomes super SM in the upper and the lower hemispheres. These surfaces coincide with the end of the turbulent atmosphere. From section 2.3.2 it is clear that the mass weighted accretion velocity is related to the mass accretion rate $\dot{M}_{\rm acc}$. The mass weighted accretion velocity can be computed from the mass accretion rate

$$v_{\rm acc} = \frac{1}{2\pi R}\frac{\dot{M}_a}{\langle\bar{\rho}\rangle}. \tag{4.56}$$

We time average this quantity between $t_a = 318T_{\rm in}$ and $t_b = 955T_{\rm in}$ with a temporal resolution of $0.8T_{\rm in}$ and get

$$v_{\rm acc}(R) \simeq -1.1\times 10^{-3}V_K(R), \tag{4.57}$$

valid for $R \in [2, 14]$, which is clearly subsonic. The accretion velocity, $v_{\rm acc}$, follows a radial dependency very close to Keplerian. The negative sign shows that accretion in the turbulent atmosphere dominates over the disk decretion and the self-organization into ring-like structures. We can compute an accretion time scale using this value of the accretion velocity, we get

$$t_{\rm acc} = \frac{R}{v_{\rm acc}} \sim 9.1\times 10^2/\Omega_K(R) = 145T_K. \tag{4.58}$$

The accretion time scale is substantially longer than than the local dynamical timescale of MRI or ejection which are of the order of T_K. Hence, there is a clear timescale separation between local dynamics and accretion as expected.

Magnetic flux transport

The evolution of the magnetic field is harder to characterize. First we need introduce the magnetic flux threading the disk

$$\Psi(R,t) = \int_0^{\pi/2} r^2 \sin\theta \left\langle B_r\right\rangle_\varphi (r = R_{\rm in},\theta,t)\,{\rm d}\theta + \int_{R_{\rm in}}^{R} R\left\langle B_z\right\rangle_\varphi (r,\theta=\pi/2,t)\ {\rm d}R. \tag{4.59}$$

We compute this flux by integrating along a surface that goes from the axis ($z = 1$ and $R = 0$) down to the inner boundary of the disk ($z = 0$ and $R = R_{in}$) and then to radius R in the disk midplane.

We first confirm that $\Psi(R = R_{\rm out})$ is constant during the entire run, indicating that the total flux within the numerical domain is conserved. To do this we compute the fluxes

$$\Psi_B = \int_0^{\pi/2} r^2 \sin\theta \left\langle B_r\right\rangle_\varphi (r = R_{\rm in},\theta,t)\,{\rm d}\theta, \tag{4.60}$$

$$\Psi_d = \int_{R_{\rm in}}^{R_{\rm out}} R\left\langle B_z\right\rangle_\varphi (r,\theta=\pi/2,t)\ {\rm d}R, \tag{4.61}$$

where Ψ_d is the magnetic flux crossing the disk mid-plane, while Ψ_B is the magnetic flux crossing the boundary condition, we notice that $\Psi_d + \Psi_B = \Psi(R = R_{\rm out})$. For the magnetic flux to be conserved in our numerical domain their sum must be constant, we clearly see this in Fig. (4.8). Furthermore, the magnetic flux at the inner radial boundary increases with time, indicating transport of the magnetic field towards the inner regions. The disk looses its magnetic field which is advected and concentrated on the boundary.

To understand this advection we show Ψ in Fig. (4.9) as a function of the radial coordinate and time. In this figure, each contour corresponds to the midplane foot-point of a poloidal magnetic field line. The magnetic field lines are advected inwards. Eventually, as shown in Fig. (4.8), the magnetic flux accumulates in the inner boundary condition, but is not lost.

It is desirable to compute an effective velocity for the magnetic field transport, v_Ψ. We compute this effective velocity by assuming the magnetic flux can be modeled following a simple advection equation, as proposed by Guilet and Ogilvie 2012

$$\frac{\partial\Psi}{\partial t} + v_\Psi\frac{\partial\Psi}{\partial R} = 0. \tag{4.62}$$

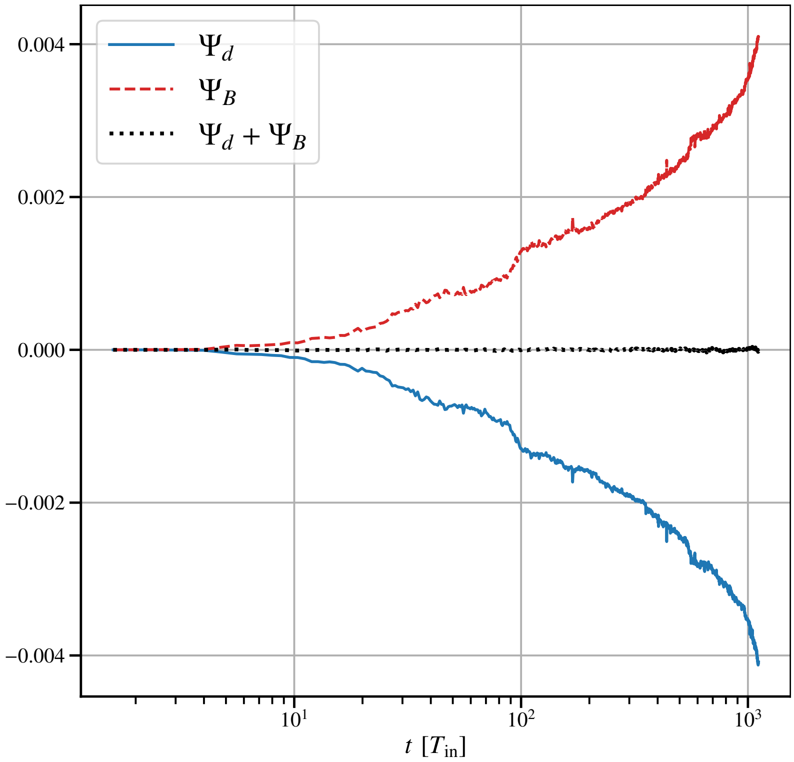

Figure 4.8: Magnetic flux crossing the inner radial boundary condition $r = r_{\rm in}$, Ψ_B, and the total magnetic flux Ψ_d crossing the disk as function of t in unites of $T_{\rm in}$. For the sake of clarity we have subtracted the initial values of both fluxes ($\Psi_B(t = 0)$ and $\Psi_d(t = 0)$).

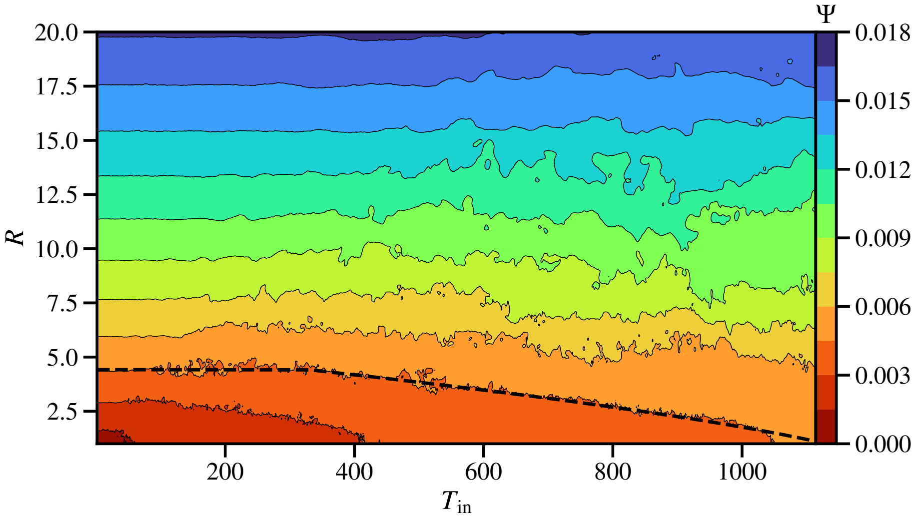

Figure 4.9: Magnetic flux threading the disk midplane Ψ, computed between the axis and R, as a function of time in innermost orbital units. Every contour line represents a field line. The dashed line shows an example of a fit using Eq.(4.66) with $R_i = 4.4$, $t_i = 328T_{\rm in}$ and $\frac{v_\Psi}{V_K} = -1 \times 10^{-3}$.

This equation is derived in section 2.4.3, in that derivation we show that v_ψ is the consequence of the competition between the turbulent diffusion and the advection of the magnetic field. In this chapter we use this equation in a purely phenomenological way, we use it to compute the transport velocity without trying to differentiate the different contributions of v_Ψ. We now compute v_Ψ and average it between

$t_a = 318T_{\rm in}$ and $t_b = 955T_{\rm in}$ with a temporal resolution of $0.8T_{\rm in}$, which provides

$$v_\Psi \sim -1 \times 10^{-3} V_K, \tag{4.63}$$

valid for $R \in [2, 11]$. For $R > 11$ we cannot conclude on magnetic flux advection, since we did not integrate for long enough to get a measurable deviation from the initial condition. As expected from Fig. (4.9) the transport velocity is negative within the inner regions of the disk. Moreover, the transport velocity follows a radial dependency close to Keplerian.

Since the field lines are advected at a fraction of the Keplerian velocity we can model their advection by computing the characteristic of Eq. (4.62) with a velocity

$$v_\Psi(R) = -a_0 V_K(R), \tag{4.64}$$

where a_0 is a positive constant. We compute the characteristic below. Here we use the fact that the magnetic field lines are going to be advected at the velocity v_Ψ, we can model their motion with the following equation

$$\dot{R}_\Psi = v_\Psi(R) = -a_0 V_K(R), \tag{4.65}$$

where R_Ψ is the radial foot point of the poloidal magnetic field line. We can solve this equation for R_Ψ and find

$$R_\Psi(t) = R_i \left[1 - \frac{3\Omega_K(R_i)}{2} a_0 (t - t_i) \right]^{\frac{2}{3}}, \tag{4.66}$$

where R_i is its initial position and t_i is the time the system needs to stabilize the transient due to the initial condition, and start advecting magnetic flux, a delay visible in Fig. (4.9). Equation (4.66) can be derived from the characteristics.

We then cross-checked the numerical value of the magnetic field transport velocity by fitting the contours of Fig. (4.9) with Eq. (4.66). These fits show a reasonable agreement with the data (Fig. 4.9, dashed line), which suggests that magnetic field lines are advected in a self-similar manner once the equilibrium of the magnetic structure is reached ($t_i \sim 30T_K(R)$).

Since $v_\Psi \propto V_K(R)$, the time scale for the magnetic field transport, namely

$$t_\Psi = \frac{R}{v_\Psi} \sim 10^3/\Omega_K(R) = 160T_K(R), \tag{4.67}$$

is comparable to the accretion time scale and substantially longer than the dynamical time scale.

Motivated by the agreement of our fits we can try to go a step further and find the explicit function $\Psi(R, t)$ by solving Eq. (4.62) for

$$B_z\left(R, t = t_i(R)\right) = B_i \left(\frac{R}{R_{\rm in}}\right)^{-\frac{5}{4}} \quad \Rightarrow \quad \Psi\left(R, t = t_i(R)\right) = \frac{3}{4} R_{\rm in}^2 B_i \left[\left(\frac{R}{R_{\rm in}}\right)^{3/4} - 1 \right], \tag{4.68}$$

where for consistency sake we choose $t_i \sim 30T_K(R)$. Since the transport velocity is only a function of radii, equation (4.62) simplifies to a simple advection equation with variable coefficients. Using the method of characteristics, we write a general solution of Eq. (4.62) as

$$\Psi(R, t) = F(\Xi), \tag{4.69}$$

$$\Xi = \int_{t_i(R)}^{t} {\rm d}t - \int_{R_{\rm in}}^{R} \frac{-1}{a_0 V_K(R)} {\rm d}R. \tag{4.70}$$

The explicit form of Ξ is found to be

$$\Xi = t - t_i(R) + \frac{2}{3} \frac{R_{\rm in}}{a_0 V_K(R_{\rm in})} \left(\left(\frac{R}{R_{\rm in}}\right)^{3/2} - 1 \right). \tag{4.71}$$

We deduce that one function $F(\Xi)$ that can fulfill the initial condition is of the form

$$F(\Xi) = c_1(\Xi + c_2)^{1/2} + c_3, \tag{4.72}$$

where c_1, c_2 and c_3 are constants. We solve for the different constants and find

$$\Psi(R,t) = \frac{3}{4}R_{\rm in}^2 B_i \left[\frac{3}{2}\frac{a_0 V_K(R_{\rm in})}{R_{\rm in}}\left(t - t_i(R)\right) + \left(\frac{R}{R_{\rm in}}\right)^{3/2}\right]^{1/2} - \frac{3}{4}R_{\rm in}^2 B_i. \tag{4.73}$$

We compute this theoretical approximation of Ψ with $t_i = 30T_K(R)$, $a_0 = 1\times10^{-3}$ and B_i fixed to our initial conditions. We display its space time diagram in Fig. (4.10), the resemblance with Fig. (4.9) is striking. We can conclude that the field advection for our fiducial simulation is linear, local and, follows a Keplerian velocity scaling. We will see in section 4.3.2 that this is not the case in strongly magnetized accretion disks.

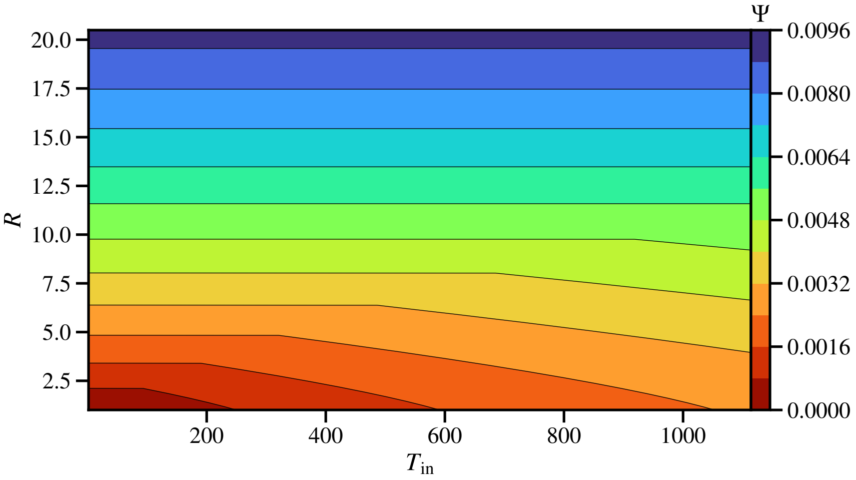

Figure 4.10: Theoretical magnetic flux threading the disk midplane Ψ, computed from Eq. (4.73) between the axis and R, as a function of time in innermost orbital units. We compute this function with $t_i = 30T_K(R)$ and $a_0 = 1\times10^{-3}$. Every contour line represents a field line. The numerical values do not agree with the ones shown in Fig. (4.9), since we do not include the magnetic flux of the boundary condition in our model.

4.2.5 Dynamic equilibrium

Assuming the total poloidal flow acceleration is negligible we get the following radial and latitudinal equilibria from Eq. (2.65)

$$\begin{aligned}\frac{\left\langle u_\phi\right\rangle^2}{r} - \frac{\left\langle B_\phi\right\rangle^2 + \left\langle \delta B_\phi^2\right\rangle}{4\pi r\langle\rho\rangle} - \frac{1}{\langle\rho\rangle}\frac{\partial\langle P\rangle}{\partial r} - \frac{1}{\langle\rho\rangle}\frac{\partial\langle P_B\rangle}{\partial r}&\\ + \frac{1}{4\pi\langle\rho\rangle}\left\langle \mathbf{B_p}\right\rangle\cdot\nabla\langle B_r\rangle = g,&\end{aligned} \tag{4.74}$$

$$\cot\theta\left[\left\langle u_\phi\right\rangle^2 - \frac{\left\langle B_\phi\right\rangle^2 + \left\langle \delta B_\phi^2\right\rangle}{4\pi\langle\rho\rangle}\right] - \frac{1}{\langle\rho\rangle}\frac{\partial\langle P\rangle}{\partial\theta} - \frac{1}{\langle\rho\rangle}\frac{\partial\langle P_B\rangle}{\partial\theta} = 0, \tag{4.75}$$

where $g = GM/r^2$ and $\langle P_B\rangle = \left(\langle B\rangle^2 + \left\langle \delta B^2\right\rangle\right)/8\pi$ is the magnetic pressure, which contains a laminar, $\langle B\rangle^2$, and a turbulent, $\left\langle\delta B^2\right\rangle$, contribution. We neglect the tension due to the latitudinal magnetic field in

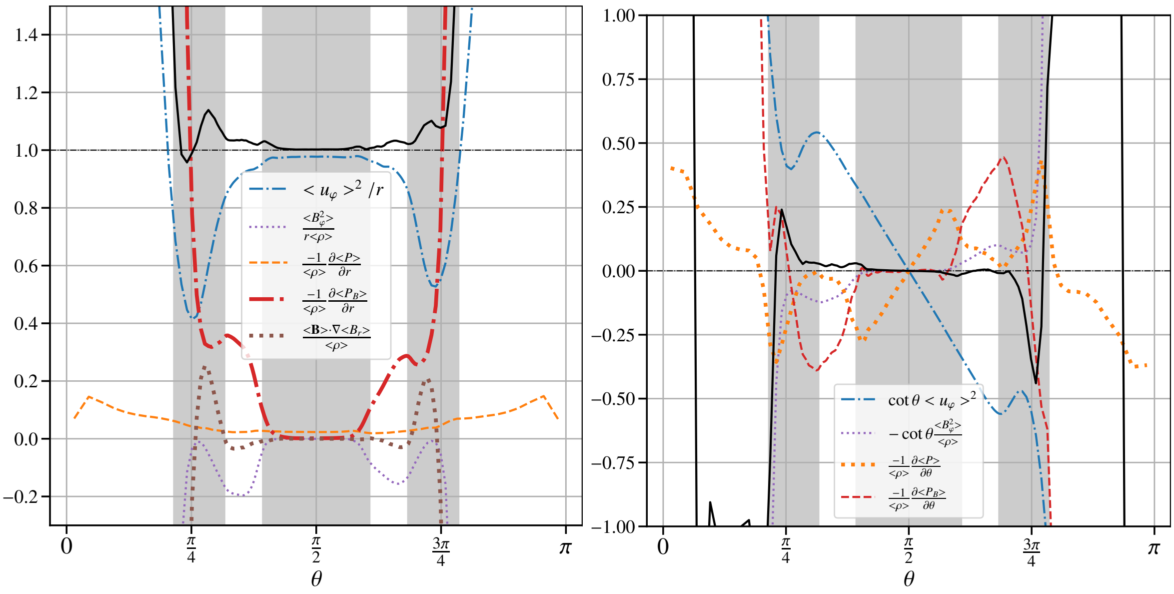

Figure 4.11: Left: Radial equilibrium (eq. 4.74). Right: Latitudinal equilibrium (eq. 4.75) as a function of the latitudinal coordinate θ. The terms are averaged between $r_1 = 8$ and $r_2 = 14$ after being normalized to g (left) or gr (right). If the system is in equilibrium (no acceleration) the sum of the terms, the black solid line , should be equal to 1 (left) or 0 (right). The shaded areas denotes the turbulent regions.

Eq. (4.75) due to its small impact in the latitudinal equilibrium. Figure 4.11 shows the latitudinal profile of the radial and latitudinal equilibria, respectively normalized to g and gr. We find that the disk region is in radial and latitudinal equilibrium thanks to the balance between the centrifugal force, $\left\langle u_\phi \right\rangle^2/r$ or $\cot\theta \left\langle u_\phi \right\rangle^2$, the gravity and the thermal pressure gradient. Hence, the disk is in hydrostatic balance as is expected from a weakly magnetized disk.

As we enter the accreting atmosphere the thermal pressure gradient becomes close to negligible, when compared with the magnetic forces. The radial and latitudinal equilibriums are then enforced by a balance between gravity, the centrifugal force, the magnetic pressure gradient and the hoop stress, $\left\langle B_\phi^2 \right\rangle/(4\pi\left\langle\rho\right\rangle r)$ or $\cot\theta\left\langle B_\phi^2 \right\rangle/(4\pi\left\langle\rho\right\rangle)$. The radial equilibrium is maintained up to the base of the outflow ($\theta \simeq \pi/2 \pm \pi/4$). At this point MHD acceleration is no longer negligible and Eqs. (4.74,4.75) are no longer a valid approximation.

The laminar and turbulent atmosphere are described by a magnetostatic equilibrium, contrary to the disk that is in hydrostatic equilibrium. This magnetostatic equilibrium is a consequence of the laminar and turbulent magnetic pressure gradients (Fig. 4.12). This situation is similar to what was proposed by Begelman et al. 2015, a disk in magnetostatic equilibrium where the magnetic pressure emerges as a consequence of turbulence. Indeed, within this region, there is a powerful average toroidal field, 20 times the vertical field at the disk mid-plane (Fig. 4.4 bottom), that changes sign within the turbulent atmosphere.

This powerful average toroidal field (situated within the laminar atmosphere) is a consequence of the fact that the laminar atmosphere is in ideal MHD. In the LA, the accretion drags the poloidal field lines inwards. The fluid is plunging into a region a higher angular velocity, which leads to enhanced shear for $\left\langle B_\varphi \right\rangle$, increasing its magnitude (Zhu and Stone 2018).

This average toroidal field is supporting the turbulent atmosphere agains gravity. The gradient of the laminar toroidal magnetic pressure allows the levitation of the TA above the disk surface (Mishra et al. 2020). Hence, the levitation of the TA causes the consumption of the toroidal magnetic field. Indeed, as we move further up in the atmosphere the toroidal magnetic field decreases (Fig. 4.4). Then, within the TA $\left\langle B_\varphi \right\rangle$ changes sign, which might be surprising at first. Such a sign change can be seen as a consequence of the argument detailed in section 2.5.4, for the outflow to be launched, the electric current traversing the disk needs to change sign. Furthermore, the toroidal magnetic field needs to be negative within the outflow region or else the Poynting flux vector would not be pointing away from the disk (see section 2.5.2)

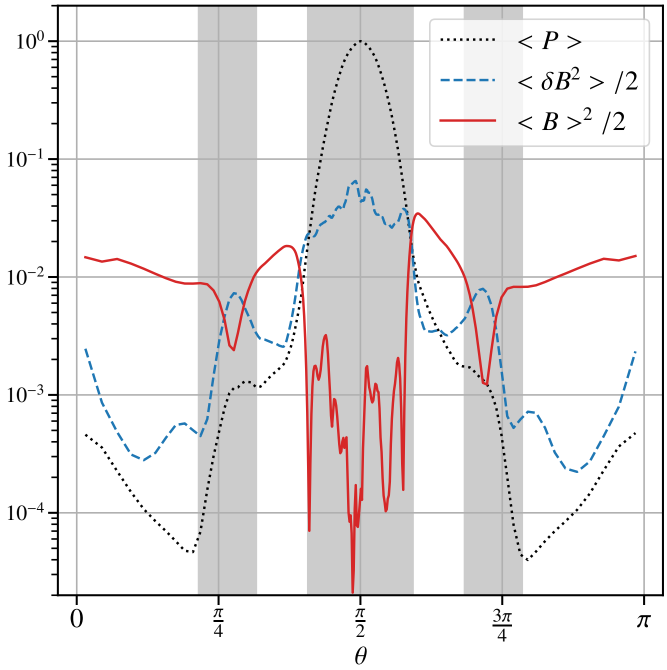

Figure 4.12: Comparison of the different pressure terms normalized to the thermal pressure within the disks mid-plane as functions of the latitudinal coordinate. The shaded areas denote the turbulent regions.

It may seem from Fig. (4.12) that turbulent magnetic pressure plays no role. However, the turbulent magnetic pressure plays a very important role on the dynamics of the system. As we discussed before, the only force capable of loading matter onto the field lines is the thermal pressure gradient, which pushes material to the surface. It is clear in Fig. (4.12) that the laminar magnetic pressure is compressing the disk surface. However, this compression is nowhere to be seen in Fig. (4.11). The turbulent magnetic pressure is counteracting the compression due to the laminar magnetic pressure. This ensures that the material can flow relatively freely from the disk to the atmosphere and enhances the mass loading in the LA region. The same process is at play for the transition between the turbulent atmosphere and the outflow. However, in this case it is the combined effect of thermal pressure and the turbulent magnetic pressure (Fig. 4.12) that allows the loading of the magnetic field lines at the base of the outflow. The reason for the reappearance of the turbulent magnetic pressure within the turbulent atmosphere will be described in section 4.2.7.

4.2.6 Super fast wind structure

In this section we compute the MHD invariants defined in section 2.5.1 for our fiducial simulation. We follow three average magnetic field lines crossing the mid-plane at $R_0 = [5, 6, 8]$ (Fig. 4.13,left). We the compute the ideal MHD invariants across the 3 different field lines anchored at the radii $R_{SM} = [3.5, 4, 7.5]$(Fig. 4.13,right). The invariant are approximately constant once the outflow leaves the turbulent atmosphere. This show that the outflow is stationary and laminar. This is consistent with the fact that $\cos\psi = \pm 1$ in the outflow region. The field lines closest to the central object are the ones that exhibit the least amount of variability in their invariants. The closer they are to the central object the more time they have to numerically converge as the dynamical time scale (Ω_k^{-1}) shortens with radii. Several features of

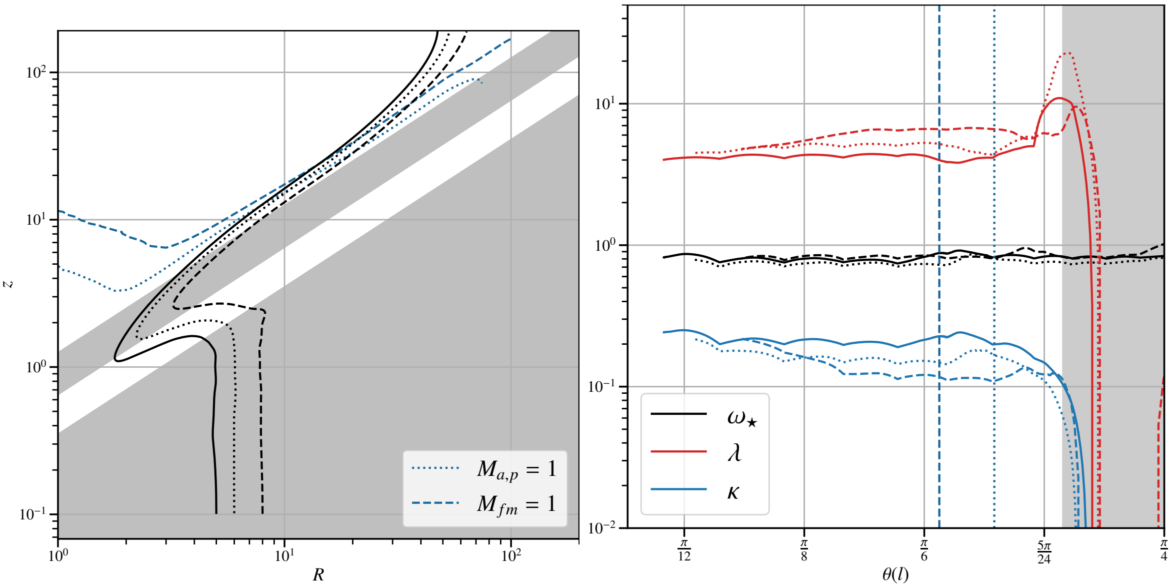

Figure 4.13: Left: mean poloidal magnetic field lines in the (R,z) plane. The blue lines define the different critical surfaces (see section 4.2.1) and they are represented as vertical lines in the lower panel. The grey zones determine the turbulent zones defined in section 4.2.1. The lower zone corresponds to the disk and the upper zone corresponds to the turbulent atmosphere. right: MHD invariants calculated along the field lines of the upper panel as functions of the latitudinal coordinate. The line style of the MHD invariants has a one to one correspondence with the field line where the invariant was calculated. The grey zone corresponds to the end of the turbulent atmosphere.

the outflow structure can be deduced from the MHD invariants:

- The rotation invariant $\omega_\star \leq 1$, indicates that the field lines rotate close the local Keplerian speed at their anchoring radii, or slightly slower. This is consistent with the values expected from self-similar models (Ferreira 1997; Lesur 2021).
- The angular momentum invariant $\lambda \simeq 5$, so the wind is effectively free ($\lambda > 3/2$). This provides $R_A^2/R_{SM}^2 = \lambda/\omega_\star \sim 8$ which is comparable to the value found by Zhu and Stone 2018. We can estimate the terminal velocity of the outflow using the magnetic lever arm (see section 2.5.4). Using this expression we find $u_{p\,\mathrm{inf}} \sim 3\,|R\Omega_K|_{SM}$.
- The mass loading invariant $\kappa \sim 0.1$ implies that the energetic content at the base of the outflow is dominated by the magnetic field and not the kinetic energy, consistent with a jet-like outflow. We also compute the mass loading within the laminar atmosphere, we find $\kappa \sim 8$. The value of κ is almost 2 orders of magnitude larger within the laminar atmosphere when compared to the outflow. This seems to indicate that the reason the laminar atmosphere is falling is because it is so heavily loaded with matter.

The Bernoulli invariant characterizes the energetic of the outflow. Figure (4.14) shows the components of the Bernoulli invariant. The positive sign indicates again that the flow is free from the potential well. When the flow reaches the end of our simulation box, its energy content is dominated by the kinetic component, the magnetic energy has been consumed, the outflow is close to its asymptotic state. We see from Fig. (4.14) that the outflow is cold, i.e. the thermal pressure term, w, is negligible. Furthermore, at the wind launching point, the outflow is dominated by the magnetic energy, and even the gravitational energy is negligible.

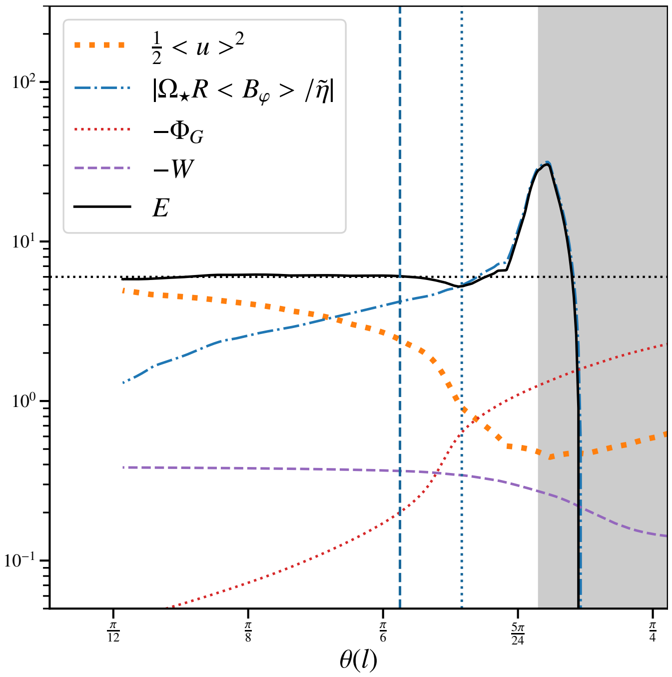

Figure 4.14: Bernoulli invariant and its components for the field line originating at $R_0 = 6$ as functions of the latitudinal coordinate θ. All quantities are normalized to $E_{K,SM} = \Omega_K^2(R_{SM})R_{SM}^2/2$. The shaded grey area corresponds to the turbulent atmosphere, the end of the turbulent atmosphere coincides with the SM surfaces. The vertical lines correspond to the different critical surfaces. The vertical dashed line is the fast magneto-sonic surface while the vertical dotted line is the Alfvénic surface, consistent with the notation figure 4.13.

Finally we also compute the MHD invariants in the south hemisphere for field lines crossing the same radii at the disk mid-plane, $R_0 = [5, 6, 8]$. We compute very similar values, confirming the symmetric nature of the system.

We distinguish if our outflow is jet-like or wind-like using the criterium defined in section 3.4.4. The jet magnetization is computed using Fig. (4.14) to find

$$\sigma = \left.\frac{-\Omega_* r \left\langle B_\varphi \right\rangle \left\langle B_p \right\rangle}{\left(\frac{\langle u\rangle^2}{2} + \langle H\rangle\right) \langle \rho\rangle \left\langle u_p \right\rangle 4\pi}\right|_{SM} \sim 8. \tag{4.76}$$

Since $\sigma > 1$ the outflow is jet-like, compatible with the observed collimation and the values of the mass loading invariant.

4.2.7 Origin of turbulence

The accreting atmosphere is divided into two distinct regions: a laminar atmosphere and above it a turbulent atmosphere (see section 4.2.1). This configuration, where a turbulent layer is localized above the disk has not been described in detail so far. It suggests that within the laminar atmosphere, the source of turbulence is quenched. It also suggest that turbulence must be reinvigorated within the turbulent atmosphere. Since the turbulent atmosphere is highly magnetized ($\left\langle \beta_p \right\rangle \leq 1$), several MHD instabilities could in principle be invoked to explain the source of turbulence (e.g. interchange or Parker instabilities). However, the main source of energy in this region is still the quasi-Keplerian shear, MRI-driven turbulence remains a possibility.

As discussed in section 2.2.3 and section 2.2.2, it is widely believed that the MRI is a weak field instability, quenched when $\left\langle \beta_p \right\rangle < 1$. However, this condition has been derived assuming that the MRI

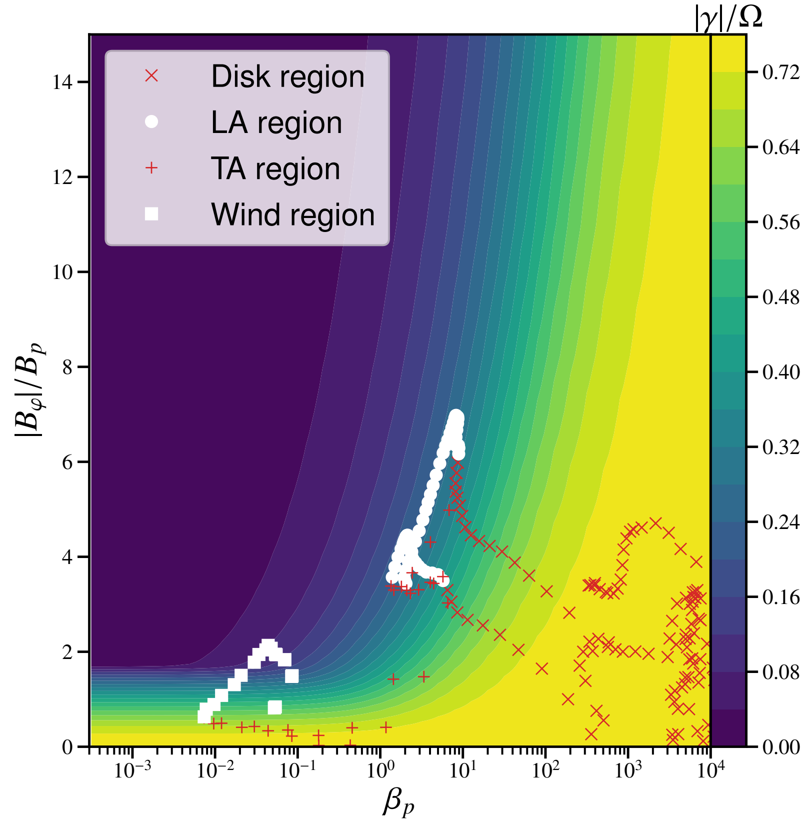

Figure 4.15: Maximum growth rate of the compressible MRI as a function of the poloidal plasma beta and the ratio between the toroidal and poloidal magnetic field, calculated using Eq. (2.52). The red points correspond to the values of the ratio of the magnetic field and the poloidal plasma beta for different regions within our simulation averaged between $r_1 = 8$ and $r_2 = 12$ (see Fig.4.4). We find that laminar regions are characterized by reduced MRI growth rates ($\lesssim 0.25\Omega_K$).

.

modes are confined within the vertical thickness of a disk in hydrostatic vertical equilibrium. In our simulations, the system is puffed up by the turbulent magnetic pressure. It could then be possible that this thicker system allows the existence of the turbulent MRI modes at high magnetic field.

In section 2.2.3 we derived a stability condition under which the MRI is suppressed in the limit of strong magnetic field (Eq. (2.53)), it reads

$$\frac{\left\langle B_\phi \right\rangle^2}{\langle B_z \rangle^2} > \frac{3}{4} \quad \text{with} \quad \left\langle \beta_p \right\rangle \to 0 \quad \Rightarrow \quad \text{stability.} \tag{4.77}$$

This condition is indeed verified in the laminar atmosphere (Fig.4.4,bottom). Since Eq.(4.77) is verified within the laminar atmosphere, the laminar atmosphere should be stable to the MRI. We super imposed the maximum growth rate computed in section 2.2.3 with our numerical results. We use the profiles of the magnetic field components and pressure of our simulations to characterize the value of the MRI growth rate within each region.

From Fig. (4.15) we find that regions where the MRI growths at a sufficient rate ($\geq 0.25\Omega_K$) correspond to the zones described as turbulent in section 4.2.1. On the contrary the MRI has a smaller growth rate within the laminar regions. We therefore conclude that the MRI is probably the main driver of turbulence within the turbulent atmosphere.

As discussed in section 4.2.5 the powerful toroidal magnetic field is consistent with the laminar atmosphere. This laminar atmosphere facilitates the winding of the magnetic field lines. Furthermore, the decrease of the toroidal magnetic field within the turbulent atmosphere is also consistent with the magnetostatic equilibrium of the atmosphere. We hypothesize that the re-ignition of turbulence is required for the establishment of a stationary magnetostatic equilibrium.

Finally, the re-ignition of turbulence will produce anomalous resistivities within the turbulent atmosphere that allow accretion thought the poloidal field lines and a steady state transition between accretion and ejection (Ferreira and Pelletier 1995). It is therefore an essential ingredient for outflow launching.

4.3 Parameter exploration

We start by validating the wedge approximation, $\Delta\varphi = \frac{\pi}{2}$, for global simulations, S2pi harbors no significant differences. Indeed, S2pi and SB4 are identical with respect to the properties of their vertical structure. In the rest of this section we will mostly ignore S2pi when we discuss those properties.

We now explore how the properties described in the section above change as we explore the parameter space by changing the initial magnetization, μ_{ini} and the geometrical thickness, ε (see Tab.4.1). In this section we compute the averages defined in section 2.3.1 for all simulations between t_1 and $t_2 = T_{\text{end}}$ (see Tab.4.1) with a $\Delta t = 0.16 T_{\text{in}}$.

We first confirm that all weak field simulations $\mu_{ini} < 10^{-3}$ converge to a steady state similar to the one described in section 4.2: a turbulent disk, an atmosphere with super sonic accretion and a super-fast wind. Therefore we address the weak field simulations first while the steady state of simulation SB2 will be described at the end of this section. To compare the initial magnetization, μ_{ini}, with the one achieved once the simulation reaches a steady state we define

$$\mu_{\text{mid}} = \left. \frac{\langle B_z \rangle^2}{4\pi P} \right|_{r,\theta=\frac{\pi}{2}} . \tag{4.78}$$

This magnetization is roughly equal to μ_{ini} for weakly magnetized simulations but not for SB2.

4.3.1 Low magnetic field simulations

We show in Fig. (4.16) the vertical structure of simulations SB3 and SEp. We see that their vertical structure is very similar to the one of simulation SB4. Moreover, we see that similarly to SB4, all weak-

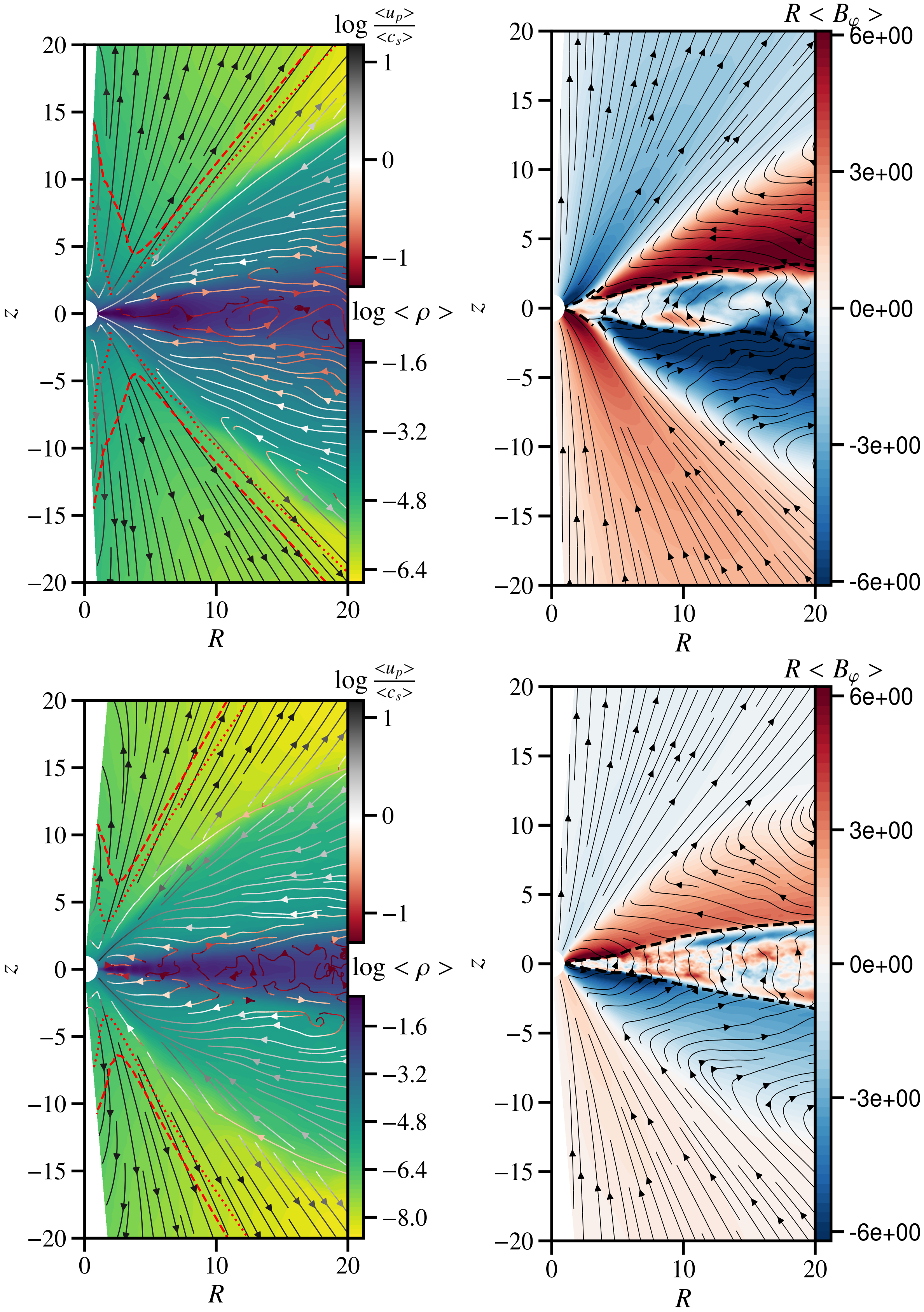

Figure 4.16: Same as bottom Fig. (4.2) but for simulation SB3 (top) and SEp (bottom).

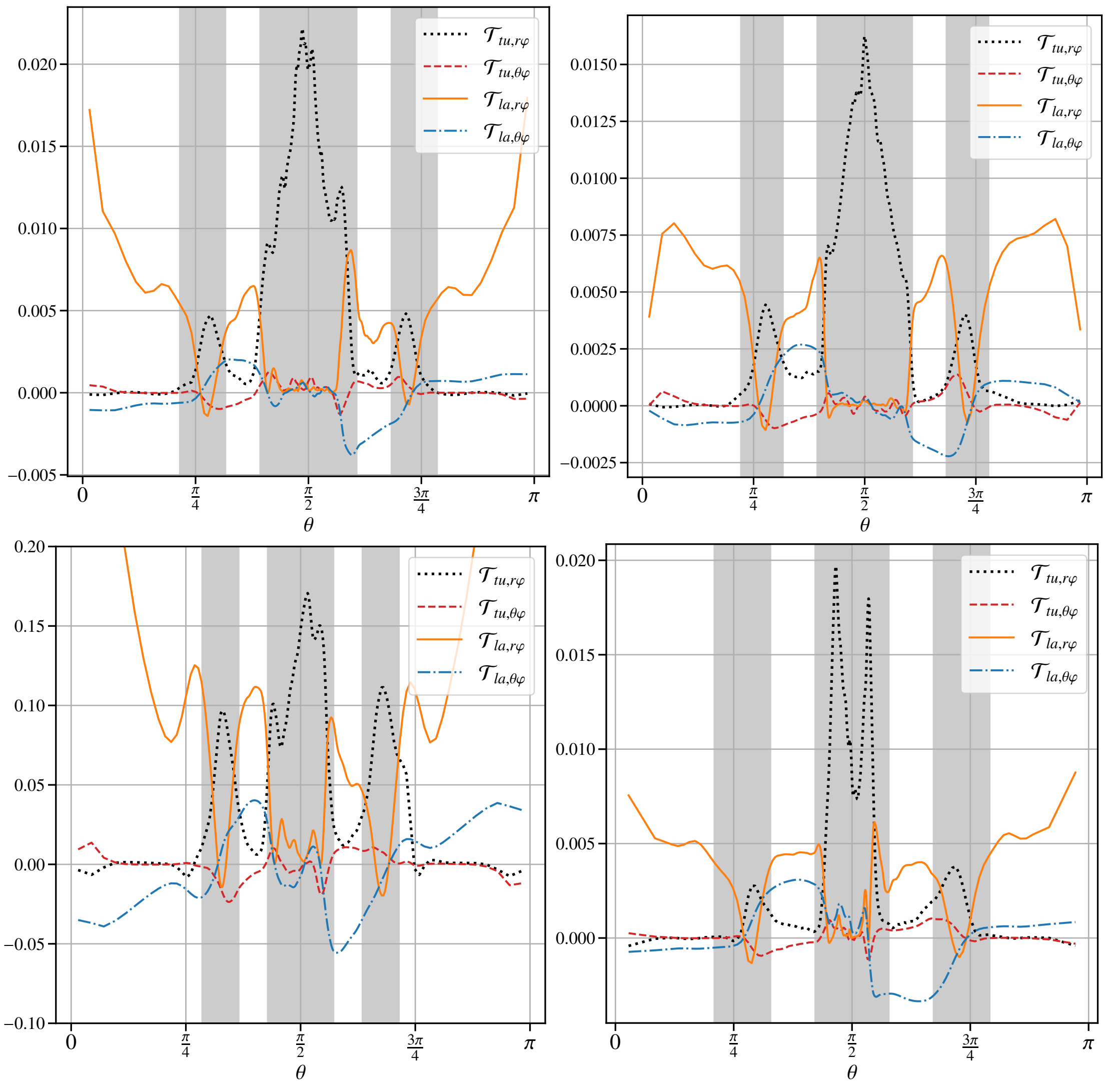

Figure 4.17: Stress vector components of $\mathcal{T}_{tu}$ and $\mathcal{T}_{la}$ normalized to the pressure at the disk mid-plane (defined in section 2.3.2) as functions of the latitudinal coordinate for simulations SB4 (top,left), S2pi (top,right), SB3 (bottom,left) and SEp (bottom,right). The shaded regions correspond to the turbulent regions defined using $\cos\psi$.

field simulations reach a equilibrium within the disk and a magnetostatic equilibrium within the laminar and turbulent atmospheres given by Eq. (4.74,4.75).

We quantify the evolution of the turbulent stratification as a function of the different parameters by comparing the extent and heights of the turbulent disk, the laminar atmosphere and the turbulent atmosphere for the different simulations. We quantify the extent and height of the region by looking at $\cos\psi$ the angle between the poloidal velocity and the poloidal magnetic field (section 4.2.1). We compare the values measured with this method and the ones given by the ratio between the turbulent and laminar torques, $\mathcal{T}_{tu}$ and $\mathcal{T}_{la}$. We show the different components of the stress tensors for the different simulations in Fig. (4.17), the shaded regions corresponding to the turbulent regions defined using $\cos\psi$. We see that the turbulent regions are those where the turbulent stress tensor dominates the angular momentum transport (consistent with section 4.2.1). Moreover, the strength of the turbulent stress tensor within the disk increases by a factor of 5 with the magnetization (from SB4 to SB3) and seems to be independent of the disk geometrical thickness.

We summarize our findings in Fig. (4.18) where we show the turbulent regions (disk and atmosphere) as shaded regions of different colors for the different simulations. We see that when the magnetic field increases (from SB4 to SB3) the disk region decreases in size. This is because the quenching of the MRI is only possible when $\left\langle \beta_p \right\rangle \sim 1$ (section 4.2.7). Hence, starting at a higher $\mu_{\rm mid}$ (lower $\left\langle \beta_p \right\rangle$ at the disk mid-plane) limits the vertical extent of the disk and pushes the transition to the laminar atmosphere at lower altitudes.

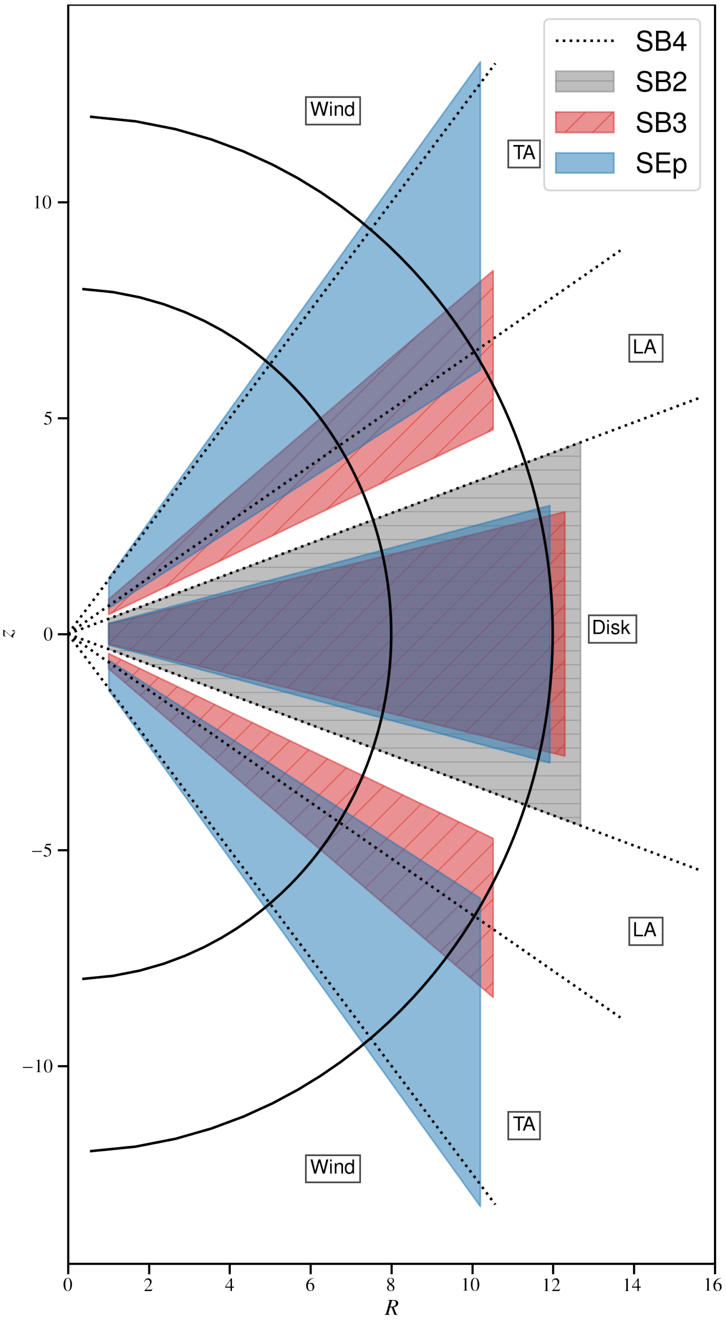

Figure 4.18: Extent of the turbulent zones (disk and atmosphere) found in the different simulations, see Tab. (4.1). As the magnetic field increases, the turbulent layer goes down and eventually merges with the turbulent disk.

In Fig. (4.18) we also see that when $\mu_{\rm mid}$ increases the turbulent atmosphere plunges towards the disk lowering the altitude of the base of the outflow. The altitude of the outflow launching surface is tightly related to the density profile. In Fig. (4.19) we show the density profiles of the different simulations normalized to their value at the disk mid-plane. We see that the simulations SB4 and S2pi converge to a similar density configuration validating the wedge approximation. Moreover, we observe in Fig. (4.19)

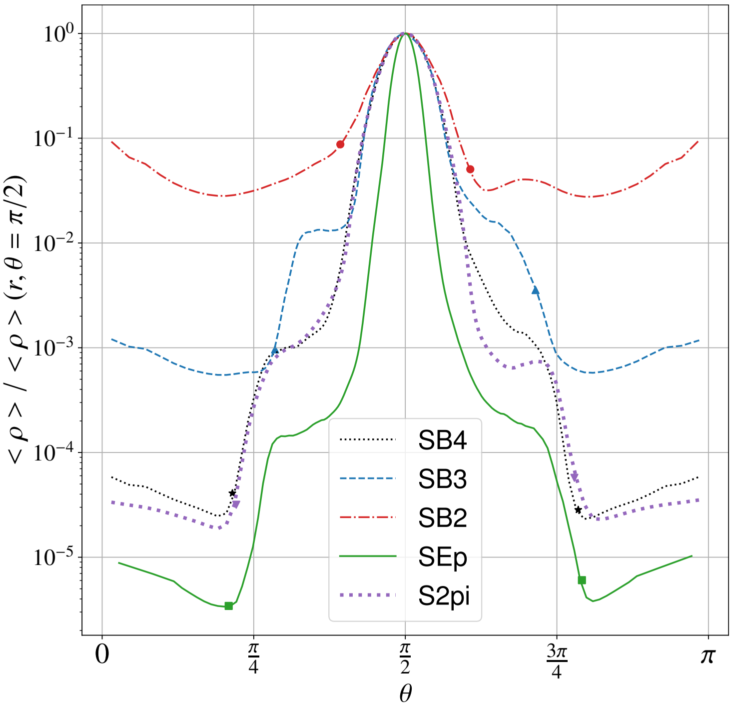

Figure 4.19: Mean density of the different simulations normalized to its value at the disk mid-plane, see Tab. (4.1). The symbols correspond to the height at which the flow reaches the SM speed. The mean profile are also averaged radially between $r = 8$ and $r = 12$.

that as $\mu_{\rm ini}$ increases the density profile becomes shallower and as a consequence, more mass is fed into the TA and the outflow. This is possibly related to the enhanced mass loading due to the push of the turbulent magnetic pressure. Indeed, increasing $\mu_{\rm ini}$ leads to a increase of $\mu_{\rm mid}$ which increases the turbulence strength (Salvesen et al. 2016; Mishra et al. 2020). This increase in turbulent strength with the increment of the disk magnetization is also verified in our simulations.

We see that as the disk geometrical thickness decreases, the vertical extent of the turbulent disk decreases (Fig. 4.18,4.19), as would be expected. Strikingly the turbulent atmosphere stays at roughly the same height compared to SB4. The height of the turbulent atmosphere mostly depends on the magnetization at the disk mid-plane and not on the disk geometrical thickness. Nonetheless, the steepness of the density profile is affected, leading to a less dense turbulent atmosphere for $\varepsilon = 0.05$. It is not clear if an even smaller ε could lead to the disappearance of the turbulent and laminar atmospheres.

The initial magnetization and the disk geometrical thickness also affects the secular evolution of the system. To show this, we compute $v_{\rm acc}$ and v_Ψ defined in section 4.2.4 and we average them between $t_a = 318 T_{\rm in}$ and $t_b = 955 T_{\rm in}$ with temporal resolution of $\Delta t = 0.8 T_{\rm in}$ for all simulations.

First we confirm that $v_{\rm acc}$ scales radially as the Keplerian velocity, we summarize the values of $v_{\rm acc}$, normalized to $V_K(R)$, in tab. 4.2. We see that as the initial magnetization increases the mass weighted accretion velocity also increases. However, the value of $\langle u_R \rangle$ within the accreting atmosphere doest not depend of the initial magnetization or ε, its value is roughly $0.3 V_K(R)$ for all weak field simulations. Therefore, the dependency of $v_{\rm acc}$ must be a consequence of the evolution of the vertical density profile. Indeed, in Fig. (4.19) we see that when μ_{ini} increases the density profile becomes shallower and the accreting atmosphere becomes denser. Furthermore, the decrease of $v_{\rm acc}$ as ε decreases is also a consequence of the density profile. We conclude that the magnitude of $v_{\rm acc}$ is tightly related to the vertical density structure.

In Fig. (4.20) we show the space time diagram of the magnetic flux for simulations SB3 and SEp. We clearly see that both simulations transport the magnetic field towards the inner boundary. The magnetic field transport velocity for simulation SB3 seems faster than the one of simulation SB4. In contrast, v_Ψ

Name	$-v_{\mathrm{acc}}\ [V_K]$	$t_{\mathrm{acc}}\ [T_K]$	$t_\Psi\ [T_K]$	$\langle\mu_{\mathrm{mid}}\rangle$
SB4	1.1×10^{-3}	144	160	2×10^{-4}
SB3	1×10^{-2}	16	31	2×10^{-3}
SEp	4×10^{-4}	400	1.1×10^{3}	2×10^{-4}
SB2 ($R>8$)	4×10^{-2}	4	5	8×10^{-2}
SB2 ($R<4$)	2×10^{-1}	1	265	2

Table 4.2: Values of the mass weighted accretion velocity defined in section 4.2.4 in units of V_K for the different simulations. We also show the accretion time scale calculated from the first column in units of the local $T_K(R) = 2\pi/\Omega_K(R)$ as well as the magnetic advection time scale in the same units, calculated from Fig. (4.21) (left). Finally, we include the mean poloidal $\left\langle\beta_p\right\rangle$ at the disk mid-plane. Quantities are temporally averaged between $t_a = 318T_{\mathrm{in}}$ and $t_b = 955T_{\mathrm{in}}$.

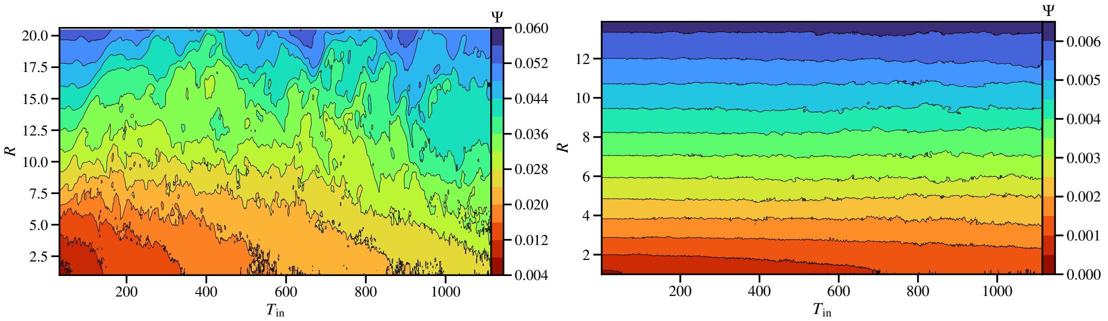

Figure 4.20: Magnetic flux threading the disk midplane Ψ, computed between the axis and R, as a function of time in innermost orbital units for simulations SB3 (left) and SEp (right). Every contour line represents a field line.

for simulation SEp seems smaller than the one of SB4. To better quantify the magnetic transport we compute v_ψ, defined in Eq. (2.106) for all our simulations. We then average this quantify in the same manner as v_{acc}. The evolution of the field transport velocity, normalized to the Keplerian velocity, is shown in Fig. (4.21,left). It is clear that v_Ψ, in the same manner as v_{acc}, approximately follows the radial scaling of the Keplerian velocity. Those trends do not apply for the inner regions of simulation SB2, that we discuss in the following section. We notice that the magnitude and behavior of the transport velocity for simulation S2pi agrees with the one of simulation SB4.

Figure (4.21) shows that when μ_{ini} increase v_Ψ/V_K also increases, v_Ψ/V_K seems proportional to $\langle\mu_{\mathrm{mid}}\rangle$. The transport velocity sharply decreases when we decrease the disk geometrical thickness.

The ratio of the field transport velocity and the mass weighted accretion velocity, v_Ψ/v_{acc}, as a function of the radial coordinate is displayed in Fig. (4.21,right). All simulations, except the inner regions of SB2, follow approximately the same dependency

$$v_\Psi \simeq v_{\mathrm{acc}}. \tag{4.79}$$

This is remarkable and must be related to the evolution of the vertical structure since, as explained above, the evolution of v_{acc} is tightly related to it.

The accretion times scale as well as the magnetic advection time scale are shown in Tab. (4.2) computed from their respective velocities. In all simulation the secular time scales t_Ψ and t_{acc} remain longer than the dynamical time scale T_K. Nonetheless, a word of caution is appropriate since for simulation SB2 the accretion time scale t_{acc} is of the order of the dynamical time scale, while t_Ψ is comparable for the outer regions of SB2. Indeed, as was discussed in section 3.1.1 for the Ohm equation (Eq. 3.5) to be valid the advection of the magnetic field needs to be negligible with respect to the other terms. Indeed, the

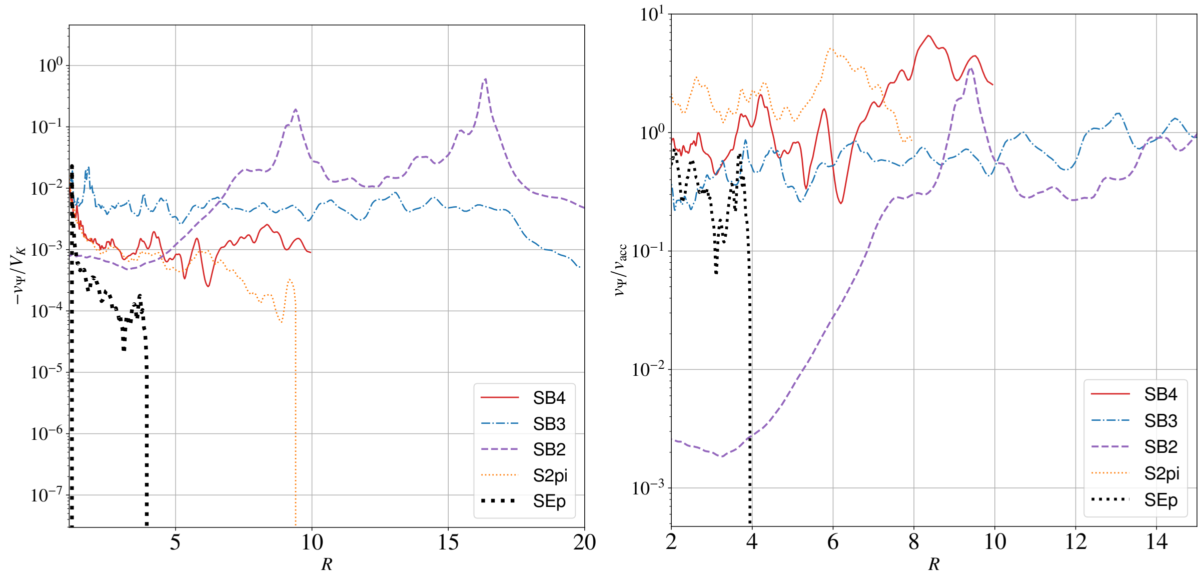

Figure 4.21: (left) Field transport velocity as a function of radius normalized to the Keplerian velocity. (right) Ratio of field and mass advection velocities as a function of radius. We truncate the transport velocity where we can no longer measure the drift of the magnetic field lines. The truncation radii corresponds to $R = 3.5$, $R = 10$, $R = 20$, for SEp, SB4 and SB3 respectively.

field transport velocity can be written as (see section 2.4.3)

$$v_\Psi = \langle u_R \rangle - \langle u_z \rangle \frac{\langle B_R \rangle}{\langle B_z \rangle} - \frac{\mathcal{E}_\varphi(t)}{\langle B_z \rangle}, \tag{4.80}$$

we see that if $v_\Psi \sim 0$ we obtain following Ohm's law[1]

$$\frac{4\pi}{c}\eta \left\langle J_\varphi \right\rangle \mathbf{e_\varphi} = \left\langle \mathbf{u_p} \right\rangle \times \left\langle \mathbf{B_p} \right\rangle . \tag{4.81}$$

Therefore, the Ohm equation is not an accurate approximation for the simulations with a high magnetic transport velocity, like the outer regions of SB2 or even SB3. In that case the advection of the magnetic field should be considered when looking for a solution of the ideal MHD equations. See for example the works of Ogilvie and Livio 2001 and Guilet and Ogilvie 2012 using an asymptotic expansion to calculate the vertical equilibrium of the disk and also the work of Contopoulos et al. 2017 using the self-similar framework.

The values of the MHD invariants for the different simulations are summarize in Tab. (4.3) as defined in section 2.5.1. They are all computed from a field line originating at $R_0 = 6$. The MHD invariants do not vary considerably from one simulation to another. This may seem surprising. However, it should be kept in mind that the wind invariants depend on the flow dimensionless properties ($\langle u_r \rangle / V_K$, $\left\langle u_\phi \right\rangle / V_K$, $\langle B_r \rangle / \langle B_\theta \rangle$, $\langle B_r \rangle / \left\langle B_\phi \right\rangle$) at the wind launching point, that is the top of the turbulent atmosphere. Since these dimensionless properties are similar between all weak-field simulations, the invariants should naturally be independent of $\langle \mu_{\rm mid} \rangle$.

4.3.2 Towards strongly magnetized disks

As stressed above, simulation SB2 differs from the other simulations because the whole disk is subject to a drastic reorganization of the vertical magnetic field, and it takes much longer to converge to a reasonable steady state. At $t_{\rm end} = 1910T_{\rm in}$, only the region below $R \simeq 7$ has reached a steady state, while the outer

---

[1] We also need to assume a resistive closure for the turbulent emf

Name	ω	λ	κ	e
SB4	0.8	5	0.2	6
SB3	0.9	4	0.4	6.5
SB2	0.9	4.5	0.75	6
SEp	0.8	5	0.2	6

Table 4.3: Values of the MHD invariants for all simulations, measured in the upper 'hemisphere' for a field line originating at $R_0 = 6$.

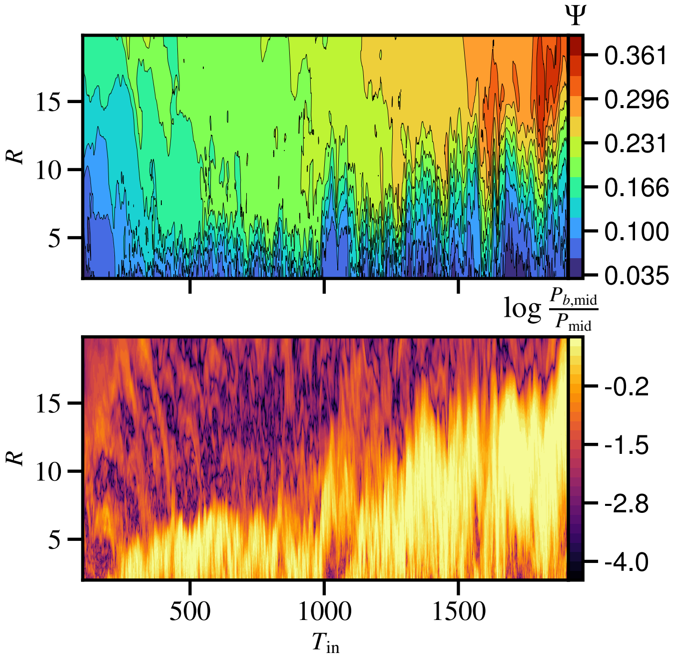

Figure 4.22: Magnetic field flux Ψ (top) defined in Eq. (4.59) and ratio $P_{b,\mathrm{mid}}/P_{\mathrm{mid}}$ (bottom) (see text) as functions of time and the radial coordinate for simulation SB2. We note that $P_{b,\mathrm{mid}}/P_{\mathrm{mid}} > \frac{\mu_{\mathrm{mid}}}{2}$ since the former contains also the turbulent magnetic pressure.

regions continue to struggle readjusting the magnetic field distribution. We show Ψ for simulations SB2 in Fig. (4.22,left), we observe that the magnetic field is violently advected in the initial stages. Simulation SB2 converges to a state where the inner regions are highly magnetized ($\mu_{\mathrm{mid}} > 0.3$) and quasi-stationary, while the outer regions stay weakly magnetized ($\mu_{\mathrm{mid}} \sim \mu_{ini}$) and where the magnetic distribution is still evolving. We define R_j as the end of the equipartition field region.

The large v_Ψ of the outer regions shown in Fig. (4.21) commands the reorganization and leads to the lack of stationarity for the outer regions. However, in the inner regions ($R_j < 7$) the transport velocity goes to 0, turbulent field diffusion balances advection leading to $v_\Psi \to 0$. When the transport velocity tends to zero the magnetic flux has no other choice but to accumulate at larger radii. The transition radius R_j increases with time as more magnetic field is being brought in. This can be clearly seen in Fig. (4.22,bottom) where we show the ratio $P_{b,\mathrm{mid}}/P_{\mathrm{mid}}$, where

$$P_{b,\mathrm{mid}} = \frac{1}{8\pi}\left[\frac{1}{2h_{\mathrm{disk}}}\int_{\theta_{d1}}^{\theta_{d2}} r\sin\theta\,\langle B_z\rangle_\phi\,\mathrm{d}\theta\right]^2, \tag{4.82}$$

$$P_{\mathrm{mid}} = \frac{1}{2h_{\mathrm{disk}}}\int_{\theta_{d1}}^{\theta_{d2}} r\sin\theta\,\langle P\rangle_\phi\,\mathrm{d}\theta, \tag{4.83}$$

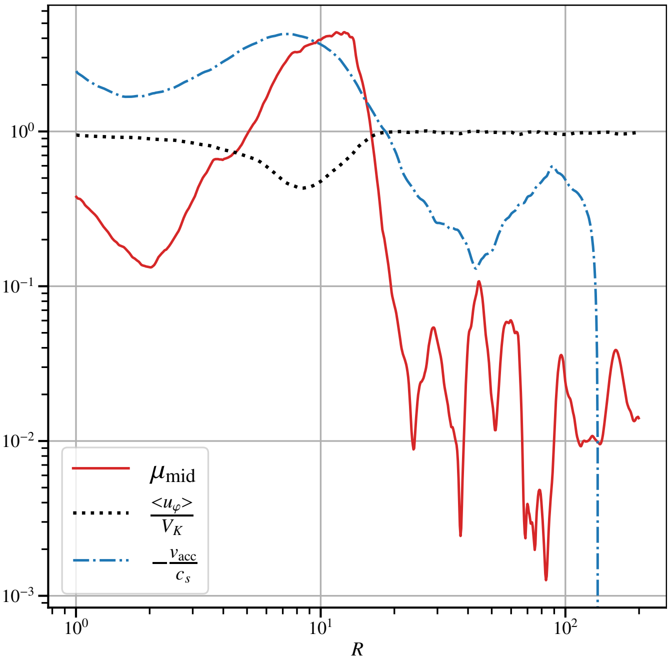

Figure 4.23: The magnetization ($\mu_{\rm mid}$), the mass weighted accretion normalized to the sonic velocity, and the toroidal velocity evaluated at the disk mid plane normalized to the Keplerian velocity as function of radius. The quantities are averaged between $t_1 = 1910T_{\rm in}$ and $t_2 = 1719T_{\rm in}$, not between $t_a = 318T_{\rm in}$ and $t_b = 955T_{\rm in}$.

and $\theta_{d2,d1} = \pi/2 \pm \arctan(h_{\rm disk}/R)$. We can see that the inner regions are dominated by the magnetic pressure. Indeed, the ratio $P_{b,\rm mid}/P_{\rm mid}$ is larger than $\mu_{\rm mid}$ since it contains the turbulent field contribution $\left\langle \delta B^2 \right\rangle$ (more details below). We measure the radial drift speed of the transition radius R_j to be

$$\dot{R}_j \sim 10^{-3} V_K(R_{\rm in}). \tag{4.84}$$

The transition radius increases in burst and while dramatic changes are happening in the disk, its evolution is highly variable.

Describing the details of this transition region is beyond the scope of this work (see discussion next section). However, we show in Fig. (4.23) the radial distribution of the magnetization ($\mu_{\rm mid}$), $v_{\rm acc}/c_s$ and $\left\langle u_\varphi \right\rangle / V_k$ (evaluated at the disk mid-plane) averaged between t_1 and t_2, we can see how they evolve through the transition. We confirm that the inner disk is highly magnetized while the outer disk stays close to its initial weakly magnetized state. The saturation value for the magnetization is slightly above the equipartition (Fig. 4.23), this may seems inconsistent with the constraint of the vertical equilibrium. However, for simulation SB2 the vertical equilibrium is highly modified by a strong $\left\langle \delta B^2 \right\rangle$ at the disk mid-plane (Fig. 4.24,left). This turbulent magnetic pressure allows for a stronger laminar magnetic field compression and thus a larger value of $\mu_{\rm mid}$.

We notice that at R_J the mass weighted accretion flow becomes supersonic, the inner regions are strongly decelerated by the turbulent and laminar torques. The components of the stress vectors are shown in Fig. (4.24,right), we can see that the laminar latitudinal torque becomes dynamically important for strongly magnetized disks. We see that the highly magnetized inner disk is still rotating close to the Keplerian speed (Fig. 4.23), it is not arrested. Nonetheless, at the transition, R_j, the toroidal velocity reaches a minimum value of roughly $0.6V_K(R)$.

As shown in Fig. (4.18) the turbulent atmosphere merges with the disk. This is consistent with the previous section, when the magnetization increases the turbulent atmosphere plunges towards the disks. This is true for the inner and outer regions of simulation SB2. The laminar atmosphere disappears and a thicker disk is formed after absorbing the turbulent atmosphere. The merging of the turbulent disk

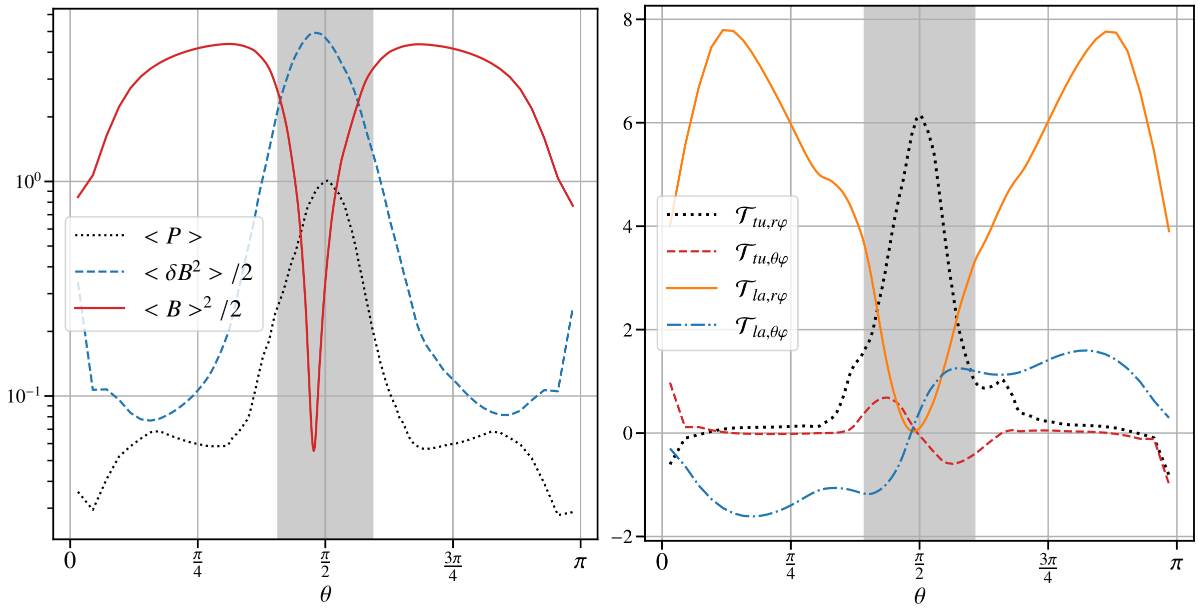

Figure 4.24: (left) Turbulent magnetic, thermal and laminar magnetic pressures as function of the latitudinal coordinate normalized to the thermal pressure at the disk midplane. (right) Stress vector components of $\mathcal{T}_{tu}$ and $\mathcal{T}_{la}$ normalized to the pressure at the disk mid-plane (defined in section 2.3.2) as functions of the latitudinal coordinate for simulations SB2. The shaded regions correspond to the turbulent regions defined using $\cos\psi$. All quantities are radially averaged within the inner regions of the simulation ($R \in [3, 6]$)

and turbulent atmosphere has direct consequences on the density profile (Fig. 4.19). As described in the previous section, the turbulent magnetic pressure determines the steepness of the density profile. Thus, as the disk magnetization increases the amount of mass lifted by the turbulent magnetic pressure increases, leading to a massive turbulent atmosphere that merges with the disk. To understand the dynamical impact of the turbulent magnetic pressure in simulation SB2, we show in Fig. (4.24,left) the profiles of the different pressures, radially averaged within the inner regions. We see that the turbulent magnetic pressure dominates at the disk midplane by almost and order of magnitude. It is thus the main driver behind the deviation of the accretion into the base of the outflow (section 2.5.4) and is quintessential in counteracting the compression of the laminar magnetic pressure, ensuring thereby a vertical balance.

We notice that the definition of the turbulent disk given by $\cos\psi$ agrees quite well with their behavior (Fig. 4.24,right). Indeed, the turbulent stress vectors only dominate the dynamics within the turbulent disk. We see that the radial turbulent stress tensor is very powerful within the disk, leading to effective values of α that are of the order of unity. We have verified that the turbulent disk of simulation SB2 satisfies the criterium of compressible MRI described above. The turbulence is consistent with the strong field compressible MRI (section 4.2.7) and leads to a turbulent disk region in magnetostatic equilibrium, much alike the turbulent atmosphere of weak-field simulations, even though the mean magnetic field is close to equipartition. Since the stratification is modified by the magnetostatic equilibrium the MRI modes have more space than within an hydrostatic disk. Hence, the maximal magnetization at which MRI can take place is larger because larger MRI modes can fit within the system.

Figure 4.25 shows the quasi-stationary inner structure of simulation SB2, averaged between $t_1 = 1719T_{\rm in}$ and $t_2 = 1910T_{\rm in}$. The magnetic topology is clearly distinct from the one observe in weakly magnetized simulations (Fig. 4.2,4.16). Its structure is remarkably similar to the one originally invoked in Blandford and Payne 1982 and later computed by Ferreira 1997. A cold and dense outflow is launched from the disk surface at $z \simeq 3.5h$, becoming soon a super Alfvénic (red dotted curve) and then super fast magneto-sonic (red dashed curve) jet.

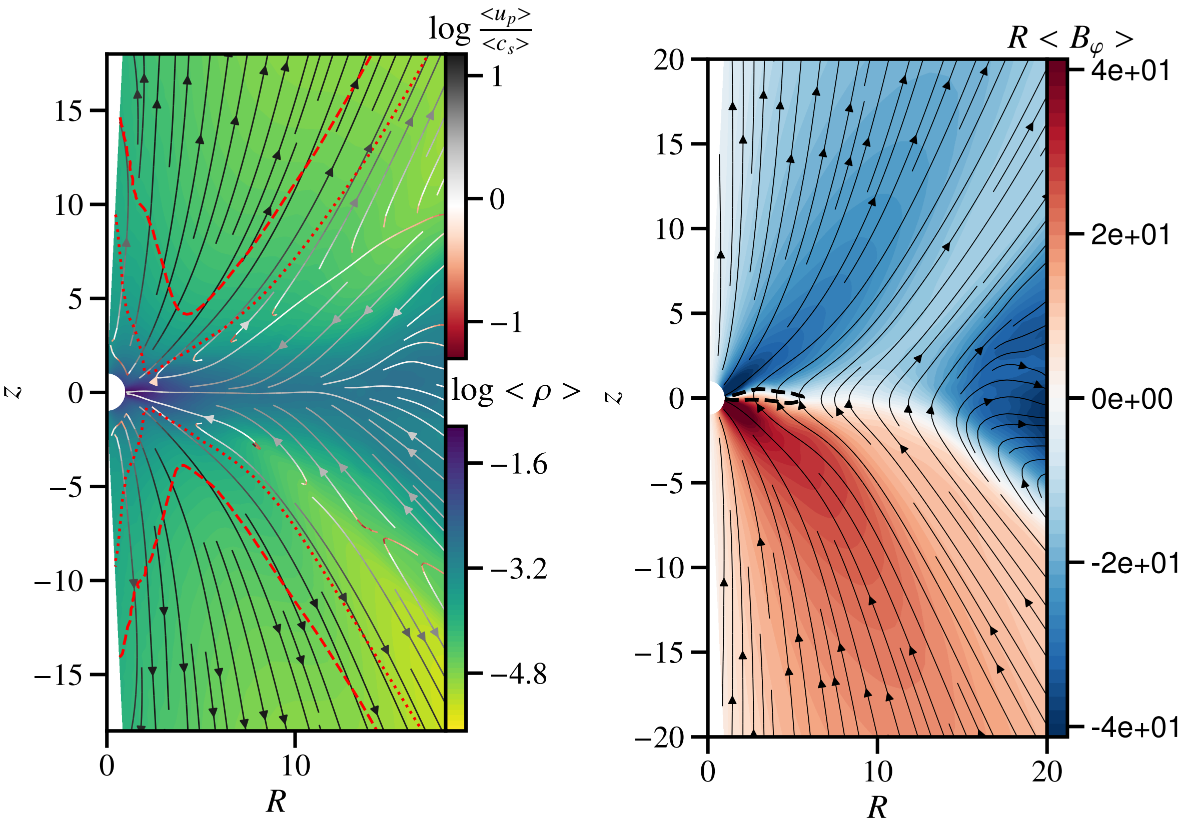

Figure 4.25: Same as bottom Fig. (4.2) but for simulation SB2.

4.4 Comparison with other work

Our results on the vertical structure of weakly magnetized accretion disk, have been already observed in the work of Zhu and Stone 2018 and later confirmed for $\varepsilon = 0.05$ in Mishra et al. 2020. However, these authors did not study in detail the dynamical role of turbulence on the appearance and stability of the vertical structure. Mainly, that the turbulent magnetic pressure is a quintessential agent in establishing the accreting atmosphere. Moreover, both authors failed to distinguish the appearance of a second turbulent layer above the accretion disk and within the accreting atmosphere, making the transition with the outflow.

Both authors did measure the field transport velocity. Zhu and Stone 2018 measures the evolution of the radial magnetic field at the inner radial boundary. They report a small amount of magnetic flux accumulation through their inner boundary albeit without providing a clear analysis. The strong field simulations of Mishra et al. 2020 are somewhat different as they do not detect considerable magnetic flux evolution, in contrast with our results. One possibility is that it may be a bias of their analysis method. Indeed, they compute the magnetic flux crossing the cylinder between $R = 0.1$ and $R = 1$. As $R = 1$ is far from their inner boundary it is possible that this region has not started accreting magnetic flux. We compute in section 4.2.4 that a local region at a distance R starts advecting magnetic flux after approximately $30T_K(R)$. We see in their Fig. 16 that in the best case scenario only 50 local orbits have been integrated at $R = 1$. Another possibility is that it may be a consequence of their disk being two times thinner than ours ($\varepsilon = 0.05$). Indeed, Fig. (4.21) clearly shows that the geometrical thickness has a tremendous impact on the magnetic field advection speed (see e.g. Lubow et al. 1994). This is an interesting aspect with potentially strong astrophysical consequences and deserves further investigations.

Magnetic field dragging has also been measured in General Relativistic MHD simulations of accretion disk around Kerr black hole (e.g. McKinney et al. 2012; White et al. 2019 and references therein, see also Liska et al. 2020). Inward field advection seems to be a generic property of ideal MHD accretion disks threaded by a large scale magnetic field (provided that $\varepsilon \sim 0.1$ or larger). GRMHD simulations also find that the magnetic flux ends up concentrated into the inner regions, leading to the build up of what has been termed a Magnetically Choked Accretion Flow (MCAF) (McKinney et al. 2012). It is more often termed Magnetically Arrested Disk (MAD) in the literature but, as we saw and also stressed in McKinney et al. 2012, the disk is still rotating. Hence, we prefer the MCAF or JED terminology. This is what we observe in simulations SB2, once the magnetic field reaches the equipartition value, the magnetic flux accretion stops, defining a transition radius, R_J with an outer disk at lower magnetization. As more magnetic flux is being advected, a violent relaxation occurs at this radius. The excess magnetic flux is expelled out leading to a progressive increase in time of R_J. This happens as long as some magnetic flux remains available in the simulation (McKinney et al. 2012). It is still unclear if this violent relaxation involves a magnetic Rayleigh-Taylor instability (RTI).

This situation is quite nicely consistent with the hybrid disk configuration proposed for the inner regions of YSO disks (Combet and Ferreira 2008; Ferreira and Casse 2013; Wang and Goodman 2017) and around black holes (Ferreira et al. 2006b). Within this framework, an inner jet emitting disk (JED, Ferreira 1997) is established until a transition radius R_J, beyond which an outer Standard Accretion Disk (SAD, Shakura and Sunyaev 1973) is settled. Because of its supersonic accretion speed associated with the launching of powerful jets, a JED provides the physical conditions allowing to explain most observational properties of X-ray Binaries (see Marcel et al. 2019 and references therein).

One of our main results is the realization of the utmost importance of the MRI in the strong field regime (Kim and Ostriker 2000) for accretion-ejection structures. While it is widely believed that the MRI can only exist in high β plasmas, Kim and Ostriker 2000 have shown that the MRI exist for arbitrary β provided that arbitrary long wavelength perturbations are allowed. In the $\beta < 1$ regime, the MRI can be quenched when the toroidal field gets too strong. We have shown that the turbulent and laminar regions of the atmosphere, which is a $\beta < 1$ region, is naturally explained by the MRI in this peculiar regime. In contrast with our simulations, White et al. 2019 find that in GRMHD simulations the MRI instability is quenched in the highly magnetized regions of the accretion disk system. Their analysis is based on the fact that the critical MRI wavelength is larger than the disk density scale height. However, they do not consider the effect of stratification on the MRI wavelength. Marshall et al. 2018 find that the radial turbulent angular momentum transport in the highly magnetized regime is deeply affected by the RTI-driven turbulence. Nonetheless, they can not conclude that the MRI is unimportant.

We can compare the parameter space explored in our simulations with the one computed in the previous chapter using self-similar solutions. The outflow invariants computed in our simulations (Tab. 4.3) are found consistent with the borders of the parameter space (Fig. 3.13). However, Fig. (3.13) shows values of λ from 2 to 100, while in our simulations $\lambda \sim 4-5$ is roughly constant. We also see in Fig. (3.13) that we have produced outflows with mass load κ ranging from a few 10^{-3} to almost unity, while our 3D simulations always provide $\kappa \sim 0.2-0.7$. This discrepancy is related to our different vertical stratification. In our simulations, the levitating turbulent atmosphere acts as a buffer between the proper turbulent disk and the ideal MHD outflow. Hence, the properties of the outflow are only determined by the turbulent atmosphere, which has pretty uniform properties across the different simulations.

The mass loading parameter, ξ, defined as the power-law exponent of the mass accretion rate, $\dot{M}_a \propto R^{\xi}$, is hard to characterize in global simulations. The radial properties of global simulations take a long time to converge. It is thus hard to measure the effect of the mean vertical magnetic field on the radial configuration of the system. Furthermore, since the system is not strictly stationary the value of ξ measured using the wind properties (see section 4.2.6) does not necessarily correspond with the value given by the radial profiles. Nonetheless, we can compute a value of ξ using the values of λ and Λ_s computed in this chapter for SB4 and the equation (see section 2.3.2)

$$\lambda \simeq 1 + \frac{1}{2\xi}\frac{\Lambda_s}{\Lambda_s + 1}. \tag{4.85}$$

Using $\lambda \simeq 5$ and $\Lambda_s \simeq 1$ we find $\xi \simeq 0.06$ which is consistent with a jet-like outflow.

We observe the opposite behavior for the outflow mass loading as a function of the magnetization in our simulations compared to our self-similar solutions. Recall that in chapter 3 we observe that weakly magnetized simulations launched denser outflows. In this chapter, we found that strongly magnetized disks produce denser outflows than weakly magnetized disks (Fig. 4.19).

This turbulent accreting atmosphere is actually missing in all works where turbulence is not self-consistently computed and must therefore be prescribed: self-similar studies (Ferreira 1997; Jacquemin-Ide et al. 2019), 2.5D MHD simulations done with alpha prescriptions (Casse and Keppens 2002, 2004; Zanni et al. 2007; Murphy et al. 2010; Stepanovs and Fendt 2016) and other semi-analytical models (Guilet and Ogilvie 2013). Our guess is that including the complex vertical stratification should allow to recover with these approaches an outflow mass load consistent with full 3D simulations. This requires however the use of numerically 'educated' profiles for all relevant turbulent effects. In the following chapter we will produce numerically educated profile for the turbulent variables.

CHAPTER 5

A turbulent closure for MRI driven turbulence

In this chapter, we construct a closure scheme for the turbulent correlations computed in our 3D global simulations, that we computed in the previous section. Our objective is to educate future simplified 2D models using this closure scheme. We construct a turbulence model by fitting the profiles of the different turbulent quantities that are dynamically important: the turbulent radial stress, $\mathcal{T}_{tu,r\varphi}$, the turbulent magnetic pressure, $\left\langle \delta B^2 \right\rangle$, and the turbulent emf, $\boldsymbol{\mathcal{E}}$.

The cheapness of effective models makes them ideal for comparison with observations. Furthermore, effective models can be used to study the long-term evolution of accretion disks, which is impossible to constrain with 3D global simulations. Hence, the main objective is to couple this turbulence model with effective 2.5D simulations or self-similar models, to upgrade the picture presented in section 3.1.1. This will lead to better effective models that reproduce the vertical structure of 3D global simulations detailed in section 4.2.1.

For the turbulence model to be able to couple with effective models, it needs to be ”universal”, the parameters deduced from the fitting procedure need to be independent of the initial conditions (μ_{ini},ε). We will achieve this universality in two steps: (1) fitting the different simulations (tab. 4.1) separately with our turbulence model, which leads to one set of parameters for each simulation. (2) We then compute the universal set of parameters by combining the different sets of parameters.

The fitting procedure, as well as the turbulence model, are detailed in the next section.

5.1 Turbulent model and fitting procedure

We attempt to model the turbulent correlations as functions of the local mean field properties of the flow (e.g. the mean plasma beta or the local average pressure, etc...). This has the advantage of being local, namely not depending explicitly on the coordinates. As explained in section 4.3 the vertical extent of the turbulent atmosphere depends on $\mu_{\rm ini}$. The locality assumption has the advantage of naturally accounting for this property.

It is known that the strength of MRI-driven turbulence scales as a power law of the local plasma beta (Salvesen et al. 2016). We discussed in section 2.4.1 that the magnitude of α_v is a power law of the local plasma beta. Furthermore, when the mean toroidal magnetic field is stronger than the mean vertical magnetic field, MRI-driven turbulence is quenched in the $\beta_p < 1$ regime (see section 2.2.3).

A possible choice of functional that takes both properties into account is then

$$\langle \delta X_i \delta Y_i \rangle = f_i(\beta_\theta, q) \, \langle Z_i \rangle \,, \tag{5.1}$$

$$f_i(\beta_\theta, q) = a_i \beta_\theta^{-n_i} \frac{b_i \beta_\theta + 1}{b_i \beta_\theta + 1 + \left(\frac{q}{q_i}\right)^2}, \tag{5.2}$$

where $\langle \delta X_i \delta Y_i \rangle$ is the quadratic turbulent correlation term that we want to model, $\langle Z_i \rangle$ is the mean field closure that we choose for that turbulent correlation, $\beta_\theta = 8\pi \langle P \rangle / \langle B_\theta \rangle^2$ is the latitudinal local plasma beta, $q = \left\langle B_\varphi \right\rangle / \langle B_\theta \rangle$ is the ratio of the toroidal and latitudinal magnetic field and (n_i, a_i, b_i, q_i) are the parameters of the model that we want to fit. The index i **distinguishes between the different turbulent quantities** modeled in this work. The functional $f_i(\beta_\theta, q)$ reduces to a simple power law on β_θ when $q = 0$. Equation 5.2 is an approximate solution of Eq. (2.52), that gives the maximum MRI growth rate in the compressible regime. It is an approximation of the compressible MRI growth rate, the derivation is not very illuminating and thus we skip it.

We define an error function to quantify the accuracy of our mean field turbulence model with respect to the turbulent correlation:

$$\Delta_i^2 = \frac{1}{N_i} \sum_j \frac{\left(\langle \delta X_i \delta Y_i \rangle_j - \langle Z_i \rangle_j f_i(\beta_{\theta,j}, q_j)\right)^2}{\left(\left|\langle \delta X_i \delta Y_i \rangle_j\right| + \left|\langle Z_i \rangle_j f_i(\beta_{\theta,j}, q_j)\right|\right)^2}, \tag{5.3}$$

where $\langle \delta X_i \delta Y_i \rangle_j$, $\langle Z_i \rangle_j$, $(\beta_{\theta,j}, q_j)$ are the different points of the turbulent and mean field profile and N_i is the total number of points. The index i distinguishes between the different turbulent quantities modeled in this work. We will minimize the function Δ_i^2 in our fitting procedure and then compute Δ_i for the purpose of comparing the accuracy of the different fits. The smaller Δ_i is the more accurate the fit is, on the contrary the closer Δ_i is to 1 the more inaccurate the fit is.

Our fitting procedure can be described as follows:

- All quantities are taken from their respective simulation. We compute $\langle \delta X_i \delta Y_i \rangle$ and calculate $f_i(\beta_\theta, q)$ from the mean field quantities from the respective simulation.

- We compute Δ_i^2 in a range $r \in [6, 10]$, $|\theta - \pi/2| < |\theta_{SM} - \pi/2|$. We do not fit turbulent components in the wind region as the turbulent correlations are not relevant to the dynamics of the system in that region (section 4.2.1).

- We then minimize Δ_i^2 using a Powell method for optimization, which leads to best fit values for the different parameters (n_i, a_i, b_i, q_i) for each simulation.

- As we explained above we want to compute a universal set of parameters that can fit all simulations. Hence, we compute an average set of parameters $(\overline{n_i}, \overline{a_i}, \overline{b_i}, \overline{q_i})$.

- We then compute an error for the average fit (computed using $\overline{n_i}$, $\overline{a_i}$, $\overline{b_i}$, $\overline{q_i}$) with respect to the turbulent profile, $\overline{\Delta_i}$. If

  $$\frac{\overline{\Delta_i} - \Delta_i}{\Delta_i} < 0.15 \tag{5.4}$$

  for all simulation we conclude that the average fit $(\overline{n_i}, \overline{a_i}, \overline{b_i}, \overline{q_i})$ is a good enough fit.

The final product is an average set of parameters able to reproduce the turbulent profiles of all simulations. We repeat this procedure for the different turbulent profiles that we model.

The definition of Δ_i^2 is not conventional and requires further discussion. The turbulent correlation, $\langle \delta X_i \delta Y_i \rangle$, can vary by several orders of magnitude. It would be hard to fit the turbulent correlation with a simple difference between the correlation and our model. We need to define a relative difference to appropriately fit the data. One possibility would be to divide the difference between the turbulent profile and the mean field model by the turbulent correlation, leading to a relative difference. However, some of the turbulent correlation can go to 0 causing the relative difference to diverge and making the minimization inconsistent. Hence, we choose to define a relative difference where we divide by the sum of the absolute value of the turbulent correlation and the absolute value of the model (Eq.5.3).

5.2 Turbulent pressure and turbulent radial stress

5.2.1 Turbulent pressure

We start by modeling the turbulent magnetic pressure. As shown in chapter 4 the turbulent magnetic pressure behaves like the average thermal pressure in the sense that it fulfills the same dynamical role. The turbulent magnetic pressure counteracts the compression of the laminar magnetic pressure and helps to deviate the accretion flow into ejection. Therefore, we model the magnetic pressure as

$$\left\langle \delta B^2 \right\rangle = f_B(\beta_\theta, q) \langle P \rangle \, . \tag{5.5}$$

We show the turbulent magnetic pressure profiles for all simulations in Fig. (5.1). Following the procedure described above we fit the turbulent profile (Eq. 5.5) for the different simulations and compile the values of the best fit as well as the values of Δ_B in Tab. (5.1). This leads to a set of 4 parameters for each simulation that we average motivated by their low dispersion around the mean. We compute the average set of parameters and get

$$\overline{a_B} = 26, \;\; \overline{q_B}^2 = 51, \;\; \overline{b_B} = 0.3 \;\; \overline{n_B} = 0.56. \tag{5.6}$$

We also compute an average error, $\overline{\Delta_B}$, from the average set of parameters for each simulation. We show its value in Tab. (5.1) and the profiles of the different fits using the average set of parameters (Eq. 5.6) in Fig. (5.1). The relative difference of $\overline{\Delta_B}$ with respect to Δ_B is at most 0.12, compatible with our imposed constraint (Eq. 5.4), we deduce that the average fit is accurate enough. We see in Tab. (5.1) that $\overline{\Delta_B} \sim 0.2 - 0.3$, the small values indicate that the fit is accurate. We will see in section 5.3 that our fits are not always as accurate.

The accuracy of the fit is also shown in Fig. (5.1), the fits using Eq. (5.6) follow the behavior of the turbulent magnetic pressure and reproduce quite well its magnitude. Interestingly, we reproduce the triple peaked behavior of the turbulent profile. This behavior is a consequence of q, when q increases turbulence is quenched and the turbulent magnetic pressure decreases. Then when $q \to 0$ the turbulence is enhanced and the turbulent magnetic pressure increases.

We note that in the limit of $\beta \gg q$ our prescription reduces to

$$\frac{\langle P \rangle}{\langle \delta B^2 \rangle} \simeq 0.04 \beta_\theta^{0.56}, \tag{5.7}$$

which is, within a factor of 2, consistent with the result of Salvesen et al. 2016 :

$$\frac{\langle P \rangle}{\langle \delta B^2 \rangle} \simeq 0.015 \beta_\theta^{0.5}. \tag{5.8}$$

We conclude that the average fit (Eq. 5.6) captures the behavior of the turbulent magnetic pressure and is consistent with prior results of MRI-turbulence (Salvesen et al. 2016) in the limit $\beta \gg q$.

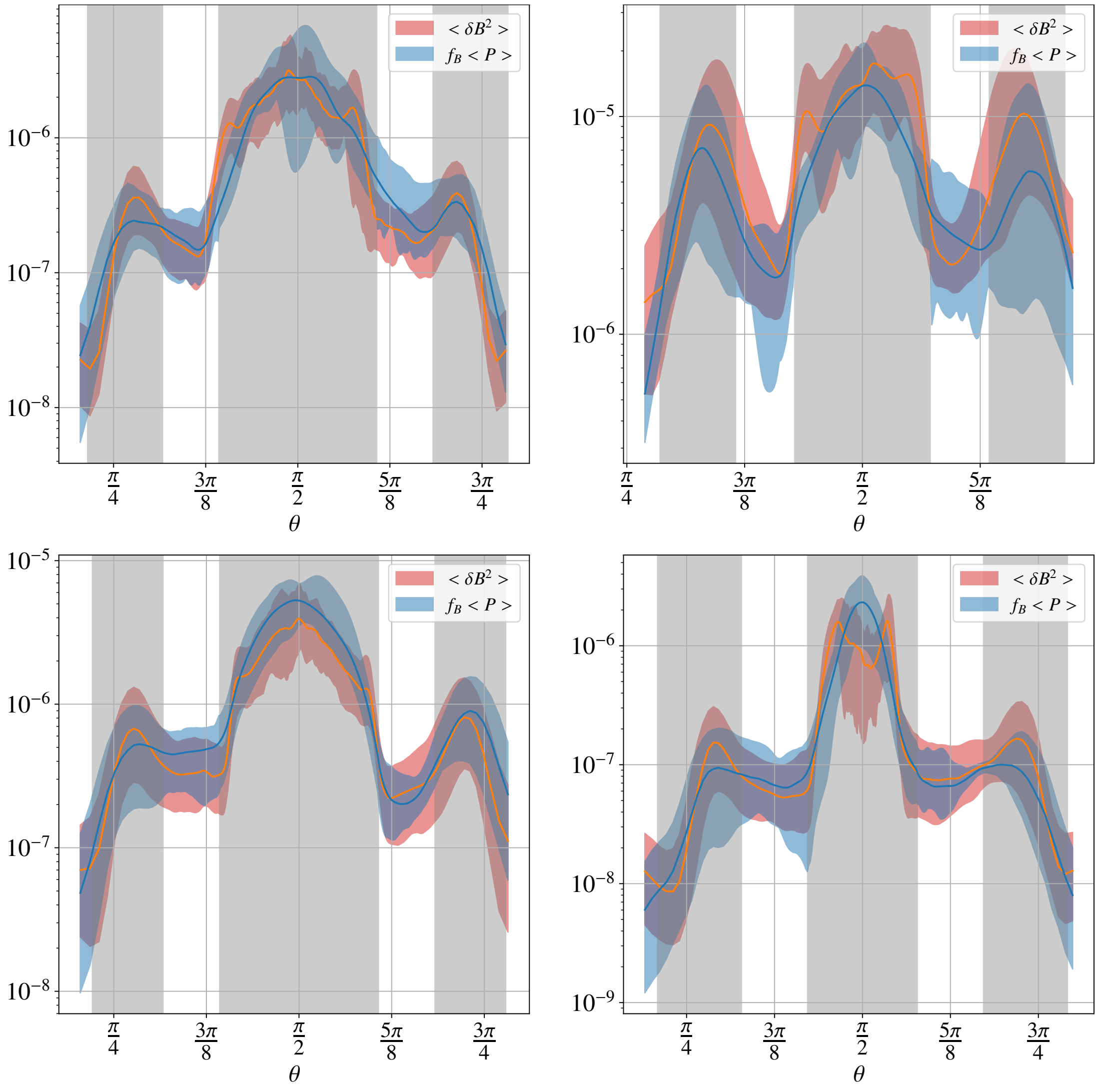

Figure 5.1: Turbulent pressure as a function of the latitudinal coordinate in red, the shaded region shows the typical deviation in the radial range, $R \in [6, 10]$, while the solid line is the radial average. In blue we show the average fit where the shaded region shows the typical deviation in the same radial range and the solid line is the radial average, the values of the average fit parameters are in Eq. (5.6). The different panels correspond to different simulations: top,left: SB4, top,right: SB3, bottom,left: S2pi, bottom,right: SEp.

	a_B	q_B^2	b_B	n_B	Δ_B	$\overline{\Delta}_B$
SB4	22.517	47.732	0.221	0.532	0.229	0.235
SB3	27.157	41.145	0.339	0.516	0.236	0.268
S2pi	24.764	50.000	0.400	0.561	0.162	0.173
SEp	29.735	65.804	0.252	0.604	0.290	0.299

Table 5.1: Best fit parameters for the turbulent magnetic pressure, the parameters being defined in Eq.(5.2). We also show the error for the best fit as well as the error with respect to average fit (Eq.5.6)

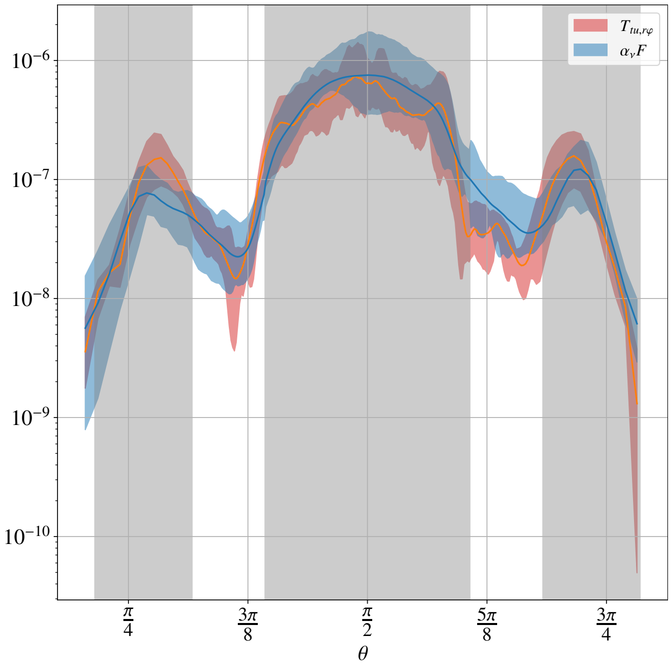

Figure 5.2: Fit example for run SB4. We show the radial stress as a function of the latitudinal coordinate in red, the shaded region shows the typical deviation in the radial range, $R \in [6, 10]$, while the solid line is the radial average. In blue we show the average fit (Eq.5.11) where again the shaded region shows the typical deviation in the same radial range and the solid line is the radial average.

5.2.2 Turbulent radial stress

We fit only the turbulent radial stress with a viscous prescription (see section 2.4.1), the latitudinal stress is found to be unimportant in the dynamics of the system (Fig. 4.17). We model the radial turbulent stress as

$$\mathcal{T}_{tu,r\varphi} = -\nu \langle \rho \rangle r \frac{\partial \langle \Omega \rangle}{\partial r} \tag{5.9}$$

$$\nu = c_s h f_T(\beta_\theta, q). \tag{5.10}$$

We follow the same fit procedure as in the previous section. The best fit parameters for all simulations can be found in Tab. (5.2). The average parameter values are computed to be

$$\overline{a_T} = 9.0,\ \overline{q_T}^2 = 7.4,\ \overline{b_T} = 0.32\ \overline{n_T} = 0.63, \tag{5.11}$$

and the average error, $\overline{\Delta_T}$, is shown in Tab. (5.2). The small values of $\overline{\Delta_T}$ indicate that the fit is accurate, this is also visible in Fig. (5.2). We compare the average error to the best fit error and find

$$\frac{\overline{\Delta_T} - \Delta_T}{\Delta_T} = 0.11 \tag{5.12}$$

in the worst case. Therefore, the average fit is a good enough model of the radial turbulent stress tensor. We show an example of a fit in Fig. (5.2) using the average parameters (Eq. 5.11). The fits for all simulations, using the average set of parameters, can be found in Appendix C, in Fig. (C.1). The fits recover the same structure as well as the magnitude of the turbulent stress. We again recover the triple peaked structure, where the turbulent profile is maximum at the disk and the turbulent atmospheres.

In the limit of $\beta \gg q$ our prescription reduces to

$$\frac{\nu}{c_s h} \simeq 9\beta_\theta^{-0.63}, \tag{5.13}$$

	a_T	q_T^2	b_T	n_T	Δ_T	$\overline{\Delta}_T$
SB4	10.183	6.643	0.239	0.650	0.241	0.251
SB3	11.986	7.116	0.353	0.638	0.304	0.316
S2pi	7.000	9.000	0.393	0.620	0.223	0.246
SEp	7.000	6.911	0.318	0.620	0.353	0.360

Table 5.2: Best fit parameters for the radial stress, the parameters are defined in Eq.(5.2). We also show the error for the best fit as well as the error with respect to average fit (Eq.5.11))

this is approximately compatible with the results of Salvesen et al. 2016, they get:

$$\frac{v}{c_s h} \simeq 11\beta_\theta^{-0.53}. \tag{5.14}$$

We conclude that the average fit (Eq. 5.11) reproduces the behavior of the turbulent radial stress and is consistent with prior results of MRI-turbulence (Salvesen et al. 2016) in the limit of $\beta \gg q$.

5.3 Turbulent electromotive forces

The turbulent electromotive force, $\boldsymbol{\mathcal{E}} = \langle \delta\mathbf{u} \times \delta\mathbf{B}\rangle$, is usually modeled with an Ohmic resistivity model (Moffatt 1978; Rincon 2019). However, more precise MHD turbulence closures rely on non-diagonal terms for the resistivity tensor, η_{ij}. When non diagonal terms are included, it is important not to introduce artificial turbulent energy sources into the dynamics of the system. To understand this constraint we project the mean induction equation with respect to $\langle\mathbf{B}\rangle$,

$$\frac{1}{8\pi}\frac{\partial\langle B\rangle^2}{\partial t} = \frac{1}{c}\boldsymbol{\mathcal{E}}\cdot\langle\mathbf{J}\rangle - \frac{1}{c}\langle\mathbf{u}\rangle\cdot[\langle\mathbf{J}\rangle\times\langle\mathbf{B}\rangle] + \frac{1}{4\pi}\nabla\cdot[(\langle\mathbf{u}\rangle\times\langle\mathbf{B}\rangle+\boldsymbol{\mathcal{E}})\times\langle\mathbf{B}\rangle], \tag{5.15}$$

this equation shows the evolution of the mean magnetic energy with time. Integrating the equation above within a fixed volume, $\mathrm{d}V$, leads to

$$\frac{\mathrm{d}}{\mathrm{d}t}\int\frac{\langle B\rangle^2}{8\pi}\,\mathrm{d}V = -\frac{1}{c}\int\langle\mathbf{u}\rangle\cdot[\langle\mathbf{J}\rangle\times\langle\mathbf{B}\rangle]\,\mathrm{d}V + \frac{1}{4\pi}\int[(\langle\mathbf{u}\rangle\times\langle\mathbf{B}\rangle+\boldsymbol{\mathcal{E}})\times\langle\mathbf{B}\rangle]\cdot\mathrm{d}\mathbf{S} + \frac{1}{c}\int\boldsymbol{\mathcal{E}}\cdot\langle\mathbf{J}\rangle\,\mathrm{d}V, \tag{5.16}$$

where the surface integral is taken over the boundary of the volume. The first term on the right-hand side represents the loss of the magnetic energy due to the work done by the Lorentz force on the flow. The second term is the Poynting flux that crosses the boundaries of the domain. Finally, the last term corresponds to the energy dissipation due to the turbulent motions. If this term is always positive it could lead to uncontrolled growth of the magnetic field energy. This imposes a sufficient condition on our mean-field closure of $\boldsymbol{\mathcal{E}}$, which can be stated as

$$\boldsymbol{\mathcal{E}}\cdot\langle\mathbf{J}\rangle \leq 0. \tag{5.17}$$

This equation is trivially respected by a resistive closure, in that case Eq.(5.17) can be simplified into

$$-\eta|\langle\mathbf{J}\rangle|^2 < 0. \tag{5.18}$$

However, in our case we were not able to fit the latitudinal emf with a purely diagonal resistive tensor. This means that we need to consider non-diagonal terms of the resistivity tensor, η_{ij}. We find that the simplest model that can reproduce the behavior of all components of $\boldsymbol{\mathcal{E}}$ is

$$\mathcal{E}_i = -\eta_{ij}\langle J_i\rangle + \delta_{w,i}[\langle\mathbf{w}\rangle\times\langle\mathbf{J}\rangle]_i \tag{5.19}$$

$$\eta_{ij} = f_{ij}c_s h \tag{5.20}$$

$$\delta_{w,i} = f_{ii}\delta_i\frac{c_s h}{\langle\Omega\rangle}, \tag{5.21}$$

where η_{ij} is a diagonal tensor and $\langle \mathbf{w} \rangle = \nabla \times \langle \mathbf{u} \rangle$. The first term is a simple turbulent resistivity closure while the second term is a shear current term (Rogachevskii and Kleeorin 2003). All non diagonal terms are taken into account by the second term $\delta_{w,i}[\langle \mathbf{w} \rangle \times \langle \mathbf{J} \rangle]_i$. This terms has the advantage of easily satisfying Eq. (5.17). This non diagonal term can lead to a mean field dynamo if certain conditions are respected (Rogachevskii and Kleeorin 2003). We will discuss if this is the case for our simulations in section 5.4

We follow the same fit procedure for the turbulent emf as the one described in section 5.1. However, there are a few differences:

- We need one more fitting parameter, δ_i, for all simulations.
- The turbulent electromotive forces are more difficult to fit as their profiles are more complicated. To enhance the convergence rate we do not consider the LA in the computation of Δ_i, in that region the turbulent terms are in general not dynamically significant.
- We compute a general set of parameters for all the components of the turbulent emf. The parameters $\overline{a_{\theta\theta}}$, $\overline{a_{rr}}$ and $\overline{a_{\varphi\varphi}}$ will be distinct for different components of $\boldsymbol{\mathcal{E}}$. While the parameters ($\overline{n_i}$, $\overline{\delta_i}$, $\overline{b_i}$, $\overline{q_i}$) will be common to all three components of $\boldsymbol{\mathcal{E}}$. This choice is motivated by measurements of the resistivity tensors in shearing box simulations (Lesur and Longaretti 2009; Gressel and Pessah 2015). They find that the different components of turbulent resistivity tensor have different magnitudes but similar profiles.

5.3.1 Toroidal component

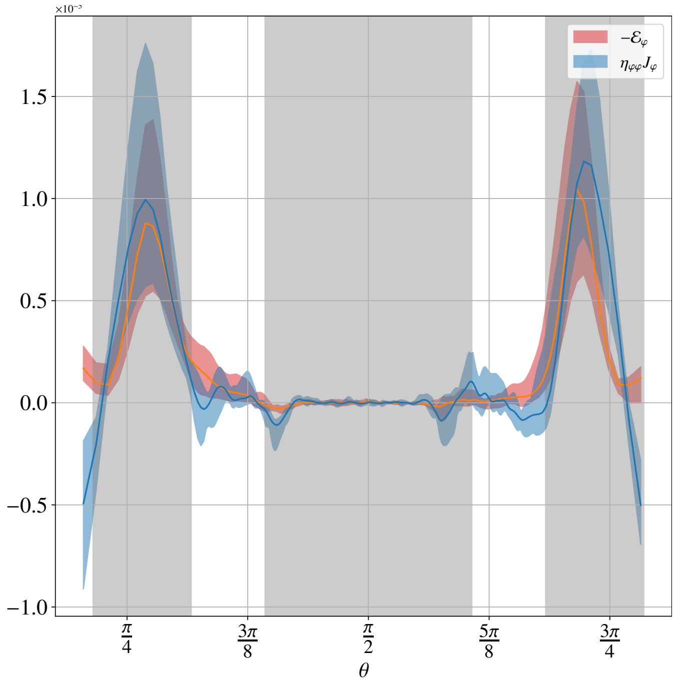

Figure 5.3: Example of fit for run SB4. We show the toroidal emf as a function of the latitudinal coordinate in red, the shaded region shows the typical deviation in the radial range, $R \in [6, 10]$, while the solid line is the radial average. In blue we show the average fit where again the shaded region shows the typical deviation in the same radial range and the solid line is the radial average.

The shear current effect is found to be negligible for the toroidal component of the turbulent emf. We do not consider it in our fit, however, we verify a posteriori that it is indeed negligible (using the value

	$a_{\varphi\varphi}$	$q^2_{\varphi\varphi}$	$b_{\varphi\varphi}$	$n_{\varphi\varphi}$	$\Delta_{\varphi\varphi}$	$\overline{\Delta}_{\varphi\varphi}$
SB4	1.373	20.000	3.000	0.591	0.590	0.595
SB3	1.617	25.000	5.000	0.600	0.491	0.497
S2pi	1.521	25.000	5.000	0.600	0.491	0.497
SEp	1.865	20.964	5.000	0.600	0.596	0.615

Table 5.3: Best fit parameters for the toroidal emf, the parameters are defined in Eq.(5.2). We also show the error for the best fit as well as the error with respect to average fit (Eq.5.25))

deduced in section 5.3.1). The absence of this non-diagonal term is important and will be discussed in section 5.4. We fit the toroidal emf with the following model

$$\mathcal{E}_\varphi = -\eta_{\varphi\varphi}\left\langle J_\varphi \right\rangle, \tag{5.22}$$

$$\eta_{ij} = f_{ij} c_s h. \tag{5.23}$$

We show an example of a fit for SB4 in Fig. (5.3). We show the average fits for all simulations in Appendix C, Fig. (C.2) and the values of the best fit parameters in tab. (5.3.1).

We note that the fit is less consistent on the laminar regions of the simulation, the non shaded areas in Fig. (5.3). This is not surprising as in those regions $\langle \mathbf{u}\rangle_p \times \langle \mathbf{B}\rangle_p = -\mathcal{E}_\varphi \sim 0$ as they are in laminar ideal MHD.

As before the average fits agree quite well with the turbulent profiles. However, the values of $\Delta_{\varphi\varphi}$ and $\overline{\Delta}_{\varphi\varphi}$ for the different simulations are larger, by more than a factor of 2, when compared with Δ_B and $\overline{\Delta}_B$. This is consistent with the quality of the fit, it is less accurate than the one for $\left\langle \delta B^2 \right\rangle$. However, even thought the fit is less accurate we can see in Fig. (5.3) that it still reproduces most of the features of the turbulent emf.

We compare the average error to the best fit error and find

$$\frac{\overline{\Delta}_{\varphi\varphi} - \Delta_{\varphi\varphi}}{\Delta_{\varphi\varphi}} = 0.03 \tag{5.24}$$

in the worst case. We see that the deviation between the average error and the best fit error is much smaller in this case. This small deviation is the consequence of the best fit being less accurate. There is not much precision to be lost from doing an average fit since the best fit is not very accurate. In contrast, the best fit for the turbulent magnetic pressure has higher precision and, thus the average fit is considerably less accurate.

This deviation is small but it is noticeable in the profile of the turbulence model for simulation SEp (Fig.C.2). Indeed, there seems to be a dependency in ε as $a_{\varphi\varphi}$ gains a factor of 2 when we decreases epsilon by 2. This deserves further examination but this would require exploring the parameter space in ε, which is postponed for future work.

Finally the average fit values for $\eta_{\varphi\varphi}$ are

$$\overline{a_{\varphi\varphi}} = 1.6,\ \overline{q_\eta}^2 = 15,\ \overline{b_\eta} = 4.1\ \overline{n_\eta} = 0.53. \tag{5.25}$$

Radial and latitudinal components

We fit the radial and latitudinal components by following the same procedure as before. We model both components as

$$\mathcal{E}_r = -f_{rr}\left(c_s h \left\langle J_r \right\rangle - \frac{c_s h}{\langle \Omega \rangle}\delta_r(\langle \mathbf{w}\rangle \times \langle \mathbf{J}\rangle)|_r\right) \tag{5.26}$$

$$\mathcal{E}_\theta = -f_{\theta\theta}\left(c_s h \left\langle J_\theta \right\rangle - \frac{c_s h}{\langle \Omega \rangle}\delta_\theta(\langle \mathbf{w}\rangle \times \langle \mathbf{J}\rangle)|_\theta\right) \tag{5.27}$$

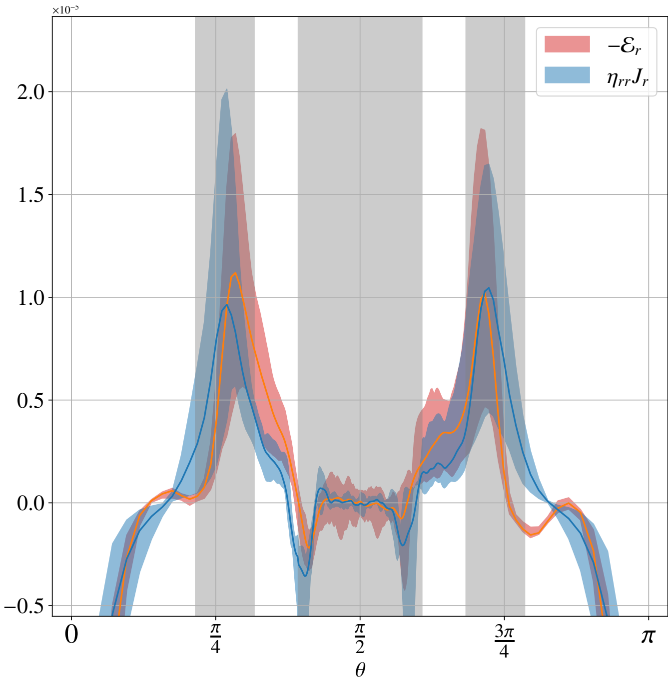

Figure 5.4: Example of fit for run SB4. We show the radial emf as a function of the latitudinal coordinate in red, the shaded region shows the typical deviation in the radial range, $R \in [6, 10]$, while the solid line is the radial average. In blue we show the best fit where again the shaded region shows the typical deviation in the same radial range and the solid line is the radial average.

	a_{rr}	q_{rr}^2	b_{rr}	n_{rr}	δ_{rr}	Δ_{rr}	$\overline{\Delta}_{rr}$
SB4	1.034	7.166	5.000	0.450	0.550	0.532	0.553
SB3	1.396	15.091	8.000	0.484	0.550	0.475	0.506
S2pi	1.302	8.000	2.000	0.500	0.100	0.567	0.570
SEp	2.127	10.000	5.000	0.600	0.534	0.596	0.611

Table 5.4: Best fit parameters for the radial emf, the parameters are defined in Eq.(5.2). We also show the error for the best fit as well as the error with respect to average fit (Eq.5.28).)

We attempt to fit with roughly the same same values of q, b and n as for $\mathcal{E}_\varphi$. We show the fit of $\mathcal{E}_r$ for SB4 in Fig. (5.4). The average fits for all simulations can be found in Appendix C, Fig. (C.3). The values of the best fit parameters can be found in tab. (5.4). The average error is bigger than the best fit error by at most 5% (tab. 5.4) and the average fits agree quite well with the turbulent profiles. The magnitudes of Δ_{rr} and $\overline{\Delta}_{rr}$ are roughly equal in magnitude to the ones of $\mathcal{E}_\varphi$. Again our fits of the turbulent emf are less accurate compared to the turbulent magnetic pressure and turbulent torque. We recover again the factor 2 of for a_{rr} when comparing the best fit of simulation SEp with the rest of the set. We compute the average fit values to be

$$\overline{a_{rr}} = 1.5,\ \ \overline{q_\eta}^2 = 15,\ \ \overline{b_\eta} = 4.1\ \ \overline{n_\eta} = 0.53,\ \ \overline{\delta} = 0.3. \tag{5.28}$$

We show the fit of $\mathcal{E}_\theta$ for SB4 in Fig. (5.5). We show the average fits for all simulations in Appendix C, Fig. (C.4) and the values of the best fit parameters in tab. (5.5). The average fits agree with the turbulent profiles, the average error is bigger than the best fit error by at most 8% (tab. 5.5). Simulation SEp again has a bigger $a_{\theta\theta}$ than the other ones. For $\mathcal{E}_\theta$ the non-diagonal terms dominate, contrary to the other components of $\boldsymbol{\mathcal{E}}$. The average fit parameters for the latitudinal component are computed to be

	$a_{\theta\theta}$	$q^2_{\theta\theta}$	$b_{\theta\theta}$	$n_{\theta\theta}$	$\delta_{\theta\theta}$	$\Delta_{\theta\theta}$	$\overline{\Delta}_{\theta\theta}$
SB4	6.844	8.000	3.193	0.500	0.119	0.534	0.575
SB3	4.000	9.158	3.213	0.500	0.371	0.572	0.572
S2pi	6.148	25.000	5.000	0.535	0.102	0.560	0.606
SEp	12.057	18.000	5.000	0.600	0.108	0.559	0.577

Table 5.5: Best fit parameters for the latitudinal emf, the parameters are defined in Eq.(5.2). We also show the error for the best fit as well as the error with respect to average fit (Eq.5.29).

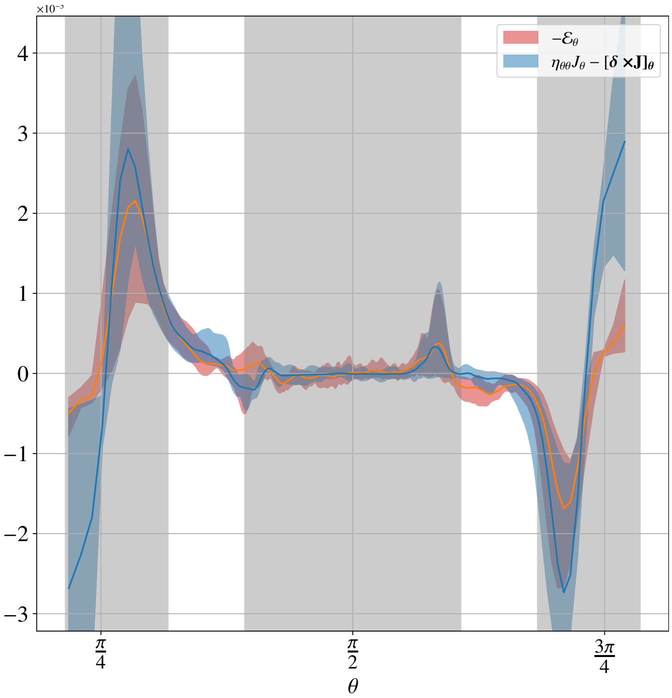

Figure 5.5: Example of fit for run SB4. We show the latitudinal emf as a function of the latitudinal coordinate in red, the shaded region shows the typical deviation in the radial range, $R \in [6, 10]$, while the solid line is the radial average. In blue we show the best fit where again the shaded region shows the magnitude range for different radii and the solid line corresponds to the radial average, the values of the best fit parameters are in tab. (5.5).

$$\overline{a_{\theta\theta}} = 6, \ \ \overline{q_\eta}^2 = 15, \ \ \overline{b_\eta} = 4.1 \ \overline{n_\eta} = 0.53, \ \ \overline{\delta} = 0.3. \tag{5.29}$$

5.4 Turbulent profiles and comparison with other work

In this section we analyze the previously computed turbulent profiles and compare them with the ones derived in other work.

Turbulent pressure

We show $f_B = \left\langle \delta B^2 \right\rangle / \langle P \rangle$ for the different simulations computed with the average parameters (Eq. 5.6) in Fig. (5.6). Figure (5.6) shows that f_B increases monotonously as we exit the disk for all simulations. We also see that when $\mu_{\rm mid}$ increases (between SB4 and SB3) the value of f_B at the disk mid-plane

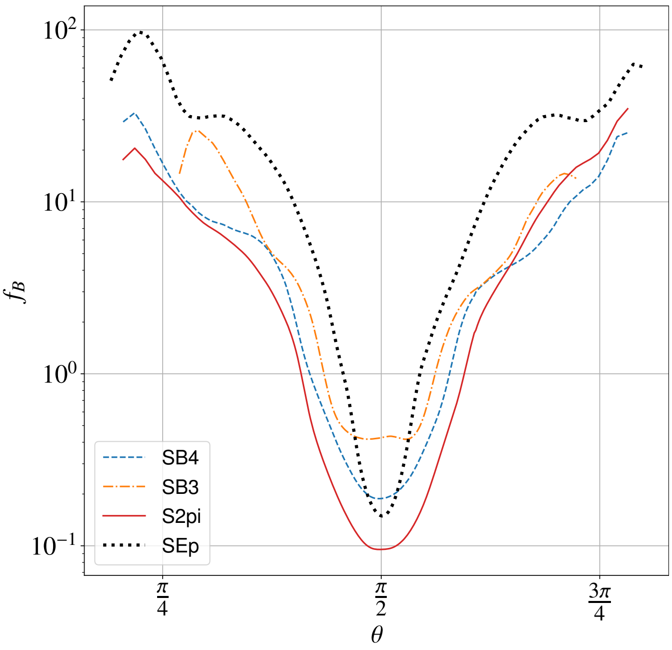

Figure 5.6: Latitudinal profile of the function $f_B = \left\langle \delta B^2 \right\rangle / \langle P \rangle$ for different simulations, this term models the latitudinal behavior of the turbulent magnetic pressure. We do not show the regions with $|\theta - \pi/2| > |\theta_{SM} - \pi/2|$, as they correspond to the wind region.

also increases, a higher magnetization leading to stronger turbulence. The profile of f_B for simulation SB4 follows a very similar behavior to the one computed for S2pi, showing again the robustness of the wedge approximation for the vertical profiles. The slope of the turbulent profiles is consistent between simulations except for simulation SEp. When the disk geometrical thickness decreases the latitudinal dependency of f_B becomes steeper, which is expected.

We compare the profiles of $\left\langle \delta B^2 \right\rangle$ (Fig. 5.1) and f_B (Fig. 5.6) to the ones obtained by Salvesen et al. 2016 (Fig.13). We see that they also find a triple peaked structure for weakly magnetized simulations. They also observe that the turbulent magnetic pressure dominates the magnetic pressure at the disk surface. However, their shearing box simulations have very different vertical structures and lack the accreting atmosphere.

Turbulent viscosity

Figure (5.7) shows the latitudinal profiles of the turbulent viscosity, ν, normalized to $V_{A0}h$. The vertical profiles of the turbulent viscosity are very similar to the ones of f_B and are identical to the one computed by Zhu and Stone 2018. The normalization to $V_{A0}h$ shows that the turbulent viscosity approximately scales with $V_{A0}h$. This is consistent with the self-similar prescription we used in chapter 3, $\nu_v = \alpha_m \mathcal{P}_m V_{A0} h$. Even the numerical value is comparable, in chapter 3 we found solutions for $\alpha_m \mathcal{P}_m > 1$ ($\alpha_m = [1, 2, 8]$ and $\mathcal{P}_m = 1$) and here we compute $\nu \sim 6 V_{A0} h$ (see below for more details). However, the vertical behavior of this profile is very different from the one we used in chapter 3. In chapter 3 we used a Gaussian that decreases with height while our fit in Fig. (5.7) increases with height.

The vertical dependency we compute for the viscosity is similar to the profile used by Guilet and Ogilvie 2013. They were inspired by the results of 3D turbulent zero-net flux simulations. In their work they model the turbulent α_v viscosity as

$$\alpha_v = f_T = \alpha_0 \frac{e^{\left(\frac{z_{SM}}{2h}\right)^2}}{1 + \left[e^{\left(\frac{z_{SM}}{2h}\right)^2} - 1\right] e^{-\left(\frac{z}{2h}\right)^2}}, \tag{5.30}$$

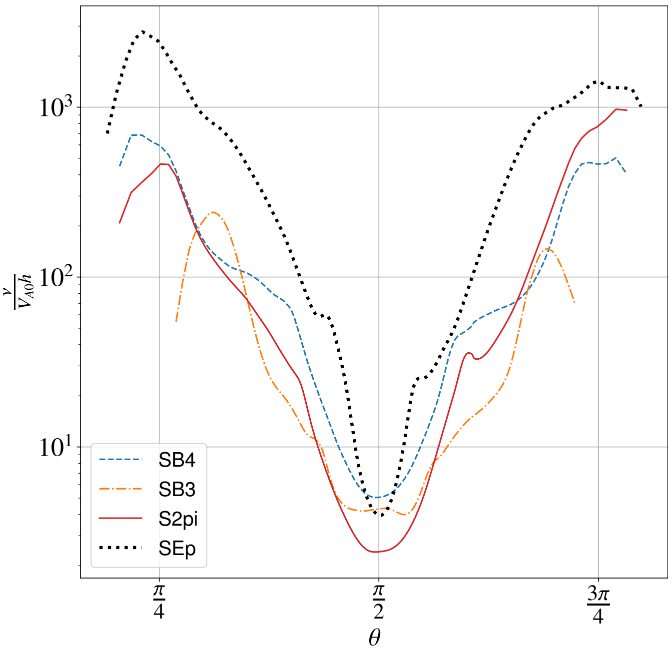

Figure 5.7: Turbulent viscosity as a function of the latitudinal coordinate for different simulations, we normalize it to the $V_{A0}h$. We do not show the regions with $|\theta - \pi/2| > |\theta_{SM} - \pi/2|$, as they correspond to the wind region.

where z_{SM} is the vertical height where the turbulence stops and the wind is launched. As we explained in section 4.3 z_{SM} and α_0 are functions of the magnetization at the disk mid-plane.

Turbulent resistivity

Since the turbulent resistivities follow roughly the same vertical behavior as the viscosity we do not show them here. Instead we analyze the behavior of the different transport coefficients, they can be found in Figure 5.8, where we redefine the turbulent magnetic Prandtl number

$$\mathcal{P}_m = \frac{\nu}{\eta_{\varphi\varphi}}, \tag{5.31}$$

and also show the ratios of the different resistivities, $\eta_{rr}/\eta_{\varphi\varphi}$ and $\eta_{\theta\theta}/\eta_{\varphi\varphi}$.

First, we see that $\mathcal{P}_m$ varies between 3 and 5 in the turbulent regions and always stays above unity. This is consistent with past results of shearing box simulations (Fromang and Stone 2009; Guan and Gammie 2009; Lesur and Longaretti 2009) that measured $\mathcal{P}_m \sim 2$. It is also consistent with the value measured by Zhu and Stone 2018 in similar global MHD simulations ($\mathcal{P}_m \sim 5$). Finally, it is to a factor of 3 consistent with the value we chose ($\mathcal{P}_m = 1$) in chapter 3 even though the profile of the diffusivity is again very different.

We also compute the turbulence level parameter defined in section 2.4.2 as

$$\alpha_m = \frac{\eta_{\varphi\varphi}}{V_{A0}h}. \tag{5.32}$$

We can evaluate this quantity at the disk mid-plane (where $q \ll \beta_\theta$) and find $\alpha_m \simeq 1.6$ which is again consistent with the self-similar parameter exploration of chapter 3.

In Fig. (5.8) we see that

$$\eta_{\varphi\varphi} \simeq \eta_{rr}, \tag{5.33}$$

this is consistent with the work of Gressel and Pessah 2015 and Lesur and Longaretti 2009. The radial and toroidal resistivities are comparable. We also see that

$$\eta_{\theta\theta} \simeq 4\eta_{\varphi\varphi}, \tag{5.34}$$

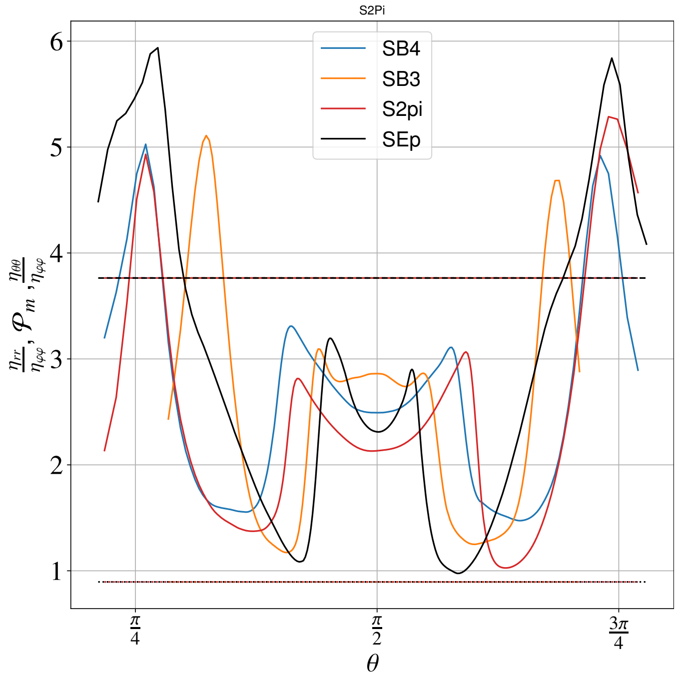

Figure 5.8: Turbulent transport coefficients as functions of the latitudinal coordinate for different simulations. The lower dotted lines correspond to $\frac{\eta_{rr}}{\eta_{\varphi\varphi}} \simeq 1$ (the straight lines at 1), while the solid lines correspond to $\mathcal{P}_m$ and the upper dotted lines correspond to $\frac{\eta_{\theta\theta}}{\eta_{\varphi\varphi}} \simeq 4$ (the straight lines at 4). We do not show the regions with $|\theta - \pi/2| > |\theta_{SM} - \pi/2|$, as they correspond to the wind region.

which is consistent with the measurements of Lesur and Longaretti 2009, they also find that the vertical resistivity is around a factor of 3 more efficient that the toroidal resistivity. These results are however at odds with our choice of the resistive tensor in chapter 3, where we chose

$$\eta_{rr} = \eta_{\theta\theta} = \eta'_m, \tag{5.35}$$

$$\eta_{\varphi\varphi} = \eta_m, \tag{5.36}$$

and $\chi_m = \eta_m/\eta'_m$. This is completely inconsistent with Fig. (5.8) and makes a comparison difficult. Nonetheless, the values of $\chi_m = [0.01, 0.1, 1, 3]$ we explored in chapter 3 need to be compared with the values of χ_m we deduce here. We can compute two values of χ_m:

$$\frac{\eta_{\varphi\varphi}}{\eta_{rr}} = 1, \tag{5.37}$$

$$\frac{\eta_{\varphi\varphi}}{\eta_{\theta\theta}} = 0.25, \tag{5.38}$$

and find that both $\frac{\eta_{\varphi\varphi}}{\eta_{rr}}$ and $\frac{\eta_{\varphi\varphi}}{\eta_{\theta\theta}}$ are consistent with the self-similar parameter exploration. However, in self-similar works, the difference $\eta_{rr} \neq \eta_{\theta\theta}$ was not considered. It is unclear if this difference will have an effect on the physics of accretion and ejection. Finally, the shape of the profiles remains very different.

Shear current effect as a dynamo mechanism

We measure also non-diagonal coefficients that need to be taken into account to properly model the turbulent emf. This is also completely absent from our modeling in chapter 3. Lesur and Longaretti 2009 and Gressel and Pessah 2015 also measure significant non diagonal coefficients. They both measure

$$\eta_{r\varphi} \sim \eta_{\varphi\varphi}, \tag{5.39}$$

while we compute

$$\eta_{r\varphi} \sim 0.3\eta_{\varphi\varphi}, \tag{5.40}$$

this is probably a consequences of our overly simplistic fit for the non-diagonal terms, only considering the shear current effect. We could have also considered other mean-field contributions to the resistivity tensor, like the Rädler effect (Rädler 1969) or the $\boldsymbol{\kappa}$ tensor (Rincon 2019). It should be noted, that the works of Gressel and Pessah 2015 and Lesur and Longaretti 2009 are performed in the shearing box approximation and thus some differences could be the consequence of the different framework.

We were able to fit $\mathcal{E}_\varphi$ without non diagonal contributions, like $\eta_{\varphi r}$. This is consistent with the measurements of Gressel and Pessah 2015. They show that $\eta_{\varphi r}$ is an order of magnitude smaller than the other components of the resistivity tensor. It is this term that is responsible of coupling the radial and the toroidal magnetic field by their vertical gradients (Rincon 2019). In its absence it would be impossible to construct a dynamo-like mechanism from the shear current effect.

Prospectives and caution

In this chapter we have computed multiple mean field closures to model the different dominant turbulent correlations of 3D simulations. We recover results that are consistent with shearing box simulations (Fromang and Stone 2009; Guan and Gammie 2009; Lesur and Longaretti 2009; Gressel and Pessah 2015; Salvesen et al. 2016). This consistency validates our analysis and gives credence to the shearing-box approximation as a good tool for quantifying MRI turbulence. The magnitude at the disk mid-plane is also consistent with our self-similar parameter exploration. However, the profile of the turbulent quantities are very different from gaussians. Finally, as detailed in chapter 4 the turbulent magnetic pressure plays a crucial role and is absent from self-similar models.

It is important to note that the functional form that we chose in section 5.1 is mostly ad-hoc. A different functional may be able to also model the turbulent structure. Nonetheless, we believe that the vertical behavior of the profiles discussed in this section is well recovered. The only way to test the validity of our mean field model is to implement it into a 2D calculation and verify that we are able to reproduce the features of the fully turbulent 3D models. This is postponed for future work.

CHAPTER 6

Conclusion and perspectives

In this manuscript we wanted to bridge the gap between 2D effective solutions and 3D global simulations of accretion disks. We also wanted to constraint the secular evolution of accretion disks. We have achieved in this manuscript several steps towards that objective. However, some questions are still unanswered.

6.1 Summary of main results

In chapter 3 we revisited the self-similar accretion-ejection solutions for cold (isothermal) magnetic surfaces. We were motivated by recent global 3D simulations of accretion disks threaded by a weak vertical magnetic field and showing the launching of jets. By allowing spatial oscillations of all quantities within the disk, we have been able to extend the previous parameter space by 4 orders in magnitude in the disk magnetization μ, namely from $\mu = 10^{-4}$ to almost unity.

We recovered the previous solutions and found a new class of MRI-like driven outflows from weakly magnetized disks. The role of MRI-like spatial oscillations is shown to be essential in order to provide the required bending of the poloidal field lines at the disk surface. Cold outflows from weakly magnetized accretion disks have the tendency to be more massive than their strong field (near equipartition) counterpart, leading to a critical Alfvén surface closer to the disk surface.

There is a continuity in behavior as μ increases. Low μ isothermal solutions are quite massive with a typical ejection index $\xi \sim 0.1$ (increasing with μ) and are mostly driven by the pressure of the toroidal field. The previously published high μ solutions are much less massive, with a typical ejection index $\xi \sim 0.01$ (decreasing with μ), thus faster and mostly centrifugally driven. These are however two manifestations of the same magnetic acceleration process, linking accretion to ejection in an interdependent way.

We also explored the influence of the turbulent parameters (α_m, χ_m) and found that our parameter space is consistent with the values computed in shearing box simulations.

Our outflows, even though more massive, still exhibit jet-like properties, and still recollimate. They are to be distinguished from the wind-like outflows that are observed in protoplanetary disks (Louvet et al. 2018; de-Valon et al. 2020), which are mostly conical. The conditions under which MHD-driven outflows recollimate and what happens after the recollimation shock is still an important open question.

The solutions that feature properties closer to wind-like outflows ($\sigma < 1$) are exhausted and may need a supplementary energy source. Indeed, some energy input must be added in order to provide a positive Bernoulli integral. A further development would thus be to include heating at the disk upper layers, as in Casse and Ferreira 2000a, mimicking the existence of irradiation from a central source. This is known to dramatically enhance the mass loss ξ as well, further decreasing σ and allowing for magneto-thermal winds. We note that, the massive solution of Lesur 2021 still recollimate. Moreover, 3D global simulation of ambipolar winds that include heating also recollimate (Cui and Bai 2021). Hence, it is

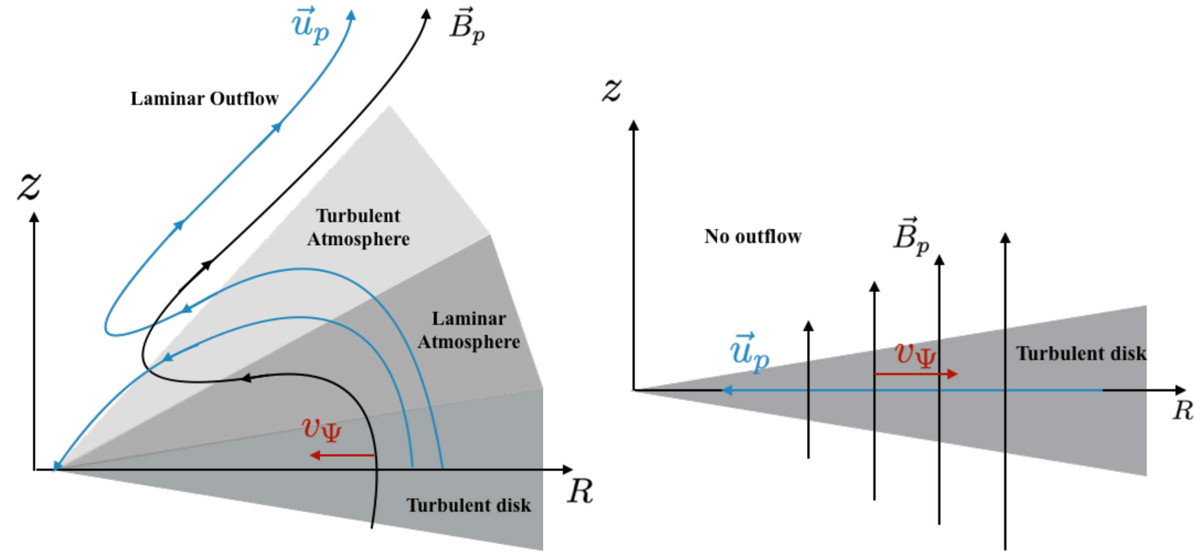

Figure 6.1: Sketch showing the magnetic topology ($\langle B_p \rangle$) and velocity field lines ($\langle u_p \rangle$) of weakly magnetized 3D simulations (left) and the standard disk model (Shakura and Sunyaev 1973) with Lubow et al. 1994 magnetic field configuration (right). We also show the direction of the field transport velocity, v_Ψ.

unclear if heating or mass loading has a clear effect on the recollimation of the outflow, at least in the case of ambipolar winds. The fact that ambipolar winds tend to be more massive than ideal MHD winds is also an interesting observation.

It is unreasonable to heat the solutions computed in chapter 3 due to the incorrect turbulence model used (incorrect profiles and lack of turbulent pressure). Indeed, the main limit of the results detailed in chapter 3 is that they depend on an incorrect turbulence model (see chapter 5). Hence, the channel mode structures, observed in our weakly magnetized solution, will probably disappear with a more accurate turbulence model.

In chapter 4 we computed 3D global simulations of magnetized accretion disks. We found that the disk vertical structure depends mostly on μ.

When the magnetization is weak ($\mu < 10^{-3}$) the system converges towards an exotic vertical configuration, where most of the accretion happens on the disk atmosphere, located above the disk up to $z \sim 10h$. Above this accreting atmosphere an outflow that becomes super fast magnetosonic is launched. The disk ($z \leq 3h$) is highly turbulent, mostly in hydrostatic equilibrium and the presence of an important magnetic turbulent pressure allows to lift up a large amount of mass into a laminar ideal MHD atmosphere. This lifted mass is basically falling in towards the central object, dragging in the magnetic field which, in turn, provides a torque that transfers its angular momentum back to the underlying disk. When the magnetic field achieves equipartition in these upper layers, MRI is re-ignited and drives a turbulence. Indeed, the transsonic accretion is achieved through the turbulent and laminar torques, the disk is accelerated by the accreting atmosphere. This complicated structure is summarized in Fig. (6.1,left).

We conclude that when a large scale vertical magnetic field is present the vertical structure is completely different from the one predicted by a Shakura and Sunyaev 1973 type model. As we can see in Fig. (6.1,right) it is hard to believe that a weakly magnetized disk could be accurately modeled by a Shakura and Sunyaev 1973 type model. Furthermore, in contrast to our simulations, a standard accretion disk is expected to diffuse its magnetic flux instead of advecting it (Lubow et al. 1994).

Indeed, in our simulations the ambient magnetic field is found to be always dragged *inwards* in the disk, at a velocity which increases with the disk magnetization. The disk vertical structure is also seen to be deeply affected, with a progressive decrease in height of the disk turbulent atmosphere. However, the outflow properties, as described by the usual MHD invariants, remain remarkably constant. This shows that the outflow is determined by the physical conditions at the disk upper layers, which remain mostly constant, rather than by the disk mid-plane properties.

In contrast with our results, MHD models including ambipolar diffusion show that the large scale vertical magnetic field is always diffused outwards (Gressel et al. 2020; Cui and Bai 2021; Lesur 2021). This could be the consequence of the different vertical structure between our ideal MHD simulations and ambipolar wind models.

Beyond a threshold on the disk magnetization, located between 10^{-3} and 10^{-2}, the global accretion-ejection configuration undergoes a drastic readjustment. The magnetic field is being accumulated into the central regions until a global equilibrium is achieved involving both the disk and its magnetosphere. The inner disk reaches a steady-state (balance between field advection and diffusion) when its magnetization achieves unity. Despite this strong field regime, the disk is turbulent and drives a super fast-magnetosonic outflow right from its surface $z \sim 3h$. The size of this inner region keeps on increasing in time, as more magnetic flux is being added from the outer regions. The mass-weighted accretion speed is supersonic in the inner region. This inner region shares a lot of properties with the near equipartition solutions of Ferreira 1997 that are also computed in chapter 3. They share a supersonic accretion flow and have identical magnetic topology. However, the self-similar solutions computed here and in Ferreira 1997 lack the turbulent magnetic pressure. This turbulent pressure will probably change the properties of the vertical structure and the mass loading of the outflow. In the transition region between the weakly and highly magnetized regions, the mass weighted accretion velocity becomes transsonic. The dynamics of this region are quite complex and their investigation is postponed for future work.

This hybrid disk configuration is relevant for the JED-SAD model first presented by Ferreira et al. 2006b and tested observationally by Marcel et al. 2019. In this model the disk is radially divided into two distinct regions: a highly magnetized inner region, called a jet emitting disk (JED, Ferreira 1997) and a weakly magnetized outer regions, called a standard accretion disk (SAD, Shakura and Sunyaev 1973). The radius R_j marks the radial transition between both disks.

Marcel et al. 2019 have shown that it is possible to reproduce the behavior of X-ray binary outbursts by using a the JED-SAD hybrid disk model. We have shown in this manuscript that a hybrid disk structure naturally emerges thanks to magnetic field transport. However, as discussed above the structure of SAD is different from the structure of a weakly magnetized accretion disk. We propose a more complex but perhaps more accurate picture in Fig. (6.2), where we show an inner highly magnetized disk and an outer weakly magnetized accretion disk. We note that, even though the magnetic and fluid structures of the JED model are similar to the strongly magnetized simulations computed here, the JED model lacks the turbulent magnetic pressure.

Finally, in chapter 5, we have constructed a turbulence model that reproduces the behavior of the turbulent correlations computed in our 3D global simulations: the turbulent pressure, the turbulent torque, and the turbulent emf. We construct this model by fitting the different turbulent correlations with a local model that depends only on the mean-field properties of the magnetic field and the gas pressure. We show that this turbulent closure is consistent with past measurements of MRI-driven turbulence performed in shearing box models. Moreover, the values of α_m, χ_m, and $\mathcal{P}_m$ computed in our turbulence model are also consistent with the parameter exploration performed in chapter 3. However, the profiles of the turbulent correlations are very different from the ones implemented in chapter 3.

6.2 Perspectives

Our first objective should be to implement our turbulent closures into a 2D effective model. This implementation will allow us to test the validity of our turbulent closures, if the new 2D models recover the results of the 3D simulations. Furthermore, we will be able to reproduce the behavior of 3D global simulation with numerically cheaper methods. Once cheaper models are possible, a complete exploration of the magnetization parameter, like the one we performed in chapter 3, should be possible. A thorough parameter exploration will allow us to better constraint the evolution of the vertical structure as a function of the magnetization. Furthermore, we should be able to accurately measure the scalings of the accretion

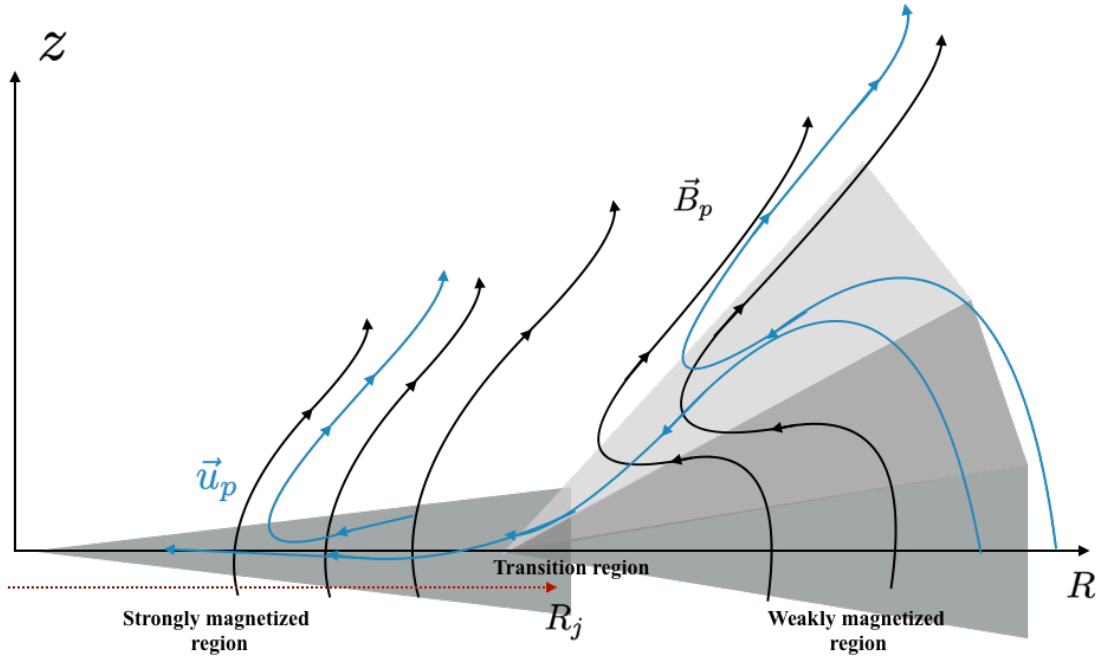

Figure 6.2: Sketch showing the magnetic topology ($\langle B_p \rangle$) and velocity field lines ($\langle u_p \rangle$) of an updated JED-SAD model where the SAD is replaced by a weakly magnetized disks.

velocity, the field advection, and the laminar torques as functions of the magnetization.

As was discussed in chapter 5, our turbulent closures have been constructed using only two different values for the disk geometrical thickness, $\varepsilon = \frac{h}{R}$. Moreover, we showed that the disk geometrical thickness affected the scaling of the turbulent electromotive forces. Hence, an exploration of the effect of the disk geometrical thickness is not possible with the turbulence model developed in chapter 5. Including the effect of the disk geometrical thickness into our turbulence model would require expensive high resolution low ε 3D global simulations.

The presence of radiative heating coming from the inner regions (star or hotter disk regions) could disturb the equilibrium of the accreting atmosphere. Indeed, it is not clear how the turbulent atmosphere will react to the effect of illumination by the inner regions. Furthermore, in this manuscript, to keep the problem mathematically tractable we have neglected the effects of the energy equation, and prescribed a locally isothermal temperature structure. More precise modeling of the energy equation will lead to better treatment of the disk thermodynamics as well as the wind mass-loading mechanism.

The weakly magnetized simulations, computed here, launch jet-like outflows that are fast, light, and re-collimate toward the axis. Magnetic lever arm values in my simulations, $\lambda \sim 5$, are too large when compared to the ones measured in CO observations of outflows $\lambda \sim 1.5$ (Louvet et al. 2018; de-Valon et al. 2020). Including radiative transfer would heat the upper layers of the disk, and which in turn could affect the mass loading of the outflow by modifying the Bernoulli invariant (Casse and Ferreira 2000a). This might lead to more massive and slower outflows with magnetic lever arm values closer to the ones measured in observations of outflows.

The impact of radiative heating could be explored using 2D effective models that accurately reproduce the accreting atmosphere. This method would be numerically cheap. However, due to the isothermal nature of our simulations, we have not measured the impact of turbulent heating. Moreover, it has been shown that convection can enhance the MRI-driven turbulent torque (Scepi et al. 2018b). Hence, the effect of radiative transfer on the energetics of the system can only be studied using global simulations of accretion disks.

Zhu et al. 2020 applied the methods of radiative transport developed in Jiang et al. 2014 to the context of FU Ori's. With this numerical method, they can solve the energy equation in a self-consistent manner. They show that the wind evacuates a considerable amount of the system energy, which could lead to

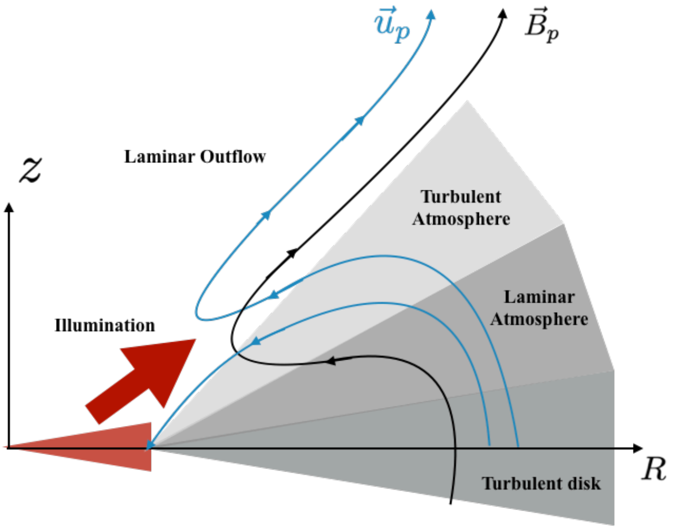

Figure 6.3: Sketch showing the illumination due to the inner regions of the accretion disk on the accreting atmosphere.

an overestimation of the observed accretion rate. In the end, the vertical structure is unmodified when compared to the case where the thermal structure is locally isothermal, the accretion is localized high above the disk surface. A fraction of the accretion energy must also be dissipated locally in this low-density region, thus we expect the production of an optically thin emission, usually referred to as a coronal emission. This 'elevated accretion' disk configuration could thus provide an explanation for the 'warm corona' component often seen in soft X rays in some active galactic nuclei (Done et al. 2012; Petrucci et al. 2018).

Illumination from the central object or the inner regions of the accretion disks (Begelman et al. 2015) could modify the vertical structure of the accretion disk, it could blow out the turbulent atmosphere (Fig. 6.3). This vertical readjustment could lead to a reorganization of the mean magnetic field topology. This reorganization could, in turn, affect the secular evolution of the disk as most of the accretion happens in the turbulent atmosphere. Moreover, the advection of the magnetic field could also be affected as it is linked to the vertical structure. Hence, radiative transport could be a key missing element, since it could modify the secular evolution of the accretion disk system.

It is now clear that a large scale vertical magnetic field is of utmost importance if we want to produce jet-like outflows. The strength of this magnetic field, measured by μ, has a dramatic influence on several properties of the accretion disk: its vertical structure, turbulence, and secular evolution. Our work opens the question of how the disk's vertical magnetic field will interact with the central object, star or black hole, and its magnetosphere.

Bibliography

[1] G. H. Herbig. “The Spectra of Two Nebulous Objects Near NGC 1999.” In: *The Astrophysical Journal* 113 (1, 1951).

[2] G. Haro. “Herbig’s Nebulous Objects Near NGC 1999.” In: *The Astrophysical Journal* 115 (1, 1952).

[3] E. Frieman and M. Rotenberg. “On Hydromagnetic Stability of Stationary Equilibria”. In: *Rev. Mod. Phys.* 32 (4 1960).

[4] L. Mestel. “A note on equatorial acceleration in a magnetic star”. In: *Monthly Notices of the Royal Astronomical Society* 122 (1961).

[5] R. Giacconi et al. “Evidence for x Rays From Sources Outside the Solar System”. In: *Physical Review Letters* 9 (1, 1962).

[6] G. H. Herbig. “The Properties and Problems of T Tauri Stars and Related Objects”. In: *Advances in Astronomy and Astrophysics* 1 (1962).

[7] D. C. Morton. “Neutron Stars as X-Ray Sources.” In: *The Astrophysical Journal* 140 (1, 1964).

[8] S. Bowyer et al. “Cosmic X-ray Sources”. In: *Science* 147 (1965).

[9] K.-H. Rädler. “On some electromagnetic phenomena in electrically conducting turbulently moving matter, especially in the presence of Coriolis forces.” In: *Veroeffentlichungen der Geod. Geophys* 13 (1969).

[10] R. M. Hjellming and C. M. Wade. “Radio Emission from X-Ray Sources”. In: *The Astrophysical Journal Letters* 168 (1, 1971).

[11] J. E. Pringle and M. J. Rees. “Accretion Disc Models for Compact X-Ray Sources”. In: *Astronomy and Astrophysics* 21 (1, 1972).

[12] H. Tananbaum et al. “Observation of a Correlated X-Ray Transition in Cygnus X-1”. In: *The Astrophysical Journal Letters* 177 (1, 1972).

[13] B. L. Webster and P. Murdin. “Cygnus X-1-a Spectroscopic Binary with a Heavy Companion ?” In: *Nature* 235 (1, 1972).

[14] N. I. Shakura and R. A. Sunyaev. “Black holes in binary systems. Observational appearance.” In: *Astronomy and Astrophysics* 24 (1973).

[15] D. Lynden-Bell and J. E. Pringle. “The evolution of viscous discs and the origin of the nebular variables.” In: *Monthly Notices of the Royal Astronomical Society* 168 (1, 1974).

[16] R. V. E. Lovelace. “Dynamo model of double radio sources”. In: *Nature* 262 (1, 1976).

[17] R. D. Schwartz. “A survey of southern dark clouds for Herbig-Haro objects and H-alpha emission stars”. In: *The Astrophysical Journal Supplement Series* 35 (1, 1977).

[18] H. K. Moffatt. “Magnetic field generation in electrically conducting fluids”. In: *Cambridge, England, Cambridge University Press, 1978. 353 p.* (1978).

[19] R. D. Blandford and A. Königl. “Relativistic jets as compact radio sources”. In: *The Astrophysical Journal* 232 (1, 1979).

[20] M. Cohen and L. V. Kuhi. “Observational studies of pre-main-sequence evolution”. In: *The Astrophysical Journal Supplement Series* 41 (1, 1979).

[21] J. E. Pringle and G. J. Savonije. “X-ray emission from dwarf novae.” In: *Monthly Notices of the Royal Astronomical Society* 187 (1, 1979).

[22] R. L. Snell, R. B. Loren, and R. L. Plambeck. “Observations of CO in L1551 - Evidence for stellar wind driven shocks”. In: *The Astrophysical Journal Letters* 239 (1, 1980).

[23] R. D. Blandford and D. G. Payne. “Hydromagnetic flows from accretion discs and the production of radio jets”. In: *Monthly Notices of the Royal Astronomical Society* 199 (1982).

[24] F. A. Cordova and K. O. Mason. “High-velocity winds from a dwarf nova during outburst.” In: *The Astrophysical Journal* 260 (1, 1982).

[25] R. E. Pudritz and C. A. Norman. “Centrifugally driven winds from contracting molecular disks”. In: *The Astrophysical Journal* 274 (1, 1983).

[26] S. Terebey, F. H. Shu, and P. Cassen. “The collapse of the cores of slowly rotating isothermal clouds”. In: *The Astrophysical Journal* 286 (1, 1984).

[27] K. Horne and M. C. Cook. “UBV images of the Z Cha accretion disc in outburst.” In: *Monthly Notices of the Royal Astronomical Society* 214 (1, 1985).

[28] J. Patterson and J. C. Raymond. “X-ray emission from cataclysmic variables with accretion disks. II. EUV/soft X-ray radiation.” In: *The Astrophysical Journal* 292 (1, 1985).

[29] R. L. Snell and F. P. Schloerb. “Structure and physical properties of the bipolar outflow in L1551”. In: *The Astrophysical Journal* 295 (1, 1985).

[30] F. C. Adams and F. H. Shu. “Infrared spectra of rotating protostars”. In: *The Astrophysical Journal* 308 (1, 1986).

[31] J. Wood et al. “High-speed photometry of the dwarf nova Z Cha in quiescence.” In: *Monthly Notices of the Royal Astronomical Society* 219 (1, 1986).

[32] S. J. Kenyon and L. Hartmann. “Spectral energy distributions of T Tauri stars - Disk flaring and limits on accretion”. In: *The Astrophysical Journal* 323 (1, 1987).

[33] C. W. Mauche and J. C. Raymond. “IUE Observations of the Dwarf Nova HL Canis Majoris and the Winds of Cataclysmic Variables”. In: *The Astrophysical Journal* 323 (1, 1987).

[34] C. R. Evans and J. F. Hawley. “Simulation of magnetohydrodynamic flows - A constrained transport method”. In: *The Astrophysical Journal* 332 (1988).

[35] A. Konigl. “Self-similar Models of Magnetized Accretion Disks”. In: *The Astrophysical Journal* 342 (1, 1989).

[36] S. Mineshige and J. C. Wheeler. “Disk-Instability Model for Soft X-Ray Transients Containing Black Holes”. In: *The Astrophysical Journal* 343 (1, 1989).

[37] S. Cabrit et al. “Forbidden-Line Emission and Infrared Excesses in T Tauri Stars: Evidence for Accretion-driven Mass Loss?” In: *The Astrophysical Journal* 354 (1990).

[38] J. E. Drew. “Winds from Disks”. In: *IAU Colloq. 122: Physics of Classical Novae* 369 (1, 1990).

[39] S. A. Balbus and J. F. Hawley. “A Powerful Local Shear Instability in Weakly Magnetized Disks. I. Linear Analysis”. In: *The Astrophysical Journal* 376 (1991).

[40] J. F. Hawley and S. A. Balbus. “A Powerful Local Shear Instability in Weakly Magnetized Disks. II. Nonlinear Evolution”. In: *The Astrophysical Journal* 376 (1991).

[41] F. Shu et al. “Star formation and the nature of bipolar outflows”. In: *The Astrophysical Journal Letters* 370 (1, 1991).

[42] A. C. Raga and L. Kofman. “Knots in stellar jets from time-dependent sources”. In: *The Astrophysical Journal* 386 (1, 1992).

[43] J. Ferreira and G. Pelletier. “Magnetized accretion-ejection structures. 1. General statements”. In: *Astronomy and Astrophysics* 276 (1993).

[44] M. Wardle and A. Koenigl. “The structure of protostellar accretion disks and the origin of bipolar flows”. In: *The Astrophysical Journal* 410 (1, 1993).

[45] J. Contopoulos and R. V. E. Lovelace. “Magnetically Driven Jets and Winds: Exact Solutions”. In: *The Astrophysical Journal* 429 (1994).

[46] J. Goodman and G. Xu. “Parasitic Instabilities in Magnetized, Differentially Rotating Disks”. In: *The Astrophysical Journal* 432 (1994).

[47] S. H. Lubow, J. C. B. Papaloizou, and J. E. Pringle. “Magnetic field dragging in accretion discs”. In: *Monthly Notices of the Royal Astronomical Society* 267.2 (1994).

[48] I. F. Mirabel and L. F. Rodríguez. “A superluminal source in the Galaxy”. In: *Nature* 371 (1, 1994).

[49] F. Shu et al. “Magnetocentrifugally driven flows from young stars and disks. 1: A generalized model”. In: *The Astrophysical Journal* 429 (1, 1994).

[50] J. Ferreira and G. Pelletier. “Magnetized accretion-ejection structures. III. Stellar and extragalactic jets as weakly dissipative disk outflows.” In: *Astronomy and Astrophysics* 295 (1995).

[51] P. Hartigan, S. Edwards, and L. Ghandour. “Disk Accretion and Mass Loss from Young Stars”. In: *The Astrophysical Journal* 452 (1, 1995).

[52] J. F. Hawley, C. F. Gammie, and S. A. Balbus. “Local Three-dimensional Magnetohydrodynamic Simulations of Accretion Disks”. In: *The Astrophysical Journal* 440 (1995).

[53] Z. Li. “Magnetohydrodynamic disk-wind connection: Self-similar solutions”. In: *The Astrophysical Journal* 444 (1, 1995).

[54] C. J. Burrows et al. “Hubble Space Telescope Observations of the Disk and Jet of HH 30”. In: *The Astrophysical Journal* 473 (1, 1996).

[55] C. F. Gammie. “Layered Accretion in T Tauri Disks”. In: *The Astrophysical Journal* 457 (1996).

[56] M. R. Hayashi, K. Shibata, and R. Matsumoto. “X-Ray Flares and Mass Outflows Driven by Magnetic Interaction between a Protostar and Its Surrounding Disk”. In: *The Astrophysical Journal Letters* 468 (1, 1996).

[57] L. Jin. “Damping of the Shear Instability in Magnetized Disks by Ohmic Diffusion”. In: *The Astrophysical Journal* 457 (1, 1996).

[58] J. M. Stone et al. “Three-dimensional Magnetohydrodynamical Simulations of Vertically Stratified Accretion Disks”. In: *The Astrophysical Journal* 463 (1, 1996).

[59] P. J. Wheatley et al. “The X-ray and EUV spectrum of the dwarf nova VW Hydri in outburst and quiescence.” In: *Astronomy and Astrophysics* 307 (1996).

[60] J. Ferreira. “Magnetically-driven jets from Keplerian accretion discs.” In: *Astronomy and Astrophysics* 319 (1997).

[61] C. Knigge and J. E. Drew. “Eclipse Mapping of the Accretion Disk Wind in the Cataclysmic Variable UX Ursae Majoris”. In: *The Astrophysical Journal* 486 (1, 1997).

[62] G. I. Ogilvie. “The equilibrium of a differentially rotating disc containing a poloidal magnetic field”. In: *Monthly Notices of the Royal Astronomical Society* 288.1 (1997).

[63] C. F. Gammie and K. Menou. “On the Origin of Episodic Accretion in Dwarf Novae”. In: *The Astrophysical Journal* 492 (1, 1998).

[64] G. I. Ogilvie and M. Livio. “On the Difficulty of Launching an Outflow from an Accretion Disk”. In: *The Astrophysical Journal* 499 (1998).

[65] M. Wardle. “The Balbus-Hawley instability in weakly ionized discs”. In: *Monthly Notices of the Royal Astronomical Society* 307 (1, 1999).

[66] F. Bacciotti et al. “Hubble Space Telescope STIS Spectroscopy of the Optical Outflow from DG Tauri: Structure and Kinematics on Subarcsecond Scales”. In: *The Astrophysical Journal Letters* 537 (1, 2000).

[67] W. N. Brandt and N. S. Schulz. “The Discovery of Broad P Cygni X-Ray Lines from Circinus X-1 with the Chandra High-Energy Transmission Grating Spectrometer”. In: *The Astrophysical Journal Letters* 544 (1, 2000).

[68] F. Casse and J. Ferreira. “Magnetized accretion-ejection structures. V. Effects of entropy generation inside the disc”. In: *Astronomy and Astrophysics* 361 (2000).

[69] F. Casse and J. Ferreira. “Magnetized accretion-ejection structures. IV. Magnetically-driven jets from resistive, viscous, Keplerian discs”. In: *Astronomy and Astrophysics* 353 (2000).

[70] S. Corbel et al. “Coupling of the X-ray and radio emission in the black hole candidate and compact jet source GX 339-4”. In: *Astronomy and Astrophysics* 359 (1, 2000).

[71] C. Dougados et al. “T Tauri stars microjets resolved by adaptive optics”. In: *Astronomy and Astrophysics* 357 (1, 2000).

[72] J. Ferreira, G. Pelletier, and S. Appl. “Reconnection X-winds: spin-down of low-mass protostars”. In: *Monthly Notices of the Royal Astronomical Society* 312 (1, 2000).

[73] T. P. Fleming, J. M. Stone, and J. F. Hawley. “The Effect of Resistivity on the Nonlinear Stage of the Magnetorotational Instability in Accretion Disks”. In: *The Astrophysical Journal* 530 (1, 2000).

[74] W.-T. Kim and E. C. Ostriker. “Magnetohydrodynamic Instabilities in Shearing, Rotating, Stratified Winds and Disks”. In: *The Astrophysical Journal* 540 (2000).

[75] A. Konigl and R. E. Pudritz. “Disk Winds and the Accretion-Outflow Connection”. In: *Protostars and Planets IV* (2000).

[76] N. Vlahakis et al. “A disc-wind model with correct crossing of all magnetohydrodynamic critical surfaces”. In: *Monthly Notices of the Royal Astronomical Society* 318 (2000).

[77] G. Dubus, J.-M. Hameury, and J.-P. Lasota. “The disc instability model for X-ray transients: Evidence for truncation and irradiation”. In: *Astronomy and Astrophysics, v.373, p.251-271 (2001)* 373 (2001).

[78] J.-P. Lasota. “The disc instability model of dwarf novae and low-mass X-ray binary transients”. In: *New Astronomy Reviews* 45 (1, 2001).

[79] G. I. Ogilvie and M. Livio. “Launching of Jets and the Vertical Structure of Accretion Disks”. In: *The Astrophysical Journal* 553 (2001).

[80] F. Bacciotti et al. “Hubble Space Telescope/STIS Spectroscopy of the Optical Outflow from DG Tauri: Indications for Rotation in the Initial Jet Channel”. In: *The Astrophysical Journal* 576 (1, 2002).

[81] F. Casse and R. Keppens. “Magnetized Accretion-Ejection Structures: 2.5-dimensional Magnetohydrodynamic Simulations of Continuous Ideal Jet Launching from Resistive Accretion Disks”. In: *The Astrophysical Journal* 581.2 (2002).

[82] J. C. Lee et al. “High-Resolution Chandra HETGS and Rossi X-Ray Timing Explorer Observations of GRS 1915+105: A Hot Disk Atmosphere and Cold Gas Enriched in Iron and Silicon”. In: *The Astrophysical Journal* 567 (1, 2002).

[83] A. N. Parmar et al. “Discovery of narrow X-ray absorption features from the dipping low-mass X-ray binary X 1624-490 with XMM-Newton”. In: *Astronomy and Astrophysics* 386 (1, 2002).

[84] C. Sauty, E. Trussoni, and K. Tsinganos. “Nonradial and nonpolytropic astrophysical outflows. V. Acceleration and collimation of self-similar winds”. In: *Astronomy and Astrophysics* 389 (2002).

[85] J. M. Anderson et al. “Locating the Launching Region of T Tauri Winds: The Case of DG Tauri”. In: *The Astrophysical Journal Letters* 590 (1, 2003).

[86] S. Corbel et al. “Radio/X-ray correlation in the low/hard state of GX 339-4”. In: *Astronomy and Astrophysics* 400 (2003).

[87] I. Rogachevskii and N. Kleeorin. “Electromotive force and large-scale magnetic dynamo in a turbulent flow with a mean shear”. In: *Physical Review E* 68 (1, 2003).

[88] P. J. Wheatley, C. W. Mauche, and J. A. Mattei. “The X-ray and extreme-ultraviolet flux evolution of SS Cygni throughout outburst”. In: *Monthly Notices of the Royal Astronomical Society* 345 (1, 2003).

[89] F. Casse and R. Keppens. “Radiatively Inefficient Magnetohydrodynamic Accretion-Ejection Structures”. In: *The Astrophysical Journal* 601.1 (2004).

[90] C. Dougados et al. “The Origin of Jets from Young Stars: Steady State Disk Wind Models Confronted to Observations”. In: *Astrophysics and Space Science* 293 (1, 2004).

[91] J. Ferreira and F. Casse. “Stationary Accretion Disks Launching Super-fast-magnetosonic Magnetohydrodynamic Jets”. In: *The Astrophysical Journal Letters* 601 (2004).

[92] M. W. Kunz and S. A. Balbus. “Ambipolar diffusion in the magnetorotational instability”. In: *Monthly Notices of the Royal Astronomical Society* 348 (1, 2004).

[93] S. Matt and R. E. Pudritz. “Accretion-powered Stellar Winds as a Solution to the Stellar Angular Momentum Problem”. In: *The Astrophysical Journal* 632 (1, 2005).

[94] T. Miyoshi and K. Kusano. “A multi-state HLL approximate Riemann solver for ideal magnetohydrodynamics”. In: *Journal of Computational Physics* 208 (2005).

[95] D. Pandel et al. “X-Ray Observations of the Boundary Layer in Dwarf Novae at Low Accretion Rates”. In: *The Astrophysical Journal* 626 (1, 2005).

[96] J. Ferreira, C. Dougados, and S. Cabrit. “Which jet launching mechanism(s) in T Tauri stars?” In: *Astronomy and Astrophysics* 453.3 (2006).

[97] J. Ferreira et al. “A unified accretion-ejection paradigm for black hole X-ray binaries. I. The dynamical constituents”. In: *Astronomy and Astrophysics* 447.3 (2006).

[98] S. Cabrit. “Jets from Young Stars: The Need for MHD Collimation and Acceleration Processes”. In: 723 (2007). Conference Name: Lecture Notes in Physics, Berlin Springer Verlag.

[99] C. Done, M. Gierliński, and A. Kubota. “Modelling the behaviour of accretion flows in X-ray binaries. Everything you always wanted to know about accretion but were afraid to ask”. In: *Astronomy and Astrophysics Review* 15 (1, 2007).

[100] A. Mignone et al. “PLUTO: A Numerical Code for Computational Astrophysics”. In: *The Astrophysical Journal Supplement Series* 170 (2007).

[101] R. E. Pudritz et al. “Disk Winds, Jets, and Outflows: Theoretical and Computational Foundations”. In: *Protostars and Planets V* (2007).

[102] C. Zanni et al. “MHD simulations of jet acceleration from Keplerian accretion disks. The effects of disk resistivity”. In: *Astronomy and Astrophysics* 469.3 (2007).

[103] C. Combet and J. Ferreira. “The radial structure of protostellar accretion disks: influence of jets”. In: *Astronomy and Astrophysics* 479 (2008).

[104] M. W. Kunz. “On the linear stability of weakly ionized, magnetized planar shear flows”. In: *Monthly Notices of the Royal Astronomical Society* 385 (1, 2008).

[105] D. M. Rothstein and R. V. E. Lovelace. “Advection of Magnetic Fields in Accretion Disks: Not So Difficult After All”. In: *The Astrophysical Journal* 677 (2008).

[106] R. P. Fender, J. Homan, and T. M. Belloni. “Jets from black hole X-ray binaries: testing, refining and extending empirical models for the coupling to X-rays”. In: *Monthly Notices of the Royal Astronomical Society* 396 (1, 2009).

[107] S. Fromang and J. M. Stone. “Turbulent resistivity driven by the magnetorotational instability”. In: *Astronomy and Astrophysics* 507 (2009).

[108] X. Guan and C. F. Gammie. “The Turbulent Magnetic Prandtl Number of MHD Turbulence in Disks”. In: *The Astrophysical Journal* 697 (2009).

[109] T. Heinemann and J. C. B. Papaloizou. “The excitation of spiral density waves through turbulent fluctuations in accretion discs - I. WKBJ theory”. In: *Monthly Notices of the Royal Astronomical Society* 397 (2009).

[110] T. Heinemann and J. C. B. Papaloizou. “The excitation of spiral density waves through turbulent fluctuations in accretion discs - II. Numerical simulations with MRI-driven turbulence”. In: *Monthly Notices of the Royal Astronomical Society* 397 (2009).

[111] R. Launhardt et al. “Rotating molecular outflows: the young T Tauri star in CB 26”. In: *Astronomy and Astrophysics* 494 (1, 2009).

[112] G. Lesur and P.-Y. Longaretti. “Turbulent resistivity evaluation in magnetorotational instability generated turbulence”. In: *Astronomy & Astrophysics* 504.2 (2009).

[113] T. K. Suzuki and S.-i. Inutsuka. "Disk Winds Driven by Magnetorotational Instability and Dispersal of Protoplanetary Disks". In: *The Astrophysical Journal Letters* 691 (2009).

[114] P. Tzeferacos et al. "On the magnetization of jet-launching discs". In: *Monthly Notices of the Royal Astronomical Society* 400 (1, 2009).

[115] C. Combet, J. Ferreira, and F. Casse. "Dead zones in protostellar discs: the case of jet emitting discs". In: *Astronomy and Astrophysics* 519 (2010).

[116] C. P. Dullemond and J. D. Monnier. "The Inner Regions of Protoplanetary Disks". In: *Annual Review of Astronomy and Astrophysics* 48 (2010).

[117] H. Ghosh et al. "Monte Carlo Simulations of the Thermal Comptonization Process in a Two-Component Accretion Flow around a Black Hole in the Presence of AN Outflow". In: *International Journal of Modern Physics D* 19 (2010).

[118] H. N. Latter, S. Fromang, and O. Gressel. "MRI channel flows in vertically stratified models of accretion discs". In: *Monthly Notices of the Royal Astronomical Society* 406 (2010).

[119] G. C. Murphy, J. Ferreira, and C. Zanni. "Large scale magnetic fields in viscous resistive accretion disks: I. Ejection from weakly magnetized disks". In: *Astronomy and Astrophysics* 512 (2010).

[120] T. K. Suzuki, T. Muto, and S.-i. Inutsuka. "Protoplanetary Disk Winds via Magnetorotational Instability: Formation of an Inner Hole and a Crucial Assist for Planet Formation". In: *The Astrophysical Journal* 718 (1, 2010).

[121] V. Agra-Amboage et al. "Sub-arcsecond [Fe ii] spectro-imaging of the DG Tauri jet. Periodic bubbles and a dusty disk wind?" In: *Astronomy and Astrophysics* 532 (1, 2011).

[122] P. J. Armitage. "Dynamics of Protoplanetary Disks". In: *Annual Review of Astronomy and Astrophysics* 49.1 (2011). arXiv: 1011.1496.

[123] X.-N. Bai and J. M. Stone. "Effect of Ambipolar Diffusion on the Nonlinear Evolution of Magnetorotational Instability in Weakly Ionized Disks". In: *The Astrophysical Journal* 736 (1, 2011).

[124] S. Fromang, W. Lyra, and F. Masset. "Meridional circulation in turbulent protoplanetary disks". In: *Astronomy and Astrophysics* 534 (1, 2011).

[125] D. Perez-Becker and E. Chiang. "Surface Layer Accretion in Transitional and Conventional Disks: From Polycyclic Aromatic Hydrocarbons to Planets". In: *The Astrophysical Journal* 727 (1, 2011).

[126] J. K. Cannizzo et al. "The Kepler Light Curves of V1504 Cygni and V344 Lyrae: A Study of the Outburst Properties". In: *The Astrophysical Journal* 747 (1, 2012).

[127] M. Coriat, R. P. Fender, and G. Dubus. "Revisiting a fundamental test of the disc instability model for X-ray binaries". In: *Monthly Notices of the Royal Astronomical Society* 424 (1, 2012).

[128] C. Done et al. "Intrinsic disc emission and the soft X-ray excess in active galactic nuclei: The soft X-ray excess in AGN". In: *Monthly Notices of the Royal Astronomical Society* 420.3 (1, 2012).

[129] J. Guilet and G. I. Ogilvie. "Transport of magnetic flux and the vertical structure of accretion discs - I. Uniform diffusion coefficients". In: *Monthly Notices of the Royal Astronomical Society* 424.3 (2012).

[130] I. Kotko and J.-P. Lasota. “The viscosity parameter α and the properties of accretion disc outbursts in close binaries”. In: *Astronomy and Astrophysics* 545 (2012).

[131] H. N. Latter and J. C. B. Papaloizou. “Hysteresis and thermal limit cycles in MRI simulations of accretion discs”. In: *Monthly Notices of the Royal Astronomical Society* 426 (1, 2012).

[132] J. C. McKinney, A. Tchekhovskoy, and R. D. Blandford. “General relativistic magnetohydrodynamic simulations of magnetically choked accretion flows around black holes: Magnetically choked accretion flows”. In: *Monthly Notices of the Royal Astronomical Society* 423.4 (2012).

[133] R. Moll. “Shearing box simulations of accretion disk winds”. In: *Astronomy and Astrophysics* 548 (2012).

[134] G. I. Ogilvie. “Jet launching from accretion discs in the local approximation”. In: *Monthly Notices of the Royal Astronomical Society* 423 (1, 2012).

[135] G. Ponti et al. “Ubiquitous equatorial accretion disc winds in black hole soft states”. In: *Monthly Notices of the Royal Astronomical Society* 422 (1, 2012).

[136] X.-N. Bai and J. M. Stone. “Local Study of Accretion Disks with a Strong Vertical Magnetic Field: Magnetorotational Instability and Disk Outflow”. In: *The Astrophysical Journal* 767.1 (2013).

[137] X.-N. Bai and J. M. Stone. “Wind-driven Accretion in Protoplanetary Disks. I. Suppression of the Magnetorotational Instability and Launching of the Magnetocentrifugal Wind”. In: *The Astrophysical Journal* 769.1 (2013).

[138] S. Corbel et al. “The ‘universal’ radio/X-ray flux correlation: the case study of the black hole GX 339-4”. In: *Monthly Notices of the Royal Astronomical Society* 428 (1, 2013).

[139] J. Ferreira and F. Casse. “On fan-shaped cold MHD winds from Keplerian accretion discs”. In: *Monthly Notices of the Royal Astronomical Society, Volume 428, Issue 1, p.307-320* 428.1 (2013).

[140] S. Fromang et al. “Local outflows from turbulent accretion disks”. In: *Astronomy and Astrophysics* 552 (2013).

[141] J. Guilet and G. I. Ogilvie. “Transport of magnetic flux and the vertical structure of accretion discs - II. Vertical profile of the diffusion coefficients”. In: *Monthly Notices of the Royal Astronomical Society* 430 (2013).

[142] G. Lesur, J. Ferreira, and G. I. Ogilvie. “The magnetorotational instability as a jet launching mechanism”. In: *Astronomy and Astrophysics* 550 (2013).

[143] R. P. Nelson, O. Gressel, and O. M. Umurhan. “Linear and non-linear evolution of the vertical shear instability in accretion discs”. In: *Monthly Notices of the Royal Astronomical Society* 435 (2013).

[144] C. Zanni and J. Ferreira. “MHD simulations of accretion onto a dipolar magnetosphere. II. Magnetospheric ejections and stellar spin-down”. In: *Astronomy and Astrophysics* 550 (1, 2013).

[145] S.-N. Zhang. “Black hole binaries and microquasars”. In: *Frontiers of Physics* 8 (1, 2013).

[146] V. Agra-Amboage et al. “Origin of the wide-angle hot H2 in DG Tauri. New insight from SINFONI spectro-imaging”. In: *Astronomy and Astrophysics* 564 (1, 2014).

[147] J. Guilet and G. I. Ogilvie. “Global evolution of the magnetic field in a thin disc and its consequences for protoplanetary systems”. In: *Monthly Notices of the Royal Astronomical Society* 441.1 (2014).

[148] Y.-F. Jiang, J. M. Stone, and S. W. Davis. “An Algorithm for Radiation Magnetohydrodynamics Based on Solving the Time-dependent Transfer Equation”. In: *The Astrophysical Journal Supplement Series* 213.1 (18, 2014). arXiv: 1403.6126.

[149] T. K. Suzuki and S.-i. Inutsuka. “Magnetohydrodynamic Simulations of Global Accretion Disks with Vertical Magnetic Fields”. In: *The Astrophysical Journal* 784 (1, 2014).

[150] L. Venuti et al. “Mapping accretion and its variability in the young open cluster NGC 2264: a study based on u-band photometry”. In: *Astronomy and Astrophysics* 570 (1, 2014).

[151] M. C. Begelman, P. J. Armitage, and C. S. Reynolds. “Accretion Disk Dynamo as the Trigger for X-Ray Binary State Transitions”. In: *The Astrophysical Journal* 809 (2015).

[152] O. Gressel and M. E. Pessah. “Characterizing the Mean-field Dynamo in Turbulent Accretion Disks”. In: *The Astrophysical Journal* 810 (1, 2015).

[153] N. Higginbottom and D. Proga. “Coronae and Winds from Irradiated Disks in X-Ray Binaries”. In: *The Astrophysical Journal* 807 (1, 2015).

[154] P. Bjerkeli et al. “Resolved images of a protostellar outflow driven by an extended disk wind”. In: *Nature* 540 (1, 2016).

[155] S. Chakravorty et al. “Magneto centrifugal winds from accretion discs around black hole binaries”. In: *Astronomische Nachrichten* 337.4 (2016). arXiv: 1602.00086.

[156] D. L. Coppejans et al. “Dwarf nova-type cataclysmic variable stars are significant radio emitters”. In: *Monthly Notices of the Royal Astronomical Society* 463 (1, 2016).

[157] M. Díaz Trigo and L. Boirin. “Accretion disc atmospheres and winds in low-mass X-ray binaries”. In: *Astronomische Nachrichten* 337 (1, 2016).

[158] S. Nagarkoti and S. K. Chakrabarti. “Viscosity parameter in dissipative accretion flows with mass outflow around black holes”. In: *Monthly Notices of the Royal Astronomical Society* 462 (1, 2016).

[159] G. I. Ogilvie. “Astrophysical fluid dynamics”. In: *Journal of Plasma Physics* 82.3 (2016).

[160] G. Ponti et al. “High ionisation absorption in low mass X-ray binaries”. In: *Astronomische Nachrichten* 337 (1, 2016).

[161] G. Salvesen et al. “Accretion disc dynamo activity in local simulations spanning weak-to-strong net vertical magnetic flux regimes”. In: *Monthly Notices of the Royal Astronomical Society* 457.1 (2016).

[162] D. Stepanovs and C. Fendt. “An Extensive Numerical Survey of the Correlation Between Outflow Dynamics and Accretion Disk Magnetization”. In: *The Astrophysical Journal* 825 (2016).

[163] Y. Zhang et al. “ALMA Cycle 1 Observations of the HH46/47 Molecular Outflow: Structure, Entrainment, and Core Impact”. In: *The Astrophysical Journal* 832 (1, 2016).

[164] W. Béthune, G. Lesur, and J. Ferreira. “Global simulations of protoplanetary disks with net magnetic flux. I. Non-ideal MHD case”. In: *Astronomy and Astrophysics* 600 (2017).

[165] I. Contopoulos, D. Kazanas, and K. Fukumura. “Magnetically advected winds”. In: *Monthly Notices of the Royal Astronomical Society* 472.1 (2017).

[166] J.-M. Hameury et al. “Hystereses in dwarf nova outbursts and low-mass X-ray binaries”. In: *Astronomy and Astrophysics* 600 (2017).

[167] T. Hirota et al. “Disk-driven rotating bipolar outflow in Orion Source I”. In: *Nature Astronomy* 1 (1, 2017).

[168] B. Tabone et al. “ALMA discovery of a rotating SO/SO2 flow in HH212. A possible MHD disk wind?” In: *Astronomy and Astrophysics* 607 (1, 2017).

[169] L. Wang and J. Goodman. “Hydrodynamic Photoevaporation of Protoplanetary Disks with Consistent Thermochemistry”. In: *The Astrophysical Journal* 847 (2017).

[170] S. M. Andrews et al. “The Disk Substructures at High Angular Resolution Project (DSHARP). I. Motivation, Sample, Calibration, and Overview”. In: *The Astrophysical Journal Letters* 869 (1, 2018).

[171] F. Louvet et al. “The HH30 edge-on T Tauri star. A rotating and precessing monopolar outflow scrutinized by ALMA”. In: *Astronomy and Astrophysics* 618 (1, 2018).

[172] G. Marcel et al. “A unified accretion-ejection paradigm for black hole X-ray binaries. II. Observational signatures of jet-emitting disks”. In: *Astronomy and Astrophysics* 615 (2018).

[173] G. Marcel et al. “A unified accretion-ejection paradigm for black hole X-ray binaries. III. Spectral signatures of hybrid disk configurations”. In: *Astronomy and Astrophysics* 617 (2018).

[174] M. D. Marshall, M. J. Avara, and J. C. McKinney. “Angular momentum transport in thin magnetically arrested discs”. In: *Monthly Notices of the Royal Astronomical Society* 478 (2018).

[175] B. Nisini et al. “Connection between jets, winds and accretion in T Tauri stars. The X-shooter view”. In: *Astronomy and Astrophysics* 609 (1, 2018).

[176] P.-O. Petrucci et al. “Testing warm Comptonization models for the origin of the soft X-ray excess in AGNs”. In: *Astronomy and Astrophysics* 611 (1, 2018).

[177] N. Scepi et al. “Impact of convection and resistivity on angular momentum transport in dwarf novae”. In: *Astronomy and Astrophysics* 609 (2018).

[178] N. Scepi et al. “Turbulent and wind-driven accretion in dwarf novae threaded by a large-scale magnetic field”. In: *Astronomy and Astrophysics* 620 (2018).

[179] B. E. Tetarenko et al. “Strong disk winds traced throughout outbursts in black-hole X-ray binaries”. In: *Nature* 554 (1, 2018).

[180] Z. Zhu and J. M. Stone. “Global Evolution of an Accretion Disk with a Net Vertical Field: Coronal Accretion, Flux Transport, and Disk Winds”. In: *The Astrophysical Journal* 857 (2018).

[181] P. Charles et al. “Hot, dense He II outflows during the 2017 outburst of the X-ray transient Swift J1357.2-0933”. In: *Monthly Notices of the Royal Astronomical Society* 489 (1, 2019).

[182] J. V. Hernández Santisteban et al. “From outburst to quiescence: spectroscopic evolution of V1838 Aql imbedded in a bow-shock nebula”. In: *Monthly Notices of the Royal Astronomical Society* 486 (1, 2019).

[183] J. Jacquemin-Ide, J. Ferreira, and G. Lesur. “Magnetically-driven jets and winds from weakly magnetized accretion disks”. In: *Monthly Notices of the Royal Astronomical Society* 490.3 (2019). arXiv: 1909.12258.

[184] F. Jiménez-Ibarra et al. “An equatorial outflow in the black hole optical dipper Swift J1357.2-0933”. In: *Monthly Notices of the Royal Astronomical Society* 489 (1, 2019).

[185] G. Marcel et al. “A unified accretion-ejection paradigm for black hole X-ray binaries. IV. Replication of the 2010–2011 activity cycle of GX 339-4”. In: *Astronomy & Astrophysics* 626 (2019). arXiv: 1905.05057.

[186] F. Rincon. “Dynamo theories”. In: *Journal of Plasma Physics* 85.4 (2019).

[187] N. Scepi, G. Dubus, and G. Lesur. “Magnetic wind-driven accretion in dwarf novae”. In: *Astronomy and Astrophysics* 626 (1, 2019).

[188] R. Teague, J. Bae, and E. A. Bergin. “Meridional flows in the disk around a young star”. In: *Nature* 574 (1, 2019).

[189] R. Tomaru et al. “The thermal-radiative wind in low-mass X-ray binary H1743-322: radiation hydrodynamic simulations”. In: *Monthly Notices of the Royal Astronomical Society* 490 (1, 2019).

[190] C. J. White, J. M. Stone, and E. Quataert. “A Resolution Study of Magnetically Arrested Disks”. In: *The Astrophysical Journal* 874 (2019).

[191] Y. Zhang et al. “An Episodic Wide-angle Outflow in HH 46/47”. In: *The Astrophysical Journal* 883 (1, 2019).

[192] O. Gressel et al. “Global Hydromagnetic Simulations of Protoplanetary Disks with Stellar Irradiation and Simplified Thermochemistry”. In: *The Astrophysical Journal* 896 (1, 2020).

[193] G. Lesur. “Magnetohydrodynamics of protoplanetary discs”. In: *arXiv:2007.15967 [astro-ph, physics:physics]* (2020). arXiv: 2007.15967.

[194] M. Liska, A. Tchekhovskoy, and E. Quataert. “Large-scale poloidal magnetic field dynamo leads to powerful jets in GRMHD simulations of black hole accretion with toroidal field”. In: *Monthly Notices of the Royal Astronomical Society* 494.3 (2020).

[195] B. Mishra et al. “Strongly magnetized accretion discs: structure and accretion from global magnetohydrodynamic simulations”. In: *Monthly Notices of the Royal Astronomical Society* 492 (2020).

[196] T. P. Ray and J. Ferreira. “Jets from Young Stars”. In: *arXiv e-prints* 2009 (1, 2020).

[197] A. Riols, G. Lesur, and F. Menard. “Ring formation and dust dynamics in wind-driven protoplanetary discs: global simulations”. In: *arXiv e-prints* 2006 (1, 2020).

[198] N. Scepi et al. “Magnetic field transport in compact binaries”. In: *Astronomy and Astrophysics* 641 (2020).

[199] A. de-Valon et al. “ALMA reveals a large structured disk and nested rotating outflows in DG Tauri B”. In: *Astronomy and Astrophysics* 634 (1, 2020).

[200] Z. Zhu, Y.-F. Jiang, and J. M. Stone. “Global 3D radiation magnetohydrodynamic simulations for FU Ori’s accretion disc and observational signatures of magnetic fields”. In: *Monthly Notices of the Royal Astronomical Society* 495 (2020).

[201] C. Cui and X.-N. Bai. “Global Three-Dimensional Simulations of Outer Protoplanetary Disks with Ambipolar Diffusion”. In: *arXiv e-prints* (1, 2021).

[202] K. Fukumura et al. “Modeling Magnetic Disk-Wind State Transitions in Black Hole X-ray Binaries”. In: *arXiv e-prints* 2103 (1, 2021).

[203] J. Jacquemin-Ide, G. Lesur, and J. Ferreira. “Magnetic outflows from turbulent accretion disks - I. Vertical structure and secular evolution”. In: *Astronomy & Astrophysics* 647 (2021). Publisher: EDP Sciences.

[204] G. Lesur. “A systematic description of wind-driven protoplanetary discs”. In: *arXiv e-prints* 2101 (2021).

[205] J.-w. Li and X. Cao. “The large-scale magnetic field advected in the corona of a thin accretion disk”. In: *arXiv e-prints* 2101 (2021).

[206] J. R. Najita et al. “High-resolution Mid-infrared Spectroscopy of GV Tau N: Surface Accretion and Detection of NH3 in a Young Protoplanetary Disk”. In: *The Astrophysical Journal* 908 (1, 2021).

[207] P.-O. Petrucci et al. “Expected disk wind properties evolution along an X-ray Binary outburst”. In: *arXiv e-prints* 2103 (1, 2021).

Appendices

APPENDIX A

Self-similar equations

For the sake of completeness, the full set of MHD equations solved are reported in this section. We define the self-similar functions $f_i(x)$ with $x = z/h$ and $h = \varepsilon R$

$$\begin{aligned} \rho &= \rho_0 \left(\frac{R}{R_0}\right)^{\zeta_4} f_4 \,, & P &= P_0 \left(\frac{R}{R_0}\right)^{\zeta_{10}} f_{10} \,, \\ T &= T_0 \left(\frac{R}{R_0}\right)^{\zeta_7} f_7 \,, & u_z &= \varepsilon u_0 \left(\frac{R}{R_0}\right)^{\zeta_3} f_3 \,, \\ u_r &= -u_0 \left(\frac{R}{R_0}\right)^{\zeta_2} f_2 \,, & \Omega &= \Omega_0 \left(\frac{R}{R_0}\right)^{\zeta_5} f_5 \,, \\ B_\varphi &= q B_0 \left(\frac{R}{R_0}\right)^{\zeta_1 - 1} f_1 \,, & a(r,z) &= a_0 \left(\frac{R}{R_0}\right)^{\zeta_0} \psi \end{aligned}$$

where the subscript ”o” stand for a quantity evaluated at the disk equatorial plane ($x = 0$). Here, $q = \mu_0 J_{r0} h / B_0$ is the normalized radial current density, $a_0 = B_0 R_0^2/\zeta_0$ the magnetic flux with B_0 the vertical field component, $\Omega_0 = \delta_0 \Omega_{K0}$ the angular velocity, $P_0 = \rho_0 \Omega_{K0}^2 h^2$ and $u_0 = m_s C_s$, with $C_s = \Omega_{K0} h$ defining thereby the accretion Mach number m_s. The shape of a magnetic surface anchored at R_0 is defined by $a(r,z) = a_0$ and is provided by $R = R_0 \psi^{-1/\zeta_0}$. The three transport coefficients ν_v, ν_m, ν_m' (see Sect. 3.1.1) are written $\nu_A = \nu_{A0} \left(\frac{R}{R_0}\right)^{\zeta_8} f_8$ where the profile is a simple Gaussian[1] $f_8(x) = \exp\left(-x^2\right)$. Inserting these self-similar functions into the set of PDE (3.2-3.5) allows to separate them into an algebraic set on the exponents ζ_i and a set of ODEs on the functions f_i. This leads to the unique solution for a near-Keplerian, gas supported, accretion disk

$$\begin{aligned} \zeta_0 &= \frac{3}{4} + \frac{\xi}{2}, & \zeta_1 &= \frac{\xi}{2} - \frac{1}{4}, & \zeta_2 &= \zeta_3 = -\frac{1}{2} \\ \zeta_4 &= \xi - \frac{3}{2}, & \zeta_5 &= -\frac{3}{2}, & \zeta_7 &= -1 \\ \zeta_8 &= \frac{1}{2}, & \zeta_{10} &= \xi - \frac{5}{2} \end{aligned}$$

where ξ is the exponent of the disk accretion rate $\dot{M}_a \propto r^{\xi}$. Defining $\tilde{f}_4 = \ln f_4$ and $f_i' = df_i/dx$, allows to express mass conservation and the equation of state as the following ODEs

$$\tilde{f}_4'(f_3 + x f_2) = (\xi - 1) f_2 - f_3' - x f_2' \tag{A.1}$$

$$f_{10} = f_4 f_7 \tag{A.2}$$

---

[1] Note that Murphy et al. 2010 used $f_8(x) = \exp\left(-2x^2\right)$, while Stepanovs and Fendt 2016 used $f_8(x) = \exp\left(-0.5x^2\right)$, namely ideal MHD starting sooner. This may explain why the latter found more massive jets than the former.

Similarly, the radial, vertical and toroidal momentum transport equations become respectively

$$
\begin{aligned}
m_s^2\varepsilon^2 f_4(-\zeta_2 f_2^2 + f_2'(f_3 + x f_2)) &= -f_4\delta_0^2 f_5^2 + \frac{f_4}{(1+x^2\varepsilon^2)^{3/2}} \\
&\quad + \varepsilon^2(\zeta_{10} f_{10} - x f_{10}') \\
&\quad + \mu q^2 \varepsilon^2 f_1(\zeta_1 f_1 - x f_1') \\
&\quad + \mu \frac{\Delta'\psi}{\zeta_0}\left(\psi - x\frac{\psi'}{\zeta_0}\right) && \text{(A.3)} \\
m_s^2\varepsilon^2 f_4(-\zeta_3 f_2 f_3 + f_3'(f_3 + x f_2)) &= -\frac{x f_4}{(1+x^2\varepsilon^2)^{3/2}} - f_{10}' \\
&\quad - \mu q^2 f_1 f_1' - \mu\psi'\frac{\Delta'\psi}{\zeta_0^2\varepsilon^2} && \text{(A.4)} \\
2f_4(f_3 + x f_2) f_5' - f_2 f_4 f_5 &= \frac{\Lambda_0}{1+\Lambda_0}\left(\psi f_1' - \frac{\zeta_1}{\zeta_0} f_1 \psi'\right) \\
&\quad - \frac{1}{1+\Lambda_0} f_{\mathrm{turb}} && \text{(A.5)}
\end{aligned}
$$

where the modified laplacian (toroidal current density) is

$$
\Delta'\psi = \psi''(1+\varepsilon^2 x^2) + \varepsilon^2[(2\zeta_0 - 3)x\psi' - \zeta_0(2-\zeta_0)\psi] \tag{A.6}
$$

and $\Lambda_0 = \frac{p}{\mathcal{P}_m \varepsilon} - 1$ is the ratio of the magnetic to the viscous torque at the disk mid plane. The function $f_{\mathrm{turb}} = f_4 f_8$ is the prescription used for the turbulent stress. While the above ODEs are valid both in the disk and in the ideal MHD jet regime, the induction equation requires to deal with each regime in a separate way.

Within the resistive disk, Ohm's law (3.5) and the induction equation (3.6) become respectively

$$
\begin{aligned}
f_8\Delta'\psi &= -\mathcal{R}_m\varepsilon^2(\zeta_0 f_2 \psi - \psi'(f_3 + x f_2)) && \text{(A.7)} \\
(f_8 f_1')' &= \varepsilon^2 x\left(f_8(\zeta_1 f_1 - x f_1')\right)' - \varepsilon^2 f_8(\zeta_1 f_1 - x f_1')(\zeta_0 - \frac{5}{2}) \\
&\quad - \chi_m \frac{\mathcal{R}_m \delta_0}{q m_s}\left(\frac{3}{2\zeta_0}\psi' f_5 + \psi f_5'\right) + \chi_m \mathcal{R}_m \varepsilon^2 \zeta_0 f_1 f_2 \\
&\quad + \chi_m \mathcal{R}_m \varepsilon^2 (f_3 + x f_2)(f_1' - f_1 \tilde{f}_4) && \text{(A.8)}
\end{aligned}
$$

where $\mathcal{R}_m = \frac{r u_0}{v_{mo}} = p/\varepsilon$ is the magnetic Reynolds number. When the ideal MHD regime becomes relevant, these equations write respectively

$$
\begin{aligned}
(f_3 + x f_2)\psi' &= \zeta_0 \psi f_2 && \text{(A.9)} \\
(f_3 + x f_2)(f_1' - f_1 \tilde{f}_4) &= \frac{\delta_0}{q m_s \varepsilon^2}\left(\frac{3}{2\zeta_0}\psi' f_5 + \psi f_5'\right) - \zeta_0 f_1 f_2 && \text{(A.10)}
\end{aligned}
$$

We need to complement this set of ODEs with an energy equation providing f_7. Isothermal magnetic surfaces are represented by $T/T_0 = 1$ along each surface anchored at a radius R_0, which translates into $f_7 = \psi^{-1/\zeta_0}$. The system of ODEs requires the following boundary values

$$
\begin{aligned}
&f_1(0) = f_3(0) = 0 \\
&f_2(0) = f_4(0) = f_5(0) = \psi(0) = f_7(0) = f_{10}(0) = 1 \\
&f_2'(0) = f_4'(0) = f_5'(0) = \psi'(0) = f_7'(0) = f_{10}'(0) = 0 \\
&f_1'(0) = -1 \\
&f_3'(0) = \xi - 1
\end{aligned}
$$

We thus get a complete set of equations that can be formally written as $M.X = P$, where M is a matrix and P a vector depending only on the variable x and the functions f_i, while X is a vector of their derivatives f_i'. Propagating the equations requires to get $X = M^{-1}P$, where M^{-1} can only be computed as long as the determinant of the matrix M does not vanish. This occurs at the disk equatorial plane $x = 0$ (which is a fixed point of nodal type) and at each critical point of the outflow (see Ferreira and Pelletier 1995 for more details). The integration cannot therefore start at $x = 0$ and a Taylor expansion must be made.

APPENDIX B

Computing the Grad-Shafranov constraint

In this section we compute the GSE equation at the Alfvén point and discuss the constraint it imposes on a shooting method like the one we use to compute the self-similar solutions. Computing the GSE at the Alfvén point leads to

$$\frac{\mathrm{d}\mathcal{B}_r}{\mathrm{d}a} - \left.\frac{\nabla a \cdot \nabla m^2}{4\pi R_A^2 \rho_A}\right|_A + g_A \Omega_* \frac{\mathrm{d}\Omega_* R_A^2}{\mathrm{d}a} + (1-g_A)\Omega_* R_A^2 \frac{\mathrm{d}\Omega_*}{\mathrm{d}a} + \left.\frac{B_\varphi^2 + B_p^2}{4\pi\rho_A}\right|_A \frac{\mathrm{d}\ln\eta}{\mathrm{d}a} = 0, \tag{B.1}$$

where $\mathcal{B}_r = \mathcal{B} - \Omega_\star^2 R_A^2$. We can compute the derivatives of the MHD invariants at the Alfvén point as

$$\left.\frac{\mathrm{d}X}{\mathrm{d}a}\right|_A = \left.\frac{\mathrm{d}X}{\mathrm{d}a_0}\right|_A = \frac{\zeta_X}{\zeta_0}\frac{X}{a_0} = \zeta_X \frac{X}{B_{z0} R_0^2}, \tag{B.2}$$

for an invariant X of radial exponent ζ_X, and ζ_0 the radial exponent of a. We can then compute the different terms like so

$$\left.\frac{B_\varphi^2 + B_p^2}{4\pi\rho_A}\right|_A \frac{\mathrm{d}\ln\eta}{\mathrm{d}a} = \frac{\zeta_4}{2}\frac{B_{pA}^2}{4\pi\rho_A B_0 R_0^2}\left(1 + g_A^2\frac{\omega\lambda}{v_A^2}\right) = \frac{\Omega_{K0}^2 R_0^2}{B_0 R_0^2}\frac{\zeta_4}{2} v_A^2 \left(1 + g_A^2 \frac{\omega\lambda}{v_A^2}\right), \tag{B.3}$$

where we use Eq. (2.153) to compute the toroidal field at the Alfvén point. We also use the fact that $B_{pA} = \sqrt{4\pi\rho_A} u_{pA}$ so that $B_{pA}/B_{z0} = \kappa v_A$. We then obtain

$$\frac{\mathrm{d}\mathcal{B}_r}{\mathrm{d}a} + g_A \Omega_* \frac{\mathrm{d}\Omega_* R_A^2}{\mathrm{d}a} + (1-g_A)\Omega_* R_A^2 \frac{\mathrm{d}\Omega_*}{\mathrm{d}a} = \frac{\Omega_{K0}^2 R_0^2}{B_0 R_0^2}\left[1 + \frac{\omega^2}{2} + \frac{\omega\lambda}{2}(4g_A - 3)\right], \tag{B.4}$$

where $\mathcal{B}_r$ is evaluated at the SM surface. The final term, of the form $\nabla a \cdot \nabla m^2$ requires some more work.

First we introduce a supplementary constraint. Indeed, self-similarity introduces a geometrical constraint by imposing a conical Alfvén surface. Along a magnetic surface, one has necessarily $B_z/B_{z0} - \frac{z}{R} B_R/B_{z0} = (R/R_0)^{-2}$. Defining the local outflow opening angle as $\tan\vartheta = B_R/B_z$, allows to write

$$\cos\vartheta - \frac{z}{R}\sin\vartheta = \frac{B_0 R_0^2}{B_p R^2}, \tag{B.5}$$

which is verified everywhere along the magnetic surface. Using, $B_{pA}/B_{z0} = \kappa v_A$ allows us to write the geometrical self-similar constraint at the Alfvén surface as

$$\cos\vartheta_A - \frac{\omega}{\kappa\lambda v_A} = \frac{z_A}{R_A}\sin\vartheta_A. \tag{B.6}$$

Since the Alfvénic mach number is only a function of the self-similar variable x, we can write

$$\nabla a \cdot \nabla m^2 = \frac{\mathrm{d}m^2}{\mathrm{d}x} \nabla a \cdot \nabla x = \frac{\mathrm{d}m^2}{\mathrm{d}x} \left[-x B_z - \frac{B_R}{\varepsilon} \right]. \tag{B.7}$$

We can then use Eq. (2.131) to compute $\left.\frac{\mathrm{d}m^2}{\mathrm{d}x}\right|_A$ by Taylor expanding next to the Alfvén point, we find

$$\left.\frac{\mathrm{d}m^2}{\mathrm{d}x}\right|_A = \frac{2}{g_A} \frac{B_{RA}}{B_{z0}} \varepsilon \left(\frac{R_A}{R_0} \right)^2 , \tag{B.8}$$

After projecting and using Eq. (B.6) we find

$$\left.\nabla a \cdot \nabla m^2\right|_A = \frac{2}{g_A} \left(\frac{R_A}{R_0} \right)^2 \frac{B_{pA}^2}{B_0} \left(\frac{\cos\vartheta_A \omega}{\kappa \lambda v_A} - 1 \right). \tag{B.9}$$

The GSE can then be simplified into

$$g_A (g_{\mathrm{GS}} - g_A) = (g_B^2 - g_A^2) \left(1 - \frac{\cos\vartheta_A \omega}{\kappa \lambda v_A} \right), \tag{B.10}$$

where

$$g_{\mathrm{GS}} = \frac{3}{4} - \frac{2 + \omega^2}{4 \omega \lambda} - \frac{\zeta_4}{4} g_B^2, \tag{B.11}$$

is another maximal value for g_A, imposed by the transverse equilibrium of the magnetic surfaces. To proceed further we need to square Eq. (B.6) this leads to

$$\left[1 + \left(\frac{z_A}{R_A} \right)^2 \right] \cos^2\vartheta_A - \frac{2\omega}{\kappa \lambda v_A} \cos\vartheta_A + \frac{\omega^2}{\kappa^2 \lambda^2 v_A^2} - \left(\frac{z_A}{R_A} \right)^2 = 0, \tag{B.12}$$

we can solve this quadratic equation to express the local outflow opening angle at the Alfvén point as a function of the MHD invariants

$$\cos\vartheta_A = \frac{\frac{\omega}{\kappa\lambda v_A} + \frac{z_A}{R_A} \sqrt{1 + \left(\frac{z_A}{R_A}\right)^2 - \left(\frac{\omega}{\kappa\lambda v_A}\right)^2}}{1 + \left(\frac{z_A}{R_A}\right)^2}. \tag{B.13}$$

Inserting the expression above into Eq. (B.10) allows to finally express the GS constraint as a quadratic equation on $X = g_A/g_B$

$$(k^2 c^2 + \cos^2\Psi_A) X^2 - 2cX(k^2 - \sin^2\Psi_A) + \frac{k^2 - 1}{k^2} (k^2 - \sin^2\Psi_A) = 0 \tag{B.14}$$

where $c = g_{\mathrm{GS}}/g_B$ and $k^2 = \kappa^2/\kappa_{\mathrm{min}}^2$ with the minimum mass load κ_{min} defined as

$$\kappa_{\mathrm{min}}^2 \lambda^3 g_B^2 = \omega. \tag{B.15}$$

This equation provides the absolute lower limit for κ in order to obtain a super-A outflow. Indeed, for $g_A = 0$ the GS constraint can only be satisfied for a minimum value $k^2 = 1$ (see Eq. B.14).

The GS constraint (B.14) shows that there are always two positive roots

$$\left.\frac{g_A}{g_B}\right|_{\pm} = \frac{c(k^2 - \sin^2\Psi_A) \pm \cos\Psi_A \sqrt{(k^2 - \sin^2\Psi_A)\left(c^2 - \frac{k^2-1}{k^2}\right)}}{k^2 c^2 + \cos^2\Psi_A}. \tag{B.16}$$

APPENDIX C

Turbulent closure fits

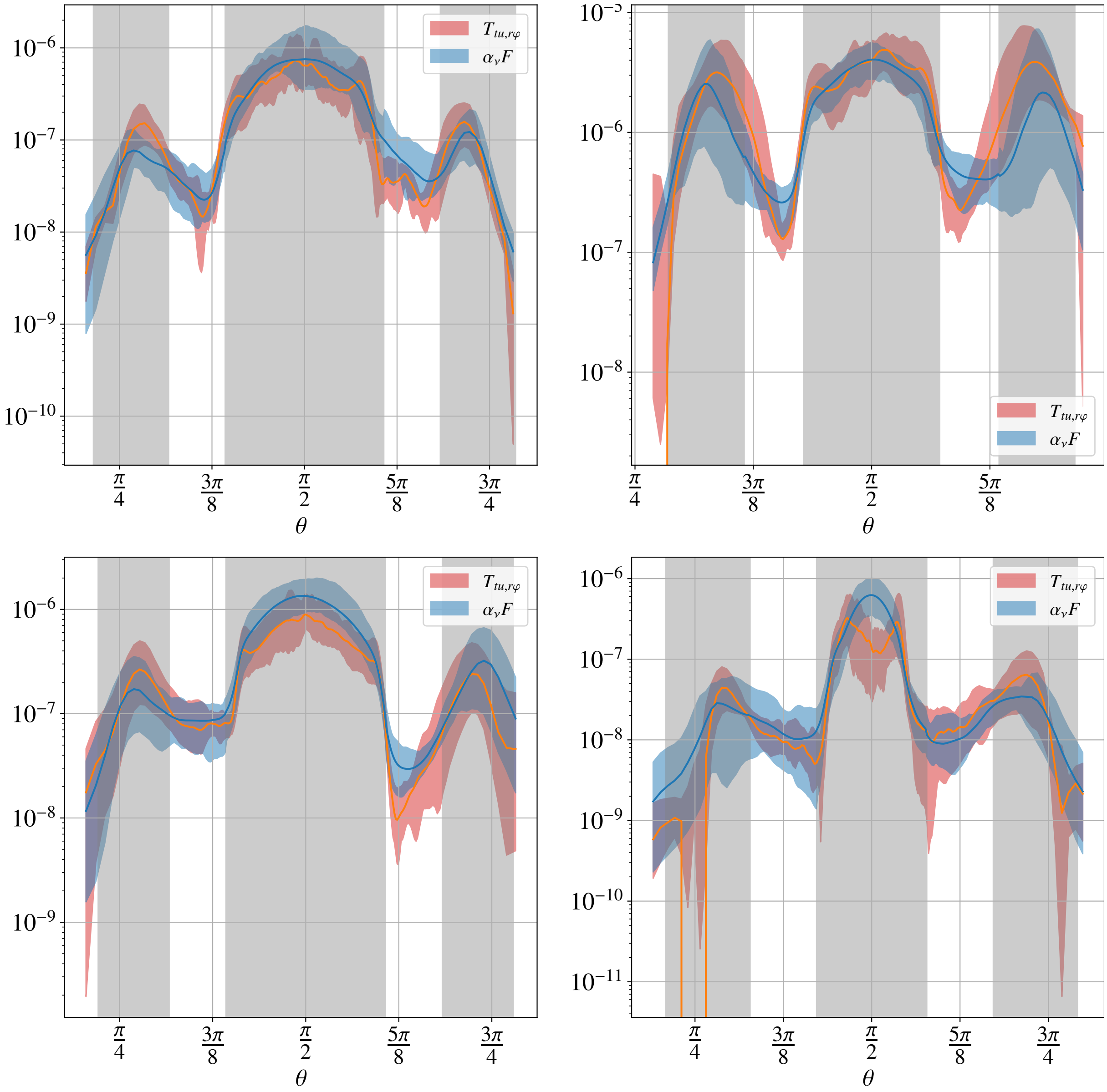

Figure C.1: Radial turbulent stress as a function of the latitudinal coordinate in red, the shaded region shows the typical deviation in the radial range, $R \in [6, 10]$, while the solid line is the radial average. In blue we show the average fit where the shaded region shows the typical deviation in the same radial range and the solid line is the radial average, the values of the average fit parameters are in Eq. (5.11). The different panels correspond to different simulations: top,left: SB4, top,right: SB3, bottom,left: S2pi, bottom,right: SEp.

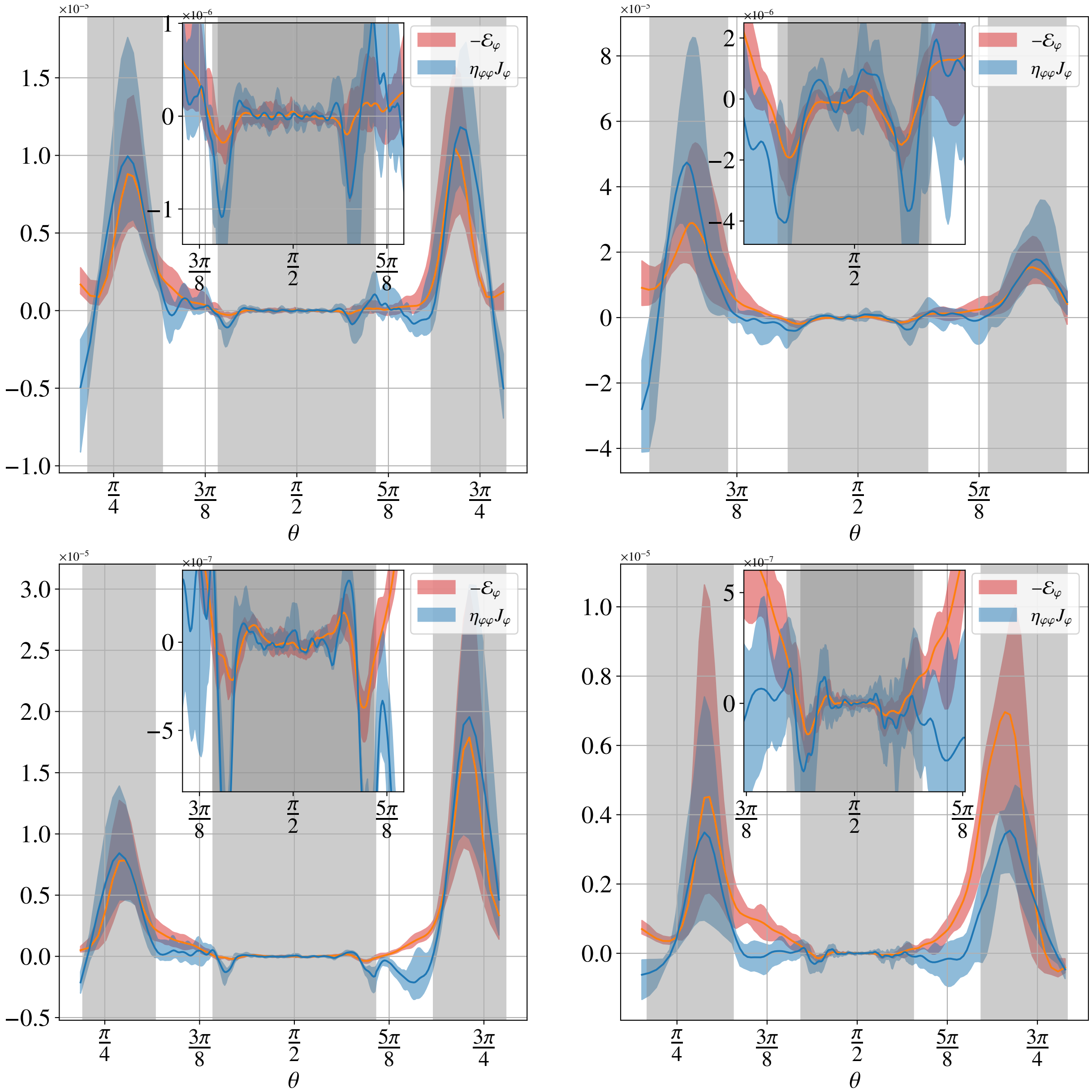

Figure C.2: Toroidal turbulent emf as a function of the latitudinal coordinate in red, the shaded region shows the typical deviation in the radial range, $R \in [6, 10]$, while the solid line is the radial average. In blue we show the average fit where the shaded region shows the typical deviation in the same radial range and the solid line is the radial average, the values of the average fit parameters are in Eq. (5.25). The different panels correspond to different simulations: top,left: SB4, top,right: SB3, bottom,left: S2pi, bottom,right: SEp.

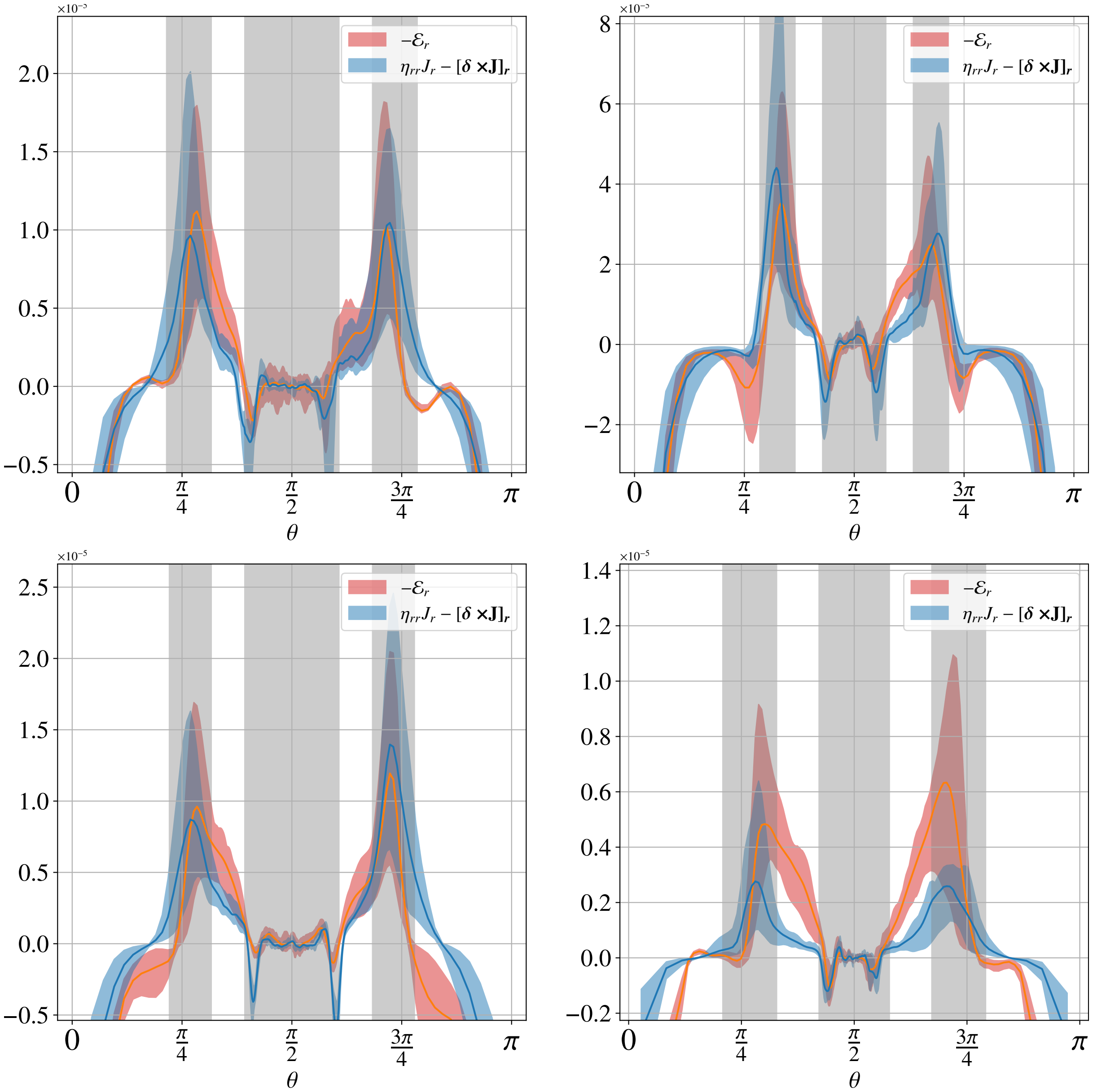

Figure C.3: Radial turbulent emf as a function of the latitudinal coordinate in red, the shaded region shows the typical deviation in the radial range, $R \in [6, 10]$, while the solid line is the radial average. In blue we show the average fit where the shaded region shows the typical deviation in the same radial range and the solid line is the radial average, the values of the average fit parameters are in Eq. (5.28). The different panels correspond to different simulations: top,left: SB4, top,right: SB3, bottom,left: S2pi, bottom,right: SEp.

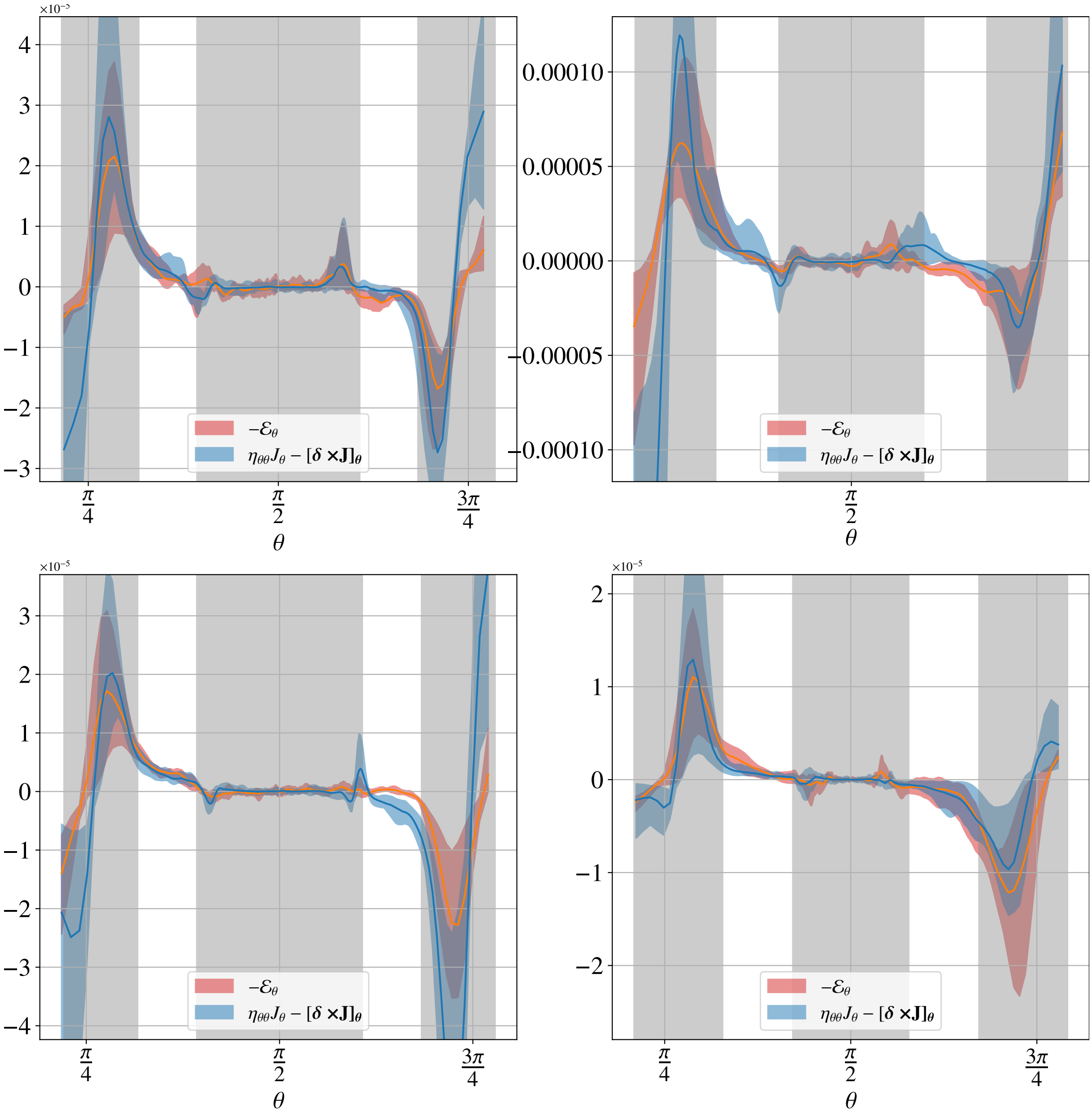

Figure C.4: Latitudinal turbulent emf as a function of the latitudinal coordinate in red, the shaded region shows the typical deviation in the radial range, $R \in [6, 10]$, while the solid line is the radial average. In blue we show the average fit where the shaded region shows the typical deviation in the same radial range and the solid line is the radial average, the values of the average fit parameters are in Eq. (5.29). The different panels correspond to different simulations: top,left: SB4, top,right: SB3, bottom,left: S2pi, bottom,right: SEp.